Dynamics of pyroclastic density currents

A thesis presented in partial fulfilment of the requirements for the degree of Doctor of Philosophy in Earth Sciences

At Massey University, Palmerston North, New Zealand

Eric Christophe Pascal Breard

2016

"The only real knowledge is experience." E.

Rare painting of a pyroclastic flow that likely occurred during the 1810 Vesuvius eruption. Alfano and Friedlander, Die Geschichte des Vesuv, plate 35.

Abstract

Pyroclastic density currents (PDCs) are the most dangerous mass flows on Earth. Yet they remain poorly understood because internal measurements and observations are hitherto non-existent. In this thesis, the first measurements and views into experimental large-scale PDCs synthesized by "column collapse" provide insights into the internal structure, transport and emplacement dynamics of dense PDCs or pyroclastic flows.

While from an outside point of view, PDCs resemble dilute gravity currents, the internal flow structure shows longitudinal and vertical complexities that greatly influence the PDCs' propagation and emplacement dynamics. Internal velocity and concentration profiles from direct observations provide the evidence of an unforeseen intermediate zone that plays an important role into the transfer of mass from the ash-cloud to the underflow. The intermediate zone is a "dense suspension" where particle cluster in bands to form mesoscale structures. These reduce particle drag and yield an extreme sedimentation rate of particles onto the newly-formed underflow. These findings call into question the existing paradigm of a continuous vertical concentration profile to explain the formation of massive layers and an underflow from ash-clouds. Instead, a sharp concentration jump occurs between the intermediate zone, with concentrations of the order of few volume percent, and the underflow, with concentrations of c.45%.

PDCs were found to be composed of 4 main zones identified as the underflow, and the ash-cloud head, body and wake. Following the evolution of the PDC structure over time allows the formation of a complex ignimbrite deposit sequence to be uncovered, reproducing experimentally the "standard ignimbrite sequence" reported from field studies. Experiments revealed that each flow zone deposited the particulate load under contrasting emplacement timescales (spanning up to 5 orders of magnitude), which are primarily controlled by the concentration of the zone.

The ash-cloud head is the most dynamic zone of the PDC, where proximally mass is intensively transferred downward and feeds the underflow front, while at all times, the finest particles are entrained upward and feed the wake through detachment of large Kelvin-Helmholtz instabilities. Subsequently, kinematic coupling between the moving underflow and overriding ash-cloud leads to a forced-supercriticality, preferentially affecting the head. The wide range of particle sizes and densities yield a spectrum of gas-transport behaviours ranging from a poorly coupled and rapid-sedimenting mesoscale regime up to a homogeneously coupled long-lived suspending regime.

Internal velocity and concentration profiles illuminate the role of boundary velocity, which yields forced-acceleration of the ash-cloud. Kinematic coupling of the ash-cloud with the underflow induces a velocity at the lower flow boundary, while shear stress at the ash-cloud/underflow wanes and results in the shrinking of the maximum velocity and concentration heights. Therefore, the ash-cloud can reach high velocities and multiply its destruction potential.

The experimental work presented in this thesis provides the first datasets of the internal physical properties of PDCs, which can be used to test the validity of current numerical models and highlight their limitations.

This thesis also presents the study of a small hydrothermal blast that occurred at Mt. Tongariro, New Zealand, on the 6th of August 2012. The study of the blast is subdivided into two phases: the PDC phase and the ballistic phase. The detailed study of the PDC along the main propagation axis highlighted the role of the longitudinal zoning of the current, which was reflected in the complex tripartite deposit architecture.

The study of the blast-derived ballistic crater field revealed a zone of high crater density that was related to the focus of ballistic trajectories around the main explosion direction. Simple inverse ballistic modelling provided evidence for a shallow blast (c. 5° above horizontal) from Te Maari. Furthermore, a comparison of ballistic block lithologies confirmed the origin of the elongated succession of craters or fissures formed by successive blasting during the eruption.

Acknowledgments

I would like to express my gratitude to those who played a role during the past three years and contributed to this academic journey that one calls a PhD.

First and foremost, I thank Gert Lube who gave me the opportunity to be part of an extraordinary large-scale project and introduced me to the marvellous Tongariro volcano with the recent Te Maari eruption. I am very grateful for the outstanding supervision he provided in all possible aspects. By sharing his knowledge, passion, and philosophy of research, the past years have been fascinating.

I am thankful to my co-supervisors Shane Cronin (University of Auckland) and Jim Jones (Massey) who helped through advices and fruitful discussions to improve my work. I also thank Greg Valentine (Univ. at Buffalo), and Joe Dufek (Georgia Tech, Atlanta) for discussion regarding the physics of pyroclastic density currents. Many thanks to Luke Fullard (Massey), with whom I became very interested in the physics of granular flows.

I feel very grateful to Anja Möbis for her immense help with the LPA analysis, to Kate Arentsen who is the pillar of VRS, to Cristian Montanaro and Bettina Scheu (LMU, Munich) with whom I had a great time studying ballistics at Tongariro and to Harry Keys (D.O.C), who allowed me to be part of the team studying the 2012 Tongariro eruption.

Thanks go to all the staff and students at Massey University, including Javier Agustin-Flores, Marco Brenna, Magret Damaschke, Gaby Gomez, Matt Irwin, Adam Neather, Natalia Pardo, Bob Stewart, Rafael Torres-Orozco, Manuela Tost, Georg Zellmer, Liza Haarhoff, David Feek, Rickus Van Niekerk, Bob Toes, Daniel Farley, Clive Bardell, Damian Jones, Anthony Wade, David Wiltshire and Jon Procter.

This PhD work has been supported through a MARSDEN grant of the Royal Society of New Zealand (MAU0906) awarded to Gert Lube, Shane Cronin and Jim Jones.

The completion of a PhD is a result of years of work and guidance that were not solely restricted to the past three years. I am thankful to Jean-Luc Le Pennec who is the first person that introduced me to pyroclastic density currents and their wonders in 2010. Furthermore, I am very grateful to Eliza Calder for reinforcing my passion for PDCs and for directing me to Gert as a potential PhD advisor.

This short tribute would not be complete without a special thanks to Layla, who has known me since my early days in geology and is my best support, my friends here (particularly those amongst "*La Familia Purili*" with whom life in PN was much better than expected), Braden for being "Mr. Awesome", Aalderik for his help with the large-scale experiment and friendship, and my family who accepted that I follow my passion *at world'end*. Nonetheless, it is not "*any"* end, Middle Earth is the most beautiful land I encountered. At last, I ought to thank Pete Jackson for portraying such paradise in LOTR, which made me dream of this country since childhood… a place where volcanoes and fantasy mingle.

Table of Contents

List of Figures

List of Supplementary Figures

List of Tables

List of Supplementary Tables

Chapter 1 - Introduction

Chapter contents

Chapter 1 – Introduction

1.1 Research problem and motivation

Pyroclastic density currents (PDCs) are the most lethal volcanic threat known to humankind. Over 200 million people are directly endangered by this common and highly dangerous phenomenon (Sulpizio et al., 2014). As ground-hugging and hot multiphase flows of particles and gas, PDCs can travel great distances at hurricane speeds with devastating consequences for life and property (Druitt, 1998). The enormous damage or impact from PDCs can at times escalate from regional to global scale (Branney and Kokelaar, 2002). The devastating impact of PDCs and their high frequency of occurrence at many volcanoes worldwide, makes research towards better understanding and forecasting the effects of PDC-forming eruptions a high priority in volcanology (Cashman and Sparks, 2013).

Pyroclastic density currents also represent one of the most spectacular and most complex natural flow processes on Earth. This can be attested by the enormous variability in their physical appearance or character (Branney and Kokelaar, 2002), as well as through the magnitude of PDC damage (Valentine, 1998). The high complexity of PDCs is also indirectly manifested through the very broad range of geometric and textural characteristics of their resulting deposits (Fisher and Schmincke, 1984; Cas and Wright, 1987). Furthermore, and from a fundamental sciences point of view, PDCs encompass an impressive range of strongly interdependent fluid- and thermodynamic states, transport regimes and processes (Dufek et al., 2015). These include for instance granular flow transport, multi-scale turbulent transport of fluid-solid suspensions, the propagation of shock-waves in compressible fluid-solid mixtures, the origin and fate of solid and fluid friction and the exchanges of matter, momentum and energy at turbulent-non-turbulent interfaces or boundary layers. The co-

existence of these processes in PDCs, as well as the wide range of spatial and temporal scales at which they occur, is largely unrivalled in nature. The scientific challenges posed by this complexity and the varied impacts of those processes probably explain why PDCs have never been a research area solely for Earth and hazard Scientists. Instead, PDCs always have and continue to puzzle geophysicists, physicists, applied mathematicians, engineers and archeologists alike.

Research on PDCs is a relatively young discipline in Earth Sciences with only approximately half a century of scientific investigation into their character and behaviour (Cashman and Sparks, 2013). Due to the multidisciplinarity of research approaches, and also through key lessons learnt during and immediately after PDC-forming eruptions (i.e. Hoblitt et al., 1981), our understanding has greatly increased over this time. This has seen the rise and fall of several contrasting schools of thought, shifts in paradigms, as well as some of the most intensely fought debates in volcanology (Branney and Kokelaar, 2002).

However, despite considerable progress and effort, PDCs still represent one of the most poorly understood volcanic processes (Cashman and Spark, 2013). In particular, a unified theory that can explain the complex PDC flow behaviour, as well as the quantitative formation of its diverse sedimentary records, and that can be confidently deployed in hazard models for public safety, is currently lacking (Dufek et al., 2015). The main reason why such a comprehensive theory is so difficult to develop is the near absence of direct observations and the lack of any quantitative measurements of the interior of PDCs. Because of the unpredictability of PDCs and due to their dangerous nature (Druitt, 1998; Wohletz, 1998; Valentine and Fisher, 2000), these measurements from within real-world flows are probably out of reach for the foreseeable future. As a consequence, there is a critical need to generate validation datasets to thoroughly test and advance existing computational hazard models. The lack of observational data also strongly hinders the advancement of robust theoretical flow

and sedimentation models. Such quantitative models would be helpful to interpret the multitude of geological deposit data for effective use in hazard planning and mitigation efforts. Because of the complexity of physical processes involved in PDCs, which are not completely understood, many aspects of PDC behaviour and hazard impact can also not yet be predicted via computational simulations. Analogue laboratory experiments are a key resource to bridge this gap and to simulate simplified processes that are thought to occur in PDCs (Dellino et al., 2007). However, most existing experimental set-ups have now been identified as suffering from issues of scale where critical forces are not able to be ratioed to represent real world flows (Andrews and Manga, 2011; Andrews and Manga, 2012; Roche, 2012; Rowley et al., 2014).

Recent development of large-scale experimental facilities has provided a novel approach to create the missing view inside PDCs (Lube et al., 2015). Experimental set-ups of different scales and purposes have been designed in Italy and in the United States for the study of PDCs with very low-particle concentrations at variable temperatures (Andrews, 2014; Dellino et al., 2014), in Mexico for research on intermediate-scale PDC analogues with very high particle concentrations at ambient temperatures (Sulpizio et al., 2013), and in New Zealand where the complete range of PDC-typical particle concentrations and a wide range of temperatures can be studied. Currently, the New Zealand eruption simulator PELE (the Pyroclastic flow Eruption Large-scale Experiment) represents the largest and most thoroughly scaled PDC experiment of its kind (Lube et al., 2015).

This thesis aims to contribute to the existing fundamental knowledge of PDC behaviour and hazard impacts and to our ability to recognize and interpret some aspects of PDC-forming eruptions from their depositional records. Two main research approaches provide the framework for this research. The largest part of this thesis describes the results of a systematic series of large-scale PDC experiments conducted at PELE (Chapters 3–5). More

than fifty large-scale experiments were successfully conducted that synthesized experimental PDCs with variable bulk particle concentrations, mass fluxes, grain-size distributions, temperatures and substrate boundary conditions. This thesis focuses on the analysis and interpretation of experiments involving flows at high bulk particle concentrations representative of the well-known end-member of PDCs, termed pyroclastic flows. The work was all conducted at ambient temperature.

The second and smaller part of this thesis reports the results of fieldwork on the August 6 2012 PDC-forming eruption of Mount Tongariro in New Zealand (Chapters 6 and 7). In late 2012, a small window of opportunity existed to sample the pristine deposits of this hydrothermal eruption at great detail, before they were largely eroded and reworked in early 2013. This field work was motivated by the need to better understand the dynamics and hazard impacts of hydrothermal eruptions and their PDC-forming aspects in particular. Nationally, results of this work were immediately shared with GNS Science, GeoNet, the Department of Conservation and the University of Canterbury for their effective use in hazard planning and mitigation in the Tongariro National Park.

While both parts of the thesis aim to further our understanding of PDCs, they also come with their own and independent sets of primary research questions and objectives. These objectives are dealt with separately in this thesis, due to the strikingly different behaviour of the experimental pyroclastic flow-type PDCs, investigated under the pre-defined objectives of a multinational research program, and Tongariro blast-like PDCs.

1.2 Research questions and objectives

The first part of this thesis on large-scale experimental PDC simulations is underpinned by the three principal research questions listed below. For each of these questions a set of specific research objectives is defined to guide the investigations.

i. *What do concentrated PDC (pyroclastic flows) look like inside?* In the absence of any real-world observations, this research question aims at using quantitative measurements of characteristic parameters from within well-scaled experimental pyroclastic flows to resolve the long-standing scientific impasse of entrenched and differing paradigms of the nature of PDCs.

   The objectives associated with research question (i) are as follows:

   O1. Test, and where necessary develop, robust methods for the measurement of flow velocity, flow density and turbulence fields in experimental flows from initiation to deposition.

   O2. Determine these fields of velocity, density and turbulence as functions of space and time as the base datasets to be used to quantify the internal flow structure and to contribute to the growing data base for the internationally attempted validation of existing PDC flow and hazard models.

   O3. Analyze the resulting internal flow structure with regards to the existence or non-existence of marked internal rheological interfaces, as well as to illuminate two contrasting hypotheses of either continuous density stratification within PDCs or the occurrence of marked density boundaries.

ii. *How are particles transported and deposited in pyroclastic flows?* Existing qualitative and theoretical models suggest that a broad range of gas-particle

transport regimes can exist in PDCs. Furthermore, well-established theoretical models of PDCs anticipate that these transport regimes will vary over time and spatially inside the current. These variations are potentially generated through particle settling, segregation and sedimentation, due to the turbulence structure within PDCs and due to the entrainment of ambient air. To answer this research question, the modes of gas-particle transport will be directly observed and quantified through appropriate non-dimensional numbers.

The objectives associated with research question (ii) are as follows:

O4. Determine the range of gas-particle transport and sedimentation processes in experimental pyroclastic flows through a combination of high-speed video imaging and characterize these through measurements of velocity, density, grain-size, entrainment coefficients and calculations of turbulence fields for a wide range of experimental conditions.

O5. Quantify the space- and time-variant internal PDC structure through appropriate non-dimensional numbers that are based on the above measurements and to relate these to the traditional PDC analogue model of gravity currents.

O6. Determine whether vertical and horizontal stratification within the experimental PDCs lead to space- and time-variant variation of gas-particle transport and how this affects the PDC destructive potential.

iii. *What are the dynamics of co-existing dense and dilute regions within PDCs and how does their interaction influence flow runout, flow structure and flow hazard potential?* Several lines of evidence suggest that PDCs are often composed of a dense underflow and an overriding dilute ash-cloud. Work under this research

question aims to acquire the first direct observations of the processes that govern PDC transport in this situation and their origin. The objectives associated with research question (iii) are:

O7. Determine how dense and dilute flow regions develop and quantify how they dynamically interact during flow runout.

O8. Investigate whether these interactions influence the PDC structure, and the flow velocity and runout length through the analyses of experimental data under a wide range of starting conditions.

The second part of this thesis, which is focused on analyzing the deposits of the 2012 PDC-forming eruption of Mount Tongariro, is based on two main research questions. Together with their sets of research objectives, these questions are detailed below.

iv. *What can the depositional record of ballistic impact craters teach us about the eruption sequence, spatial distribution, and geometry of lateral explosions at the origin of PDC-forming hydrothermal eruptions?* High-velocity blast-like PDCs and impacts from more than 20,000 ballistics were the most significant hazards during the 2012 Tongariro eruption. Neither of these two hazards, and particularly their interplay, are well understood and consequently, in New Zealand, quantitative hazard models for these two processes did not exist prior to the eruption.

The rare preservation of the ballistic impact craters and the early recognition of the hazards associated with them in the 2012 event define the following research objectives:

O9. Develop a method that allows the use of the complete and spatially variable stratigraphic record of a hydrothermal eruption to reconstruct the sequence, order and spatial distribution of events. Apply this method to the August 6 2012 Tongariro eruption with an emphasis on the ballistic record and test this against independent records from direct observations and geophysical monitoring data.

O10. Apply conventional ballistic modelling techniques to delineate the source locations of individual explosions and to approximate the poorly understood starting conditions of blast-like PDCs.

v. *How can the depositional record of blast-like hydrothermal PDCs be used to learn about the flow structure, gas-particle transport and deposition dynamics of these frequent hazards?* The PDC deposits of the August 6 2012 Tongariro eruption present a rare complete record of such events.

Field and laboratory work on these deposits was motivated by the following research objectives:

O11. Develop a type stratigraphy for hydrothermal PDC deposits and use sedimentological data to interpret the transport and emplacement conditions of the Tongariro event.

O12. Thoroughly review theoretical flow models for dilute PDCs and blasts and apply the most robust of these to approximate the PDC structure and hazard impact potential.

1.3 Thesis outline and structure

This thesis comprises eight chapters, and an appendix including specific datasets included in digital appendices. After this introduction, a literature review describing the main concepts based on the sedimentology and physics used in volcanology to characterize PDCs is presented (Chapter 1). Chapter 2 presents the methodology of this thesis and includes a description of the large-scale apparatus PELE, the measurement methods used in large-scale experiments, as well as the scaling of the synthesized PDCs. The second section of the thesis (Chapters 3–5) reports the results of the large-scale PDC experiments. It is composed of three individual chapters that target research questions 1-3. Chapters 3-5 are presented in the layout and length requirements of three international peer-review journals to which work has been submitted for publication.

Chapter 3 targets research question (i) and describes the first 'view' inside PDCs in the form of a short research letter. Here the discovery of mesoscale turbulence structures in PDCs is presented. Experimental measurements characterizing this 'intermediate' gas-particle transport regime are shown to demonstrate the importance of this transport regime for the formation of underflows from an ash-cloud. Furthermore, Chapter 3 describes how the formation of complex PDC deposits (i.e. the so-called standard ignimbrite unit) can be linked to the flow structure and to the deposition timescales of different PDC flow regions.

Chapter 4 presents a full-length research article that provides further details on how the internal flow structure of PDC develops during runout (research question ii) and it introduces direct observations and measurements inside the flows to determine the nature of gas-particle transport (research question ii). This chapter highlights that the vertical velocity and density structures of concentrated PDCs differ in some fundamental aspects from existing theoretical models and explains this through the dynamics of interacting dense and dilute flow regions.

Together with measurements of entrainment of air into the flows and characterization of flow turbulence, the traditional gravity current model of the PDC structure is updated to account for the here-discovered transport processes. The data are also used to image the flow-internal distribution of dynamic pressure, together with the damage potential of PDCs. These data also highlight the occurrence of successive pressure pulses, which should be considered in the interpretation of PDC impacts on infrastructure and landscapes.

Chapter 5 presents a full-length research article with a focus on research question (iii) of the dynamics of co-existing dense and dilute PDC flow regions. This chapter presents the discovery of forced supercriticality of PDCs as an important state of PDC motion resulting from this interaction. It is shown that forced supercriticality allows PDCs to travel considerably faster and further than predicted by earlier theoretical models. Furthermore, dimensional analysis is used to develop a semi-empirical model that allows the prediction of the 'invisible' internal flow structure and vertical distribution of dynamic pressure from snapshots of the outer geometry of the PDC.

The third section of the thesis presents the studies of the PDC-forming eruption of Tongariro on August 6 2012. Chapter 6 presents a full-length article published in the Journal of Volcanology and Geothermal Research that aims at answering research question (iv). Here, stratigraphic data from fieldwork are used to identify the source vents and the order of multiple hydrothermal explosions of the volcano. Furthermore, it is shown that the analysis of the spatial distribution of ballistic impact craters can be used to characterize the velocity and geometric shape of hydrothermal eruptions, which trigger the formation of blast-like PDCs.

Chapter 7 presents a full-length research article published in the Bulletin of Volcanology that addresses research question (v). A sedimentological analysis of the deposits of the blast-like PDCs of the Tongariro eruption is used to establish a type model for PDC deposits of this

kind. The sedimentary data, in combination with topography data, are also used to constrain the internal structure of blast-like PDCs as well as PDC deposition.

Finally, this thesis is concluded with a synthesis and conclusion (Chapter 8). The initial research questions and objectives are revisited and a summary is provided along with suggestions for future directions of research in the field of PDCs.

Information included in the thesis appendices tries to serve the following purposes. Firstly, copies of three additional research articles are provided, which resulted from major contributions of the thesis author as a second author in other aspects of the large-scale experimental work and in the emergency response to the 2012 Tongariro eruption. These articles are added here, because certain aspects of the results in Chapters 3–7 are based on information and data documented in these articles. Secondly, under the framework of several research programmes funded by the Royal Society of New Zealand Marsden Fund and the New Zealand Natural Hazards Research Platform, as well as the International Association of Volcanology and Chemistry of the Earth Interior and the Volcanology Cyber-infrastructure VHub, large-scale experimental data derived in this thesis form part of the first international and freely available validation dataset for PDC models. A selection of the (considerably larger) raw dataset is documented in electronic form as appendix A.

Thirdly, selected video files of large-scale experiments termed supplementary videos in Chapters 3–5 are included in appendices A. These are intended to help visualise important aspects of the new processes described in these Chapters.

1.4 Literature review

1.4.1 Terminology

A compilation of terms used in this thesis is provided in the following list.

Ash: description of volcanic particles which are smaller than 2 mm in diameter.

Base surge: a turbulent volcanic density current that flows generally radially outward from the base of a partially collapsing vertical eruptive column produced during phreatomagmatic or hydromagmatic eruptions.

Bedform: describes the surface configuration of a bed as well as the three dimensional architecture of a group of strata such as dunes, ripples or planar beds.

Bedset: a sequence of beds that can be distinguished by their internal structure, color, grain-size and that are usually separated from other bedsets by unconformities.

Bomb: volcanic clast larger than 63 mm of diameter with a juvenile origin.

Block: volcanic clast larger than 63 mm of diameter with a non-juvenile origin.

Flow regime: this term describes the hydraulic conditions of non-cohesive flows that develop bedforms.

Fluidization: condition reached when the gravitational force applied to a bed of particles is balanced by fluid particle drag due to upward propagating gas. Fluidization is thought to occur in near close-packing flows.

Hydrovolcanic: all volcanic eruptions that involve the interaction between meteoric or connate water and lava, magmatic heat or gases.

Ignimbrite: pyroclastic density current deposit composed of variable proportion of ash, pumice and lithics. While the term has usually been historically used to describe welded large-volume PDC deposits, it can be used for pumice-rich PDC deposits regardless of their size.

Juvenile: describes the fresh fragments of volcanic particles produced during an eruption. Typically, glass shards and free crystals are juvenile clasts.

Lapilli: volcanic particle between 2 and 63 mm in diameter.

Lateral blast: laterally directed expulsion of particles caused by rapid decompression of a lava dome or hydrothermal system. Intense ballistic showers and associated PDCs are formed and are characterized by very high velocities (often exceeding 100 m s^{-1}).

Lithic: fragment that is not juvenile, but rather picked up by erosion from the substratum, or during the explosion. It can also be picked up on the way through the crust by magma.

Pore pressure: fluid pressure inside a fluid-particle mixture as measured in the granular matrix. Elevated pore pressure can develop as a result of fluid-particle drag when the mixture has a low permeability.

Transport system: the system carrying particles in the flow until deposition.

Welding: process of compaction and sintering of hot ductile PDC deposits that gives rise to a reduction in porosity and deformation of glass shards.

1.4.2 History

Although encounters between pyroclastic density currents and humans must have tragically occurred in history a countless number of times, the most famous early written description of

a PDC was made by Pliny The Younger who witnessed the AD 79 Vesuvius eruption (Italy). He described the pyroclastic density currents thus: "*Now came the dust, though still thinly, I look back: a dense cloud looms behind us, following us like a flood poured across the land*". Despite this early observation, it was not until the 19th century that more detailed eyewitness accounts of PDCs were made.

The largest and deadliest volcanic eruption in recorded history is attributed to Mount Tambora (Indonesia) on April 10 and 11th 1815. More than 88,000 people died from direct and indirect causes (Zollinger, 1855). A witness described it thus: "*About 7 P.M. on the 10th of April, three distinct columns of flame burst forth near the top of Tomboro Mountain, all of them apparently within the verge of the crater, and after ascending separately to a very great height, their tops united in the air in a troubled confused manner. In a short time the whole Mountain next to Saugur appeared like a body of liquid fire extending itself in every direction. The fire and columns of flame continued to rage with unabated fury until the darkness, caused by the quantity of falling matter, obscured it at about 8 P.M. Stones at this time fell very thick at Saugur-some of them as large as two fists, but generally not larger than walnuts; between 9 and 10 PM ashes began to fall, and soon after a violent whirlwind ensued, which blew down nearly every house in the village of Saugur, carrying the tops and light parts away with it; In the part of Saugur adjoining Tomboro, its effects were much more violent, tearing up by the roots the largest trees, and carrying them into the air together with men, houses, cattle, and whatever else came within its influence".* It is thought that the PDCs that wiped out the village of Tambora were caused by collapse of an eruption column (Stothers, 1984).

Early Europeans have in Papua New Guinea witnessed eruptions that involved PDCs at Manam volcano. In 1919, a missionary described: "*the red stream of lava could be clearly*

seen, but ceased to flow, and dense grey-coloured clouds of vapour were emitted from the crater. When the rumbling ceased a grey brown halo of dust encircled the mountain, which gradually spread for miles over the mainland".

In August 26 1883, an eruption "shook the world". Krakatoa, an Indonesian volcano, erupted and violent tsunamis and PDCs claimed over 36,000 lives. A terrifying eye-witness account was provided by a settler who survived the PDCs that travelled over 40 km across the sea: "*Suddenly, it became pitch dark. The last thing I saw was the ash being pushed up through the cracks in the floorboards, like a fountain. I turned to my husband and heard him say in despair ' Where is the knife?' . . . I will cut all our wrists and then we shall be released from our suffering sooner.' The knife could not be found. I felt a heavy pressure, throwing me to the ground. Then it seemed as if all the air was being sucked away and I could not breathe. . . . I felt people rolling over me . . . No sound came from my husband or children . . . I remember thinking, I want to . . . go outside . . . but I could not straighten my back . . . I tottered, doubled up, to the door . . . I forced myself through the opening . . . I tripped and fell. I realized the ash was hot and I tried to protect my face with my hands. The hot bite of the pumice pricked like needles . . . Without thinking, I walked hopefully forward. Had I been in my right mind, I would have understood what a dangerous thing it was to . . . plunge into the hellish darkness . . . I ran up against . . . branches and did not even think of avoiding them. I entangled myself more and more . . . My hair got caught up . . . I noticed for the first time that [my] skin was hanging off everywhere, thick and moist from the ash stuck to it. Thinking it must be dirty, I wanted to pull bits of skin off, but that was still more painful . . . I did not know I had been burnt."*(Scarth, 1999).

On May the 8th 1902 there occurred one of the most sudden volcano-related tragedies known. After weeks of unrest, Montagne Pelée volcano produced a PDC that reached the city of St

Pierre, located 7 km from the source, killing ~28,000 people and leaving only one or two survivors (Tanguy, 1994). A witness of the eruption described: "*the ground was shaking, not as in an earthquake, but as if tremendous battles were going on within the mountain… All of a sudden, Montagne Pelée appeared to shiver and a kind of groaning was emitted by the crater. The air seemed dead. I was deafened by a fearsome, awful noise. It looked as if all was broken. A flash more dazzling than a lightning happened… A the same time, a cloud that formed on the summit of the Montagne Pelée literally fell on Saint-Pierre with such rapidity that it was impossible for anyone to escape*".

Another witness described the following: "*Then I saw coming out from L'Etang Sec a river of heavy fumes, exceeding dark. These fumes flowed as fluffy clouds with a sinister noise…One could hear the cracking sound of all that went broken, uprooted, crushed by this rolling ram…covering all as with a shivering black shroud.*

The 1980 eruption of Mount St. Helens provided many insights through direct observation of the blast and also from eyewitness accounts of people that sometimes were caught within it (Rosenbaum and Waitt, 1981): "*a very strong wind, which blew flames from a campfire flat along the ground and held braids of hair out horizontally, preceded the blast cloud by about 10-15 s. The witnesses were able to move about in the wind with little trouble, and no trees were toppled by it. No noise was associated with the approach of the cloud, and no concussion or loud noise was noted prior the cloud's arrival. When the cloud arrived, it became totally black and all of the trees seemed to come down at once. The witnesses were instantaneously buried in a combination of timber and "ash" and probably fell into a hole left by a root ball of a blown-over tree. They could talk to each other but see could see nothing. After perhaps 10 s, it got very hot. At this time they could hear their hair "start to sizzle" as it was singed. One witness, who is a baker, estimated the heat to be like a 300 °F*

oven. Pitch boiled out of trees and remained hot enough to cause minor burns several minutes later. The sky cleared suddenly after several minutes and remained clear for a few more minutes. Then a dense ash fall began again."

While rare, witness accounts of pyroclastic density currents at different places and times depict very similar features. They are fast moving, hot currents that overwhelm topography and can be produced by eruption-column collapse, dome collapse or lateral explosions. Interestingly, from distance and at night, hot PDCs have been often confused with lava flows because particles over 450°C emit visible light (Fig. 1.1A). Most commonly, ash-sized particles cool down much more rapidly than coarser clasts, thus ash clouds sometimes mask PDC incandescence at night. In most cases long-exposure photography reveals ash cloud components of PDCs at night (Fig. 1.1.B).

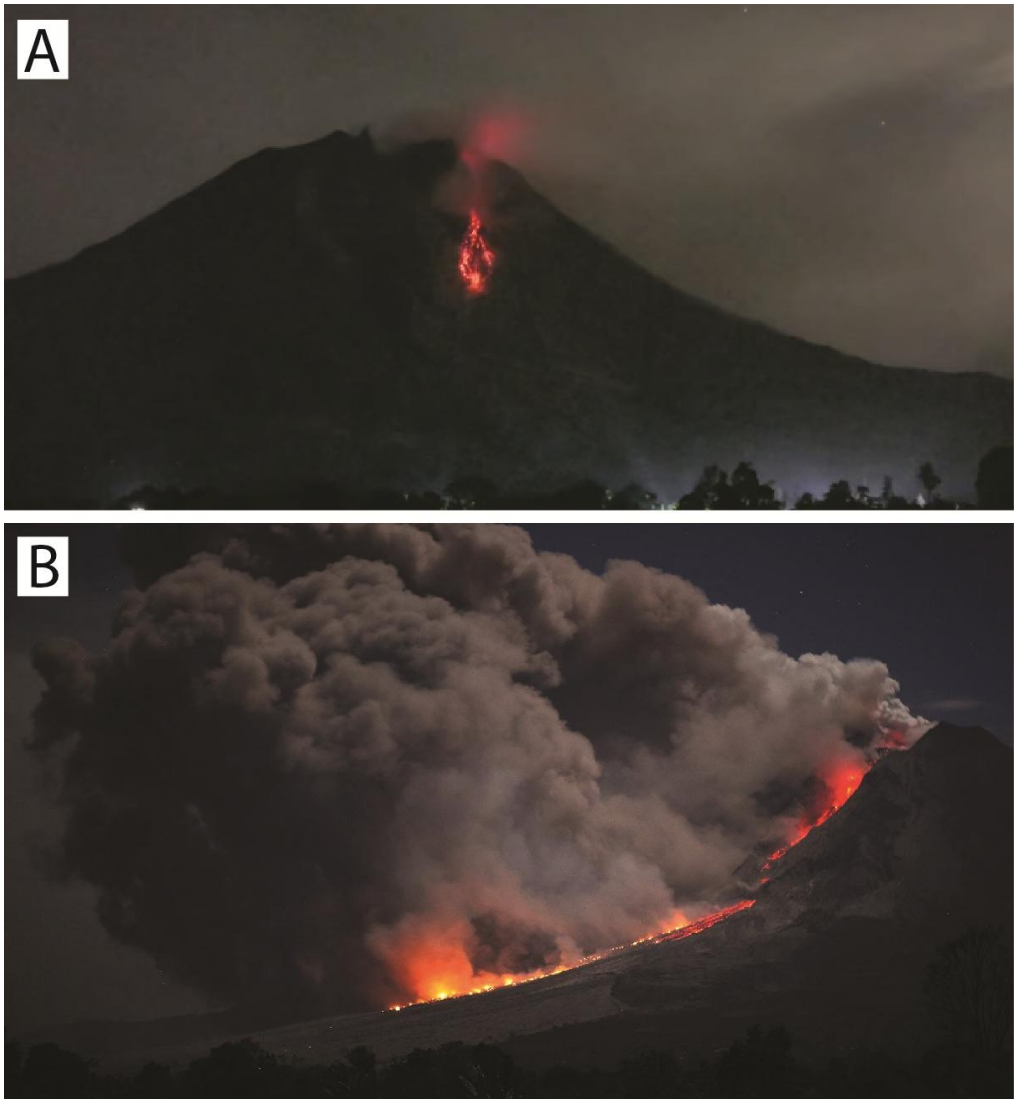

Fig. 1.1. A: A dense PDC at night that looks like a lava flow, Sinabung volcano (Indonesia). B: Picture of a hot and dense PDC at Sinabung volcano (Indonesia). Long exposure allows us to visualize the ash cloud that is cooler (not glowing). Courtesy Richard Roscoe, Photovolcanica

1.4.3 Introduction to pyroclastic density currents

Pyroclastic density currents are inhomogeneous multiphase, ground-hugging flows, composed of hot gas and particles that travel at high velocities (at times hundreds of km hr^{-1}) under the influence of gravity and, because of their greater density than the surrounding atmosphere, to spread over huge areas (Freundt and Bursik, 1998; Wohletz, 1998; Freundt et al., 2000). PDCs have repeatedly threatened lives around the world and sometimes they have been at the origin of large-scale tragedies (Nakada and Ballard, 2000). Despite their deadly

potential, PDCs remain the least well understood of all volcanic phenomena (Cashman and Sparks, 2013). Their extreme violence prevents all direct observations and internal measurements of material properties or physical dynamics. Thus, pyroclastic density currents have been studied at a distance and via multidisciplinary studies encompassing sedimentological, theoretical, numerical, or analogue experimental approaches that involved geologists, physicists, mathematicians and engineers (Druitt, 1998; Sulpizio et al., 2014)

The drive to understand the threat of PDCs to numerous populations living in the proximity of active volcanoes has led to a growing research effort into their properties over the last few decades, with bursts of study occurring especially after large and deadly explosive eruptions (Fig. 1.2).

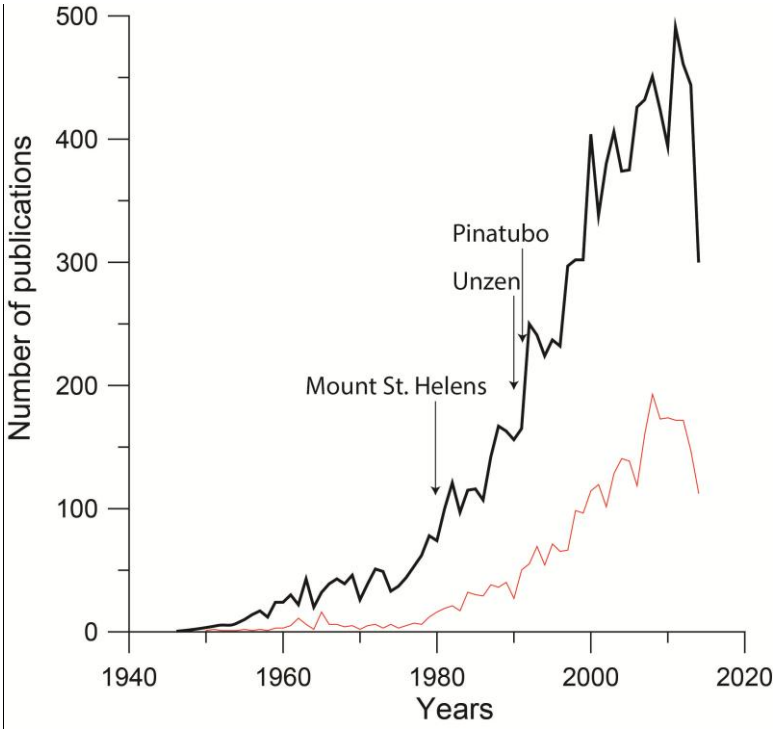

Fig. 1.2. Plot of the number of publications dealing with pyroclastic density currents against time (years) (black line) and the number of those publications that are peer-reviewed articles (red line).

Pyroclastic density currents can be produced by a large variety of volcanic processes, including the collapse of eruption columns, domes and lava fronts, the "boiling over" of low

pyroclastic plumes, and the explosive blasting of pressurized domes, hydrothermal systems or parts of a volcanic flank (Druitt, 1998) (see Section 1.4.5.1). PDCs can be short-lived and unsteady or long-lived and quasi-steady phenomena, and they can be derived from magmatic or phreatomagmatic fragmentation processes (Fisher and Schmincke, 1984; Cas and Wright, 1987; Druitt, 1998). Furthermore, PDCs envelop a very wide spectrum of transport and depositional processes and they produce a large variety of deposit characteristics. Despite a poor understanding of the relationships between deposit and parental flow, most of our current knowledge of PDCs stems from sedimentological studies of their deposits (i.e Branney and Kokelaar, 2002).

PDC deposits

PDC deposits have been investigated for the past 60 years, to understand the origin of small to massive-scaled pre-historic PDC deposits (Smith, 1960; Fisher and Waters, 1970; Ragan and Sheridan, 1972; Crowe and Fisher, 1973) as well as to make sense of major observed events such as the 1980 blast of Mount St Helens (i.e. 1980 blast of Mount St Helens, Hoblitt et al., 1981) or the 2010 eruption of Merapi (Cronin et al., 2013; Komorowski et al., 2013b). In some cases, geological records permitted the reconstruction of eruption scenarios and the understanding of the relationships of PDCs in the context of plinian eruptions and caldera-collapse episodes such as in the eruptions of Vesuvius in 79 AD (Sigurdsson et al., 1985), Krakatoa 1883 (Carey et al., 1996) or that of Toba in c.73,500 yrs BP (Rose and Chesner, 1987).

PDC deposits are extremely variable in every single aspect; they can cover areas from few thousands of square metres up to tens of thousands of square kilometres, be found at distances from few hundred meters up to 150 kilometres from source and represent large

volumes of over 1000 km^3 (Lindsay et al., 2001; Cas et al., 2011; Brown and Andrews, 2015). Deposits have also been found separated by bodies of water from their sources, proving the ability of parent flows to cross water for even tens of kilometers (Aramaki and Ui, 1966; Dufek and Bergantz, 2007a; Druitt, 2014). PDC deposits can be compositionally zoned, such as the famous Crater Lake ignimbrite (Bacon, 1987), or more commonly composed of a single type of lava, ranging from mafic (basaltic) to acidic (rhyolitic) in composition (Wilson et al., 1995; Silva Parejas et al., 2010). PDC deposits can be massive to stratified and show multiple grading, i.e. normal and reverse, density and size grading (Fisher and Schmincke, 1984). These deposits are often composed of multiple units emplaced at cold (<100°C), medium (100–300°C) or hot (>300°C) temperatures. Typically, PDC deposits are poorly sorted mixtures of pumice and lithic lapilli and ash composed of free crystals and vesicle wall-type glass shards (Branney and Kokelaar, 2002). They can be loose, compacted, partially-to-completely indurated and may show various degrees of welding (Sheridan and Wang, 2005; Quane and Russell, 2005). Deposits can take the shape of low-profile sheets (Walker et al., 1980), fans, shields, valley-fills or lobes (Branney and Kokelaar, 2002; Brown and Branney, 2004; Brown and Branney, 2013) and vary in thicknesses from few millimeters up to >100 m (Wilson, 1985; Brown and Andrews, 2015).

Internal flow properties

The lack of internal observations and measurement of concentration and velocity has left volcanologists with only the opportunity to infer plausible internal flow structure and transport mechanisms from PDC deposits and destruction patterns (Druitt, 1998). Based upon the geometry of PDC deposits in relation to the topography, two end-member flow regimes have been proposed: the dilute PDC called "*pyroclastic surge"* that would emplace thin

topography veneer deposits and can be seen as a turbulent ash-cloud, and the dense regime previously called "*pyroclastic flow*" that would specifically emplaced thick ponded units from a near close-packing concentrated flow. These are detailed in section 1.4.5. However, there have also been observations and interpretations made from deposits that concentrated PDCs are always composed of "flow" and "surge" portions (Druitt, 1998).

Furthermore, PDCs have been repeatedly compared to other currents (i.e. saline and turbidity gravity currents) for which numerous experiments have been undertaken since the 1970's (Parker et al., 1987; Simpson, 1997). Very few studies of PDCs have had the opportunity to obtain kinematic properties of PDCs and these were focused on the concentrated portion of small to medium-scale PDCs (Lube et al., 2007a; Lube et al., 2011).

After discussing the hazards of PDCs and detailing trigger mechanism that yield PDC formation, in further sections, I detail how, from the aspects of different PDC deposits, scientists inferred different particle transport mechanisms in PDCs with a specific physics for each transport mechanism. Thereafter, past and current analogue and numerical models of PDCs are reviewed and their respective main findings and limitations are explained.

1.4.4 Pyroclastic density currents hazards

Pyroclastic density currents (PDCs) are amongst the most dangerous types of mass flow on Earth and the most deadly volcanic phenomenon, responsible for 48% of volcano-related fatalities (Nakada and Ballard, 2000). Their high destructive potential has been repeatedly demonstrated, for instance during the 79 AD eruption of Vesuvius that buried Herculaneum (Italy) (Sigurdsson et al., 1982), the 1902 eruption of the Montagne Pelée that killed ~28,000 people and destroyed St. Pierre (Martinique) (Boudon and Lajoie, 1989; Lajoie et

al., 1989; Tanguy, 1994) and the 1980 Mount St. Helens (United States) eruption that surprised even the prepared observers (Lipman and Mullineaux, 1981).

The hazards of PDCs include their ability to bury or sweep away almost everything in their path as a result of high temperatures (Scott et al., 2008; Zanella et al., 2008) and high dynamic pressures that can escalate to those of nuclear blasts ~100 kPa (Valentine, 1998; Sulpizio and Dellino, 2008), and perhaps shocks propagating through the mixture (Scolamacchia and Schouwenaars, 2009). The dynamic pressure is one of the main factors behind the destructive power of PDCs. It is typically a measure of the average kinetic energy per unit flow volume (Valentine, 1998; Clarke et al., 2002). The ruins of Pompeii, Italy (Gurioli et al., 2005), St. Patrick's village, Montserrat (Baxter et al., 2005) and the forest along with soil completely stripped bare at Mount St. Helens, USA (Lipman and Mullineaux, 1981), provided vivid testimonies of the dynamic pressures of PDCs. Furthermore, impact forces of large particles transported by dilute PDCs increase their impacts (Esposti Ongaro et al., 2008).

Many volcano hazard maps have been traditionally based upon deposit interpretations. However, PDC deposits are commonly only partially preserved. Thin deposits of dilute PDCs in particular are easily erodible. Therefore, many events may be missing from the geological record, or the maximum extent of previous events is often underestimated (Scott and Tilling, 1989). This raises questions about many volcano hazard maps have underestimated the PDC-related hazards.

High temperatures and very fine ash particles have lethal impacts on humans and animals (Baxter et al., 1998; Baxter et al., 2008). Ash particles may enter lungs and cause death by asphyxiation, while internal burns and lung damage may also be caused by the high gas temperatures. The commonly observed pugilistic pose of people killed from dilute ash-cloud

PDCs is related to a death by high temperature (Mastrolorenzo et al., 2001). Furthermore, the concentrated and dilute portions of PDCs do not commonly inundate the same area. Typically, the dilute ash-clouds often detach or decouple from the lower concentrated underflow that remains confined in valleys. The detachment of the ash cloud from the underflow was observed or inferred from several eruptions (Rose et al., 1977; Nairn and Self, 1978; Fisher, 1995; Druitt and Kokelaar, 2002; Ogburn et al., 2014). For example, at Soufriere Hills Volcano, Montserrat, on June 25th 1997, a dilute surge formed from detachment of the ash-cloud from the main undercurrent and killed 19 people with 400°C temperatures (Loughlin et al., 2002). The underestimation of this process has led to many tragedies, such as in 1991 at Unzen volcano (Yamamoto et al., 1993). Similarly, the 2010 PDCs of Gunung Merapi, Java, Indonesia caused >350 fatalities, mostly in the outer fringes of the area affected, where only dilute currents passed (Jenkins et al., 2013). Ash clouds are known to detach or lift-off from a related basal underflow, especially after traversing a rapid break in slope or valley bend (Yamamoto et al., 1993; Loughlin et al., 2002; Charbonnier and Gertisser, 2011; Lube et al., 2011). This is often referred in the literature as an ash-cloud surge (Nairn and Self, 1978; Bourdier and Abdurachmann, 2001). Ash-cloud surges may also form when barriers are encountered by a flow (Sigurdsson et al., 1987; Fisher, 1995). Despite these observations, there is little known about flow decoupling processes.

PDC may also induce additional hazards such as tsunamis. Examples include Krakatoa, Montagne Pelée and the Aniakchak caldera (Lacroix, 1904; Latter, 1982; Waythomas and Neal, 1998). Dense PDCs can enter the sea, for instance, and travel as a pyroclastic turbidity current, while more dilute components of the PDC can travel across the water (Freundt, 2003; Dufek and Bergantz, 2007b).

Because of the complex nature of PDCs, unpredictability and variability of natural events, the understanding of PDC dynamics and accurate assessment of their hazards is one of the greatest challenges to present-day volcanologists.

1.4.5 PDC deposits

1.4.5.1 Trigger mechanisms

Pyroclastic fountaining

Many pyroclastic density currents form directly from the gravitational collapse of a gas-thrust jet-forming plume wherein part of the column fails to entrain enough air to become dominated by buoyancy forces and therefore collapses the fountain onto the ground (Sparks et al., 1997). This process can either be short-lived or form a single pulse collapse associated with a vulcanian or plinian plume (Fig. 1.3A; Clarke et al., 2002; Branney and Kokelaar, 2002). Subsequently, a plinian eruption column may form (Fig. 1.3.B) and develop above the pyroclastic fountain. Hence, a pumice fall can be associated with the deposition from the PDC (e.g. Sparks et al., 1985). In this case, low pyroclastic fountaining may lead to the formation of "*boiling-over*" that is only cursorily described in the literature (Cas and Wright, 1987; Fisher and Schmincke, 1984; Branney and Kokelaar, 2002). The low height reached by the column before collapse provides a critical initial velocity and particle concentration that dictate flow dynamics. The boiling-over mechanism has been envisaged as a process that could occur for hours rather than minutes (Fig. 1.3C, Branney and Kokelaar, 2002). Some historic examples of low-column collapse are the post-1980 Mount St. Helens eruptions (Hoblitt, 1986) and some collapses of Soufriere Hills Volcano in the 1990's (Cole et al., 2002).

The gas phase in a PDC results from both the exsolution of dissolved volatiles from the magma and incorporation of ambient air either into the eruption column (where present) or

during flow propagation (i.e. Bursik and Woods, 1996). Typically, columns are expected to have particle concentrations of < 1% if the amount of gas contained in the magma that can be exsolved is greater than 3% of the mass fraction (Sparks et al., 1978b). However, columns denser than 1% are likely to frequently occur because: 1) lithic debris can be picked up from the conduit or crater/vent, 2) local high concentrations can originate in convective instabilities at the column margin (Carey et al., 1988), 3) large particles can decouple from the medium and fall back (Bursik, 1989), 4) the amount of volatiles in the erupted magma can be heterogeneous, as well as the rheology and temperature, as indicated by diverse compositions and vesicularities of pumices from the same eruption (Wright and Walker, 1981; Mellors and Sparks, 1991; Pardo et al., 2014b), 5) the decompression of magma is likely heterogeneous, by analogy with the structure of jets and shock experiments (Sugioka and Bursik, 1995; Alidibirov and Dingwell, 1996) and therefore induce high degrees of unsteadiness in the column that may survive for a substantial period of time (Sparks et al., 1997; Clarke et al., 2002).

The particles transported in a PDC can vary in size from <1μm up to several metres in diameter, and may range in character from pumice to crystals and lithic/country rock fragments. Typically, most pyroclasts within these currents are juvenile, resulting from magmatic fragmentation. They are produced either in the upper conduit in the case of eruption columns, or at the surface when domes/lava flows explode or disintegrate after collapse. The density of juvenile clasts varies widely from 300 to 2700 kg m^{-3} and greatly depends on the composition and vesicularity (Cashman and Scheu, 2015). Aside from juvenile fragments, PDCs transport lithic fragments incorporated from the conduit or crater and/or from the substrate. In some cases, e.g., with blasts, collapses of crater rims/domes or in hydrothermal settings, PDCs can be rich in country rock fragments.

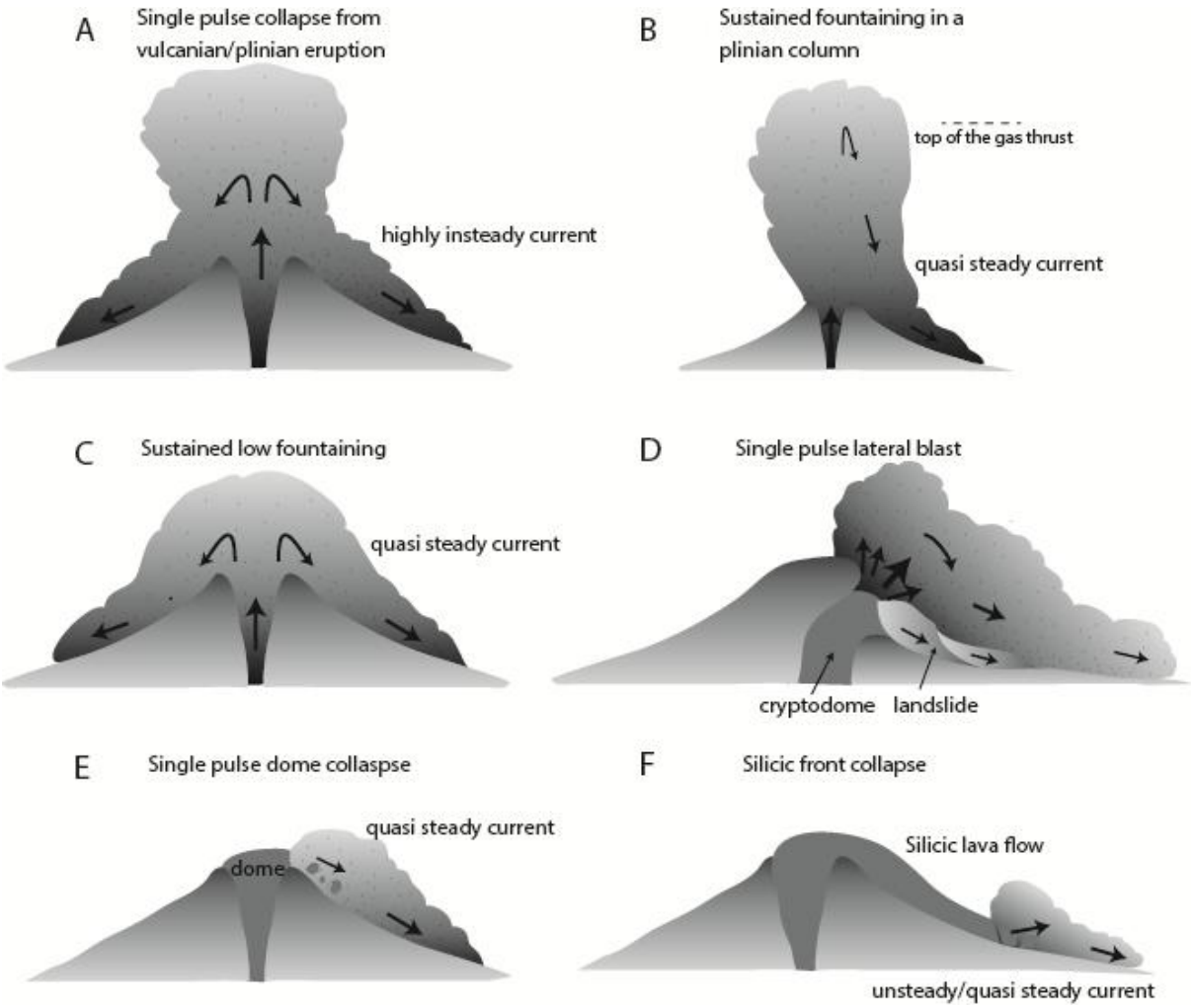

Fig. 1.3. Origins of "magmatic" pyroclastic density currents. A: Short single-pulse current derived by momentary collapse of a plinian column. B: Sustained current derived from prolonged pyroclastic fountaining. The height of the jet (gas thrust) that feeds the current may vary and is transitional into (C). C: A sustained current derived from prolonged low pyroclastic fountaining (boiling-over) explosive eruption. This lacks the kinetic energy derived from the potential energy of a high fountain. It may be accompanied by a buoyant eruption column (not shown) that does not feed the current. This may also be accompanied by the collapse of vent-proximal piles of agglutinate that feed scoria-and-ash flows (Lube et al., 2007a). D: Current with a single (or multiple) surge derived from lateral blasts initiated by catastrophic decompression of a magmatic and/or hydrothermal system. E: Single surge current derived from a collapsing lava dome or flow front. Hot rock avalanches generate turbulent density currents. F: Deposit-derived pyroclastic density current caused by gravitational collapse and avalanching of a loose ignimbrite or a rhyolite lava flow front. The current may be single surge or more sustained where the collapse is retrogressive. Most ignimbrite deposits derive from current type (B) and (C), which may involve periods of quasi steady flow. Many may include significant components derived from currents type (F). PDC generation mechanisms summarized from Branney and Kokelaar (2002) and Lockwood and Hazlett (2010).

Dome collapse

After the pyroclastic fountaining, dome collapse is the second most common mechanism generating PDCs (Fig. 1.3E). Lava dome are mounds of viscous lava and rocks that accumulate at a vent. Commonly, lava domes are comprise intermediate to silicic lava (andesite-rhyolite) that can either grow at the surface or within a volcanic structure to create a cryptodome (Calder et al., 2015). Lava domes can collapse by several mechanisms: 1) thrust force can push a portion of the dome outwards, 2) gas overpressurization, often associated with rapid emplacement of gas-rich lava, makes domes prone to explosive collapse, 3) slope oversteepening and 4) propagation of thermal fractures that are generally prominent when the dome advances over steep slopes (Fink, 1990; Calder et al., 2015). Gravitational collapses of lava domes involve further breakage, abrasion and vesicle rupture of fragmented dome material as the clasts propagate downslope, forming significant quantities of fine ash particles (Rose et al., 1977). Many volcanoes are well-known for hosting dome-collapses for example the Merapi volcano in Indonesia (Abdurachman et al., 2000; Newhall et al., 2000; Voight et al., 2000; Walter et al., 2015), Unzen volcano in Japan (Yamamoto et al., 1993; Ui et al., 1999) and Soufriere Hills at Montserrat (Cole et al., 2002; Wadge et al., 2014).

Lateral blasts

Some pyroclastic density currents originate after rapid-decompression of a dome or cryptodome, exploding laterally as decompression jets (Fig. 1.3D). The most famous example is the 1980 lateral blast from Mount St. Helens, where the decompression of a cryptodome was triggered by partial flank collapse of the volcano. Partial flank collapses have also generated lateral blasts of magmatic origin at Bezymianny (Russia), Soufriere Hills Volcano (Montserrat) (Belousov et al., 2007) or hydrothermal origin at Bandai volcano (Japan)

(Glicken and Nakamura, 1988; Yamamoto et al., 1999) and Mt. Tongariro (New Zealand, Lube et al., 2014).

Other mechanisms at the origin of PDCs

Pyroclastic density currents can be produced from the destabilization of silicic lava flow fronts (Fig. 1.3.G) or from the remobilization of ignimbrite deposits (Branney and Kokelaar, 2002). Furthermore, PDCs can result from the interaction of magma with water in phreatomagmatic eruptions (Houghton et al., 2015; Zimanowski et al., 2015) or from the interaction of lava with ice or snow (Belousov et al., 2011).

1.4.5.2 Field characteristics of PDC deposits

Classification of PDCs: paradigm of pyroclastic flow and pyroclastic surge

Most of the field studies rely upon analysis of the deposit architecture, sedimentology and stratigraphical reconstruction, of the PDC deposits (Sparks and Walker, 1973; Sparks, 1976). When modern volcanologists looked at PDC deposits for the first time (post-1960's), their knowledge was based upon sedimentological principles derived from fluvial, marine and alluvial fan deposits and they applied these sedimentological principles to PDC deposits. The seminal work of hydraulic engineer Rouse (1961) provided a better understanding of the physics of dilute suspension and Fisher (1966) was one of the pioneer volcanologists who applied the physics of water-particle currents to PDCs, despite their extreme difference of density. McTaggart (1960) was the first volcanologist to use the analogy between fluidized beds and concentrated PDCs, previously called 'nuee ardentes', and at the time created great

debate (Brown, 1962) about the source of the gas which has not hitherto been answered (see section on fluidization transport mechanism).

In the following years, further debate had arisen from observations of the sedimentological structures that divided the deposits into two groups. The first group of deposits were thin, fine-grained, cross-bedded and wavy and planar laminated sequences able to mantle the topography (Fisher and Waters, 1970; Fisher, 1979) while the second group of deposits were thick, unbedded to poorly bedded, poorly sorted tuff and tuff breccias which were often ponded in depressions (Sparks, 1976) (Fig. 1.4). This two-fold classification separated two contrasting flow regimes known as the concentrated versus dilute regimes. However, both concentrated and dilute regimes were also subsequently found to occur in block-and-ash flows, as inferred from direct observations and interpretations of deposits by Taylor (1958). Nevertheless, the paradigm of dilute (pyroclastic surge) versus concentrated (pyroclastic flow) PDCs was born.

The eruption of the Mount St. Helens in 1980 was a significant moment in the development of understanding of PDCs. This eruption was closely monitored and observed, providing a wealth of data that allowed volcanologists to infer that a possible intermediate state existed between dilute and concentrated PDCs, as massive layers were laid down by a very large dilute ash-clouds and in most places the massive layer was nearly veneering topography (Fisher, 1990). Subsequent studies of PDC deposits showed intercalation of massive beds within stratified units in complex sequences (Fisher and Schmincke, 1984; Sohn and Chough, 1989; Chough and Sohn, 1990; Sohn, 1997).

Fig. 1.4. Basaltic-andesite massive ignimbrite overlain by stratified units of similar composition at Llaima volcano, Chile. Such outcrop depicts the dichotomy of PDC deposits as the massive, thick gray layer is overlain by thin beds that display multiple bedforms.

Distinctions between pyroclastic surge and pyroclastic flow deposits were soon not only based upon the occurrence or absence of bedforms and/or their architecture with respect to the topography but also on their median and sorting grain-size characteristics (Walker, 1971; Walker, 1983) (Fig. 1.5).

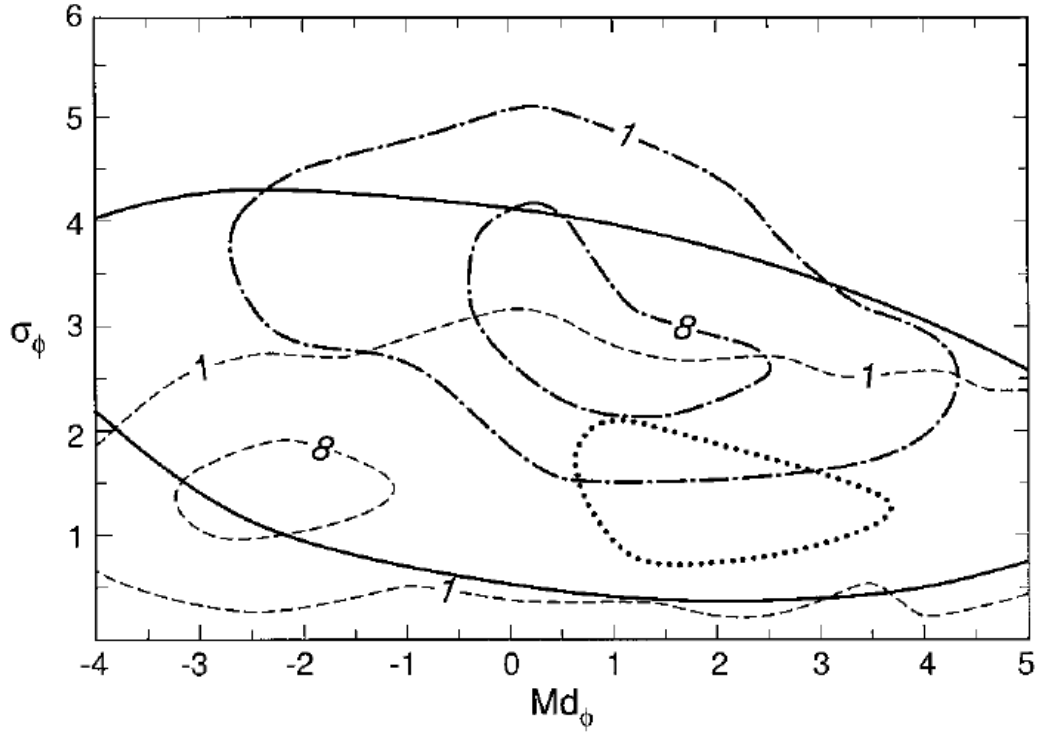

Fig. 1.5. Median (MdΦ) and sorting (σΦ) showing different fields drawn depending on whether they are from pyroclastic surge (solid line), cross bedded deposits from Ubehebe crater (USA) and Taal volcano (Philippes) (dotted line), fallout (dashed-line), pyroclastic flows (point and dash alternate), (solid line). Modified from Fisher and Schmincke, 1984).

Deposits from pyroclastic flows and stratified deposits fields show very little overlap and exhibited marked differences in sorting. However, the complete surge field shows overlap with all other fields, including the fallout field. This was interpreted by Walker (1983) as evidence of a spectrum of characteristics existing between pyroclastic surge and flows. However, confusion between terms quickly arose in the literature; for instance the use of the term ignimbrite to refer to the deposit of pyroclastic flows in the review chapter of the first edition of Encyclopedia of Volcanoes (Freundt et al., 2000) while in the review of Branney and Kokelaar (2002), the term ignimbrite solely refers to pumiceous and ash-rich flows.

At the end of the 1980's, dilute PDCs were envisaged as density stratified flows (Valentine, 1987) where concentration near the bed can reach the concentration of concentrated flows

(~50 % vol. concentration) therefore explaining the formation in some cases of massive layers from overall dilute flows (<1% particle vol. concentration) (Wohletz, 1998).

En masse versus aggradation paradigm

Despite a clear and simple description of ignimbrites as an ash and pumice- rich PDC deposit, which ignores any constraint on volume, composition and bedform, ignimbrite deposits were preferentially attributed to concentrated PDCs from 1970's to early 2000's. This was because of the influential paradigm of the *standard ignimbrite flow-unit* that was idealized from small scale pyroclastic flow deposits and inferred to reflect the internal PDC structure (Sparks et al., 1973; Sparks, 1976; Wilson and Walker, 1982). Authors had postulated that the flow deposited *en masse*, which would be equivalent to a quasi-instantaneous "freezing" of the flow and complete preservation of the vertical flow structures. Sparks and Walker's seminal work encountered very little opposition until the 1990's when the concept of a *flow-boundary zone* was introduced (Branney and Kokelaar, 1992).

In the 1970's, Sparks and Walker's school of thought buried another that was introduced by Fisher (1966) in its infancy. Fisher was one of the first to imagine deposition from PDCs as the result of progressive *aggradation*. Fisher (1966) hypothesized that ignimbrites were deposited from low-density currents, whose concentration at the base was high enough to inhibit turbulence and sorting during deposition. The concept was later revisited by Branney and Kokelaar (1992, 2002), who envisaged that ignimbrites reflect the conditions of the lower portion of the flow that undergo deposition (flow-boundary zone) rather than representing the vertical parent flow structure. Following the seminal review of Branney and Kokelaar, (2002), PDC deposits have been less regarded as a proxy of the internal flow structure and more that the deposits reflected the conditions of the flow-boundary zone (Branney and

Kokelaar, 2002; Brown and Andrews, 2015). Their work was highly influential and tended to focus interpretations of ignimbrites towards dilute PDCs, which was helped by the development of dilute gravity current physics (See section 1.4.9). The term of pyroclastic density current also became prevalent in the literature from the early 2000's as it is a non-genetic term encompassing all types of flows and therefore does not associate the density current with any initiation mechanism, deposit or transport mechanism.

In the following sub-section, a short summary of the PDC deposit characteristics that are commonly encountered on volcanoes worldwide is presented.

Deposits from small volume, dilute PDCs

Small volume magmatic eruptions can form dilute ash-clouds that typically travel 1-10 km from source that were called "pyroclastic surge" in the literature. Deposits left behind are commonly thin-bedded, stratified, cross-stratified, massive or planar bedded (Sohn and Chough, 1989; Chough and Sohn, 1990) (Fig. 1.6). Lateral facies variations are very common and generally show the disappearance of the massive bedding and cross-bedding with increasing distance from source while the lamination and thin-stratification are more pronounced, which has been interpreted as a result of energy loss of the current over distance (Chough and Sohn, 1990; Valentine and Fisher, 2000) (Fig.1.7). Dune bedforms of few meters in length are often formed (Sigurdsson et al., 1987; Douillet et al., 2013; Douillet et al., 2014).

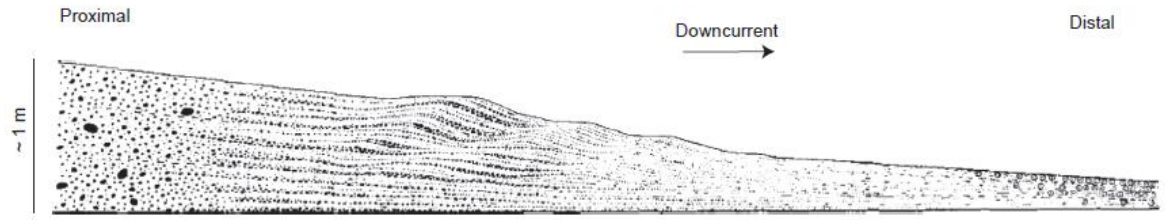

Fig. 1.6. Typical downstream transitions in pyroclastic density currents deposits of the Songaksan tuff ring, Cheju Island, South Korea, over a distance of 2 km. Modified from (Chough and Sohn, 1990).

Fig. 1.7. Cross bedding and dune bedforms in a phreatomagmatic sequence of pyroclastic surges, Cap d'Agde, France.

Base surges are a particular type of surge recognized since the 1960's as being generated by phreatomagmatic eruptions related to magma-water interaction (Moore, 1967; Fisher and Waters, 1970; Fisher and Schmincke, 1984). Base surges often spread out as radial clouds across land or the sea (Fig. 1.8). Typically, base surges leave deposits that resemble magmatic surge deposits but they often show fewer fine-grained bedforms (Wohletz, 1998). Accretionary lapilli, made of fine-ash particles accreted onto each other, are often found in

pyroclastic surge deposits when water as a steam phase is abundant (i.e. Valentine and Fisher, 2000).

Fig. 1.8. Base surge spreading out during the eruption of Te Maari, 21st of November 2012. Picture by Lomi Schaumkel.

Another distinct type of pyroclastic surge known as a *ground surge* was recognized in the 1970's (Sparks and Walker, 1973). Ground surge deposits (typically <1 m thick) are found at the base of thick massive layers (often >5 m) and are characterized by thin planar to cross bedding. The origin of the ground surge deposits is thought to be related to the formation of a dilute flow front forming ahead of a more concentrated flow (Sparks et al., 1973).

Typically, deposits from dilute PDCs thin exponentially with distance and veneer topographic obstacles and subsequently show a progressive diminution of the median grain-size while the grain-size sorting increases (Wohletz and Sheridan, 1979).

Lateral blasts

Lateral blast deposits show common features, regardless of their origin (magmatic or hydrothermal). They are often deposited upon a highly eroded surface and are tripartite. The first unit is a massive to normally graded unit with a base enriched in vegetation, soil and large lithic clasts. The second unit is commonly stratified and shows a large variety of bedforms, from dune-bedded to planar bedded; the third unit is rich in fine ash and laminated (Fig. 1.9) (Hoblitt et al., 1981; Siebert et al., 1987; Fisher, 1990; Tanguy, 1994; Belousov, 1996; Belousov et al., 2007; Kilgour et al., 2008). Depending on the eruption, the last unit may contain a large amount of accretionary lapilli. Typically, blasts deposits show similar features to surge PDC deposits (exponential thinning, progressive fining) (Fisher et al., 1983; Belousov and Belousova, 2000; Belousov et al., 2007; Lube et al., 2014). Furthermore, local densification of the flow in relation to the response to topographic barrier is common (Druitt, 1992; Druitt, 1998).

Fig. 1.9. Tripartite hydrothermal blast deposit from the 2012 Upper Te Maari eruption. Note the massive, stratified and topmost laminated (appearing massive in the picture) units.

Small volume, concentrated pyroclastic density currents

Concentrated pyroclastic density currents form either block-and-ash flows when originating from a dome-collapse (Fig. 1.10), or pumice flows when originating from other mechanisms such as column collapse (Brown and Andrews, 2015).

Fig. 1.10. Block-and-ash flow at Sinabung volcano (Indonesia) in July 2015. Courtesy of Umar Rosadi.

Block-and-ash flows (BAFs) commonly involve small volumes (10^3–10^6 m^3) and flows travel distances < 15 km at velocities of 10–100 m s^{-1} (Freundt et al., 2000; Hall et al., 2015). BAFs are strongly controlled by the topography and are typically confined in valleys and ravines on proximal volcanic slopes but sometimes spread out on flat areas to form fans. BAF deposits can be thicker than 10 m in valleys and thinner on the interfluves (<10 cm) (Lube et al., 2011). These deposits differ from ignimbrite by the composition of dense (1700–2700 kg m^{-3}) clasts and can be clast or matrix supported (Fig. 1.11). BAFs are always poorly sorted and can transport boulders up to 10 m wide in an ashy matrix (Cole et al., 2002; Charbonnier and

Gertisser, 2011). Their emplacement temperature can be extremely high (>600°C) as indicated by prismatically jointed clasts (Cole et al., 1998). Typically in BAFs, clasts are angular or sub-angular. Distal parts of the deposit can be enriched in fine-ash and may show steep snout-like accumulation of large blocks (> 1m in diameter) (i.e. Branney and Kokelaar, 2002).

Fig. 1.11. Block-and-ash flow deposit, Mont-Dore, France. Note the ashy matrix that support angular blocks that are from the dome from which the collapse initiated.

Another common type of concentrated PDC is pumice or scoria flows that contain a high amount of pumiceous/scoria clasts. These flows are highly influenced by the topography and in some case spread across flat areas; in such cases they commonly form lobes with associated levées (e.g. small-scale PF from Ngauruhoe, Lube et al. (2007b) or pumice flows from Lascar volcano (Calder et al., 2000) (Fig. 1.12). Lobes form as a result of particle size and density segregation mechanisms (Pouliquen et al., 1997; Pouliquen and Vallance, 1999) (Fig. 1.12, the margins of lobes are enriched in large pumices which are even visible from

large distances). Usually, large pumices are present on the edge, top and on the front of the small-scale PDC deposit due to a process of filtering of the fine particles that concentrate at the base of the flow during motion. Conversely, dense lithics rather show a coarse-tail grading, where coarsest clasts would be preferentially deposited proximally and the maximum lithic clast size would decline with distance (Calder et al., 2000; Sulpizio and Dellino, 2008).

Fig. 1.12. Complex of multiple pumice flow lobes at Lascar volcano, Chile. (Courtesy of Patrick Whelley, NASA Goddard Space Flight Centre).

Large PDC deposits

Most of the large > 1 km^3 PDC deposits are ignimbrites (adopted here as pumice and ash-rich deposits) which show the widest range of volumes (up to 1000 m^3), grain-size variations (median grain-size diameter varies from 50 μm to 50 cm), deposit bedforms (massive, stratified, dune bedded), thickness variations (from 0.1–500 m thick) and greatest extent from source (up to 140 km). Ignimbrite can be ponded in calderas while others are deposited atop 1 km high obstacles (i.e. Taupo ignimbrite; Wilson, 1985). Ignimbrites depict every characteristic that was introduced in the previous section on small PDCs, which make their interpretation very complex (Branney and Kokelaar, 2002). Trying to interpret ignimbrite deposits in terms of their parent flow properties is difficult and has divided the volcanology community. By way of example, the famous Taupo ignimbrite has been envisaged as being emplaced by both a dilute current (Valentine, 1987; Dade and Huppert, 1996; Wilson et al., 1997), as well as by a concentrated PDC (Wilson, 1985).

1.4.6 Transport mechanism

Fluid turbulence

Fluid turbulence is a support mechanism that exerts fluid lift and drag on particles with settling velocities smaller than or comparable to the upward component of the eddy velocity (Rouse, 1939; Allen, 1984). At low concentration (~<1%), clasts interactions are negligible and fluid turbulence can be the dominant clast-support mechanism during transport. When a mixture is transported by fluid turbulence, vertical segregation of the particle as a function of settling velocity occurs (Valentine, 1987). In a low energy current, only fine ash can be transported by such a mechanism, while in energetic currents (high velocities), large grain-sizes can be transported instead (Freundt and Bursik, 1998). Fine ash particles that can be transported even at low velocities are found across the whole current height and constitute the

suspension population. Other clasts may only travel intermittently by fluid turbulence and form the intermittent suspension population, whereas the largest clasts may only travel on the substrate and constitute the traction population. The threefold classification oversimplifies the processes because clasts can change support mechanisms over time and also there is no sharp distinction between the three populations (Allen, 1984). The three populations can be distinguished, for instance, by their grain-size distributions by sequential fragmentation and transport (SFT) analysis (Wohletz et al., 1989). Segregation by eddies near the bed may form fines-poor lenses when eddies encroach on the lower-flow boundary and selectively entrain fine clasts from the substrate according to their size and densities (Li and Komar, 1992). Repeated passage of eddies has been inferred from the occurrence of fines-poor lenses within fine-rich ignimbrites (Wilson, 1985).

Rolling, sliding, saltation

Particles can experience drag forces exerted by the dusty gas and give rise to particle rolling or sliding at the lower flow boundary. This process is known as "traction" (Middleton and Southward, 1984). These transport mechanisms have been mainly envisaged in dilute suspension (Middleton and Southward, 1984) but is also envisaged in high concentration flows where lithics can roll along the flow base, where their transport is helped by clast interactions and buoyancy (Branney and Kokelaar, 2002; Roche et al., 2013a). These lithic blocks can be found at any level within PDC deposits because as the flow boundary migrated upward their height reflected the height of the compacted deposit aggraded at the time of their deposition (Branney and Kokelaar, 2002).

In currents with no net deposition, several grain-sizes may travel by saltation, a process which describes any "leaping" movement of clasts at the interface. The lower zone of an ash-

cloud where saltation is prone to occur is the saltation zone. The thickness of this zone is highly variable depending on the grain-size involved in saltation. Saltation was observed as being related to bounding (Bagnold, 1956; Bagnold, 1973; Dufek and Bergantz, 2007b) and fluid drag and intermittent suspension by fluid turbulence (Einstein and Chien, 1955). Delinger (1987) proposed that clasts saltate along the interface between an ash-cloud and underflow in bipartite PDCs so that concentration of clasts decrease upward from a granular flow (c. 50%) to low values in the ash-cloud (<1%). Furthermore, clasts have been envisaged to bounce because of their own momentum due to gravity, this saltation is called "debris fall" by Sohn and Chough (1993). This type of saltation could be highly effective on slopes near or higher than the angle of repose of the saltating material (Fuji and Nakada, 1999; Miyabuchi, 1999).

Granular temperature

Granular flow theory is important in understanding pyroclastic density currents (Branney and Kokelaar, 2002). In high concentration flows (commonly > few percent), collisions between clasts can cause clasts to move quasi-randomly about the average direction of motion (Bagnold, 1954; Savage, 1979). The vibrations of the clasts are analogous to the thermal motion of molecules in the kinetic theory of gases, therefore, the term of granular temperature has been used (Savage, 1983; Savage, 1984; Campbell, 1990). Similar to thermodynamics of gases, the granular temperature generates pressures that govern the rate of mass and momentum exchange. Nevertheless, the granular temperature cannot be auto-sustained as collisions are inelastic and mechanical energy dissipates as thermodynamic heat so that it must be maintained by shearing. Granular temperature is scaled roughly to the square root of the shear rate, or velocity gradient (Campbell and Brennen, 1985). Campbell (1990) argued

that a flow under high shear can expand because of the dispersive pressure discovered by Bagnold (1954) and thus viscosity of the granular mass could be reduced. At high-shear rates, the granular mass reach a "liquefied state" and is hypothesized as an important support mechanism in moderate to high concentration flows (Bagnold, 1954; Lowe, 1976). Flows dominated by granular temperature are thought to be either *true grainflows*, wherein the interstitial fluid does not play a role, or *modified grainflows* in which the effects of intergranular fluid can modify the whole flow behaviour (Lowe, 1982; Iverson and Vallance, 2001). The underflow of PDC may exhibit a behaviour within the spectrum between *true and modified grainflows* as a function of the content of dusty gas (Branney and Kokelaar, 2002).

Quantitative application of the granular flow theory to natural PDCs is limited because fluid pressures, granular temperatures and concentrations are likely highly time-variant (e.g. Iverson and Vallance, 2001).

Fluidization

Fluidization has long been held as the solution to explaining the high apparent mobility of concentrated PDCs, as well as the grading, sorting and elutriation pipes seen in ignimbrites (McTaggart, 1960; Sparks, 1976; Sparks et al., 1978b; Wilson, 1980; Carey, 1991; Druitt et al., 2007; Girolami et al., 2007; Roche, 2012). In gas-fluidized dispersion, an upward gas flux exerts a drag force on particles and supports their weight so that the concentrated flow behaves like a fluid (Kunii and Levespiel, 1991). However, owing to the large range of particle sizes transported in concentrated PDCs (from ~1µm up to few meters wide), only the fine particles can be fully supported by the gas phase (Sparks, 1976; Wilson, 1980). This is also suggested by the fact that large gas fluxes that would be capable of supporting the large and dense lithics would also elutriate all the fines from the mixture, which contrasts with the

common observation of high ash content in most concentrated PDC deposits (Walker, 1983; Branney and Kokelaar, 2002; Brown and Andrews, 2015). In fact the source of gas is a large problem in such theory. Volcanologists have rarely been specific as to what is the source of the gas involved in the particle fluidization. In fact, depending on the source of gas, multiple fluidization types have been hypothesized. For instance, grain-self fluidization has been envisaged to be due to the exsolution of juvenile gas from ash and pumice particles (Sparks, 1978) or from steam or snow entrained or from the burning of vegetation. Sedimentation fluidization has also been proposed and could be driven by escaping interstitial gas during hindered settling. Also, decompression fluidization was invoked to form under column collapse in which gas fluxes are produced by rapid decompression of air at the base of a tall collapsing column (Druitt and Sparks, 1982) or in lateral blasts (Branney and Kokelaar, 2002).

In bulk self-fluidization, clasts are supported by the upward escape of air that has been entrained at the front, as suggested initially by McTaggart (1960) to explain the increase in runout of experimental flows with temperature by incorporation of "cold" ambient air and heating from the flow. Similarly, experiments of fine-grained granular material initiated in drums have shown both periodic and continuous ejection of particles ahead of the flow (Bareshino et al., 2008). These observations have been explained as self-fluidization. Similar processes were observed in thin flows in analog experiments where the flow entrained the air underneath the flow from between interstices of the rough surface, which led to the enhancement of the runout (Chedeville and Roche, 2014, 2015).

Classification of PDC deposits by Branney and Kokelaar, 2002.

Branney and Kokelaar (2002) introduced a new, twofold classification of pyroclastic density currents as either *fully dilute* currents where intergranular collisions are negligible or

granular fluid-based pyroclastic density currents in which interparticulate collisions dominate. This classification is based upon processes that occur and dominate the lower flow-boundary that are reflected in the deposit. Their two-fold classification of pyroclastic density currents is mindful of the assumed continuous spectrum of current and Branney and Kokelaar (2002) inferred that all gradations between the fully dilute and granular fluid-based are possible.

In fact, at the root of their classification is the interpretation of massive layers as being deposited from a dilute current. Nonetheless, their definition is not absolute (there is no defined threshold of concentration that separates the fully dilute from the concentrated) as particle concentrations in the boundary zone have never been measured in PDCs. This classification was intended to reduce the errors in interpretations of PDCs deposits by simply avoiding the link between the deposit facies and the parent flow transport mechanisms.

Mobility

While deposit facies are now hardly thought to be a useful proxy of the transport mechanism of parent PDCs (Branney and Kokelaar, 2002), the overall distribution of the deposit has been used as a tool to assess the mobility of the flow. The non-dimensional ratio of the area (A) divided by the volume$^{2/3}$ (V) of a given deposit is a parameter proposed by Dade and Huppert (1998) to assess the degree of mobility of debris avalanche. The same ratio has been employed with pyroclastic density current deposits (Calder et al., 1999). PDCs are grouped by types in the mobility plot $A/V^{2/3}$ as a function of volume (Fig. 1.13) and there is overlap between the mobility fields of concentrated PDCs (pumice and block-and-ash flows) with the mobility of field of debris avalanches. In contrast to debris-avalanches, there is no clear relationship between the mobility and the volume of PDCs (Calder et al., 1999, Fig. 1.13).

Furthermore, a clear dichotomy forms between the dilute and concentrated regimes. Pyroclastic surges and blasts, for which the inferred principal transport mechanism is considered to be as turbulent transport, are more mobile by an order of magnitude than most pumice and block-and-ash flows for which the granular temperature and fluidized transport regimes have been invoked (Fig. 1.13). The separation between dilute and concentrated transport regimes appears to be around a mobility value of ~400. Calder et al. (1999) have demonstrated that the mobility of PDCs is neither a primary function of the temperature nor the amount of initial gas in the mixture. They envisaged that the density and particle size could rather be the main control mechanisms on the mobility of concentrated PDCs and the amount of fines may play the leading role in controlling PDC mobilities. In dilute flows, fine ash will easily be suspended in turbulent transport and lead to very long runout distances and widespread areas of dilute PDCs (Branney and Kokelaar, 2002). In concentrated flows, the fines content greatly influences the mobility of fluidized beds as they can be easily fluidized (Roche, 2012) but also greatly influences the mobility of dry granular flows (Jop et al. 2006). The greater amount of fines in PDCs may be the key to understanding why, for similar volumes, concentrated PDCs are more mobile than debris avalanches (See Fig. 1.13). This hypothesis has also been proposed by Hayashi and Self (1992) who based their analysis upon the ratio (H/L) of vertical height (H) and horizontal length (L) travelled by the pyroclastic material. These authors concluded that fluidization was not the origin of the greater mobility of the PDCs relative to debris-avalanches, but rather due to differences in their material properties.

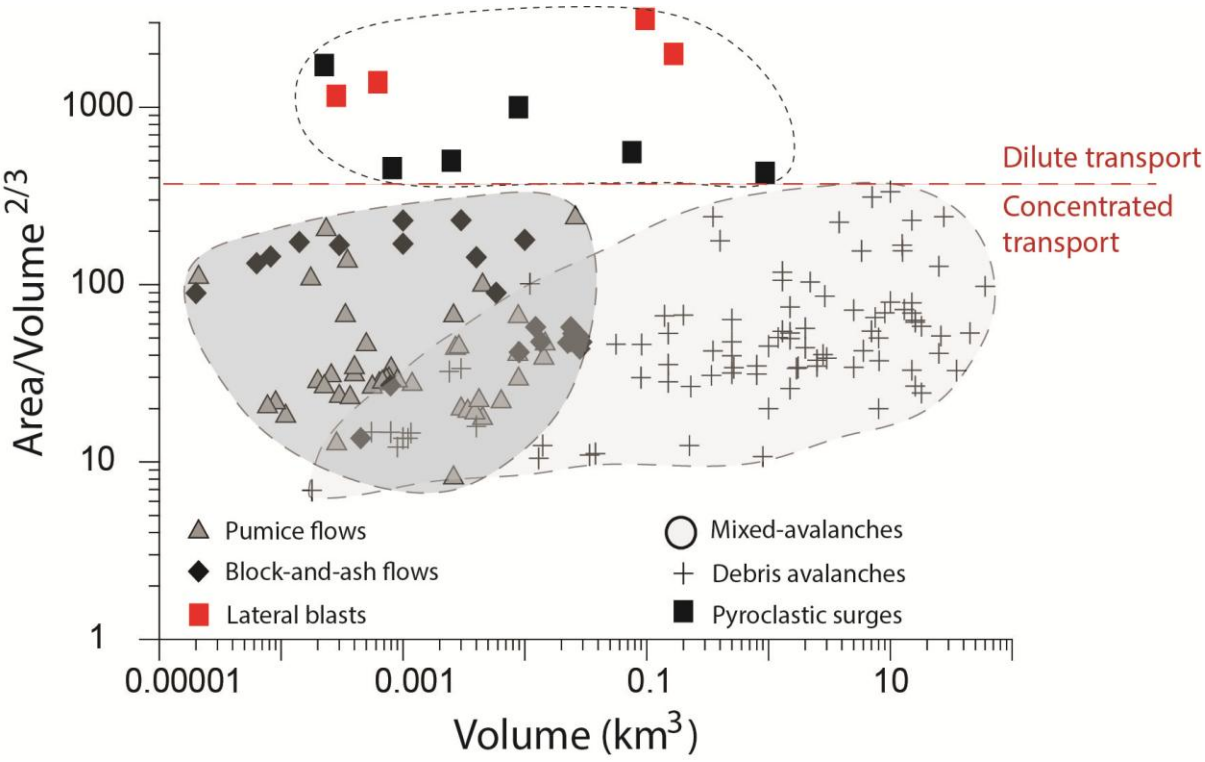

Fig. 1.13. PDC and debris avalanche mobility plot. The mobility is assessed as the non-dimensional ratio of the Area/Volume$^{2/3}$ for data of pyroclastic density currents separated into pumice flows, block-and-ash flows, pyroclastic surges and lateral blasts. Data from debris avalanches are indicated as a comparison. The red line separates dilute transport from concentrated transport regimes. Data have been combined from Hayashi and Self, 1992; Yamamoto et al., 1999; Calder et al., 1999; Fujinawa et al., 2008; Komorowski et al., 2013; Lube et al., 2014.

In the two following sections, the physics of different transport mechanisms is presented and distinction made between dilute and concentrated PDCs.

1.4.7 Physics of PDCs

1.4.7.1 Physics of dilute PDCs

The current set of equations describing the physics of dilute PDCs is borrowed from the fluid dynamics of (generally monodisperse) water-particle suspension flows. Although the sedimentological structures produced by water and surge bedforms (dunes, ripples etc.) display similarities with a Reynolds (Re) number that can be of the same order of magnitude,

the viscosity may vary by two orders of magnitude and the density contrast between water and particle is far different from the contrast between air and particle.

Pyroclastic surges have been modeled as gravity currents divided into two vertical parts separated at the level where velocity achieves a maximum and where shear stress approaches zero. The velocity profile of the lower part follows a logarithmic law and is influenced by the roughness of the surface. Particles are suspended into the flow if the turbulent shear velocity exceeds their fall velocity. The velocity profile of the lower part can be expressed by the following relationship:

$$V = U^* \left[8.48 + 5.75\, log\left(\frac{h}{K}\right)\right] \quad (1)$$ (Allen, 1970)

with U^* being the shear velocity, h the height and K is the size of the roughness elements.
At the base of the current, the particle concentration profile and sedimentation depends on the average Rouse number *Pn* defined as:

$$Pn = \frac{1}{C_{avg}} \sum_i C_i \frac{W_i}{KU^*} \quad (2)$$ (Middleton and Southward, 1984; Valentine, 1987)

C_{avg} is the maximum average particle concentration of the current, C_i is the average volume concentration of a particle of the settling velocity class W_i (Valentine, 1987). A finite value of settling velocity implies a vertical concentration gradient. In the limiting case of Pn =2.5, the unsuspended load is lost from the flow (Middleton and Southward, 1984). A concentration profile through the current can be defined as:

$C = C'[\frac{\eta'(1-\eta)}{\eta(1-\eta')}]^{Pn}$ (3) (Valentine, 1987)

With C the particle volume concentration, C' the particle volume concentration at reference level, η' a dimensionless reference level and η is the ratio of the height above the base and the current's total thickness.

The flow a concentration volumetric profile can be defined:

$C = Co[\frac{\eta'(1-\eta)}{\eta(1-\eta')}]^{P_n}$ (4) (Valentine, 1987)

where C is the particle volumetric concentration, *C*o is the flow particle volume concentration, P_n is the average Rouse number of the suspension, η is the dimensionless height and η' is the dimensionless reference level.

The settling velocity of particles is largely dependent on the Reynolds number (Re), which is a dimensionless parameter characterizing the level of unsteadiness of the continuous phase (liquid or gas) and it is defined as follows:

$Re = \frac{\rho VL}{\mu}$ (5)

where V and L are characteristic velocity and length scales of the flow, and μ corresponds to the dynamic viscosity of the flow. The flow is laminar when Re $\leq$ 1 and fully turbulent when Re is > 10^4 and between the boundary is the transition between the two regimes (Dimotakis and Catrakis, 1999).

The density gradient within horizontally stratified currents is related to the Brunt–Väisälä or buoyancy frequency *N*.

$$N = \left[0.5\,\pi\left(\frac{g}{H}\,\frac{Pn}{\eta(1-\eta)}\right)\right]^{0.5} \quad (6)$$ (Valentine, 1987)

where *H* is the total flow thickness.

The buoyancy frequency *N* defines the ultimate frequency of internal waves in a stratified current. To summarize, a surge is composed of the sum of density interfaces upon which the waves travel. Eddies created by turbulence can move parcels of the currents to different levels, where it can be denser or lighter than the interface in which it was generated; thus, either gravity or buoyancy will tend to return the parcel to its original level (Valentine, 1987). This gives stability to the current. When stratification is stable, the turbulence process is dampened (Kneller and Buckee, 2000). Burgisser and Bergantz (2002) demonstrated that eddies tend to be smaller and faster in high concentration gradients such as the base of the current, where eddies improve the carrying capacity of the flow more efficiently than eddies located in the more dilute part above.

Finally, an important parameter is the Richardson number *Ri* which is defined as the ratio of the potential to kinematic energy. When applied to surges it gives:

$$Ri = \frac{-gH}{\rho}\,\frac{\left(\frac{d\rho}{d\eta}\right)}{\left(\frac{dV}{d\eta}\right)^2} \quad (7)$$ (Valentine, 1987)

At this stage, analytical or even empirical relationships for true, strongly stratified, unsteady and dilute gas-particle mixture flows and relationships between flow characteristics and bedform evolution still require a great effort of fundamental research.

1.4.7.2 Dynamic of concentrated PDCs

The physics of concentrated PDCs is equivalent to either the physics of granular flows or to the physics of fluidized beds.

Granular flows have been well studied in pharmaceutical or civil engineering sciences, for example, but there is no granular flow model approaching the Navier-Stokes equivalent for Newtonian fluids. Granular flows are defined as *dry* when fluidization effects are non-operant because of a poor permeability or due to a limited source of gas. In dry media, inelastic interactions between particles results on energy loss, and flow dynamic is related to the Savage number that is defined as the ratio of inertial shear stresses to quasi-static gravitational stresses associated with friction:

$$Sa = \frac{\rho_p \dot{\gamma} d^2}{(\rho_p - \rho_g) g h_c} \quad (9) \quad \text{(Savage, 1984)}$$

with ρ_p and ρ_g the particle and gas density respectively, $\dot{\gamma}$ the shear rate, d the particle diameter, h_c the current height, g the acceleration of gravity. The current dynamics are governed by particle interactions at high shear rates (Sa>0.1) whereas the frictional stresses are governed by the flow when Sa>0.1, respectively (Savage and Hutter, 1989a). The frictional dense regime is achieved on an inclination close to the angle of repose of the material and steady motion occurs by a balance of gravitational and frictional forces. The granular media is considered as a Coulomb material with a constant friction coefficient (μ) and a friction angle (ϕ) so that:

$$\mu = \tan(\phi) = \frac{\tau}{\sigma} \quad (10)$$

where τ and σ are the shear and normal stresses.

Recently, a new rheology, which is viscoplastic, has been proposed and explains very well the velocity profiles of dry granular flows (Jop et al., 2006). The friction coefficient is linked to a non-dimensional number called the Inertial number *I* which represents a ratio between two timescales:

$$I = \frac{t\_micro}{t\_macro} = \frac{\dot{\gamma} d}{\sqrt{P/\rho_p}} \quad (11) \quad \text{(da Cruz et al., 2005)}$$

Where t_micro $= \frac{d}{\sqrt{P/\rho_p}}$ is the microscopic time scale related to the typical time scale of rearrangement and t_macro = $1/\dot{\gamma}$ is a macroscopic time scale related to the mean shear rate (Jop et al., 2006).

The analytical expression of the friction, which is described by the authors as phenomenological, is the following:

$$\mu(I) = \mu_1 + \frac{\mu_2 - \mu_1}{\frac{I_0}{I} + 1} \quad (12)$$

For monodisperse glass beads in three dimensions, μ_1 is = tan 21°, μ_2 is = tan 33° and Io = 0.3. The equation (12) predicts an increase of the friction as the inertial number increases (Andreotti et al., 2013). In contrast, the kinetic theory of gases predicts a decrease of the friction coefficient with I (Andreotti et al., 2013).

Gas-fluidization is an important concept in the physics of PDCs and serves as one of the most cited concepts to explain PDC mobility (Sparks, 1976; Roche et al., 2002; Gravina et al., 2004; Girolami et al., 2010; Roche, 2012). Fluidization is achieved when ascending gas supports vertically downward moving particles and is thought to occur in PDCs either when gas is released from particles or by incorporation of air during flow. Most of our current concepts of gas fluidization in granular beds comes from engineering studies (Geldart, 1986).

The (vertical) gas flow exerts a drag force onto solid masses so that friction eventually decreases and the flow becomes weightless. Both pore-fluid pressure P_d and superficial gas velocity increase u_g can be related by the Ergun equation (composed of laminar and turbulent terms) in the case of a steady flow:

$$P_d = \left(\frac{150(1-\phi^2)\eta_g u_g}{\phi^3 d^2} + \frac{1.75(1-\phi^2)\rho_g u^2{}_g}{\phi^3 d} \right) h \quad (13)$$ (i.e. Girolami et al., 2008, 2010)

where h and ϕ are the height and the porosity of the column, d the particle diameter, η_g the gas dynamic viscosity, ρ_g the gas density.

At $u_g = u_{mf}$ or minimum fluidization velocity, the weight is fully supported expressed as:

$$P_{d,mf} = (\rho_p - \rho_g)(1-\phi)gh \quad (14)$$

where ρ_p is the particle density.

(The pore pressure can be estimated at u_{mf} when neglecting the influence of the gas (low density of the gas as opposed to the density of the particles) in the flow weight, so that:

$$P_{mf} = [\rho_p(1-\phi)gh] \quad (15)$$

When, the flow is weightless or fluidized, it has a fluid-like behaviour (Girolami et al., 2008; Roche, 2012). An expression of the minimum fluidization velocity u_{mf} and the hydraulic permeability k can be obtained:

$$u_{mf} = \frac{k P_{mf}}{\eta_g h} \quad (16)$$

Equation (11) is derived when the u_{mf} equals the laminar term of the Ergun equation (Roche 2012).

$$k = \frac{\phi^3 d^2}{150(1-\phi^2)} \quad (17)$$

When fluidization stops, the granular column loses its pore-pressure through a process of diffusion and the particle frictional behaviour is enhanced. The diffusion of the pressure can be defined as follows:

$$\frac{\partial P}{\partial t} = \frac{\mathrm{D}\,\partial^2 \mathrm{P}}{\partial \mathrm{h}^2} \quad (18) \quad \text{where } \mathrm{D} = \mathrm{k}/(\eta_g\, \phi\, \beta)$$

D is the hydraulic diffusion coefficient and β is the gas compressibility (equals to the inverse of the absolute gas pressure), and the duration of pressure diffusion t_d is proportional to the timescale:

$$t_d \sim \frac{h^2}{D} \quad (19) \text{ (Iverson, 1997).}$$

It has been shown that homogenous fluidization of fine particles of 0.1–0.5mm with densities respectively of 2.2 and 0.5 g cm^{-3} can be achieved (Druitt et al., 2007; Girolami et al., 2008). When defluidization occurs, diffusion of the gas trapped in the flow has been observed, as well as coupled deaeration and sedimentation processes within the flow. Experimental studies on PDCs have shown the major influence of the fines content is to decrease u_{mf} and u_{de} (deaeration rate) (Druitt et al., 2004; Druitt et al., 2007). Moreover, high temperature of the mixtures (>200°C) as well as shear decreases the effect of the interparticulate cohesion link

to moisture (Druitt et al., 2007) and also acts as an inhibiter of the gas channeling often observed in static fluidization experiments (Wilson, 1980; Wilson, 1984b; Gravina et al., 2004).

They are still multiple unknowns about the physics of concentrated PDCs. Most unknowns are related to the fact that a range of regimes probably coexist in PDCs, but the physics has been only defined for end-member regimes in other fields of science. Therefore, a single model cannot explain all transport behaviours.

1.4.8 Modelling of PDCs

PDCs are extremely complex natural phenomena that have only been poorly recorded or internal processes seldom witnessed. The typical approach taken to partially describe aspects of their dynamics involved major simplifications leading to models that can at most account only for end-member flow situations. PDCs are in a mathematical sense a good example of a chaotic system, because their dynamic is largely dependent on small variations of initial conditions; and they are also dependent on the complex boundary parameters interacting with the flow, such as the topography. Simplifying the number of variables is a useful approach because a 'perfect' model of PDCs would need a complete understanding of the conditions describing pre-, syn- and post- -flow states. PDCs display a polydispersity as well as polydensity of their clasts (Freundt and Bursik, 1998) that lead to the conclusion that variable transport and deposition regimes may co-exist subsequently and influence the flow behaviour.

1.4.8.1 Experimental modelling of PDCs

1.4.8.1.1 Dilute flows

Pyroclastic surges or dilute PDCs have been envisaged as gravity-driven flows, commonly known as gravity currents. Gravity currents move because of the density contrast between the flow and the ambient fluid (Simpson, 1997); such contrast arises from the presence of particles transported within the current. The dynamics of gravity currents are relatively well understood for a large range of conditions (Simpson, 1997; Huppert 2006). Most of the basics of the physics of gravity currents have been verified in small to medium scale experiments which have commonly taken the form of lock-exchange experiments (Fig. 1.14; i.e Simpson, 1972; Huppert and Simpson, 1980; Britter and Simpson, 1978; Gladstone et al., 2004). Typically, lock-exchange experiments were undertaken by releasing a saline fluid into water where the density contrast between both fluids was small. The outcomes of these experiments were applied to the behaviour of pyroclastic surges and turbidity currents. Experiments have shown that flows are mostly inertial where the densimentric Froude number approaches a value of 1.2 (Huppert and Simpson, 1980). The morphology of a gravity current was defined as comprising a head where the wake forms at its rear, followed by a body (sometimes called tail) of smaller thickness. Simpson and Britter (1979b) have shown that the velocity at the rear of the head and front of the body can exceed by 30% the flow front velocity, and invoked possible exchange between the body and head.

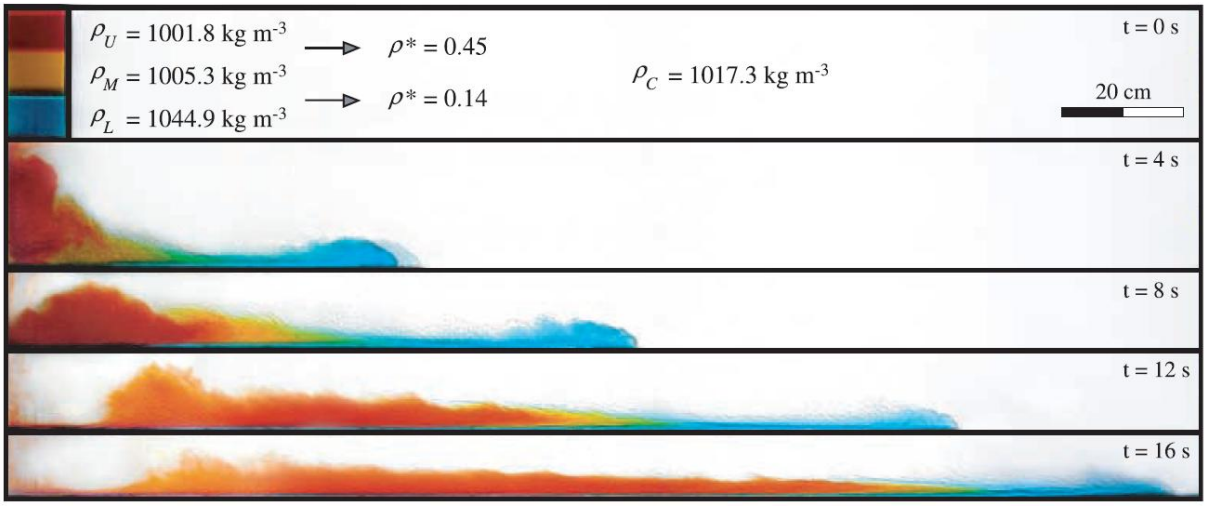

Fig. 1.14. Photographs of three-layered saline currents in lock-exchange experiments (modified from Gladstone et al., 2004).

In lock-exchange experiments, the current goes through various phases; in the slumping phase the flow collapses and propagates at nearly constant velocity (Huppert and Simpson 1980). The authors interpreted the constant velocity phase as the result of the counterflow of light fluid at the channel top while the denser fluid flows at the bottom, as predicted from mass conservation equations. Alternatively, the constant phase can also be explained by a balance of inertia and buoyancy forces with resistance to the flow (Hogg and Pritchard, 2004). Finally, the energy of the current dissipates by interaction with the ambient light fluid and viscous forces come to dictate the flow dynamics (Huppert and Simpson, 1980).

In lock-exchange experiments, particle-laden flows have ambient also been generated and box-models developed from two-fluid experiments have been shown to appropriately describe their propagation (Bonnecaze et al., 1993). Further experiments have been undertaken where the fluid of the gravity current was lighter than the ambient fluid and the light fluid was particle-laden. This is an analogy of dilute, hot PDCs wherein hot air is lighter than ambient "cold" air (Sparks et al., 1993). However, most lock-exchange experiments involved mono-disperse grain-size distributions, which differ from natural examples.

Therefore, bidisperse and polydisperse distributions were tested (Gladstone et al., 1998) and non-linear effects of the distribution on the flow dynamics were found. Adding a small amount of fines to a coarse-rich flow induced more effects than the opposite effect and box models failed to reproduce the flow behaviour (Dade and Huppert, 1995). Other experiments of bidisperse particle-laden flows wherein particles were in hydrodynamic equivalence generated deposits displaying normal grading of the coarse particles while the fines deposition was intrinsically dependent on the particle volumetric concentration (Choux and Druitt, 2002).

From experiments, the role of entrainment of the ambient air into the flow has been quantified as a function of non-dimensional numbers such as the Richardson number or Froude numbers. This has allowed derivation of empirical laws (Ellison and Turner, 1959; Parker et al., 1987) that have been used in a wide range of models of gravity currents (i.e. Bursik et al., 1996). Entrainment of the surrounding fluid occurs along the flow surface through turbulent billows related to Kelvin-Helmholtz instabilities forming at the flow-ambient interface. From experiments, entrainment is commonly thought to be negligible (<0.01) for subcritical current where Fr<1, while the entrainment coefficient takes values of 0.01–0.1 for a Froude number exceeding 1 (Parker et al., 1987). Entrainment is a very important quantity as it influences the dilution rate of the flow over distance that can result in the flow either stopping or rising once the density difference between the flow and ambient reach an Froude number of 1 (i.e. Bursik and Woods, 1996).

It is noteworthy to mention that most experiments involved low Froude numbers, commonly around 1.4 or below while the Reynolds number was also rarely greater than 10^4 (known as the fully intermediate to turbulent regime threshold).

1.4.8.1.2 Dense flows

Concentrated flows represent the other end-member of PDCs and are characterized by particle volumetric concentrations near those of loose packing. In these PDCs, the momentum is thought to be transferred primarily by the solid phase. Dense granular and gas-particle flows (fluidized) are the two end-members in the concentrated flow field (Branney and Kokelaar, 2002; Sulpizio et al., 2014).

Dry-granular flows

Particle interactions in dry, coarse-grained PDCs were investigated in shear-cell experiments by Cagnoli and Manga (2004, 2005), in which they confined a pumice bed between vertical and co-axial cylinders. Experiments provided evidence that energy dissipation occurs within a layer characterized by a high-degree of collision at Savage numbers up to 0.4 while the upper layer acted as a non-sheared layer moving in plug-like manner. These results were commensurate with coulomb friction behaviour wherein reverse segregation of the coarse light clasts and normal segregation of the coarse dense clasts was observed.

Experiments on concentrated granular flows involved collapse of a granular axisymmetric or dam-break piles and have shown that the runout is controlled by the ratio of the height over the length of the column (Lube et al., 2004; Lajeunesse et al., 2004; Lube et al., 2005). Particles initially located at a superficial level in the column were quickly overtaken by the flow front and constituted the basal thin layer (Lube et al., 2004). Such a layer was delimited by a dynamic interface which separated moving from static (deposited) particles and could propagate towards the free-surface during emplacement. Velocity profiles in the moving layer

depicted an upper low shear zone that propagated as a plug while the middle zone showed a near linear gradient and finally a lower near exponential decreasing region (Fig. 1.15).

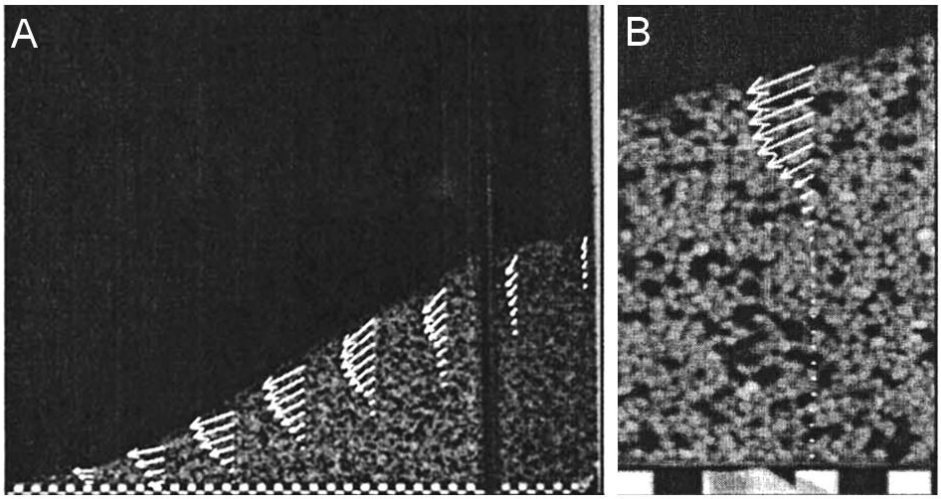

Fig. 1.15. Example of vertical velocity profiles in granular flows (Modified from Lube et al. 2004).

From dam-break experiments, Lube et al. (2004) questioned the role of the coulomb friction coefficient and showed that it affects the flowing material solely in the stopping phase. Furthermore, the shape and size of particles has been shown to influence the flow runout because of the control of the two parameters on the interparticulate friction (Balmforth and Kerswell 2005). Granular flow experiments have also highlighted that the proportion of fines in a bipartite mixture greatly influences the flow kinematics and runout (Roche et al., 2005; Phillips et al., 2006) and that mobilization of erodible substrate on steep slopes can markedly influence the flow runout (Mangeney et al., 2010).

Nearly quasi static regimes are usually described by a plastic model (Nedderman and Laohakul, 1980) while a kinetic theory has been developed to account for the granular gas regime where the flow behaves as a more dilute flow (Jenkins and Savage, 1983). Furthermore, dense fluid regimes are well-rendered by a viscoplastic rheology, as shown in unidirectional cases (GDR-MiDi, 2004). The latter rheology was improved to account for 3D

behaviour by assuming the flows were incompressible (Jop et al., 2006), where, with the right high-packing fractions and initial boundary conditions, constitutive equations matched experiments well (Pouliquen, 1999).

Boundary layers have been shown to affect granular flow kinematics. For example, wall frictional forces can affect the velocity up to 2/3 of the width (Louge and Keast, 2001) while lower flow boundary conditions can influence the flow velocity. In thin flows, where the thickness is scaled to few tens of grains only, a nearly linear sheared vertical profile of the velocity is exhibited (Berton et al., 2003; Delannay et al., 2007). Thick flows, in contrast, show Bagnold scaling in the core of the flow with lower velocities at the base, and at large inclinations the flows are more dilute at the base and inverted density profiles are obtained (Taberlet et al., 2007).

Gas-particle flows

While gas-particle flows were mostly studied in static fluidization experiments, several experiments have highlighted the importance of the gas phase through fluidization processes. Fluidization occurs when the weight of the particles is balanced with the drag force applied from an upward gas flux. This configuration is well known in engineering and was shown to induce high-pore pressure at the base of the flow when the weight of the flow is partially to fully supported. However, owing to the polydispersity of natural pyroclastic mixtures, it has been shown that only a range of small particles can be fully supported and that complete fluidization of PDCs is unlikely (Sparks, 1976). In static experiments, it has been shown that the fines content greatly influences the degree of fluidization of the mixture (Gravina et al., 2004; Druitt et al., 2007). Furthermore, while channeling was thought to be influential at room temperature because of inter-particle cohesion in fines-rich ignimbrite (Wilson, 1980; Wilson, 1984a), experiments with shear and high temperatures have demonstrated the

possibility of suppressing channels and ensuring support of the bed by fluidization (Druitt et al., 2007). However, the source of the gas is still unknown and as a result, once the supply of the gas has been suppressed, the flow dynamics is largely controlled by the rate of diffusion of the high-pore pressure.

Dam-break experiments on highly concentrated air-particle flows were performed to investigate the transport and emplacement dynamics of the dense PDC end-members. Fine smooth glass bead particles were released after their fluidization into a horizontal channel and showed that their behaviour depends on the diffusion timescale of the high-pore pressure that developed under fluidization conditions (Roche et al., 2008; Roche, 2012) (Fig. 1.16).

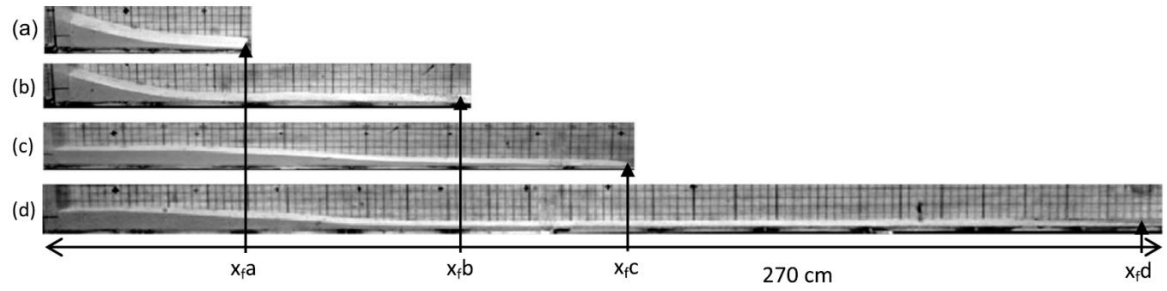

Fig. 1.16. Deposit of initially non-fluidized flows (a) on smooth substrate and (b) on a 3 mm "rough" substrate, and of initially fluidized flows on (c) smooth substrate and (d) "rough" substrate. (Modified from Chedeville and Roche, 2014).

Due to the fine grained-nature of the analog material used, pore-pressure diffusion was slow compared to the timescale of the flow propagation. Because of the gravitational collapse of the column in dam break experiments, these are considered as analogues of real-world PDCs. Flows can be either propagating as inertial flows having a high-mobility or as dry granular flows under a more frictional regime. Initially, the inertial flow velocity scales to the initial column height and the velocity of the front is constant during the slumping phase. Once the pore-pressure has decreased by diffusion, the flow enters the frictional regime and stopping phase where the flow behaves as dry frictional granular flow (Roche, 2012). Flows are composed of a sliding head where slip-velocity develops at the lower interface while the body

is characterized by a no-slip boundary condition wherein the deposit is aggraded. Experiments on erodible beds suggested that erosion from the sliding head can occur and was hypothesized as a result of the pressure difference between the ambient in the erodible bed and the low pressure developing at the sliding interface (Roche et al., 2013a).

Similarly to granular flows, the amount of fines markedly increases the potential for the flow to behave in an inertial regime because fine particles require low upward gas-velocity to be fluidized. Furthermore, the expansion of the flow under a fluidization regime can control the rate of aggradation of the mixture, as was shown from polydisperse and fine grained natural flows (Girolami et al., 2008; Girolami et al., 2010).

1.4.8.1.3 The rise of large-scale experiments

A major issue of experimental volcanology applied to PDCs is the correct scaling. For instance, Burgisser (2005) demonstrated that dilute PDCs have never been properly scaled. A novel solution employed to overcome previous scaling problems is to experimentally generate large-scale analogue flows that can match dynamic and kinematic scaling of their natural counterparts. The first experiments on large-scale PDCs generated dilute currents by collapse on a sub-horizontal surface of a natural pyroclastic mixture (Dellino et al., 2007; Doronzo and Dellino, 2011) and proved the great potential of such change of scale (Fig. 1.17). One of the advantages of the Italian experiment (located near Bari in southern Italy) resides in the use of a natural pyroclastic mixture (fallout) which ensures a wide range of coupling mechanisms between the gas and the solid phases.

In such experiments (Fig. 1.17), obstacles could be put in the flow path and dynamic pressure estimates obtained (Doronzo and Dellino, 2011). However, internal measurements and observations were not obtained. Instead, numerical modelling was used to interrogate the concentration and velocity fields (Doronzo et al., 2011) while matching the flow outer shape.

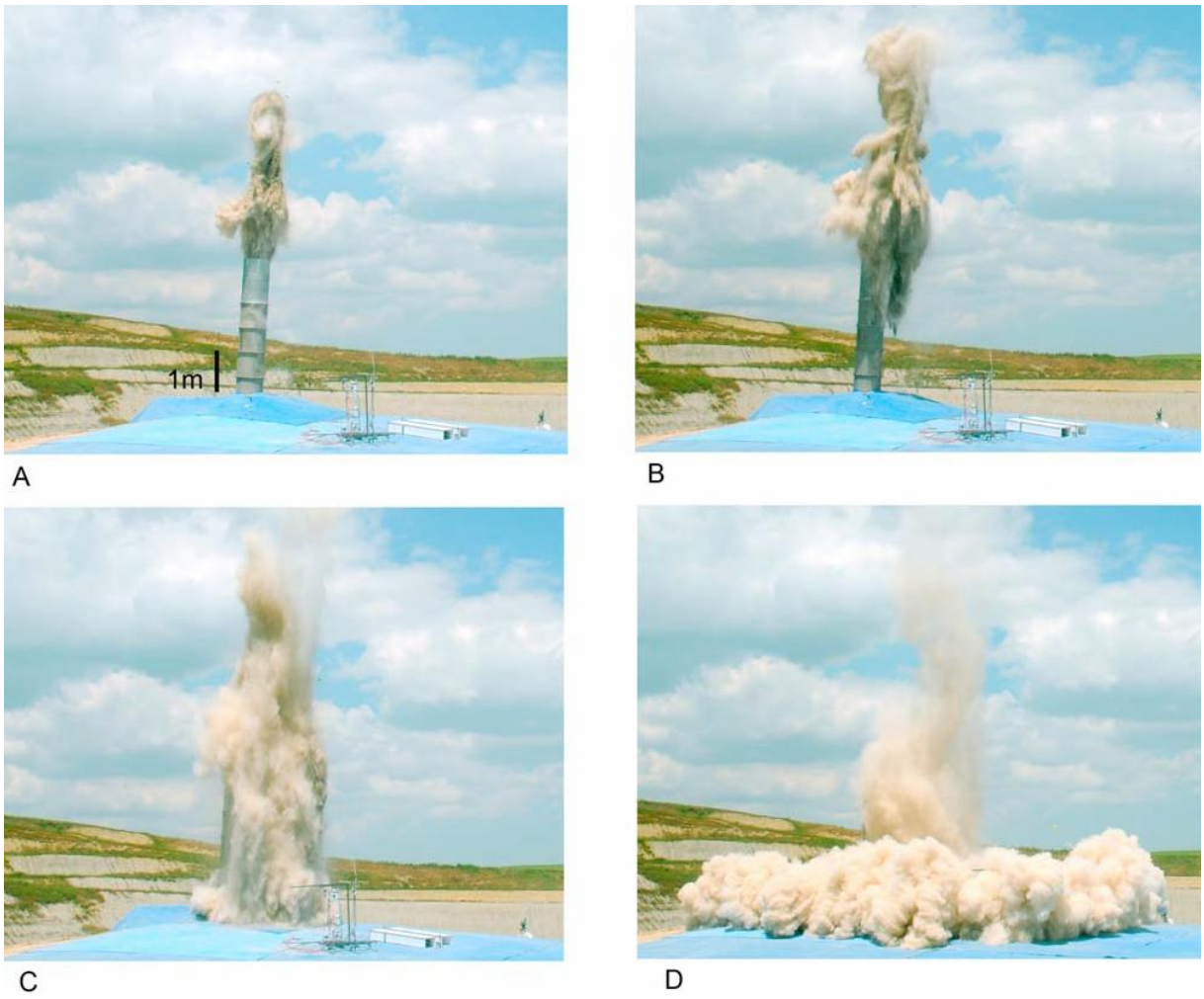

Fig. 1.17. Sequence of pictures taken from an experiment of column collapse. A: Initiation of the column at the conduit exit. B: Start of the column collapse. C: Impact of the dense collapsing column on the ground and initiation of the PDC. D: Propagation of the density current.

Similarly, large-scale experiments targeting the formation of maar volcanoes have proven the obvious advantage of undertaking large-scale experiments (Ross et al., 2013; Graettinger et al., 2014; Valentine et al., 2014).

Another large-scale setup has been built at the Smithsonian Institution Museum Support Centre in Suitland (MD, USA). The experimental apparatus known as "the tank" is 8.5x6x2.5 m^3 in volume and is not air tight but in direct communication with ambient air of the laboratory. In these experiments, windows have been installed and allow direct-observation,

helped by the use of three orthogonal laser sheets to visualize the flow as internal sheets. The material use was a micrometre-sized fine powder of talc that was released into the tank from a conveyer belt (Fig. 1.18). Experiments at ambient and high temperatures were undertaken, and revealed that hot currents surprisingly spread less than currents at ambient temperature (Andrews, 2014). From these extremely low density and low turbulent flows, a better understanding on the generation of co-ignimbrite plumes has been obtained and results provided evidence that lateral entrainment can be few times higher than vertical entrainment. Furthermore, Andrews and Manga (2011) have shown that currents can surmount topographic barriers 1.5 times higher than the flow height. Nonetheless, owing to the extremely low velocity and density of the flow and small range of particle size and density, these experiments represent the very end-member of the dilute flows.

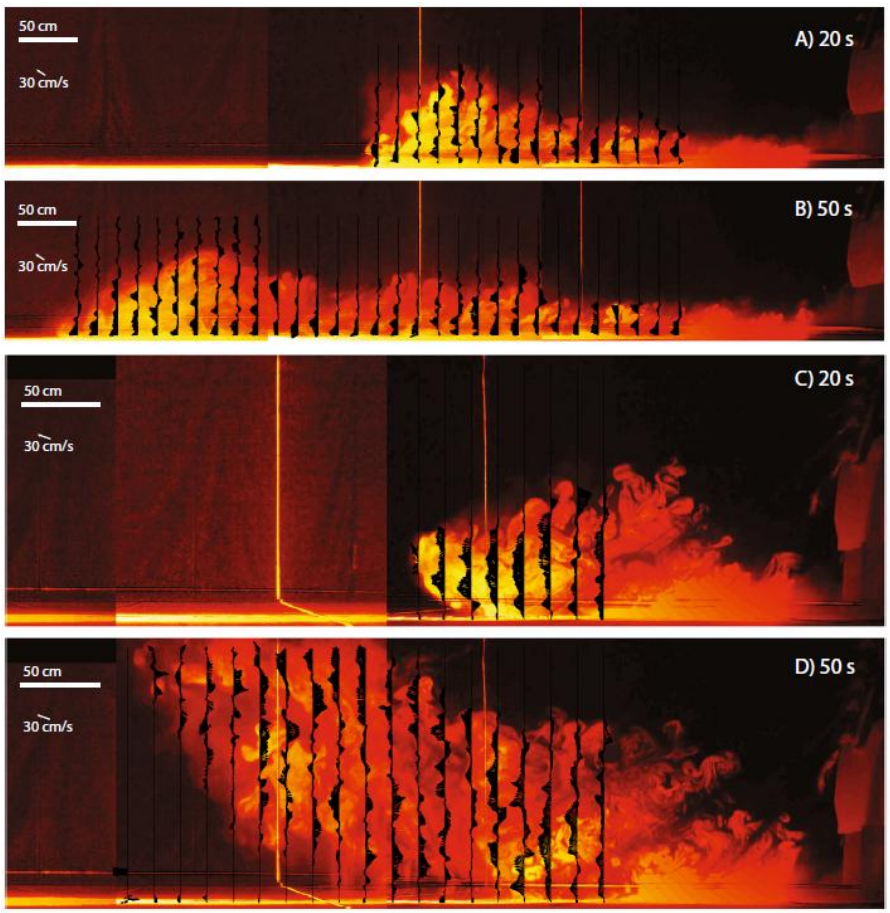

Fig. 1.18. Experimental flows at ambient (A) and (B) temperature and heated (C) and (D). Time-averaged velocity fields are shown and depict the complexity in the rising buoyant plume. Modified from Andrews (2014).

Over the past two years, a large scale facility located at Massey University has demonstrated its ability to produce scaled-PDCs encompassing dense granular to fully turbulent and dilute flows. This facility is described in detail in Chapter 3 and the experimental work of the present thesis was undertaken at this facility. The uniqueness of the setup allows column collapse of natural pyroclastic mixtures to generate flows that can propagate at velocities exceeding 25 m s^{-1} and can reach distances up to 35 m from source. The setup allows internal measurements of velocity fields and concentration estimates, along with direct observations of transport and deposition processes. Experimental deposits span a wide range of facies with the common formation of massive to laminated units (Fig. 1.19) (Lube et al., 2015).

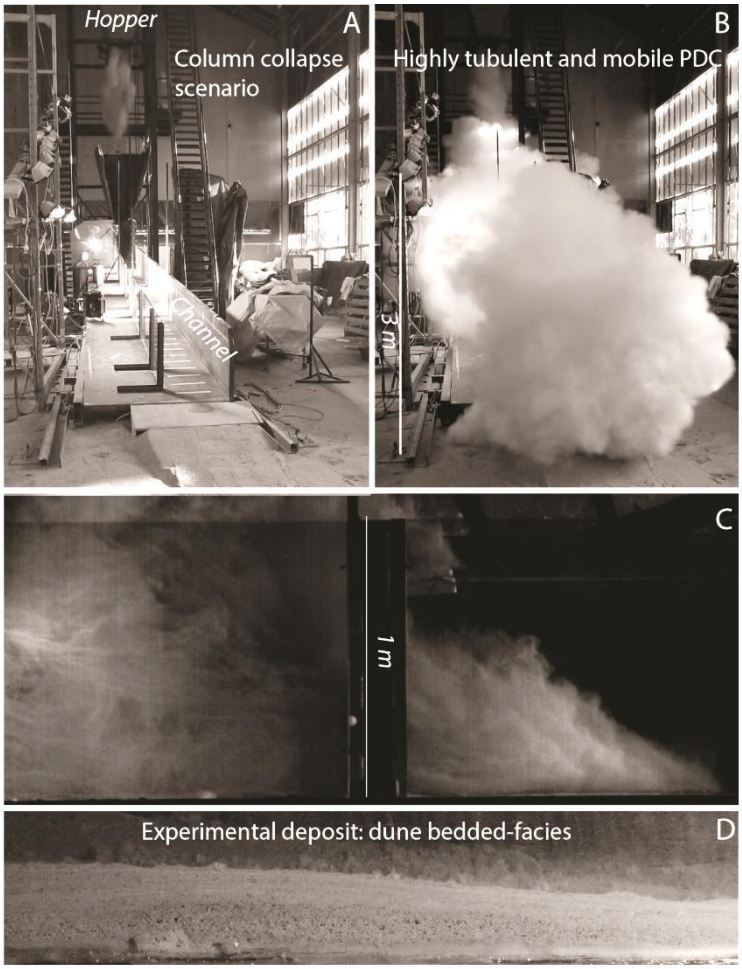

Fig. 1.19. Experimental PDCs and example of depositional sequence. A: Initiation of the column collapse from the hopper. B: Sideview of a fully dilute and turbulent PDC. C: Sideview of the internal structure of a concentrated ash-cloud. D: Cross section through a dune-bedform generated in "dilute" experiments.

By synthesizing PDCs with the eruption simulator PELE, the friction-weakening mechanism of pyroclastic flows that was named 'aero-planing' has been demonstrated (Lube and Breard et al., *in review*). Through direct measurements of particle concentration and velocity, the formation of a high-sheared and low-concentration basal zone has been illuminated. In the basal zone, particle volumetric concentration can be as low as c.20 vol.%. This "inverted density" zone formed conditionally and solely under effective partial-slip boundary conditions and was subsequently observed while the particulate weight was fully transferred onto high-pore pressures. Similar low-concentration zones have been observed in granular flow experiments (i.e. Taberlet et al. 2007). Dynamics of these granular flows was well

predicted by the μ(I) theory, where μ is the friction coefficient and I the inertial number (Jop et al. 2006). However, these authors have not observed large modification of the friction coefficient as a result of the low concentration zone. Conversely, Lube and Breard et al. (*in review*) demonstrated that the friction coefficient is a function of inertial number (*I*), the degree of bed support and particle concentration. The negative pressure (with respect to atmospheric pressure) formed at the base of the slipping underflow provides an attractive force that retains the high-pore-pressure of the overlying current over time scales that exceed by 1 order of magnitude the theoretical gas retention time. Hence, high pore-pressures and associated low frictions were sustained over longer distances. Development of aero-planing explains the extreme runout potential of pyroclastic density currents, by providing an efficient way for PDCs to retain their high-pore pressures.

1.4.9 Numerical modelling

Introduction

Numerical modelling is a very useful tool to assess the complexity of PDC dynamics and has been increasingly developed over the past few decades. There are multiple types of models; here a short overview of the models of PDCs is presented.

Overall, models intend to solve the conservation of mass momentum and energy equations. Here is an example of momentum equation:

$$\frac{\partial}{\partial t}\rho u + \nabla . (\rho u u) = -\nabla P + \nabla . \tau + \rho g$$

$\frac{\partial}{\partial t}\rho u$ describes the velocity change with time according to the flux of momentum $\nabla . (\rho \boldsymbol{u}\boldsymbol{u})$, driving the stresses that act on the flow at any locations. These stresses are induced by the

pressure differential $-\nabla P$, mechanical stresses $\nabla.\tau$ and gravity ρg. The influence of these stresses depends upon the physics of the simulated flow (Roche et al., 2013b). The closure of the model required input of the initial conditions (i.e. starting mixture density and grain-size distribution), boundary conditions (i.e. flux input, topography) and constitutive equations (i.e equations relating stress and velocity) (Dufek et al., 2007). Numerical simulations are required to solve conservation equations because they contain partial derivatives and their solutions are often too complex to be solved analytically. Most of the time, exact solutions do not exist and the standard method is based upon the discretisation of equations in space and time in order to obtain the approximated solution attributed to the nodes of the discretized space or grid (Toro, 2001).

Kinetic model

The earliest simulations of PDCs were to simplify the flow as a rigid block whose motion was calculated from a simplification of the conservation of the momentum equation. The motion of a block is driven by gravity, following the topography and by a resistive law. The latter law was approximated as a constant basal friction term, as well as a viscous term that varies with velocity and a turbulent or collisional term which is a function of the square root of the velocity. Therefore the resistive term takes the following form: $a_0+a_1u+a_2u^2$ (Sheridan and Malin, 1983; McEwen and Malin, 1989; Saucedo et al., 2005). Building upon this model, Wadge et al. (1998) used a kinetic model to simulate the inundation area of dense flow at Montserrat while incorporating the possibility for the ash-cloud to have a greater extent. Nevertheless, the kinetic model oversimplifies physical mechanisms as it does not account for sedimentation, density variations, and entrainment and cannot be used for dilute PDCs. The usefulness of this tool lies in the rapid time of calculation; in fact the demand for rapid

estimates of runout for assessment of pyroclastic flow hazards are often needed during volcanic crises.

Discrete element model (DEM)

In this model, the motion of individual particles is resolved by solving Newton's equation of motion. The only direct application of such a model was made by Mitani et al. (2004). In their study, they resolved the grading of particles while there was no interstitial fluid and interpreted the model as showing that coarse-tail grading can be formed without any influence of the fluid (gas). DEM cannot solve more than ten million particles and therefore cannot be used to assess the particle dynamics of a flow, as ten million ash-size particles would fit into a large glass. Discrete element modelling is used in combination with multiphase modelling and used in a number of cases of numerical modelling of granular flows (i.e. Taberlet et al., 2007 and references therein).

Dilute-1D models

Dilute flows have been modelled using an approximation of a well-mixed and fully dilute current while assuming conservation of mass and volume in order to describe the thickness and kinematics of the flow head. Basing their analysis upon scaling relationships that were derived from a box model and lock-exchange experiments (Dade and Huppert, 1995), Dade and Huppert (1996) have attempted to describe real-world flow emplacement such as the Taupo ignimbrite. Another approach has included the conservation of thermal energy and entrainment (Bursik and Woods, 1996). These approaches were useful to constrain the conditions under which PDCs can propagate before lift-off under various conditions.

However, because of the assumption of a lack of stratification and in case of the Froude number (Dade and Huppert, 1996), these are only applicable to very dilute flows (Dufek et al., 2015) and the interpretation of such models need to take into account the large uncertainty inherent in them.

Depth-averaged models

In depth-averaged models, the discretization takes the form of a column where the flow properties are averaged across the flow height. Furthermore, the 3D equations are vertically integrated. One important assumption is that the flow length is much greater than the flow height so that vertical displacements are negligible. The mass of the column is considered to either move as a unique velocity or at a fixed velocity profile, depending on the rheology chosen (Roche et al., 2013b). The depth-averaged approach has been widely used to model granular flows (Savage and Hutter, 1989b) and dense geophysical flows such as mudflows, landsides or lahars with the TITAN2D model or VolcFlow (Heinrich et al., 2001; Pitman et al., 2003; Kelfoun and Druitt, 2005; Patra et al., 2005; Lucas and Mangeney, 2007). The same models were used to reproduce the runout and deposit extent of underflows of pyroclastic flows (Patra et al., 2005; Charbonnier and Gertisser, 2009; Charbonnier and Gertisser, 2011).

The depth averaged method is a very efficient tool for reproducing the motion of dense flows as their depth averaged density is assumed to be nearly constant in time and space. Conversely, the density of dilute flows is highly variable over time and space and cannot be resolved efficiently with depth averaged methods. The main questions arising from these models lies in the rheology used, which is approximated by a first-order law describing the physical behaviour. Wide ranges of rheologies have been used and span frictional, constant,

viscous Bingham or Voellmy laws. The most common approximation uses a frictional behaviour or Coulomb rheology (Patra et al., 2005) in which collisions are assumed to dominate the behaviour of granular flows. In such a rheology, acceleration (due to gravity) of the flow on slopes higher than the friction angle is predicted. However, Kelfoun et al. (2009) and Kelfoun (2011) showed that this rheology does not explain the propagation of pyroclastic flows, even when tuned with velocity-dependent stress, and instead proposed a plastic rheology. Using a plastic rheology, depth-averaged models reproduced the extent and deposit architecture while also forming levees and rounded bulbous frontal lobes (Kelfoun, 2011). While Coulomb friction stipulates that the basal shear stress is dependent on the flow thickness, plastic rheology predicts that the basal shear stress is independent of the thickness of the flow but is not physically explained. In fact, not even fluidization explains such behaviour, because plastic rheology stipulates that the thicker the flow, the lower the friction coefficient. Pyroclastic flows depict similarities to long-runout debris avalanches, which could indicate that they behave with somewhat similar rheology (Kelfoun et al., 2008). Using depth-averaged models has the advantage of its speed of calculation because of the averaging of the third dimension and can be a great tool for hazard management.

The recent discovery of the aeroplanism of pyroclastic flows (Lube and Breard et al., *in review*) predicts that the friction coefficient is correlated to the formation of a low concentration zone formed when slip-velocity overcomes a threshold value. Thick natural flows are likely to also be associated with larger velocities (as it is the case for debris avalanches). This could explain how large underflows could develop high basal slip-velocities and therefore be associated with low friction. By way of example, the diffusion of the pore-pressure for underflows of 1–5 m in thickness should be suppressed for minimum basal slip velocities of 5–10 m/s and corresponding depth-average velocities of c.10–20 m/s.

These velocities are in good agreement with direct-observations of BAFs and pumice flow velocities (i.e. Calder et al., 1999; Lube et al., 2011; Hall et al., 2015).

Multiphase models

Spatial and temporal variations of the physical properties necessary to model dilute PDCs with "accuracy" requires a horizontal and vertical mesh. In multiphase simulations, the dusty gas and the particles are treated differently. Particle and gas properties are averaged and attributed to nodes of the mesh. All phases, which comprise various grain-sizes and gas of various compositions, share the same virtual mesh while the phases interact with each other. Wohletz et al. (1984) was the first to use this method. Over the next decade, computational power increased and allowed more complex models (Valentine and Wohletz, 1989; Wohletz and Valentine, 1990; Dartevelle et al., 2004).

Current multiphase numerical models have been developed from the initial K-FIX (Kachina with Fully Implicit eXchange) developed in Los Alamos laboratory to model the interaction of steam and water in nuclear reactors (NV, USA) (Rivard and Torrey, 1977; Rivard and Torrey, 1978; Rivard and Torrey, 1979) and was modified and used as the DASH code for volcanic purposes (Valentine and Wohletz, 1989; Valentine et al., 1991). K-FIX was further modified at the Illinois Institute of Technology (IIT code) and gave birth to the PDAC2D code used specifically to model volcanic plumes and related PDCs (Neri et al., 2003a). Complexity was added to models with the introduction of the vapour phase added to the gas and solid phases by Dobran et al. (1993) and Neri and Dobran (1994). Their modification of the code allowed estimation of spatial particle segregation as they involved polydisperse mixtures (Neri et al. 2003). Until recently, studies were limited to 2D or axisymmetric cases. Nowadays, the development of 3D multiphase modelling (Ongaro et al., 2007; Neri et al.,

2007) has allowed researchers to model very complex PDCs over complex terrain, such as the 1980 Mount St. Helens blast (Esposti Ongaro et al., 2011; Esposti Ongaro et al., 2012). In parallel, from the IIT code, the NIMF (Non-Isothermal MultiParticle Fluidisation) code was developed and transformed at the National Energy Technology Laboratory and Oak Ridge Laboratory into the MFIX code that describes the hydrodynamics, heat transfer and chemical reactions in systems with fluid-solid interactions (Syamlal and O'Brien, 1993; Syamlal, 1994; Syamlal, 1998). The adaptation of the MFIX code to geophysical systems (G-MFIX) required accounting for the universal atmospheric profile, volumetric variations of the gas phase, large eddy model (Zehner and Schlunder, 1970), and the sub-grid turbulent heat flux (Dartevelle, 2003; Dartevelle, 2004). Currently, In G-MFIX, an Eulerian-Eulerian-Lagrangian (EEL) approach is used in which separate continua are used to model both the gas and the particle phases. In the multi-continua (Eulerian-Eulerian) approach, individual particle phases and carrier fluid has independent conservation equations for mass, momentum and energy, along with drag coupling between phases (Dufek and Bergantz, 2007c). Steam when formed possesses its own conservation of mass coupling. In dilute regimes, Dufek and Bergantz (2005) used a rheology that assumes binary inelastic particle collisions whereas at high particle concentration a plastic rheology is used (Syamlal, 1994). The code was used for 3D eruption simulations and deposit comparisons with the Kos Plateau Tuff (Dufek and Bergantz, 2007b) and the in-situ production of ash in concentrated PDCs (Dufek and Manga, 2008).

The complexity of multiphase codes used in the PDAC and G-MFIX models is by far higher than any other models so far but these are constrained by two mains issues: 1) multiples laws used have not been validated for PDCs, 2) models require an enormous computational cost. Therefore, we are far from using these models as an applicable solution in hazard assessment.

1.4.10 Summary and future perspectives

PDCs remain a highly complex problem for the scientific community and understanding the key controls on their dynamics are a real challenge. Only hypotheses on the sedimentation (all process that accompany particles into the current down to the flow boundary-zone) process can be made based on their deposits because they reflect the deposition processes affecting particles in the flow-boundary zone until definitive rest.

Dilute and turbulent currents would produce thin stratified deposits and usually massive deposits that thicken in valleys are related to highly concentrated flows. Models for each end-member have been developed with many assumptions. On one hand, for dilute currents one assumes that interaction between particles is negligible, particles are homogenized by turbulence and grains settle down from the current following an exponential law. On the other hand, for pyroclastic flows it is still not clear whether fast (*en masse* like) or slow progressive aggradation dominates the sedimentation process (Branney and Kokelaar, 2002). Unifying the end-members presents significant difficulties because each model has incompatible assumptions. Nevertheless, we know that a continuum exists in PDCs, not only between different currents but also inside a single current that can display laterally and vertically variable transport mechanisms and settling processes (Burgisser and Bergantz, 2002; Sulpizio et al., 2014).

A simple deposit can lead to two opposite interpretations of the flow dynamics (i.e Taupo ignimbrite) (Dade and Huppert, 1996; Wilson et al., 1997). Still unresolved, this example summarizes the struggle for volcanologists to link deposits to physical parameters of the flow. One of the emerging methodologies is using large-scale experiments that can reproduce PDCs with variable regimes because they will allow producing natural scaled-PDCs with a natural volcanic material and tracking the evolution of the current structure and sedimentation

along the flow runout path but also relating properties of the final deposits to the dynamics of their parent current.

The present thesis provides a dataset of PDC internal behaviour, presenting findings from the largest pyroclastic density current experiments to date. The following chapter 2 describes the experimental setup and experimental methods used to produce experimental PDCs from column collapse of natural pyroclastic mixtures.

Chapter 2 – Material and Methods

Chapter contents

Chapter 2 – Methods

2.1 Large scale experimental setup

2.1.1 Introduction to the setup

The lack of direct observations and internal measurements of the physical properties of pyroclastic density currents drove Dr. Lube and Prof. Cronin to build a PDC test facility at Massey University (NZ), where large-scale and high-energy experimental PDCs can be synthesized under controllable and safe conditions. After an initial working phase of testing a small-scale prototype PDC generator, followed by the design and development of the full-scale facility together with a suitable sensor and data-recording infrastructure, the man-made volcano named "PELE" (Pyroclastic flow Eruption Large-scale Experiment) was first deployed in June 2013.

Supported by the Royal Society of New Zealand Marsden Fund, Massey University and by a team of New Zealand-based and overseas collaborators, PELE was designed and constructed as a long-term investment into research on PDCs with several objectives in mind. These included:

- Establishing a sufficiently large test facility that allows the repeated synthesis of a wide range of PDC transport and deposition processes through particle-gas currents of natural volcanic material and air, which are dynamically and kinematically well-scaled to their natural counterparts.
- Understanding the nature of gas-particle interaction in PDCs through direct observations and measurements, and linking this information to important aspects of their runout dynamics and hazard potential.
- Deriving the first quantitative validation or benchmark datasets for PDCs that can be deployed to test and potentially improve numerical PDC models.

- Using the readily adaptable setup infrastructure to elucidate the influence of various internal and boundary conditions (e.g. initial flow conditions; material properties; temperature; substrate geometry, roughness and erodibility; and interaction with landscapes and structures) on flow behaviour in systematic series of experiments.

The large-scale experimental setup was built to create mass flows involving natural volcanic particles and air, which provide natural stress coupling between the different phases (solids and gas) and facilitate comparison with real-world counterpart flows. PELE is the second large-scale facility targeting PDCs in the world and extends the work undertaken at the first large-scale setup built in southern Italy, which generates PDCs after collapse of a volcanic column that is shot upward. The Italian large-scale setup generates fully turbulent and relatively dilute flows that spread axysimetrically from source (Dellino et al., 2007). Furthermore, another medium- to large-scale experiment setup has been built at the Smithsonian Institute (Washington D.C., USA) that involves the collapse of an analog mixture of talc from a conveyer belt and generates fully dilute analog flows (Andrews, 2014).

The setup, experimental protocol, methodology and scaling of PELE experiments have been thoroughly documented by Lube et al. (2015). Furthermore, Chapters 3–7 include an individual and detailed method specific to each chapter. Therefore, the present chapter aims at summarizing information specific to the general experimental setup.

2.1.2 Introduction to the experimental procedure

The synthesis of experimental PDCs is subdivided in three steps: i) the preparation, ii) the experimental flow and measurements, and iii) the analysis. The preparation phase encompasses a routine of tasks for each experiment that includes 1) the preparation of the

material, which involves the sampling of the material in the field, drying in an oven, and preparation of the initial blend (see section 2.2); 2) setting the channel inclination and width; 3) calibration of sensors; 4) setting up the cameras and lights; 5) semi-automated filling of the hopper and setting the hopper height; 6) shrouding; 7) connection of the pneumatic door release to pressurized gas; and finally 8) triggering the opening of the hopper doors. This task marks the onset of the second step of the PDC synthesis ("the experimental flow and measurements"), which is subdivided into 4 phases described below:

Phase 1: *The collapse*. The flow phase begins with the controllable collapse of mixtures of pyroclasts and air onto an inclined surface. During the fall, the mixture accelerates and dilutes through stretching. This phase duration is dependent on the mass-flow rate.

Phase 2: *Impact and initial expansion.* The impact zone consists of an inclined section bounded by two walls, which guide the flow into the channel. The impact is followed by rapid expulsion of air and particles, which expand and accelerate along the channel. In this phase the mixture becomes highly turbulent and reaches velocities up to ~30 m s^{-1}.

Phase 3: *PDC phase.* The flow propagates 12 m into the inclined channel that vertically bounds the flow up to 0.6 m high. Once leaving the channel, the flow propagates unbounded up to 35 m from source.

Phase 4: *Deposition.* Deposition starts during the PDC phase, but lasts much longer as the ash-cloud can expand vertically and form a 500–2000 m^3 co-ignimbrite plume that settles over hours depending on the grain-size distribution of the starting mixture.

During each of these four phases, various measurements of the flow are obtained and are fully described in the section 2.3. The third step of the experiments consists of the analysis of

the various measurements obtained, using specific software and calculations described further in the section 2.3.

The number of experiments is limited by the complexity and timescale of the tasks that must be fulfilled in order to perform a single experiment. The entire preparation phase can take weeks and involves helpers for multiple steps.

2.1.3 The apparatus

The PELE experimental apparatus is composed of 4 main structural components: 1) the tower and hopper, 2) the shroud, 3) the inclinable channel and 4) the horizontal section (Fig. 2.1A):

1) *The tower and the hoppers*. The 13 m high tower supports two hoppers (A and B) through which the mixture initiates a vertical collapse. Hopper B is fixed on the upper platform of the tower, whereas hopper A can be moved up and down by an elevator-like system, thereby ensuring the possibility to vary the drop height. The present thesis focuses on experiments undertaken with the large hopper B; therefore only hopper B is detailed in the further section.

Hopper B is made of 5 mm thick stainless steel plates and composed of a body part, which is a rectangular prism in shape, and three trapezoidal additional sections that can be mounted onto each other at the base. Sections have variable width of 0.35, 0.5 and 1 m and a constant length of 1.2 m. The total length of the hopper exceeds 3 m when all the sections are assembled and the hopper has a volume of 4.2 m^3. Fig. 2.2 shows the hopper with two sections added to the rectangular portion. The hopper is mounted on 4 ZEMIC loadcells (model H8-C3-1.5t-4B1) with individual capacities of 1500 kg. These loadcells are connected to a computer that logs the discharge of the hopper, which is steady (Fig. 2.3B). The ideal geometry of the hopper for steady discharges of natural volcanic material was determined by

a range of procedures. This included measurements of the internal and basal frictional properties of the material using a Jenicke shear-cell apparatus (Lube et al., 2015), theoretical modelling of hopper discharge using the semi-empirical relationships established in the engineering literature (Drescher, 1992), and an intensive set of experiments using a 0.75 m^3 prototype hopper with fully adjustable geometry. In hopper B, the trigger of the trapdoor opening is realized remotely and initiates the "eruption column collapse" as a descending stream of air and particles. Pushing the trigger opens a solenoid valve (Fig. 2.4B) that releases pressurized gas of 120 psi into an air piston (Fig. 2.4A), which activates the trapdoor release (Fig. 2.4C).

2) *The shroud.* The shrouding for the column was made with thick tarpaulin that was tight on each end to minimize entrainment of the ambient air on the boundaries. Hence, the column forms a dense central core region with a constant cross sectional area.

3) *The inclinable channel*. The 12 m long channel is inclinable from angles of 6–25^o and installed on a rail that allows it to be positioned underneath the hoppers for all inclinations. The mechanical inclination is achieved through oil piston. The width of the chute can be varied from 0.35–1 m and vertical walls, composed of steel and toughened 10 mm thick glass panels, are 0.6 m high (Fig. 2.1B). The channel base is instrumented with basal pore pressure and load cell sensors. Furthermore, vertical profiles of infrared sensors and sediment samplers are also implemented on the channel.

4) *Outflow*. A horizontal surface section, where the flow propagates without bounds, extends the flow runout to ~35 m before it becomes blocked by a 10 m high cliff section (Fig. 2.1C).

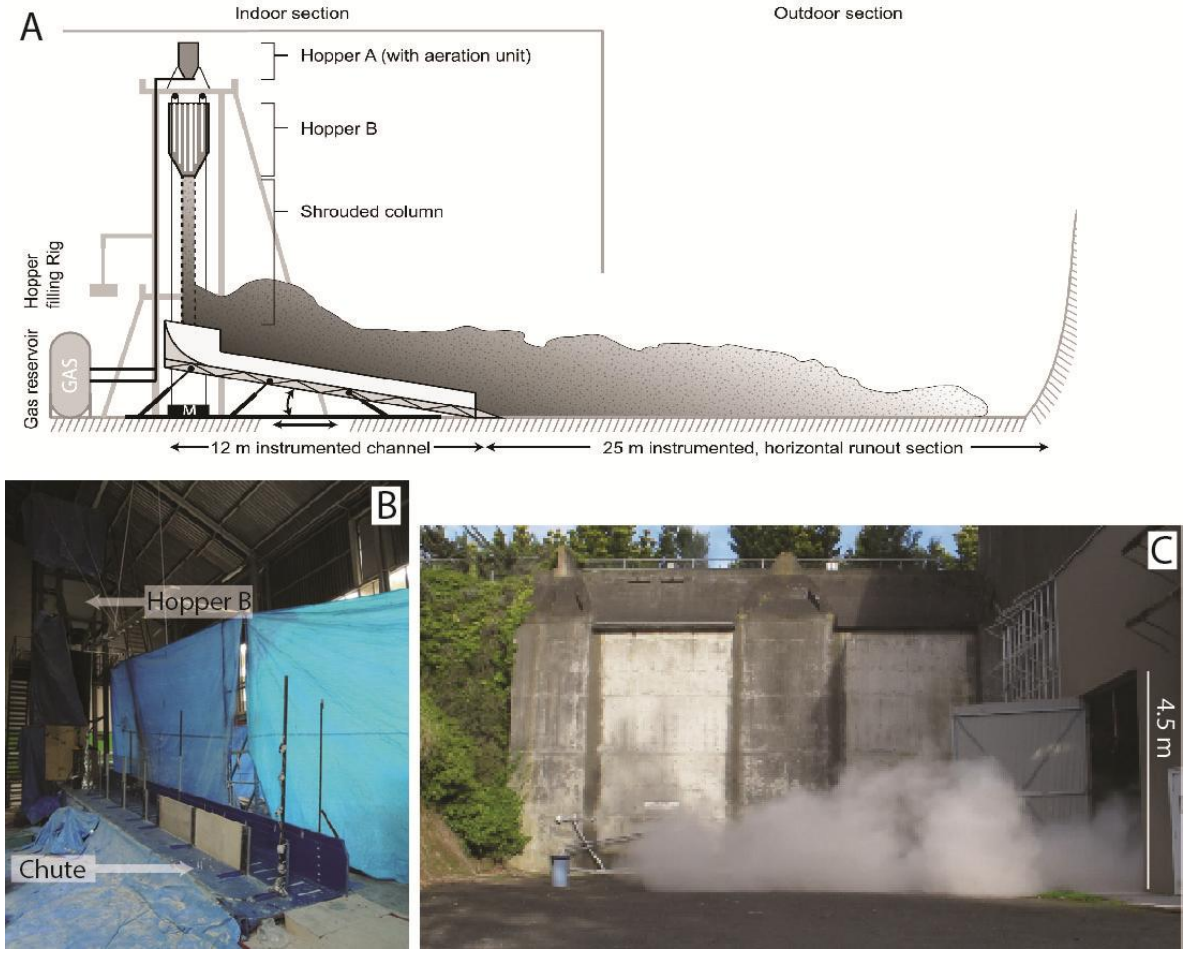

Fig. 2.1. PELE components. A: Sketch of the PDC generator depicting the four main components (Tower, free-fall section, chute, flat section), modified from Lube et al., (2015). B: Overview photograph of the indoor setup. C: Overview photograph of the outdoor section.

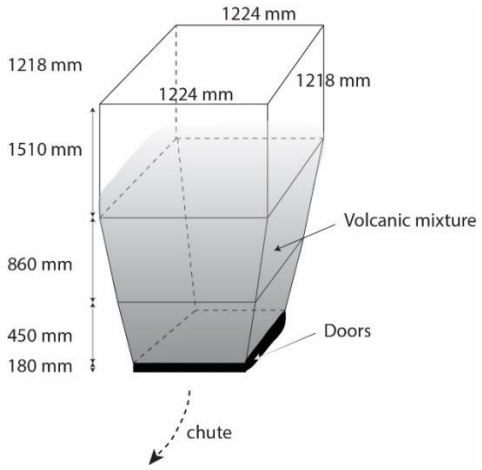

Fig. 2.2. Sketch of hopper B and dimensions.

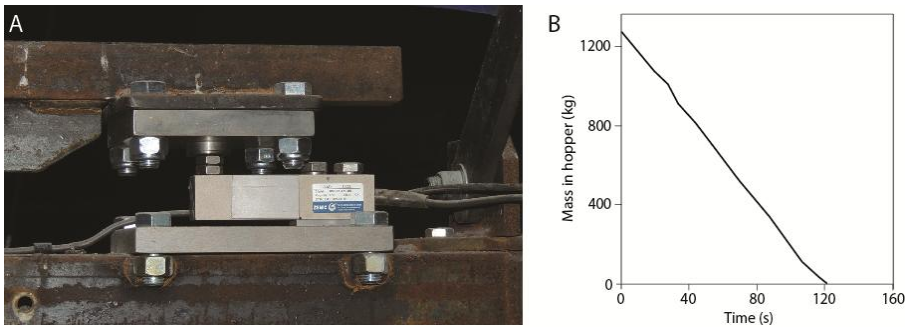

Fig. 2.3. Picture of one of the four 1.5t loadcells implemented to the hopper to measure the time-variant mass discharge rate. B: Mass discharged over time from the hopper B for a 0.5x1.2m^2 area of discharge.

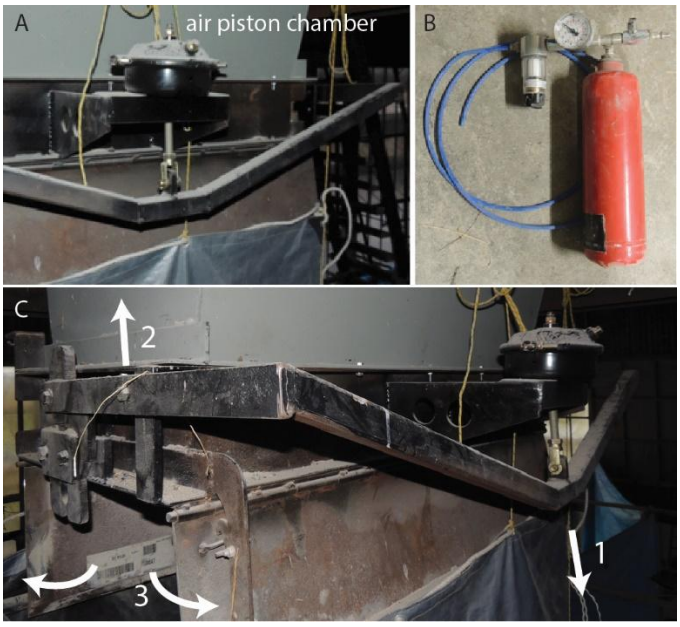

Fig. 2.4. Air piston that opens the trapdoor. B: Compressed air bottle with solenoid valve. C: the trapdoor opening mechanism.

2.1.4 Initial and boundary conditions

By analogy with column collapse on volcanic slopes of a volcano, PELE generates experimental PDCs by the controlled collapse of variably diluted gas-particle suspensions onto the inclinable channel, which is an effective process to synthesize a wide range of replicable flow conditions through a systematic variation of starting and boundary conditions.

PELE was designed to allow systematic and independent change of several initial PDC flow conditions, including the physical characteristics of the gas-particle mixture at the instance of impact. Initial and boundary conditions are summarized from Lube et al. (2015) in Table 2.1.

The main initial parameters that can be varied are the velocity and the particle volumetric concentration at impact, which are both dictated by the hopper mass discharge rate and drop height. The impact velocity varies as a function of drop height, and ranges between 4.7 and 11 m s^{-1}. Data of fall velocity with respect to drop height is presented in the figure 2.5.

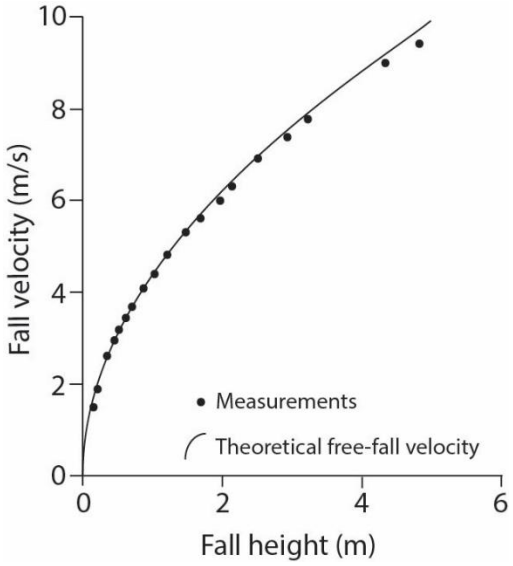

Fig. 2.5. Velocity of the front of the collapsing column with distance from the trapdoors. The black dots are the experimental data and the black line is the free fall velocity predicted from Newton's law as $V = (2gh)^{0.5}$, where V is the velocity, g the gravitational acceleration (9.8 ms^{-2}) and h is the drop height.

Furthermore, the impact volume flux can be varied from 2.8–6.5 $m^3 s^{-1}$, the impact mass flux from 32–1037 kg s^{-1}, and the impact particle volumetric concentration can span values of 0.5 to 18.5%.

Shrouding of the collapsing column prevents any large entrainment of ambient air (Lube et al., 2015). Column dilution occurs dominantly through stretching over distance as the column accelerates while falling, as described by Eq.(2.1):

$$\rho_I = \frac{Q_{MH}}{A_I U_I} \qquad (2.1)$$

where Q_{MH} is the mass flow rate measured by the load cells, ρ_I is the mixture density concentration at impact, A_I is the area of impact and U_I is the impact velocity. The impact velocity is measured by mapping over time the location of the falling column front until impact.

Parameter and symbol	Min	Max
Initial solid mass M_i	< 100 kg	4150 kg
Hopper Mass discharge Q_{MH}	31 kg s^{-1}	1590 kg s^{-1}
Channel width W_C	0.35 m	1 m
Channel inclination β	6°	25°
Mixture temperature T_H	10°C	300°C
Impact velocity V_I	4.7 m s^{-1}	11 m s^{-1}
Impact mass flux Q_{MI}	32 kg s^{-1}	1037 kg s^{-1}
Impact volume flux Q_{VI}	2.8 $m^3 s^{-1}$	6.5 $m^3 s^{-1}$
Particle volumetric concentration at impact θ_I	0.5 %	18.5 %

Table 2.1. Initial and boundary conditions of experiments and ranges of flow parameters at impact.

Furthermore, the temperature of the initial mixture can be adjusted up to 300°C and the grain-size varied (see section 2.1.3).

The primary boundary condition that can be adjusted is the inclination of the channel height and width, which can be varied from 6–25° and 0.35–1 m respectively. The substrate roughness can be varied by implementing sandpaper or an erodible bed of sand to gravel.

2.1.5 Reproducibility

Through repeating experiments, the degree of reproducibility has been explored. Experiments have demonstrated that the flow runout, flow shape, large eddies, and deposit shape are reproducible within an error of ~5–10%. Smaller features, such as small eddies, vary from one experiment to another. The largest source of error in experiments arose from the heterogeneity of the mixture within the hopper that can lead to a variability of the mass flow rate (up to 10% difference). Hence, the filling was semi-automated to reduce the possible spatial heterogeneity of the grain-size distribution and compaction.

2.2 Material

The experiments were conducted with the natural pyroclastic material from the rhyolitic AD 232 Taupo ignimbrite (Wilson, 1985; Hogg et al., 2012) (Fig. 2.15A, B and C). After collection, the pyroclastic material was dried in large ovens and stored in hermetic boxes of 55 l, which prevented any moisture from penetrating the mixture.

Systematic variations of the pyroclastic mixture can be obtained by blending two separate facies of the Taupo ignimbrite (Fig. 2.15.D) (Lube et al., 2015). The first facies (Taupo ignimbrite) was collected westward of Taupo city and it is a proximal medium-ash-dominated ignimbrite showing a unimodal grain-size distribution with a median grain-size of c.1.4Φ (Fig. 2.6B).

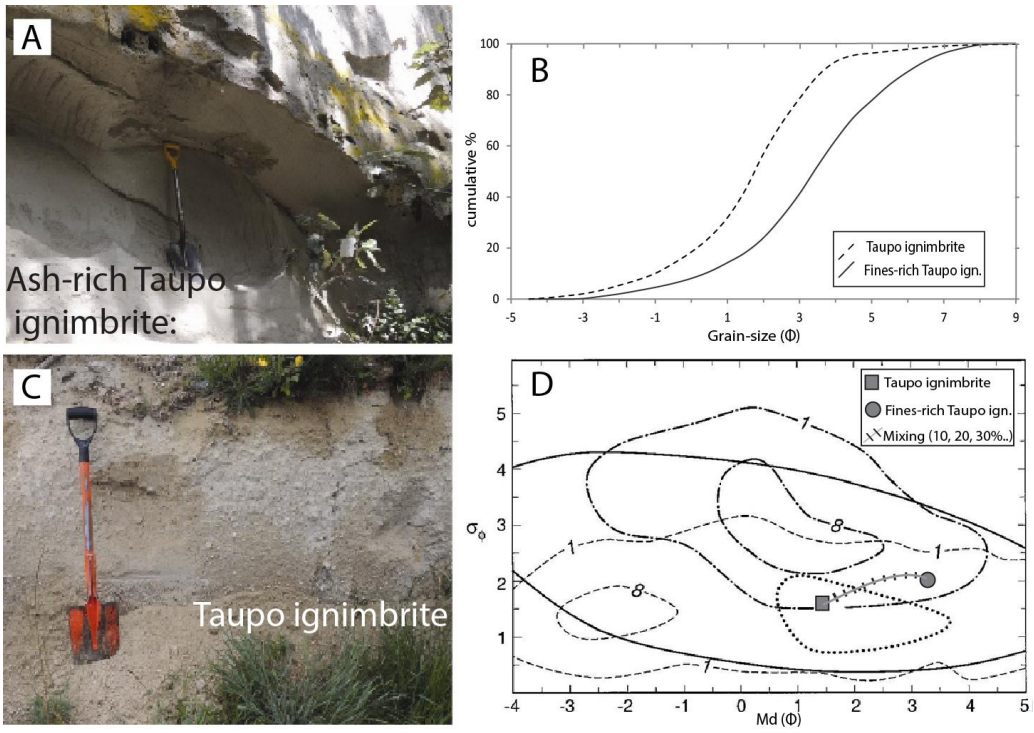

Fig. 2.6. Outcrop picture of the ash-rich Taupo ignimbrite near Hatepe. B: Grain-size distribution of the two facies use to create the initial experimental mixture. C: Outcrop photograph of the location where the Taupo ignimbrite facies is sampled near Taupo city. D: Median grain-size diameter versus sorting coefficient following Walker (1983) of the two deposits and path of the two-component mixture with different proportions of mixing.

The second facies is the polymodal fines-rich base of the proximal Taupo ignimbrite collected near Hatepe, which is characterized by a median at c. 3.3Φ (Fig. 2.6B). By blending both components in various proportions, various grain-size distributions of natural PDC mixtures can be achieved (Fig 2.6D). Both facies are composed of glassy highly vesicular pumice and ash with loose quartz, feldspar and titanomagnetite crystals, and dense lithics. The bulk density of the material varies depending on the blending from c. 840 kg m^{-3} (100% Taupo ignimbrite) to 1010 kg m^{-3} (100% Fines-rich Taupo ignimbrite). Furthermore, the bulk solid density of the material composing the two ignimbrite facies varies from 400 kg m^{-3} for clast sizes coarser than 8 mm to approximately 2600kg m^{-3} for particles finer than 63 microns (Fig.2.7B).

The internal and basal friction angles of the blend (Fig. 2.7A) used in the experiments presented in Chapters 3–5 are 39° and 36.5°, respectively (Lube et al., 2015).

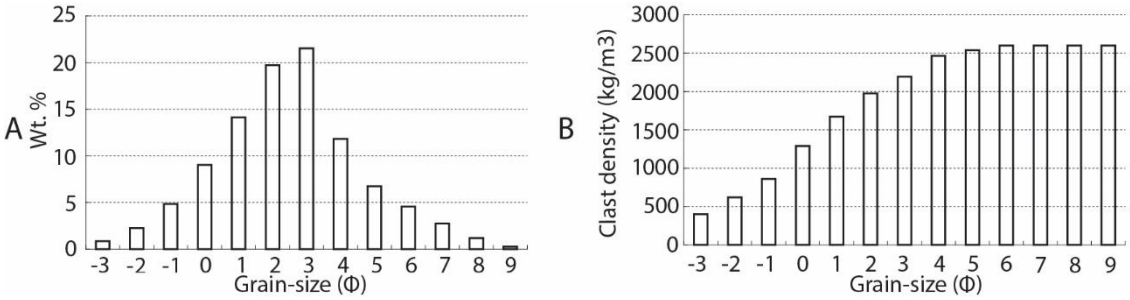

Fig. 2.7. A: Grain-size distribution of the blend of 17% of the fines-rich Taupo ignimbrite facies with 83% of the Taupo ignimbrite. B: Averaged clast density versus grain-size of the 17-83% blend.

2.3 Measurements, sensors and software

During and after the passage of the flow, multiple measurements are obtained from various sensors. For simplicity, measurements are divided into flow measurements recorded during the experiment and deposit measurements that are obtained post-experiment.

2.3.1 Sensors for flow measurements

The list of flow measurements and associated sensors is summarized in Table 2.2.

Three National Instrument data loggers were used to record the sensor signals at typical working sampling rates of 1000 Hz. The opening of the trapdoors (onset of the experimental eruption) triggered an electric signal that had multiple purposes. Three signals are sent to the data loggers and five others to a system of high-speed light-emitting diodes positioned into each camera's view. Such a system ensures a 0.001 s accuracy of synchronization between optical and digital data.

Sensor	**Frequency of the measurement**	**Flow measurement**
Medium to low speed camera	30–240 Hz	Flow outline, flow height, flow front kinematics, large eddy sizes
High speed camera	340–2000 Hz	Velocity fields Volumetric rate of filling of samplers Eddy size Vorticity Entrainment of ambient air
Load cell	1000 Hz	Mass of the flow
Pore pressure	1000 Hz	Basal pore pressure, degree of fluidization
Near IR-sensor	1000 Hz	Particle vol. concentration

Table 2.2. Flow measurements with associated sensors and measurement frequency.

High speed camera

Three high-speed cameras operating at 340–2000 frames per seconds record typically < 2 m^2 views of the passing current (Fig. 2.8). A 16,000 W lighting system illuminated the fields of view of the high-speed cameras to allow the capturing of sequences at ultra-short shutter speeds and high frame rates.

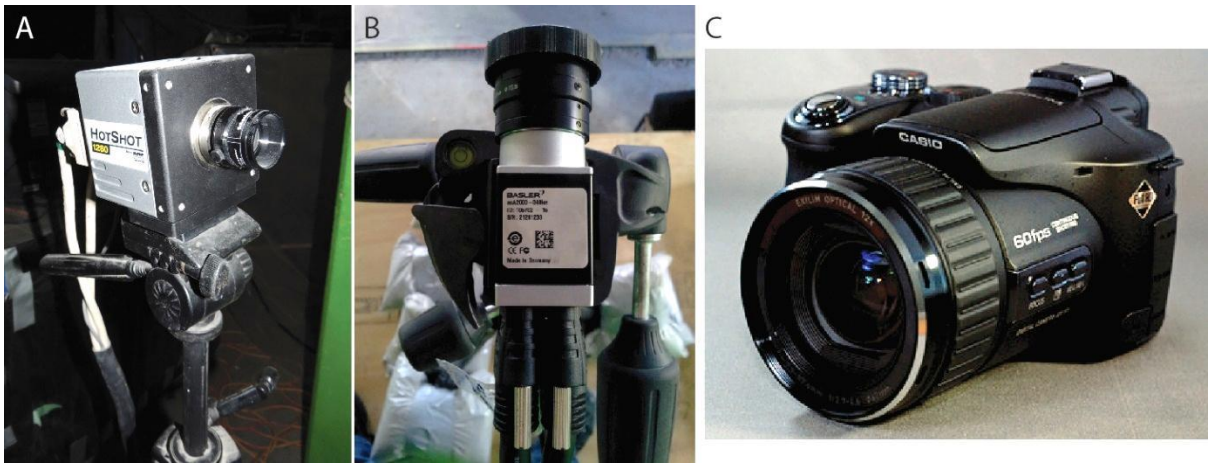

Fig. 2.8. Picture of the NAC HotShot 1280 high speed camera. B: Picture of the Basler acA2000-340km high speed camera. C: Casio Exilim EX-F1.

The images recorded by the high-speed camera were processed by PIVlab software (Thielicke and Stamhuis, 2014) that calculates the time-resolved velocity fields that yield estimates of multiple parameters, such as the entrainment rate of the ambient fluid, particle settling velocity or vorticity, and particle concentration (further described in section 2.3.2). The vorticity, which is a pseudovector field, describes the local rotation of a continuum near some point, as could be seen by an observer travelling within the flow. The vorticity field is calculated from a velocity field (obtained through PIV analysis) and is defined as the curl $\vec{w}$ of the rotational flow velocity $\vec{u}$: $\vec{w} \equiv \nabla\vec{u}$. The calculation of the vorticity (whose dimension is s^{-1}) gives a representation of the degree of turbulence in a mixture. The vorticity helps to visualise and measure the size of the different vortices or eddies within the flow.

Low to medium speed cameras

Three fast cameras operating at 30–240 fps and three normal cameras (24–30 fps) were positioned at various places, distances and angles to record the downstream evolution of the

outer flow structure. Mapping of the flow outline by combining successive sideviews allows subsequent measurements of the flow height at any locations. The use of front and sideviews generates the basic data resource to measure the position of the flow front as a function of time (Fig. 2.8A).

Pore pressure and load cells

Four MEAS piezoresistive differential pressure transducers (154N-1G) were installed into the chute floor to record the basal pore pressure of the passing current (Figs. 2.9, 2.10A and 2.10B). Because of the fine-grained nature of the experimental flow, I used a superposition of steel and nylon meshes installed flush with the chute base and 1 mm above the sensor. In this setup, the pressure sensors recorded the total pressure of air in the thin gap between the sensor and the mesh, i.e. the sum of static and dynamic pressures relative to atmospheric pressure. Two of the four pore pressure transducers were mounted together with two load-cell sensors able to measure up to 1 and 20 kg, respectively, ensuring very good accuracy (0.1 %) of the measurement. The loadcells were s-beam (MEAS DBBSM series) designed for force measurement, which were specifically manufactured to measure compression and tension on inclined surfaces (Fig. 2.10).

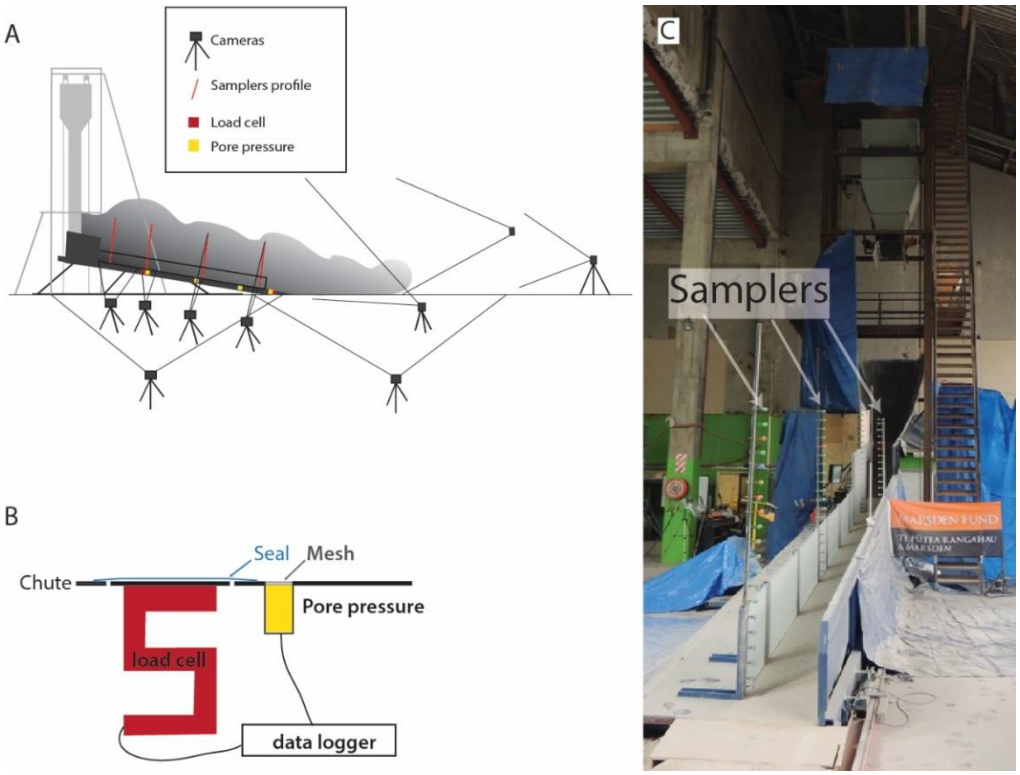

Fig. 2.9. A: Sensor locations in the large-scale setup. B: Load-cell and pore pressure sensor installed into chute floor. C: Picture of the experimental setup with sediment samplers installed in vertical profiles.

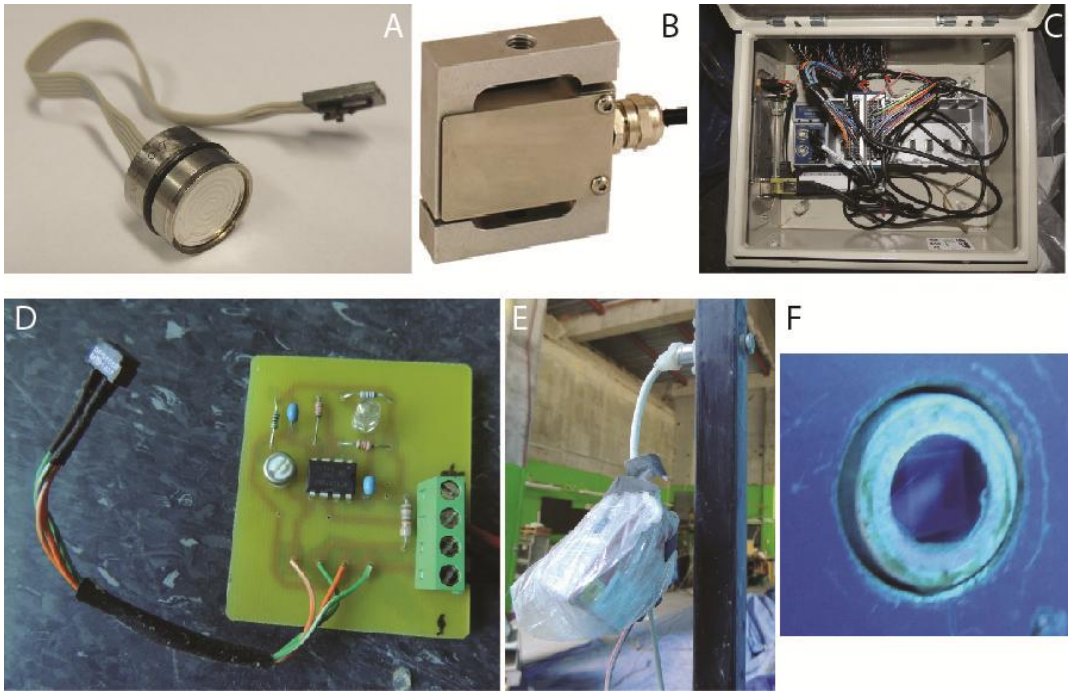

Fig. 2.10. A: MEAS piezoresistive differential pressure transducer (154N-1G). B: MEAS DBBSM S-Beam load-cell transducer. C: 64 channel National Instruments data logger. D: Electronic board that amplifies the signal of the near-IR OBP608B sensor. E: Infrared sensor placed in a vertical profile. F: Glass cover slip protecting the sensor from impact and abrasion.

Sediment samplers

A total of 64 opaque sediment catchers were installed in vertical arrays (Fig. 2.10C). They allowed sampling of the particles transported at different heights (spacing of 0.05 and 0.1 m) and further time-averaged analysis of the grain-size transported at various heights.

Transparent glass tubes were used as sediment samplers that would be filmed, thus allowing time-resolved measurements of the filling rate and sampling of the grain-size distribution at various time steps. Glass tubes were opened on the upstream side to collect the flow over the tube cross-sectional area and contained a mesh of 80 µm at their downstream side with <1 mm wide particles, therefore creating an impermeable barrier for particles but permeable for air (Lube et al., 2015).

Near IR sensor

Near infra-red reflective transducers developed by OPTEK Technology that emit an electromagnetic wavelength of 890 nm from an LED and measure, with a NPN silicon phototransistor mounted by its side how much light is reflected by any object at a distance ranging from 1.27 to 9.5 mm (Fig. 2.8D-F). These sensors were mounted in vertical arrays and used to test the possibility of using the grayscale of images as a proxy for the flow density (See section 2.3.2). In order to prevent damage of the sensor from abrasion or impact of particles, the sensors were mounted into custom made aluminum tubes and protected by a thin rounded glass cover slip (Fig. 2.8F). The output range of the near-IR sensors was initially from 0–4V and was amplified to 0–9V in order to obtain data of a better resolution.

2.3.2 Flow measurement – Particle concentration

Measurements of particle concentration involve multiple sensors. The method varies for low and high concentrations. The following sections contain a summary of the methods to measure particle volumetric concentration; more detailed method sections are provided in individual chapters.

2.3.2.1 Measuring high concentration > ~5–10%

Time-averaged particle volumetric concentration

Depth-averaged particle concentrations for the highly concentrated portion of the flow were computed from the two-dimensional velocity fields using a constant, time-averaged vertical expansion determined by comparing the volumes of flow and deposit past an observer location.

Time-resolved particle volumetric concentration

This method has only been used to resolve height and time-variant particle concentrations of dense PDCs (Lube and Breard et al., in review).

The height- and time-variant particle solids concentrations of the flow were computed numerically by solving the advection equation using the two-dimensional velocity fields obtained through PIV: $\phi t + (u\phi)x + (v\phi)y = 0$

where ϕ is the solids-fraction, *u* and *v* are the horizontal and vertical components of velocity, respectively, which are known (measured by particle image velocimetry). A first order finite-

volume upwind type method was used to discretise the governing equations, such that the flux was evaluated at the boundary of each cell. The boundary conditions used in the analysis were: upper boundary: ϕ=0 and lower boundary: a reflective boundary was used so that no mass can leave the grid from below. This is implemented by the use of a ghost cell with ϕ(x,0)=ϕ(x,1), and v(x,0)=-v(x,1) and transmissive (or free inflow/outflow) side boundaries. This was implemented by also using ghost cells such that ϕ(0,y)=ϕ(1,y), and u(0,y)=u(1,y) on the left boundary, and ϕ(N+1,y)=ϕ(N,y), and u(N+1,y)=u(N,y), assuming N number of cells in the x- direction. The height of the upper boundary (between dense underflow and ash-cloud) and the depth-averaged mass were updated in each time step through the experimentally determined values of flow height and flow mass. To ensure convergence, I also tested that the Courant-Friedrichs-Lewy (CFL) condition was satisfied at each time step.

2.3.2.2 Measuring medium to low concentration < 5–10%

Time-averaged point measurement of concentration

Time-averaged particle volumetric concentration was estimated by combining time-averaged velocity data v_{avg} at the height of the opaque sediment sampler of area A_s and measurement of the total mass contained in the sampler m_s. The time-averaged particle concentration C_{avg} is obtained from the formula: $C_{avg} = m_s / v_{avg} A_s \rho_s t$, with t as the total flow passage and ρ_s is the averaged solid density in the sampler.

Time-resolved point measurements of concentration

Point measurements of time-resolved particle volumetric concentration of dilute flows involved a combination of transparent samplers that were recorded by a high-speed camera

and near IR-sensors. Near-IR sensors were installed as two vertical profiles at 2 and 3.2 m from source with sensors spaced as indicated in Table 2.3.

Sensor	1	2	3	4	5	6	7	8	9	10	11	12	13	14	15	16	17	18	19	20
Height (cm)	0.7	1	1.3	1.6	1.9	2	2.7	3.5	5	7	11	18	35	60	75	95	115	135	155	175

Table 2.3. Vertical spacing of the near-IR sensors from the channel base.

These sensors were manually calibrated using a grayscale, thus ensuring matching of the response between every sensor and various grayscales. An example of the relationship between grayscale and voltage is presented in Figure 2.11.

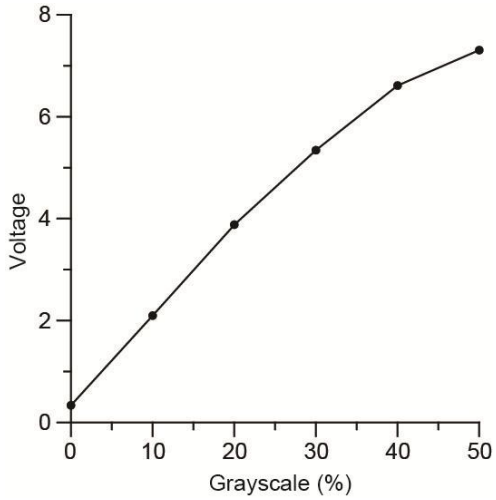

Fig. 2.11. Grayscale versus voltage measured by near-IR sensor. 0% gray corresponds to white and 100% would be black.

High-speed footage of the tubes that collected particles from the flow allowed measurements of the time-variant mass of material transported in the flow at a given height (Fig. 2.12A and B). Knowing the tube area (=4.4 cm^2), deposit density and the time-variant velocity (obtained through PIV), time-variant concentration data were obtained and plotted against the voltage measured by the IR-sensors located 0.1 m from the tube (Fig. 2.12C). The time-variant delay

between the measurement from the IR-sensor and the material being captured in the tube has also been accounted for.

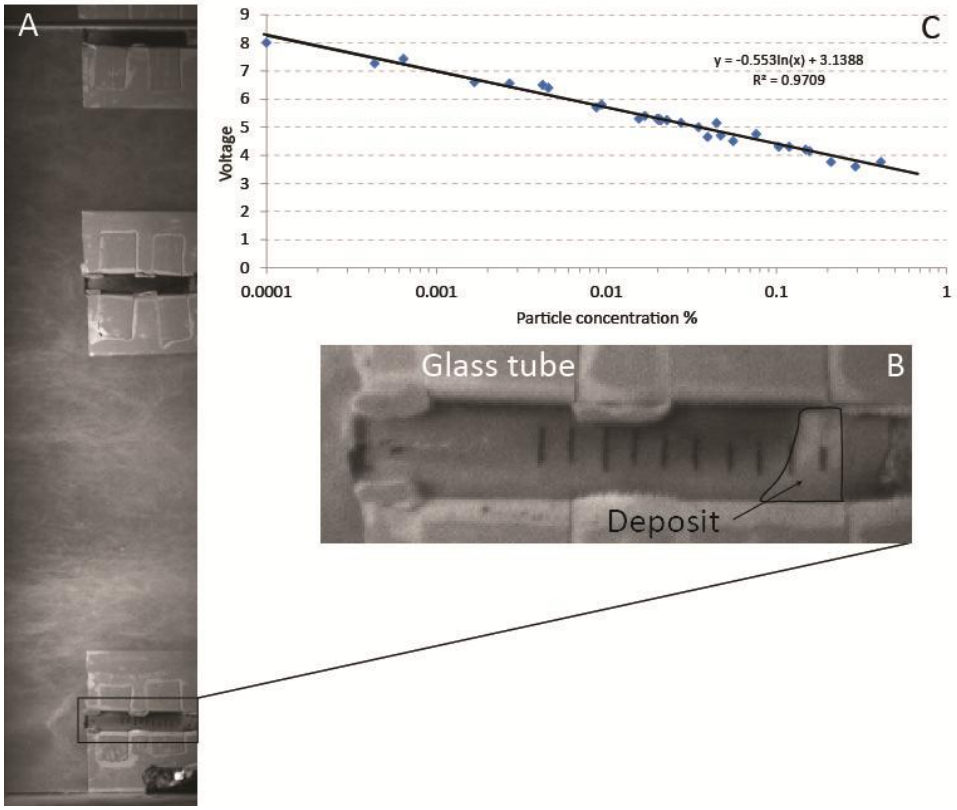

Fig. 2.12. A: Picture of the flow with three tubes installed. B: Close-up of the glass tube sampling particles. C: Calibration curve between the voltage of the IR-sensor and the particle volumetric concentration measured from the tubes.

Time-resolved continuous measurement of concentration

A method was designed to obtain continuous measurements of particle volumetric concentration by combining the grayscale of images with the point measurement of near-IR sensors.

The first step consisted of measuring the time-variant median grayscale of the flow entering the transparent tube, which was evaluated with ImageJ® over a small area close to the near-IR sensor and typically with a length 0.005 m and a width of 0.005 m.

The second step consisted of finding the mathematic expression of the median grayscale versus the particle volumetric concentration as measured with the method described in the previous section. An empirical power law of the following form was derived: $C_p = a*Md(gray)^k$, with C_p as the particle concentration and Md(gray) as the median gray. The parameter "a" was found to be constant and to take the value of $5x10^{-8}$, while k was dependent on the illumination. In order to test the error of this method, I used time-variant measurements of the median grayscale (converted into particle concentrations) and velocity to obtain an estimate of the mass that was deposited in the tubes and found a very good agreement of 89-95% between the estimates and measurements of the masses.

The third step consisted of applying the same method to any experiments for which high-speed movies and mass were collected and measured in sediment samplers, and for which the exponent "*k*" must be found. After the experiment, the sediment mass m_m captured by the samplers was weighed. The flow transports particles of solid density ρ_p within a particle volumetric concentration C_p, and enters the sampler of area A at a velocity v. At the height of the sampler, time-variant measurements of the median grayscale can be converted into a concentration C_p ($C_p = a*Md(gray)^k$) using an assumed value of k. Moreover, the time-variant velocity can be calculated at the height of the grayscale analysis. From the concentration and velocity data, the mass flow rate can be calculated and upon its integration between the arrival time of the flow at t_0 and the final stage at t_f , an estimation of the mass m_e in the sampler is calculated. The formula of the integration is indicated below:

$$\int_{t_0}^{t_f} v * A * C_p * \rho_p = mass\ of\ sediment\ collected\ in\ sampler = m_e$$

Owing to the heterogeneous lighting of the flow, the exponent "*k*" is unknown initially and can vary spatially. The right value of k is found by fitting the estimated mass, m_e obtained

through integration of the mass flow rate to the measured sediment mass, m_m. A similar process is required at the height of each sampler. Once the value of k is known with respect to height, the time-variant concentration can be derived.

2.3.3 Software

All sensor data were logged into a custom program built with the LabVIEW (Laboratory Virtual Instrument Engineering Workbench) software, which exports data as an Excel file.

High-speed movies were cut into frames with software called VirtualDub, in order to undertake image analysis with the PIVlab program implemented in MATLAB (Thielicke and Stamhuis, 2014). PIVlab is a Particle Image Velocimetry program that allows measurements of two components (streamwise and cross stream velocities), as well as the shear rate and vorticity, which is a pseudovector field that describes the local spinning motion of a continuum near a point. Other custom-made codes have been implemented into MATLAB to allow derivation of time-variant velocity profiles at a given location. Median grayscales of images were obtained using the ImageJ® program.

2.4 Grain-size analysis, density measurements and componentry

Grain-size analysis of deposits and material in the sediment samplers was achieved by wet sieving the grain-size fractions over 500 μm; smaller fractions were analyzed with a laser particle analyzer (LPA). Similarly, Tongariro PDC samples were separated in two fractions with a cut at 500 μm, but the samples were dry sieved because the particles were not sensitive to abrasion. Grain-sizes obtained separately from the hand-sieving and from the LPA were smoothly combined together without fitting.

Particle densities were characterized as a function of the grain-size with the GeoPyc 1360 Envelop Density Analyzer for lighter-than-water particles and with the heavy liquid method for particles denser than water.

The shape factor of the particles is required to obtain accurate estimates of the particles' settling velocity (Dellino et al., 2005). The shape factor was estimated by determining the sphericity and circularity of the particles. Particles were photographed under a microscope in order to obtain measurements of the cross sectional area of the grains. The ratio of the equivalent sphere area and the actual surface area of the particle, which approximates the particles as scalene ellipsoids, is the sphericity. This parameter alone does not account well for the particles with irregular contours. Therefore, the circularity parameter was required, which is defined as the ratio of the largest particle parameter and the perimeter of circle equivalent to the largest cross-sectional area of the particle. The shape factor corresponds to the ratio of the sphericity over the circularity (Dellino et al., 2005).

2.5 Scaling of the experimental PDCs

The kinematic and dynamic scaling of dilute to concentrated experimental flows is the only guarantee of the geological verisimilitude of experiments. Indeed, well-scaled experiments ensure that entire classes of processes are not overlooked, missed or misinterpreted and represent natural behaviour (Burgisser et al., 2005). The gas-particle scaling of the PELE experimental flows has been fully described in the introduction to PELE published in Lube et al. (2015). Consequently, in this section a summary of the scaling of PELE is provided.

Within Tables 2.4 and 2.5, the dimensional and non-dimensional bulk scaling of the dilute and concentrated PDCs are respectively compared with current estimates from natural PDCs.

Parameter	Nature	PELE
Particle diameter (m)	10^{-6}–10^{-1}	10^{-6}–10^{-2}
Particle density (kg m^{-3})	300–2600	300–2600
Fluid density (kg m^{-3})	0.6–1.2	1–1.3
Dynamic viscosity of the fluid (kg m^{-1} s^{-1})	$1x10^{-5}$–$4x10^{-5}$	$1x10^{-5}$–$3x10^{-5}$
Flow velocity (m s^{-1})	10–200	<2–30
Reynolds number	$3.3x10^{6}$–$6.7x10^{9}$	$1.5x10^{4}$–$2.8x10^{7}$
Stokes number	$1.1x10^{-3}$–$9.7x10^{7}$	$7.4x10^{-5}$–$4.6x10^{4}$
Stability number	$2.8x10^{-6}$–$9.7x10^{9}$	$7.1x10^{-7}$–$4.6x10^{5}$
Froude number	0.1–10	0.1–5
Richardson number	$2x10^{-4}$–$1.1x10^{1}$	$1x10^{-3}$–$4.5x10^{1}$
Dune amplitude/flow thickness	$1x10^{-5}$–$3x10^{-2}$	$2.5x10^{-3}$–$1.5x10^{-1}$
Deposit area/volume$^{2/3}$	200–2000	100–2000

Table 2.4. Bulk flow scaling of natural dilute PDCs and PELE experimental currents, and comparison of non-dimensional deposit length scales. Natural PDC ranges are from Burgisser et al. (2005).

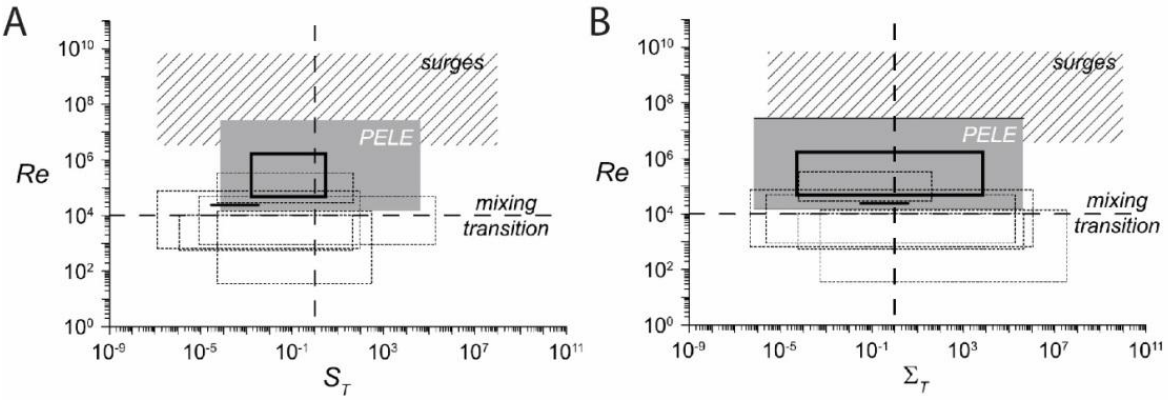

Fig. 2.13. Estimates of Reynolds number (Re), Stokes number (S_T) and Stability number ($\sum_T$) for natural pyroclastic surges (dashed lines) and PELE large-scale experimental flows (grey box). Estimates of scaling parameters were compiled by (Burgisser et al., 2005). Comparison with recent large-scale experiments from Dellino et al. (2007) and talc experiments by Andrews (2014) is made (black solid line). Modified from Lube et al. (2015).

.

Parameter	Nature	PELE
Particle diameter (m)	10^{-6}–10^{-1}	10^{-6}–10^{-2}
Particle density (kg m^{-3})	300–2600	300–2600
Fluid density (kg m^{-3})	0.6–1.2	1
Particle volumetric concentration	30–60 %	40–60 %
Dynamic viscosity of the fluid (kg $m^{-1}.s^{-1}$)	$1x10^{-5}$–$4x10^{-5}$	$1x10^{-5}$–$3x10^{-5}$
Underflow velocity (m s^{-1})	10–30	<2–15
Mass number	$1x10^{2}$–$2x10^{3}$	$1x10^{2}$–$1.5x10^{3}$
Bagnold number	$1x10^{-2}$–$1x10^{2}$	$1x10^{0}$–$1x10^{2}$
Darcy number	$1x10^{2}$–$1x10^{4}$	$1x10^{0}$–$1x10^{3}$
Froude number	1.6–9.6	1.5–6.2
Savage number	$1x10^{-9}$–$1x10^{-7}$	$1x10^{-6}$–$1x10^{-5}$
Pore pressure number	$1x10^{-4}$–$1x10^{1}$	$1x10^{-2}$–$1x10^{2}$

Table 2.5. Scaling parameters of natural concentrated PDCs (Natural PDCs) and for the dense underflow in the large-scale experiments. Natural PDC data are from Roche (2012).

The high velocities of PELE experimental flows (up to 30 m s^{-1}) and high flow thicknesses up to 2–3 m confer the flows' high Reynolds numbers, which characterizes as a non-dimensional ratio of inertial and viscous forces. When Re<1, the flow is laminar, whereas the flow is in an intermediate regime for $1<Re<10^{4}$ and turbulent when $Re>10^{4}$ (Burgisser et al., 2005). PELE produces dilute flows that exceeds the lower bound of the 10^{7} (Table 2.2); therefore, flows are fully turbulent and fall within the field of natural pyroclastic surges (Fig.2. 11). Furthermore, the Froude number, which characterizes the ratio of buoyancy over gravitational forces and leads to the subdivision of flows into critical (when Fr<1) and supercritical (when Fr>1), shows a wide range that encompasses critical and supercritical flow behaviours (Table 2.2).

Owing to the wide grain-size distribution (1 µm to >15 mm) and the large-scale of the experiments, scaling of the feedback between gas and particles and degree of coupling between both phases (solid and gaseous) through the Stability and Stokes numbers, respectively, can be assessed. Stokes and Stability numbers display a wide range, which

implies that a wide spectrum of gas-transport regimes exist in PELE experimental flows (Fig. 2.10). Furthermore, the broad range of experimental deposit facies formed in experiments (including massive, graded, dune-bedded, stratified and laminar bedforms) are similar to natural examples. For instance, dune bedforms produced by PELE are scaled to natural pyroclastic surge dune counterparts (Table 2.2). Experimental flow mobilities, which are approximated by the non-dimensional ratio $A/V^{2/3}$, are between 100–2000 for dilute currents and 10–100 for the concentrated flows, which fall into the natural field of pumice flows and pyroclastic surges/blasts, respectively (Lube et al., 2015).

Concentrated PDCs synthesized by PELE display a wide range of Bagnold, Darcy and Savage numbers that describe the ratio of collisional solid stresses over fluid viscous shear stresses, the solid-fluid interaction stresses over the collisional solid stresses, and the collisional solid stresses over the frictional solid stresses, respectively (Iverson, 1997). This implies that the concentrated PDC behaviour spans a wide spectrum defined by two end-member flow regimes known as *dry granular flow*, where the role of the fluid phase is negligible and solid collisions dominate the dynamics, and as a *fluidized bed* regime, wherein fluid shear stresses dominate. In such fluidized regimes, pore pressure can develop.

PELE is able to create gas-particle PDC analogues that are dynamically and kinematically well-scaled for dense to dilute regimes, which ensures natural stress coupling between the gas and solid phases. PELE is the first experimental setup that creates flows that largely overlap within all natural scales, particularly regarding Stokes, Stability and Reynolds numbers (Burgisser and Bergantz, 2005), extending the previous scaling ranges reached by other medium to large-scale experimental facilities at Bari (Dellino et al., 2007) or the Smithsonian Institute (Andrews and Manga, 2012). Therefore, the scaling analysis of PELE flows gives confidence that experiments reproduce well the dynamics of real-world PDCs.

Chapter 3 – Revealing the internal structure of pyroclastic density currents

Chapter contents

This Chapter is based on a paper presently in review in Nature Geoscience. Therefore, the style of this chapter is conformed to the Journal requirements.

For clarity, the Methods section has been included in the main text.

Participating authors:

Eric C. P. Breard (designed and undertook the experiments, collected and analysed the data, interpreted them and wrote the manuscript).

Gert Lube (conducted experiments with ECPB, manuscript editing and discussion)

Jim R. Jones (manuscript editing and discussion)

Josef Dufek (manuscript editing and discussion)

Shane J. Cronin (manuscript editing and discussion)

Greg A. Valentine (manuscript editing and discussion)

Anja Moebis (helped with analysis of the mixture density and samplers analysis)

Chapter 3 – Revealing the internal structure of pyroclastic density currents

3.1 Introduction

Volcanic eruptions are at their most deadly when pyroclastic density currents (PDCs) sweep across landscapes to devastate everything in their path (Francis and Baker, 1977; Fink and Kieffer, 1993). Immeasurable in real-life, the internal dynamics underpinning these volcanic hazards could never be directly observed (Cashman and Sparks, 2013; Dufek et al., 2015). Here I reveal the first quantitative views inside PDCs by synthesising their natural flow behaviour in large-scale experiments. These prove the classic hypothesis (Fisher and Schmincke, 1984) that PDCs segregate vertically into a basal underflow of highest mass flux and an upper ash-cloud of greatest volume. The ash-cloud also segregates longitudinally into a leading head and a trailing body region. However, in contrast to previous descriptions of these flows, mesoscale structures where particles are concentrated into dendritic structures strongly control the coupling between the underflow and ash-cloud. These unprecedented experiments trace flow dynamics from initiation to deposition, and can explain the spatial and temporal evolution of real-world deposits. The internal structure contrasts markedly with long-standing paradigms of rigid, co-existing zones of dense and dilute transport regimes (Lacroix, 1904; Fisher, 1979; Druitt, 1998) and a hypothesized continuous gradation between them (Branney and Kokelaar, 2002; Sulpizio et al., 2014). Instead, concentrated laminar and dilute fully turbulent transport regimes are linked through a zone of intermediate turbulence and concentration. Dynamic transfers of mass and momentum between these zones dictate the internal stratification and evolution of PDCs. This discovery opens new pathways to interpret volcanic deposits quantitatively and has fundamental implications for the prediction of PDC behaviour in numerical hazard models.

For more than 50 years, the transport and deposition of pyroclastic density currents has remained amongst the most hotly debated issues in volcanology (Sparks, 1976; Francis and Baker, 1977; Sparks et al., 1978b; Palladino and Simei, 2002; Sulpizio et al., 2014). Due to their unpredictability and extreme violence, PDC deposits have been relied upon to infer flow dynamics (Fisher and Schmincke, 1984). PDC deposits range from those devoid of bedforms to highly stratified types (Fisher, 1979). These extremes led to the conceptualization of two end-members of PDCs, one as a pyroclastic flow of high particle concentration, and the second as a dilute pyroclastic surge (Valentine, 1987). Pyroclastic flows are typically modelled as dry granular flows (Patra et al., 2005) or fluidized beds (Wilson, 1980) and surges as dilute, turbulent ash-clouds (Bursik and Woods, 1996). Attempts have been made to unify these end-members, both theoretically (Burgisser and Bergantz, 2002) and with numerical modelling studies (Dufek and Bergantz, 2007c). However, large uncertainties remain about the multiphase physics of coupled dense/dilute particle-gas transport.

3.2 Methods

3.2.1 Generating PDC in large-scale experiments

Our experiments were conducted at the eruption simulator PELE (described in detail in Lube et al., 2015), a unique test facility to synthesize the natural behaviour of PDCs. The experimental PDCs of up to 6 tonnes of natural volcanic material and air attain velocities of 7–32 m s^{-1}, flow thicknesses of 2–4.5 m, and runout lengths of >35 m (Lube et al., 2015). The particle-gas currents are synthesized by the gravitational collapse of variably concentrated suspensions of volcanic particles and air from an elevated hopper onto an instrumented runout section. PELE is operated inside a 16 m high, 25 m long and 1μm wide

disused boiler house and comprises: (I) a 13 m high tower and elevator holding a 4.2 m^3 hopper through which a pyroclastic mixture is discharged at variable discharge height; (II) a shrouded, fall section (up to 9 m) below the suspended hopper; (III) a 12-m long, 0.5 m wide and 0.6-m high inclinable channel section with a rough steel base (basal friction angle of 36.5°); and (IV) a 30-m long flat runout area of concrete (basal friction angle of 37.5°) that extends outside the building. Experiments were undertaken at ambient temperature, with an eruption column fall height of 3 m, a constant hopper discharge rate of 825 kg s^{-1}, and with the channel uniformly sloping at 19°.

The experimental particle mixture was prepared by blending two different deposits of the AD 232 Taupo Ignimbrite (Lube et al., 2015). The mixture had a unimodal grain-size distribution with a median diameter of 250 μm, an average clast density of 1950 kg m^{-3}, and contained 10 wt.% of very fine ash material (particles <63 μm) (supplementary Fig. 3.1).

Additional details of the experimental set-up, the experimental protocol, properties of the volcanic material and measurement techniques are provided in Lube et al. (2015), while some analytical methods specific to our results requiring further explanation are given below.

3.2.2 Sensors and analytical methods.

Two high-speed cameras operated at 600–1000 frames per second, and four normal speed cameras operated at 24–240 frames per second recorded flow passage and sedimentation from a range of viewing angles. Two-dimensional velocity and vorticity fields were computed via particle-image-velocimetry (PIV) using the software PIVlab. Vorticity measurements reported in Figure 3.4 use a smallest interrogation windows of 0.04 m that represents the minimum length-scale of eddies displayed. Vertical profiles of particle

concentration in the ash-cloud displayed in Figure 3.4 were determined using an empirical relationship between concentration and the median grey-scale of high-speed images that accounts for local variation in illumination and grain-size distribution. This function was determined using vertical profiles of sediment samplers that capture the mass of sediment, M_S, passed a location across the sampling cross-sectional area A. The local median grey scale is a function of particle concentration and takes a power-law form where concentration is a fitted function of M_S, A, flow velocity U and time. The validity of the empirical relationship between the median value of the image grey scale and particle concentration and the minimum range of quantifiable concentrations (c. 10^{-5}–10^{1} %) was determined through direct measurements of local time-variant mixture density[21]. For the direct measurements of mixture density, ρ_M I recorded with high-speed video the sequential filling of transparent, horizontally oriented glass tubes with cross-sectional area, A_p. The tubes were open on the upstream side to collect the flow over the tube cross-sectional area and contained an 80 μm mesh at their downstream side impermeable for particles and permeable for air. Mixture density is obtained as $\rho_M(t) = Q_{VF}(t)\rho_S/A_P U_i(t)$, where Q_{VF} is the volumetric rate of sediment accumulation in the tube, ρ_S is the non-compacted bulk material density, U_i is the velocity of the flow before entering the tube (measured by PIV), and t is time.

Depth-averaged particle concentrations for the underflow reported in Figure 3.4 were computed from the two-dimensional velocity fields using a constant, time-averaged vertical expansion determined by comparing the volumes of flow and deposit passed an observer location. The range of time-variant particle concentrations for the underflow (displayed as a box in Figure 3.4) was computed numerically solving the advection equation. Time- and depth-averaged concentration values for the different ash-cloud regions (head and body)

were determined by integrating local time-averaged mass flux data from vertical profiles over the time of passage for the head and body regions.

Local rates of underflow thickening, T_U, reported in the text were computed as the ratio:

$$T_U = \frac{C_{LC}\ W_{LC}}{(1-\emptyset)},$$

where C_{LC} and W_{LC} are the depth-averaged particle concentration and depth-averaged settling velocity respectively in the lower 5 % of the ash-cloud, and $\emptyset$ is the porosity of the underflow.

3.3 Results

Here I report on gas-particle flows produced by the gravitational collapse of 1.5 tons of volcanic material in the largest PDC experiments ever undertaken (supplementary Fig. 3.1, supplementary Movie 1 in Appendix A). As in nature, experimental currents of pumice, ash and air were synthesized by 'eruption column collapse' of mixtures of natural volcanic particles and air, which impacted onto an inclined and glass-sided channel (Fig. 3.1). The resultant flows travelled out to >25 m and were observed with high-speed cameras over several seconds of propagation.

Upon impact, the fully turbulent suspension rapidly expanded and accelerated to reach initial velocities of 16 m s^{-1} (Fig. 3.2a). This was short-lived, and by at least 3.1 m from source (Fig. 3.2b, supplementary Movie 2 in Appendix A), the initially homogeneous suspension (containing 9.5 vol% particles) had vertically segregated into a basal *underflow* and an overriding *ash-cloud*. Both ash-cloud and underflow regions were dynamically and kinematically scaled to natural flows (supplementary Tables 3.1 and 3.2).

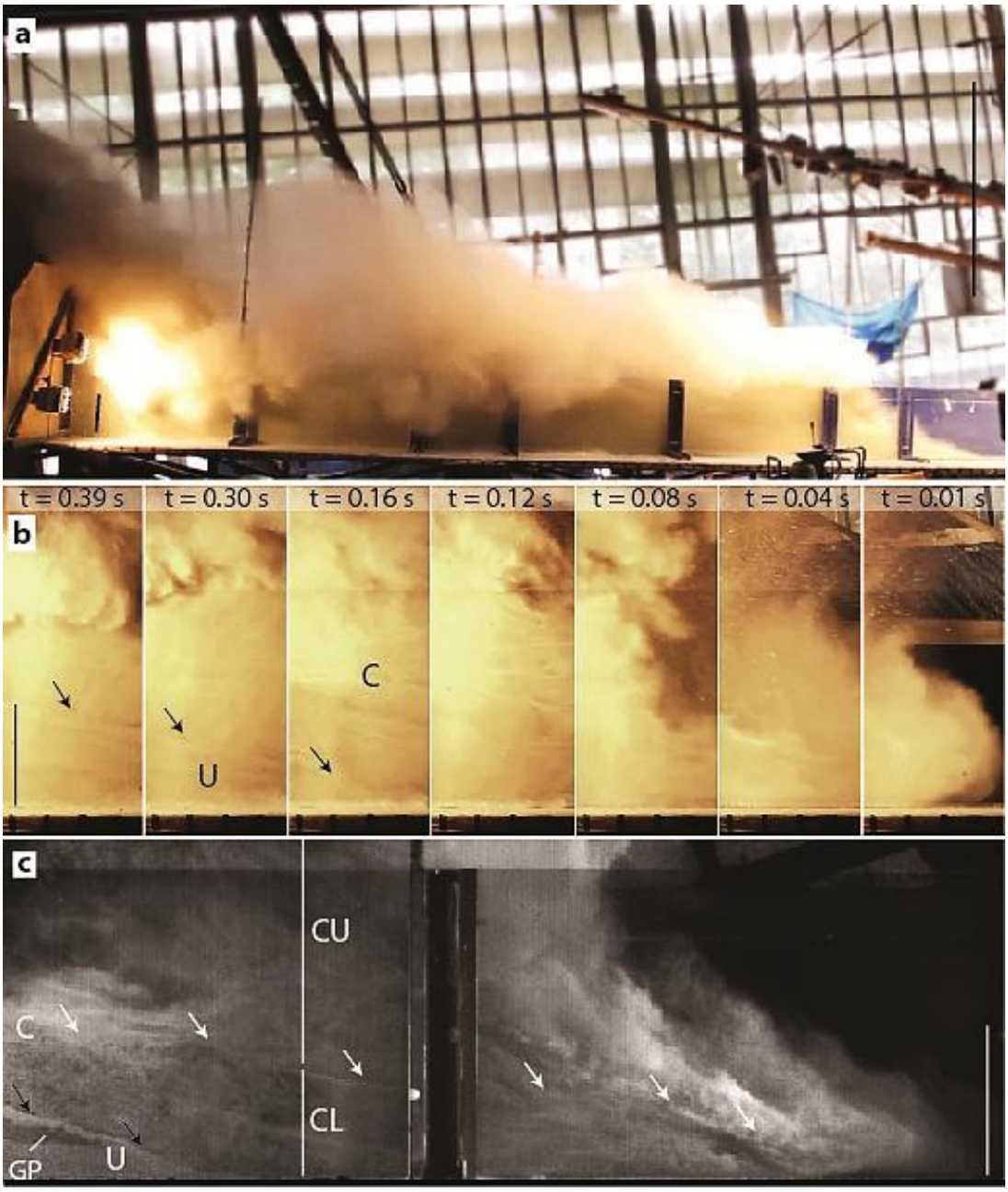

Fig. 3.1. Synthesizing pyroclastic density currents in large-scale experiments. a, side view of an experimental pyroclastic density current at the eruption simulator PELE. b, the lower 0.95 m of the flow at a runout distance of 3 m at different times. c, passage of the head region at 3 m. Arrows highlight the interfaces between underflow (U) and ash-cloud regions (C) (black), and between intermediate (CL) and high turbulence (CU) zones of the ash-cloud, respectively. Rapid sedimentation of dendritic clusters of mesoscale turbulence entraps gas pockets (GP) in the underflows. Vertical scaling bars are 0.3 m long.

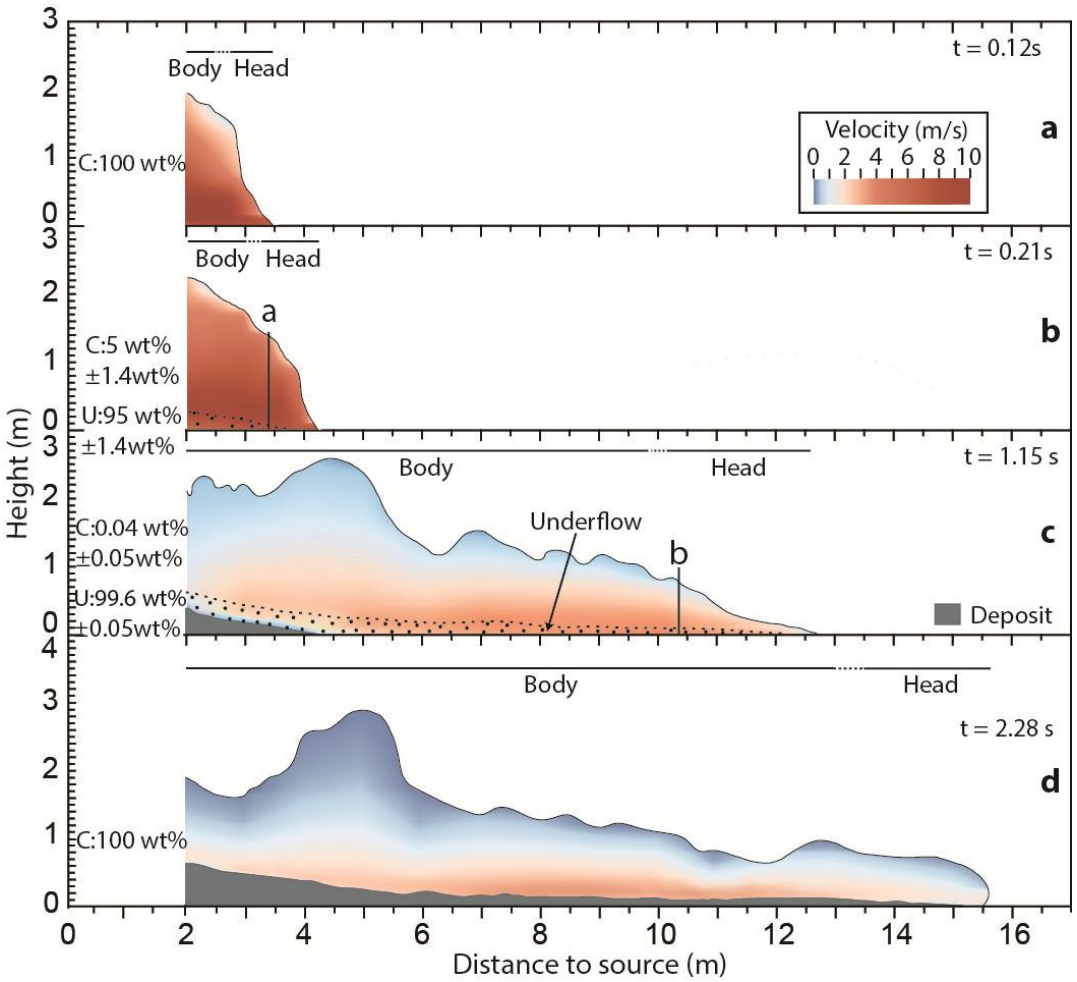

Fig. 3.2. Evolution of the internal flow structure and velocity fields. a-d, Longitudinal cross-sections of the advancing experimental PDC at four different times. Black solid line, dotted line and grey area demark upper flow boundary, top of underflow and aggrading deposit, respectively. Extents of head and body regions of ash-cloud and relative proportions of the mass of particles transported in underflow (U) and ash-cloud (C) regions are shown also. Two vertical lines annotated "a" and "b" indicate the location of the proximal and intermediate observer locations referred to in figure 3.4.

After this initial segregation event, 95% of the mass was transported in the underflow, reaching 99.6% by 10.3 m from source (Fig. 3.2c). The ash-cloud also segregated longitudinally into a gravity current with a highly inertial *head* (Froude numbers 1.4–3) and a trailing *body* where inertial and gravitational forces balanced (Froude numbers 0.9–1.2). The head comprised a leading section that preceded the underflow and a rear section that rode atop of it, while the *body* moved on top of the remaining underflow (Fig. 3.2). These segregation processes generated flow regions of markedly contrasting (depth- and time-

averaged) particle concentration (supplementary Fig. 3.2). During passage of the current at 3.1 m, the underflow was the most concentrated region at 45 vol% (Lube and Breard et al., In Review). The head contained 5.5×10^{-1} vol% particles, while the body transported 8×10^{-2} vol% particles on average. Further downstream at 10.6 m, the head and body regions were each diluted by an order of magnitude due to sedimentation and entrainment, while the concentration of the underflow remained high.

The vertical and longitudinal flow segregations are key to link sediment transport to deposit characteristics. The ash-cloud head transported 40 to 65% of the entire ash-cloud mass and emplaced the earliest and farthest reaching depositional unit at the bottom of the inclined channel and onto a flat runout zone. Deposited from 9–25 m in ~0.3 seconds and at a deposition rate of ~3.5 mm s^{-1} (Fig. 3.3a, b), this unit was a thin and crudely laminated layer rich in high-density particles.

This was directly overlain by the deposit of the underflow that reached a runout length of ~15.2 m. Vertical aggradation occurred at a very fast rate of 450–550 mm s^{-1} (Fig. 3.3c, c). This rapid "freezing" left a deposit representing a snapshot of the underflow's structure in motion (Roche, 2012). The underflow deposit depicts a fines-rich base, followed by a massive central portion and coarse pumice-rich top.

The ash-cloud body, which during segregation became enriched in very fine and low-density ash particles, formed an up to ~8 m high and ~24 m long co-ignimbrite cloud that was deposited last. The normally graded and thinly laminated unit initially deposited at a rate of 0.1–0.5 mm s^{-1}, which subsequently slowed to ~10^{-2} to 10^{-5} mm s^{-1} (Fig. 3.3d). Thus, the total PDC deposition time-scale spanned five orders of magnitude, and was composed of three depositional units emplaced by the head, underflow and body regions.

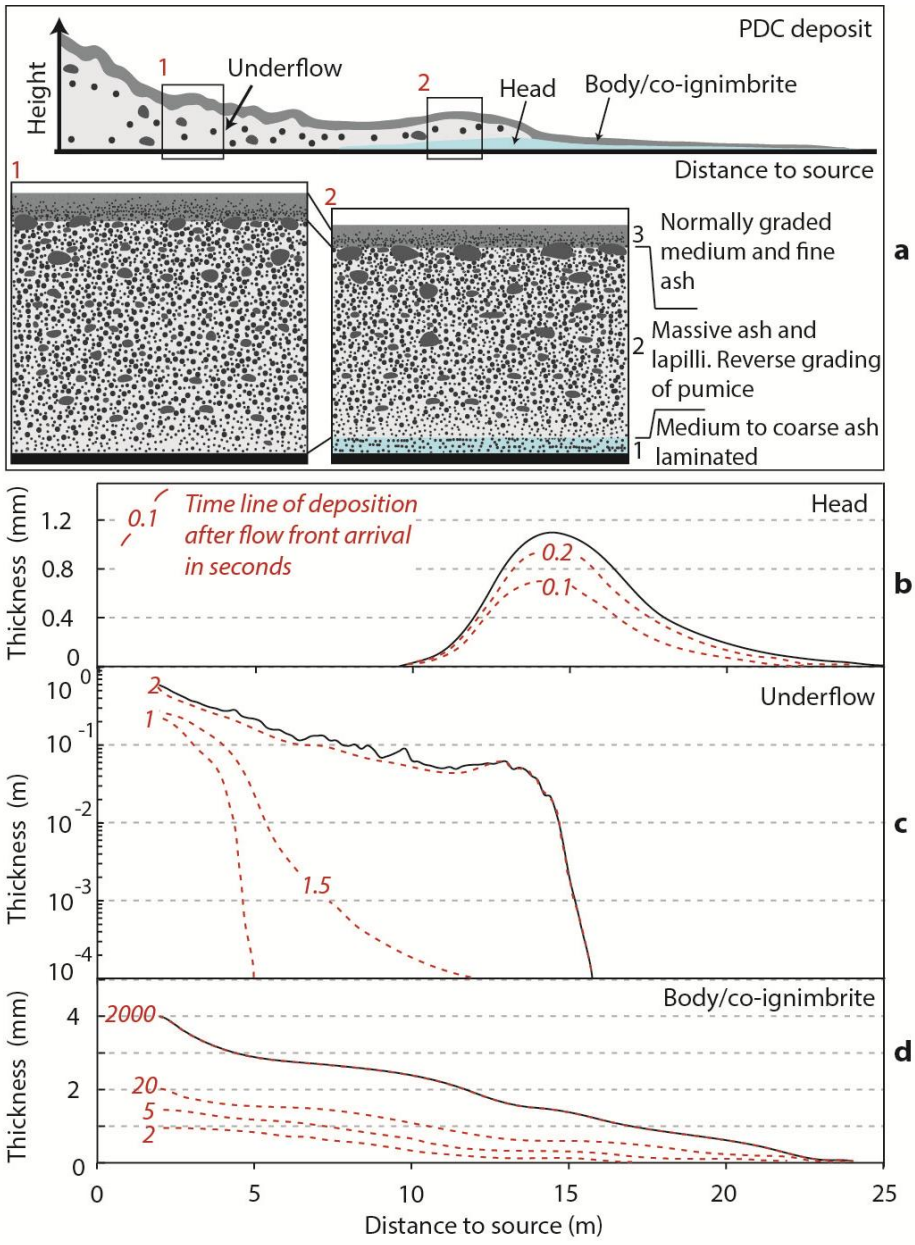

Fig. 3.3. Experimental deposit and time-scale of deposition. a, Sketch of the experimental deposit sequence (not to scale) correlating the three depositional units to the parent zones of the flow (head, underflow, body/co-ignimbrite). Two vertical 'outcrop' sections "1" and "2" highlight the sediment structure with the standard ignimbrite flow unit deposited only in an intermediate runout zone. b-d, thickness-distance plot (black line) and isochrones of deposition (red dashed lines) for the head, underflow and body regions, respectively.

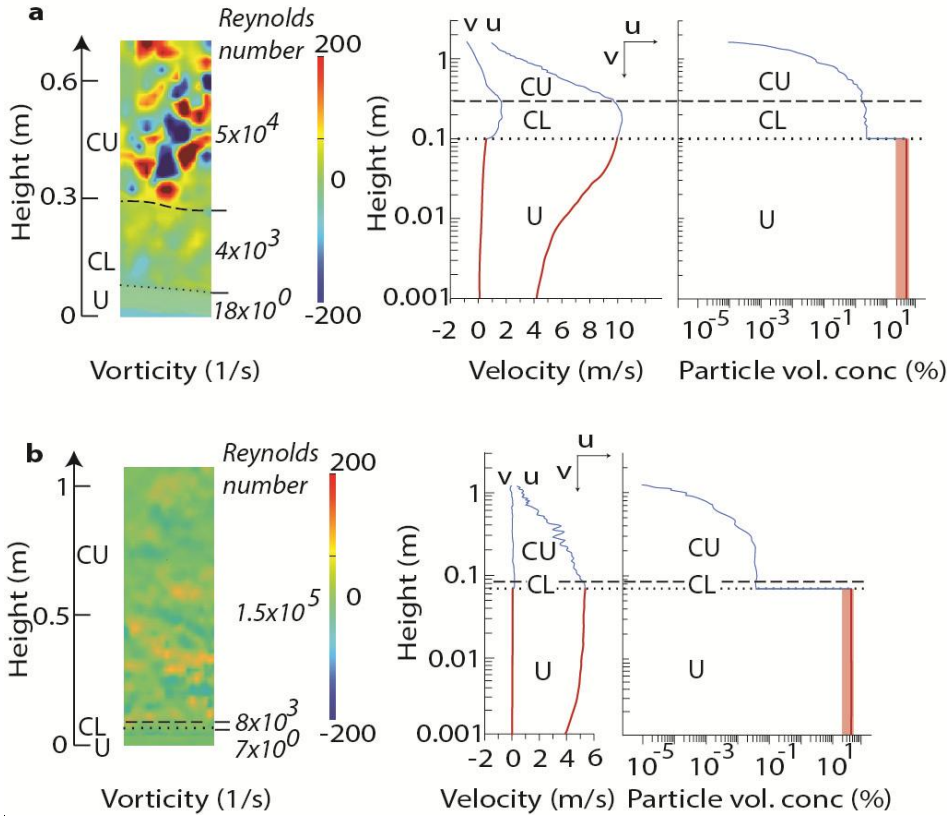

Fig. 3.4. Internal structure of experimental PDCs. a, vertical profiles of vorticity, horizontal and vertical velocity components, and particle concentration at 3.1 m from source during passage of the rear of the head. b, same as a at a runout distance of 10.6 m. Dotted and dashed lines demark interfaces between underflow (U), intermediate (CL) and high turbulence (CU) zones of the ash-cloud, respectively, with their depth-averaged Reynolds numbers given also. For the underflow, red solid lines show depth-averaged particle concentrations. Light-red bar indicates maxima (in the central part) and minima (at the base and top of underflow).

The deposit structure of our large-scale experiments reproduced the natural sequence and sedimentary features of real-world deposits. For the case of pumice-rich eruptions this classic sequence is referred to as the standard ignimbrite unit (Sparks et al., 1973; Sparks, 1976). Using the famous Grotte di Castro ignimbrite (180–166 ka) as an example (Sparks et al., 1973; Palladino et al., 2010), the experimentally determined sedimentation rates yield first-order estimates of the emplacement time of natural deposits. In the ignimbrite deposits, we associate the basal 0.1 m-thick fine-ash layer with deposition from the head. This would have taken ~30 seconds to accumulate. It is overlain by an 11 m-thick unit comprised of a fines-rich base and a massive top, which we associate with the underflow; this would have

been emplaced in only ~20 seconds. The capping 0.6 m-thick fine ash with weak normal grading was deposited from the ash-cloud body (and co-ignimbrite cloud), which I estimate would have taken ~3.5 hours.

The footprints of the three depositional units associated with the underflow and the head and body regions of the ash-cloud only partially overlap (Fig. 3.3a). This gives an explanation on why the 'ground layer' (Sparks and Walker, 1973) of PDC deposits is locally absent in some natural deposit sequences, but is present in others (Sparks, 1976; Palladino and Valentine, 1995; Branney and Kokelaar, 2002).

While the head, underflow and body regions emplaced distinguishable depositional units, the three flow regions do not move and evolve independently. This is best shown through high-resolution vertical profiles of velocity, particle concentration and vorticity (a measure of the degree of turbulence) during passage of the rear of the ash- cloud head (Fig. 3.4a), prior to the arrival of the ash-cloud body. At this point, the flow shows three zones of contrasting turbulence: a lower, 0.1 m-thick, laminar zone (Reynolds numbers, *Re* of 10^0–10^1, using the dynamic viscosity approximation after ref. 26 and the thickness of the zone as the relevant length scale), representing the underflow; a middle 0.2-0.4 m-thick zone of intermediate turbulence (*Re* of 10^3); and an upper, 1.1 m-thick, fully turbulent zone (*Re* of 10^4–10^5). Reynolds number estimates within the intermediate zone need to be cautiously interpreted, as the inhomogeneous structure dominates the zone more than bulk inertial effects and dynamic viscosity approximations in dense suspension are poorly constrained (Agrawal et al., 2001; Zhang and VanderHeyden, 2002).

The laminar underflow had a slip boundary with the substrate at velocities of ~4 m s^{-1}. A sharp concentration change between the underflow and the middle zone occurred over only a few millimetres and is visible in high-speed videos (supplementary Movie 3 in Appendix

A). Here particle concentrations declined abruptly from c. 20 to 2 vol%. However, this was not accompanied by a sharp velocity change, which instead changed smoothly across this interface (Fig. 3.4a), and so demonstrates an efficient momentum transfer from the underflow into the ash-cloud. The change in Reynolds number from c. 18 to c. 4,000 is due to the concentration change and associated apparent viscosity, which is much lower for the more dilute system.

The middle zone is acting as a boundary layer and characterised by low shear and particle concentration is relatively height invariant between 1–2.5 vol% (Fig. 3.4a). In contrast, the upper zone shows high vorticity as the flow becomes fully turbulent. In the upper ash-cloud particle concentration and velocity declined strongly upwards, which resulted in strong shear, significant entrainment, and hence intense billowing. The rapid changes in concentration, velocity and vorticity between the middle and upper zones occurred across a broad interface of several centimetres in thickness.

In the head, in the intermediate zone, the ratio of the eddy rotation time and the particle response time to unsteady forcing by gas turbulence (the Stokes number) (Burgisser and Bergantz, 2002) is close to unity (0.9–1.6). The stability number (Burgisser and Bergantz, 2002), a measure of the residence time of solids in an eddy, is also close to unity (0.3-0.8). This is a condition discovered in multiphase physics that favours strong feedback between solid and gas phases (Agrawal et al., 2001; Zhang and VanderHeyden, 2002; Burgisser et al., 2005), but one that has not been simulated in any computational PDC model yet. The feedback leads to the formation of mesoscale turbulence structures where particles form in a dendritic pattern, and migrate into low-shear zones (Agrawal et al., 2001). Such mesoscale structures are highly abundant in the lower (low-shear) part of the ash-cloud head (supplementary Fig. 3.2). They occur as dendritic clusters of higher particle concentration

than the surrounding mixture and strongly affect flow stratification and sedimentation (Fig. 3.1c, supplementary Movie 3). By contrast, in the body Stokes and Stability numbers near the underflow rapidly decline to values of 10^{-1} order, respectively while Reynolds numbers increase up to 10^{6}. This indicates highly turbulent transport with better coupling between solid and gas phases.

The discovery of mesoscale clusters in PDCs has major ramifications for the exchange of mass between zones and the consequent runout dynamics. The occurrence of mesoscale clusters is known to dampen local turbulence and to force a local decrease of particle drag coefficients (Zhang and VanderHeyden, 2002). This process effectively counters the high aerodynamic resistance expected in (viscous) concentrated suspensions through hindered settling (Gidaspow, 1994). In fact, the low-shear zone of the head had extremely high particle settling velocities of ~1.7 m s^{-1} (Fig. 3.4a), commensurate with the terminal settling velocity in clean air of the median-sized particles transported in the intermediate zone (~250 μm).

The high particle settling rate implies a thickening of the underflow at 60 ± 10 mm s^{-1}, consistent with a mass balance calculation using the vertical component of velocity and the cloud concentration. The mass flux from ash-cloud and underflow regions between 3.1 and 10.6 m from source, illustrated by downward velocity components (Fig. 3.4), results in a strong dilution of the head (0.55–0.08 vol%). This increases the mass of the underflow by ~5%. Translated to natural PDC scales, this indicates a significant mass flux from the ash-cloud into the underflow; e.g. resulting in underflow thickening by 1.8 m during 30 seconds of propagation and 36 m in 10 minutes. In other words, the PDC head constantly feeds the frontal part of the advancing underflow. The associated momentum transfer promotes a high mobility of the coupled head-underflow system.

3.4 Conclusion

Viewing inside pyroclastic density currents establishes a relationship between flow behaviour and deposit architecture. This opens new pathways for geologists to interpret the dynamics of past PDC-forming eruptions quantitatively. The discovery of a dynamically evolving vertical zoning in PDCs replaces previous paradigms of the internal PDC structure. The hypothesized continuous spectrum of particle-gas transport between fully dense and fully dilute regimes does not occur. Instead, these end-member regimes are spatially separated and coupled through a regime of intermediate particle concentration and turbulence. The occurrence of mesoscale clusters within the intermediate regime and dynamic transfers of mass and momentum between regions provide fundamental insights for advancing computational PDC hazard models. These processes may be similarly relevant to other types of geophysical mass flows including snow avalanches and submarine turbidity currents.

3.5 Supplementary material

Parameter	Nature	PELE
Particle diameter (m)	10^{-6}–10^{-1}	10^{-6}–10^{-2}
Particle density (kg m^{-3})	300–2600	300–2600
Fluid density (kg m^{-3})	0.6–1.2	1
Dynamic viscosity of the carrier phase (kg m^{-1}s^{-1})	$1x10^{-5}$–$4x10^{-3}$	$1x10^{-5}$–$5x10^{-3}$
Flow velocity (m s^{-1})	10–200	<2–20
Reynolds number $Re = \frac{\rho UL}{\mu}$	$1x10^{4}$–$6.7x10^{9}$	$1.5x10^{4}$–$2x10^{6}$
Stokes number $S_T = \frac{1}{f}\frac{\Delta\rho D^2}{18\mu}\frac{\Delta U}{\delta}$	$1.1x10^{-3}$–$9.7x10^{7}$	$7.4x10^{-5}$–$4.6x10^{4}$
Stability number $\Sigma_T = \frac{S_T}{Fr^2} = \frac{\tau_v g}{f\Delta U} = \frac{U_T}{\Delta U}$	$2.8x10^{-6}$–$9.7x10^{9}$	$7.1x10^{-7}$–$4.6x10^{5}$
Particle Froude number $Fr = \frac{U}{\left[(\rho_p - \rho_g)gD\right]^{0.5}}$	0.1–20	0.3–10
Richardson number $Ri = \frac{(\rho - \rho_o)gH}{\rho_o U^2}$	$2x10^{-4}$(-$5x10^{0}$*) – $1.1x10^{1}$	$1x10^{-3}$–$4.5x10^{1}$

Supplementary Table 3.1. Bulk flow scaling of natural dilute PDCs (Burgisser and Bergantz, 2005) and PELE experimental currents. *V* and L are characteristic velocity and length scales of the flow. μ corresponds to the dynamic viscosity of the flow. ρ is the mixture density and ρ_o is the ambient medium density. *D* is the particle diameter. * Estimates of the range of negative values of the Richardson number corresponding to hot PDCs with buoyancy reversal is based on the study of volcanic plume (Carazzo et al., 2015) and PDCs (Dufek, 2016).

Parameter	Nature	PELE
Particle diameter (m)	10^{-6}–10^{-1}	10^{-6}–10^{-2}
Particle density (kg m^{-3})	300–2600	300–2600
Fluid density (kg m^{-3})	0.6–1.2	1
Particle volumetric concentration	30–60 %	40–60 %
Dynamic viscosity of the fluid (kg m^{-1} s^{-1})	$1x10^{-5}$–$4x10^{-5}$	$1x10^{-5}$–$3x10^{-5}$
Underflow velocity (m s-1)	10-30	<2–15
Bagnold number $Ba = \frac{c^* \rho_p \dot{\gamma} D^2}{\mu_g}$ With $c^* = \left[c^{\frac{1}{3}}/(c_0{}^{\frac{1}{3}} - c^{\frac{1}{3}})\right]^{1/2}$	$1x10^{-2}$–$1x10^{2}$	$1x10^{0}$–$1x10^{2}$
Darcy number $Da = \frac{\rho_g}{\rho_s}\frac{D^2}{Re_p kc}$	$1x10^{2}$–$1x10^{4}$	$1x10^{0}$–$1x10^{3}$
Froude number $Fr = \frac{U}{\left[(\rho_p - \rho_g)gD\right]^{0.5}}$	1.6–9.6	1.5–6.2
Savage number $Sa = \frac{\rho_p \dot{\gamma} D^2}{(\rho_p - \rho_g)gh_c}$	$1x10^{-9}$–$1x10^{-7}$	$1x10^{-6}$–$1x10^{-5}$

Supplementary Table 3.2. Underflow scaling of natural PDCs (Roche et al., 2012) and PELE experimental currents. Where ρ_p and ρ_g the particle and gas density, $\dot{\gamma}$ the shear rate, μ_g the gas dynamic viscosity, D the particle diameter, h_c the current height, g the acceleration of gravity. c denotes the flow concentration during propagation, c_o is the maximum concentration at loose packing, γ is the shear rate. $\underline{k}$ is the permeability of the granular medium. Re_p is the particle Reynolds number defined as follows: $Re_p = 2DU\rho_s / \mu$.

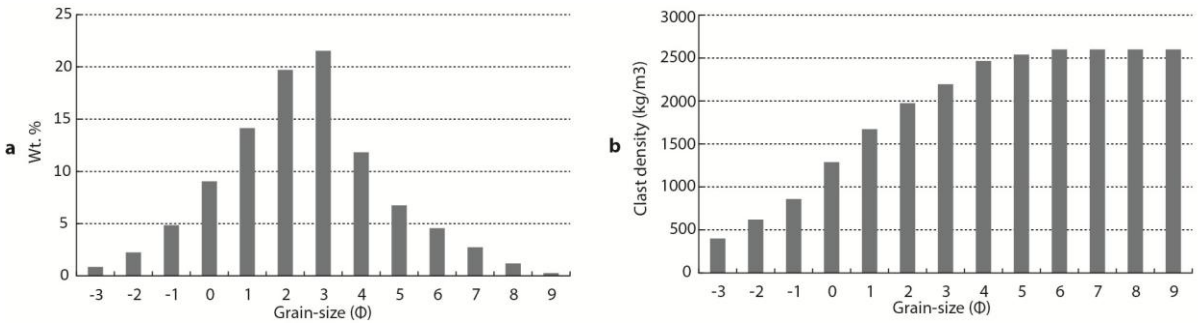

Supplementary Fig. 3.1. Grain-size and particle density distributions. a: Grain-size distribution of the initial experimental mixture. b: density distribution of the natural volcanic particles composing the experimental mixture. The average particle density is 1950 kg m^{-3}.

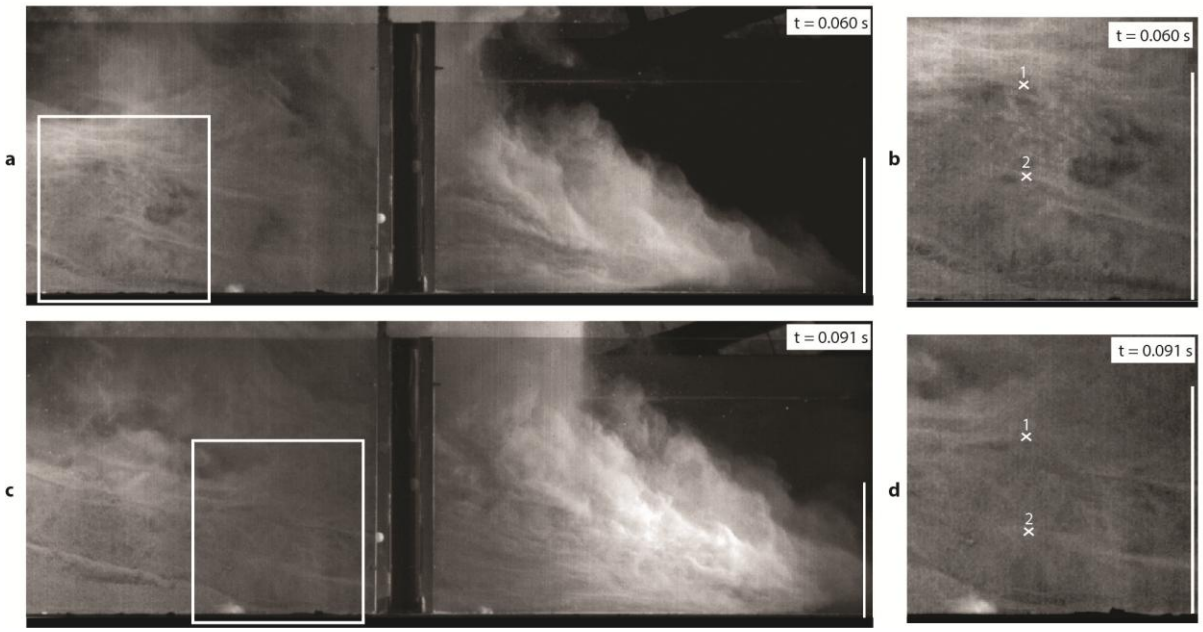

Supplementary Fig. 3.2. Mesoscale turbulence structures in large-scale PDC experiments. Still-images from a high-speed movie of the flow at 3.1 m from the source at 0.06 (a, b) and 0.09 (c, d) seconds after flow front arrival. Mesoscale structures occur in the middle zone of intermediate turbulence and take the form of dentritic clusters of particles. White crosses in (b) and (d), numbered 1 and 2, depict the same features in both images and illustrate the rapid sedimentation of the mesoscale structures at velocities of ~1.7 m s^{-1}. Vertical white bars are 0.3 m long.

Chapter 4 – Inside pyroclastic density currents – uncovering the enigmatic flow structure and transport behaviour in large-scale experiments

Chapter contents

This Chapter is based on paper submitted to Earth and Planetary Science Letter.

Participating authors:

Eric C. P. Breard (designed and undertook the experiments, collected and analysed the data, interpreted them and wrote the manuscript).

Gert Lube (conducted experiments with ECPB, manuscript editing and discussion)

Chapter 4 – Inside pyroclastic density currents – uncovering the enigmatic flow structure and transport behaviour in large-scale experiments

4.1 Introduction

PDCs are the most hazardous volcanic mass flows on Earth (Druitt, 1998; Valentine and Fisher, 2000; Branney and Kokelaar, 2002; Sulpizio et al., 2014). Their high velocity, dynamic pressures and particle cargo generate an extremely high destructive power (Valentine, 1998; Clarke and Voight, 2000). Frequent losses of life and severe damage to infrastructure at volcanoes worldwide (Valentine, 1998; Baxter et al., 2005; Jenkins et al., 2013; Komorowski et al., 2013b) make better understanding and forecasting of future events a high priority for research in volcanology (Cashman and Sparks, 2013).

This task is impeded by several obstacles. The transport of particles and gas in PDCs is amongst the most complex fluid mechanical processes in nature, involving highly variable gas-particle and particle-particle interactions with length-, time- and energy-scales encompassing several orders of magnitude (Esposti Ongaro et al., 2012; Dufek et al., 2015). This results in a broad spectrum of possible transport regimes from dense granular flows to dilute fully turbulent behaviour (Druitt, 1992; Sulpizio and Dellino, 2008). There are no direct observations of the interior of PDCs. This leaves large uncertainties in the selection and validation of appropriate physical models to simulate PDC transport and destruction behaviour computationally (Neri et al., 2003b; Esposti Ongaro et al., 2005; Esposti Ongaro et al., 2008; Esposti Ongaro et al., 2011; Doronzo and Dellino, 2011; Esposti Ongaro et al., 2012; Dufek et al., 2015). To test computational PDC models, and also to try to understand the flows better, researchers have traditionally relied upon deposits to infer PDC behaviour

(Sparks et al., 1973; Sparks and Walker, 1973; Sparks, 1976; Hoblitt et al., 1981; Wilson, 1985; Fisher, 1995; Belousov, 1996; Palladino and Simei, 2002; Sulpizio et al., 2007; Belousov et al., 2007; Fujinawa et al., 2008; Kilgour et al., 2008; Brown and Branney, 2013; Lube et al., 2014; Breard et al., 2015). Resulting qualitative transport and deposition models have evolved strongly over the past decades, heavily guided by insights gained from experimental studies of the dense and dilute transport regimes expected to occur in PDCs (Druitt, 1992; Branney and Kokelaar, 2002).

Understanding of PDCs advanced through major shifts in paradigms that sought to explain their internal structure, transport and deposition (Fisher and Schmincke, 1984; Wilson, 1985; Fisher, 1990; Fisher, 1995; Bursik and Woods, 1996; Freundt and Bursik, 1998; Sulpizio et al., 2014). Early models envisaged a simple longitudinally-variable flow structure dominated by one type of transport behaviour (Fig. 4.1A). Several lines of argument point towards vertical segregations of the PDC into two co-existing regions: a basal dense underflow of highest mass flux and an overriding dilute ash-cloud of higher volume (Fig. 4.1B). Uncertainties remain as to on whether dense and dilute (end-member) transport regimes are bounded by strong rheological interfaces, or whether these two extremes are connected through a gradual continuum of regimes of intermediate concentration and turbulence (Branney and Kokelaar, 2002).

To date, the lack of any quantitative data from within real-world flows has resulted in somewhat diverging pathways of PDC research through fieldwork on deposits, theoretical and computational models, and experimental work. Studies on deposits lack a general theory to quantitatively linking sediment characteristics to transport behaviour. Significant advances in numerical multiphase models result in detailed simulations of the PDC structure and transport (Dufek and Bergantz, 2007b; Dufek and Bergantz, 2007c; Esposti Ongaro et al.,

2011; Esposti Ongaro et al., 2012), but validation datasets to test, improve and generalize them are absent. Furthermore, laboratory analogues are increasingly recognised as suffering from issues of scale in replicating the inertia of particles (Choux and Druitt, 2002; Andrews and Manga, 2011; Chedeville and Roche, 2014).

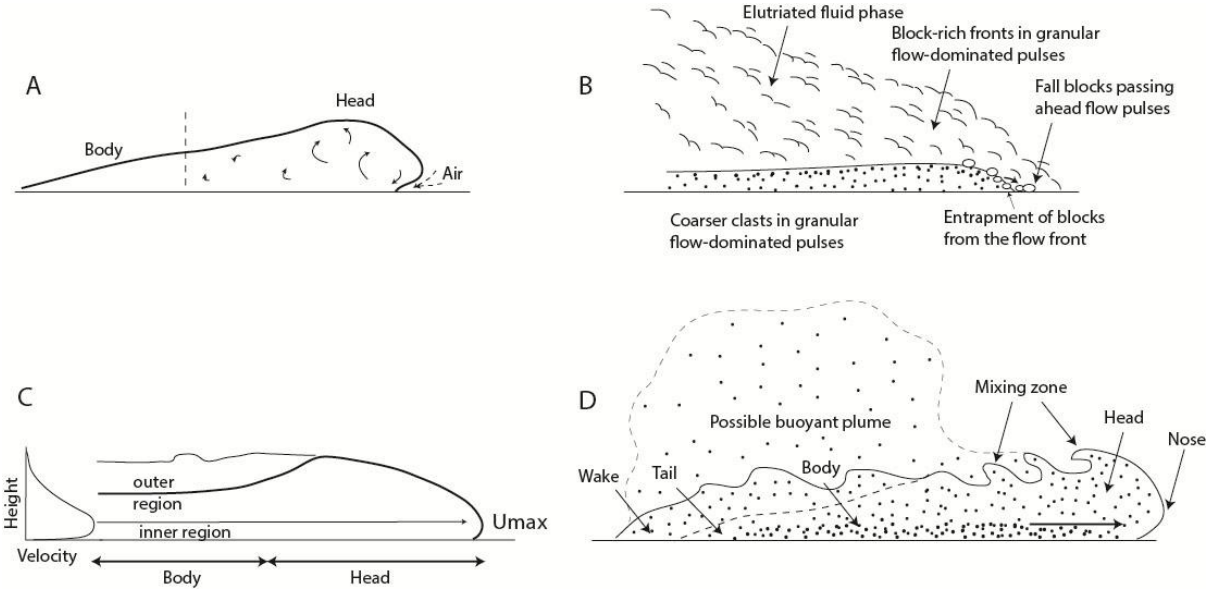

Fig. 4.1. Schematic representation of gravity and pyroclastic density currents. A: Schematic diagram of the anatomy of a concentrated PDC, modified from Wilson and Walker, 1982. B: Schematic illustration of a concentrated PDC, modified from Sulpizio and Dellino, 2008. C: Typical schematic diagram of a gravity current with inner and outer regions defined by the velocity profile. D: Generalized structure of a dilute PDC with a head intergradational into a body with an overriding mixing zone and trailing wake, modified from Branney and Kokelaar, 2002.

Here I report the results of large-scale PDC experiments conducted at the eruption simulator PELE, which currently constitutes the largest and most rigorously scaled volcanic flow test facility of its kind (Lube et al., 2015). I describe the internal flow structure and its evolution during runout through observations with high-speed video and measurements of velocity and concentration fields. The data analysis aims to test current qualitative PDC models and to provide insights to several major gaps in current understanding: in what ways do PDCs differ from the current analogue of dilute aqueous (particle-laden) gravity currents (Fig. 4.1C), how

is the presence of a dense underflow at the base of the PDC affecting flow transport and sedimentation behaviour, and what is the nature of coupled particle-gas transport in PDCs?

4.2 Methods

4.2.1 Synthesizing PDCs in large-scale experiments

Experiments were undertaken at the large-scale eruption simulator PELE (fully described in Lube et al. 2015), located at Massey University (New Zealand). PELE is a unique facility that synthesizes nature-scaled PDCs of up to 6 tonnes of natural volcanic material and air, which can reach velocities of 7–30 m s^{-1}, flow thicknesses of 2–4.5 m, and runout lengths of >35 m (Lube et al., 2015). Particle-gas currents are generated by the controlled gravitational collapse of concentrated suspensions of volcanic particles and air from a hopper onto an instrumented runout section (supplementary Fig. 4.1A). PELE is located within a 16 m high, 25 m long and 18 m wide unused boiler house and is composed of: (I) a 13 m high tower and elevator holding a 4.2 m^3 hopper through which a pyroclastic mixture is discharged at variable discharge height; (II) a shrouded, fall section (up to 9 m) below the suspended hopper; (III) a 12-m long, 0.5-m wide and 0.6-m high inclinable channel section with a rough steel base (basal friction angle of 36.5°); and (IV) a 30 m long flat runout area of concrete (basal friction angle of 37.5°) that extends outside the building. Experiments were conducted at ambient temperature (~15°C), with an eruption column fall height of 3–5 m, a constant hopper discharge rate of 825 kg s^{-1}, and with the channel uniformly sloping at 9–19°.

The experimental volcanic mixture was a blend of two different deposits of the 232 AD Taupo Ignimbrite (Hogg et al., 2012). The mixture had a unimodal grain-size distribution with a median diameter of ~250 μm, an average clast density of 1950 kg m^{-3}, and contained 10 wt.% of very fine ash material (particles <63 μm) (supplementary Figs. 4.1B and C).

4.2.2 Sensors and analytical methods

The experimental PDC was recorded from a range of viewing angles with 2 high-speed cameras shooting at 600-1000 frames per second, and 4 moderate to normal speed cameras that ran at 24–240 frames per second.

Two-dimensional velocity and vorticity fields were computed via particle-image-velocimetry (PIV) using the software PIVlab (Thielicke and Stamhuis, 2014). Prior the image analysis, raw images were filtered to enhance the PIV (Stamhuis, 2006) with CLAHE and Wierner denoise algorithm implemented in PIVlab.

Vertical profiles of particle concentration in the ash-cloud were determined using an empirical relationship between concentration and the median grey-scale of high-speed images that accounts for local variation in illumination and grain-size distribution. This function was determined using vertical profiles of sediment samplers that captured the mass of sediment, M_S, passed a location across the sampling cross-sectional area A. The local median grey scale is a function of particle concentration and takes a power-law form where concentration is a fitted function of M_S, A, flow velocity U, and time. The validity of the empirical relationship between the median value of the image grey scale and particle concentration and the minimum range of quantifiable concentrations (c. 10^{-5}–10^{1} %) was determined through direct measurements of local time-variant mixture density (Lube et al., 2015). For the direct measurements of mixture density, ρ_M I recorded with high-speed video the sequential filling of transparent, horizontally (parallel to slope) oriented glass tubes with cross-sectional area, A_p. The tubes were open on the upstream side to collect the flow over the tube cross-sectional area, and contained an 80 μm mesh at their downstream side impermeable for particles and permeable for air. Mixture density is obtained as $\rho_M(t) = Q_{VF}(t)\rho_S/A_P U_i(t)$, where Q_{VF} is the volumetric rate of sediment accumulation in the tube, ρ_S is the non-compacted bulk

material density, U_i is the velocity of the flow before entering the tube (measured by PIV), and t is time.

Depth-averaged particle concentrations estimates for the underflow were obtained from the two-dimensional velocity fields using a constant, time-averaged vertical expansion determined by comparing the volumes of flow and deposit passing an observer location. Time- and depth-averaged particle concentrations values for the different ash-cloud regions (head and body) were computed by integrating local time-averaged mass flux data from vertical profiles over the time of passage for the head and body regions.

Concentration profiles and contours, and the dynamic pressure map were computed using the kriging interpolation and projected as logarithmic contours in Surfer 13.0. Dynamic pressure, P_{dyn} is calculated as follows:

$$P_{dyn} = \frac{\rho\, u^2}{2} \qquad (4.1)$$

where u is the horizontal component of velocity and ρ is the flow density.

4.2.3 Non-dimensional number estimates

Reynolds number

The Reynolds number (Re^{**}) is a dimensionless parameter characterizing the level of unsteadiness of the continuous phase (liquid or gas) and is defined as follows:

$$Re^{**} = \frac{\rho UH}{\mu^{**}} \qquad (4.2)$$

where U and H are depth averaged velocity and height of the flow, respectively. μ corresponds to the dynamic viscosity of the flow. The flow is laminar when $Re^{**} \leq 1$ and

fully turbulent when *Re*** is > 10^4, and between these two values lies the transition between the two regimes (Dimotakis and Catrakis, 1999).

The flow density ρ can be related to the particle volumetric concentration C and the particle $\rho_s$and gas densities ρ_g as follows:

$$\rho = \rho_g(1 - C) - \rho_s C \qquad (4.3)$$

One can define the mass ratio $M^* = \rho_s C / \rho_g(1 - C)$ and use this ratio to estimate the bulk dynamic viscosity μ^{**} which takes into account the viscous stress by both the gas dynamic viscosity (μ) and the collision viscosity given by: $\mu^{**} = \mu(1 + M^*)^2$ (Marble 1970, Wohletz, 2000).

Densimetric Froude number

The densimetric Froude number Fr' is the ratio of flow inertial to buoyancy forces:

$$Fr' = \frac{U}{\sqrt{\frac{g(\rho - \rho_o)}{\rho_o} H cos(\theta)}} \qquad (4.4)$$

with U as the depth-averaged velocity, ρ and ρ_o are the flow and ambient density respectively, H is the height over which the velocity is averaged and θ is the slope angle to horizontal.

Stokes and Stability numbers

Stokes S_T and Stability Σ_T numbers estimates require measurements of largest eddy diameter, mean velocity and settling speed (Burgisser and Bergantz, 2002).

$$S_T = \frac{U_T \, \Delta U_i}{g\delta} \qquad (4.5)$$

$$\Sigma_T = \frac{U_T}{\Delta U_i} \qquad (4.6)$$

where U_T is the terminal fall velocity, ΔU_i is the eddy rotation velocity, g is acceleration due to gravity and δ is the eddy diameter. In order to show the full range of particle transport regimes occuring within experimental PDCs, I have used estimates from experiments at 9 and 19 degrees. Eddy diameter and velocity estimates were height-variant as well as time-variant and obtained with PIV analysis. Stokes and Stability numbers do not directly relate the settling velocities to the flow velocity, but to the eddy rotation velocity in its stead. The mean velocity of the eddy U and its rotation velocity ΔU_i are related as follows (Pope, 2000; Burgisser et al., 2005).

$$\Delta U_i \cong U \frac{\sqrt{88}}{4e^2} \qquad (4.7)$$

Velocities and maximum eddy size data were averaged over 0.01–0.05 s, thus allowing us to determine the grain-size distribution transported within such regime. Particles were captured by transparent samplers mounted as 4 vertical profiles from 0.05 to 2 m high, located at 3.1, 5.4, 8.4 and 11.5 m from source. High-speed recordings of the filling of samplers during flow passage allowed us to obtain time- and height-variant grain-size data. Samples were hand-sieved for fractions >500 μm and smaller fractions were analysed with a laser particle analyser. The median grain-size diameter, 15th and 85th percentiles were computed using GRADISTAT 8.0. From the median grain-size, Stokes and Stability numbers represent the "average" transport behaviour of a grain-size distribution transported at a given ΔU_i within an eddy of diameter δ. Furthermore, 15th and 85th percentiles were used to assess the range of particle transport behaviour around the "average".

The settling velocity U_T of particles through a fluid is described as follows (Dellino et al., 2005) :

$$U_T = \frac{1.2065\mu\left(\frac{D^3\, g\left(\rho_s-\rho_f\right)\rho_f\Psi^{1.6}}{\mu^2}\right)^{0.5206}}{d\rho_f} \qquad (4.8)$$

where Ψ is the shape factor, d is the particle diameter, ρ_s is the particle density, ρ_f is the fluid density, μ is the fluid dynamic viscosity and D the particle diameter. The shape factor Ψ was determined following the method of Dellino et al. (2005). The grain-size variant density was estimated using the heavy liquid method for half-phi intervals (Lube et al. 2015).

4.3 Results

4.3.1 Viewing inside experimental PDCs

During free fall, the gas-particle mixture accelerated and diluted to reach a particle concentration of 9.5 vol% and a vertical velocity of 7.7 m s^{-1} at impact. Upon impact, the fully turbulent suspension accelerated further to reach initial downslope velocities of 16 m s^{-1} (Fig. 4.2 at 0.12 s). By 0.21 s after impact, the mixture had vertically segregated into a basal underflow and an overriding ash-cloud (Fig. 4.2 at 0.21 s). During passage at 3.1 m from source, 95% of the mass resided in the underflow, increasing to 99.6% by 10.3 m from source. By 0.21 s, the ash-cloud had also started to longitudinally segregate into an ash-cloud head and a trailing ash-cloud body (Fig. 4.2). Detachment of large Kelvin-Helmholtz instabilities from the rear of the head fed a dilute ash-cloud wake above the ash-cloud body. From here onwards the c. 0.5–0.8 m-thick body was directly overlain by the c. 0.25–3 m-thick wake. The vertical and longitudinal segregation processes produced flow regions of strongly contrasting (time- and depth-averaged) particle concentration. For instance, during

passage of the flow at 3.1 m, the underflow had an average particle volumetric concentration of 45%, the head 5.5×10^{-1} vol%, the body 7.4×10^{-2} vol% and the wake 6×10^{-3} vol%. The concentration of the underflow remained high until bed solidification and deposition (Lube and Breard et al., 2015). The other three regions diluted by an order of magnitude, each due to sedimentation and entrainment during runout to >25 m. While the characteristics of the highly mobile underflow are described in Lube and Breard et al. 2015, the behaviour of the ash-cloud is detailed in this chapter.

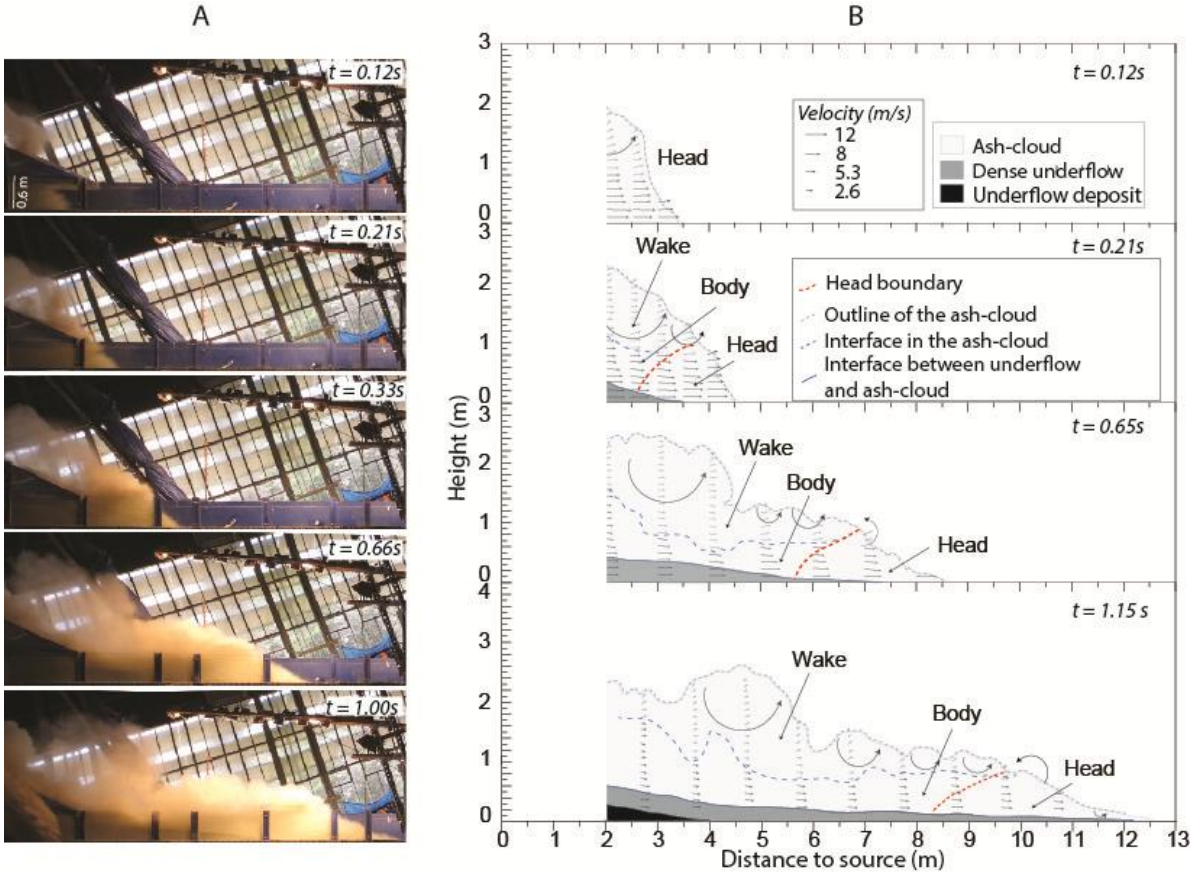

Fig. 4.2. Photographs of the experimental flows and internal velocity fields for various time steps. A: Photographs of the flow for 5 time steps. Note the progressive formation of a wedge-shape snout, and the appearance of an underflow layer underneath the ash-cloud. B: Longitudinal cross-sections of the advancing experimental PDC at four different times. Grey dotted line, grey dashed line, solid line, dotted line, grey area and black area demark upper flow boundary, a visible diffuse interface within the ash-cloud separating the wake from the body, top of underflow and aggrading deposit, respectively. Extent of head and body regions (separated by a broad interface represented in a red dashed line) are indicated.

Ash-cloud head. The head consisted of a leading section that preceded the underflow and a rear section that rode above it (Fig. 4.3A). The leading part comprised an elevated (0.01–0.15 m high) nose above a 0.02–0.2 m-long particle-free region, demonstrating the overriding of ambient air (Fig. 4.3B). Two different types of frontal instabilities occurred also. In the proximal part of the runout section and up to c. 6 m, where the front of the underflow lagged at least a meter behind the nose, a few decimetres-high lobes-and-cleft instabilities formed (Fig. 4.3E and G). Further downstream, where the front of the underflow had migrated closer to the nose, 0.01–0.05 m-thick fingering instabilities were impulsively ejected forwards from the head (Fig. 4.3F). These appeared highly mobile, had particle concentrations of c. 0.1–1 vol% and were enriched in large pumice lapilli and high-density ash-sized material (Fig. 4.3H and I).

Behind the nose, the strong shear between the head with the still ambient air generated successions of Kelvin-Helmholtz instabilities (K-H instabilities, Fig. 4.3A). Where K-H detached from the leading steep part of the head, they were rapidly re-entrained by thicker regions from behind (Fig. 4.3C and H). The largest K-H formed rearwards of the thickest part of the head (Fig. 4.3A), where they also detached, strongly decelerated, and formed the growing wake of the ash-cloud.

Internally, the head contained a large, asymmetric (0.5–1.2 m high and 0.8–4m long) and anticlockwise rotating vortex that was overprinted by smaller-scale eddies. New particles were entering the vortex from its basal rear part, while some of the coarse and high-density material left it through the frontal instabilities; a significant proportion of material sedimented onto the moving underflow (see also Breard et al., 2015), and part of the fine and low-density material detached into the Kelvin-Helmholtz instabilities as described above. Vertically, an

upper part of well- to moderately-well mixed particle and gas phases overlaid a lower up to 0.4 m-thick region comprising dendritic mesoscale clusters (Fig. 4.3D).

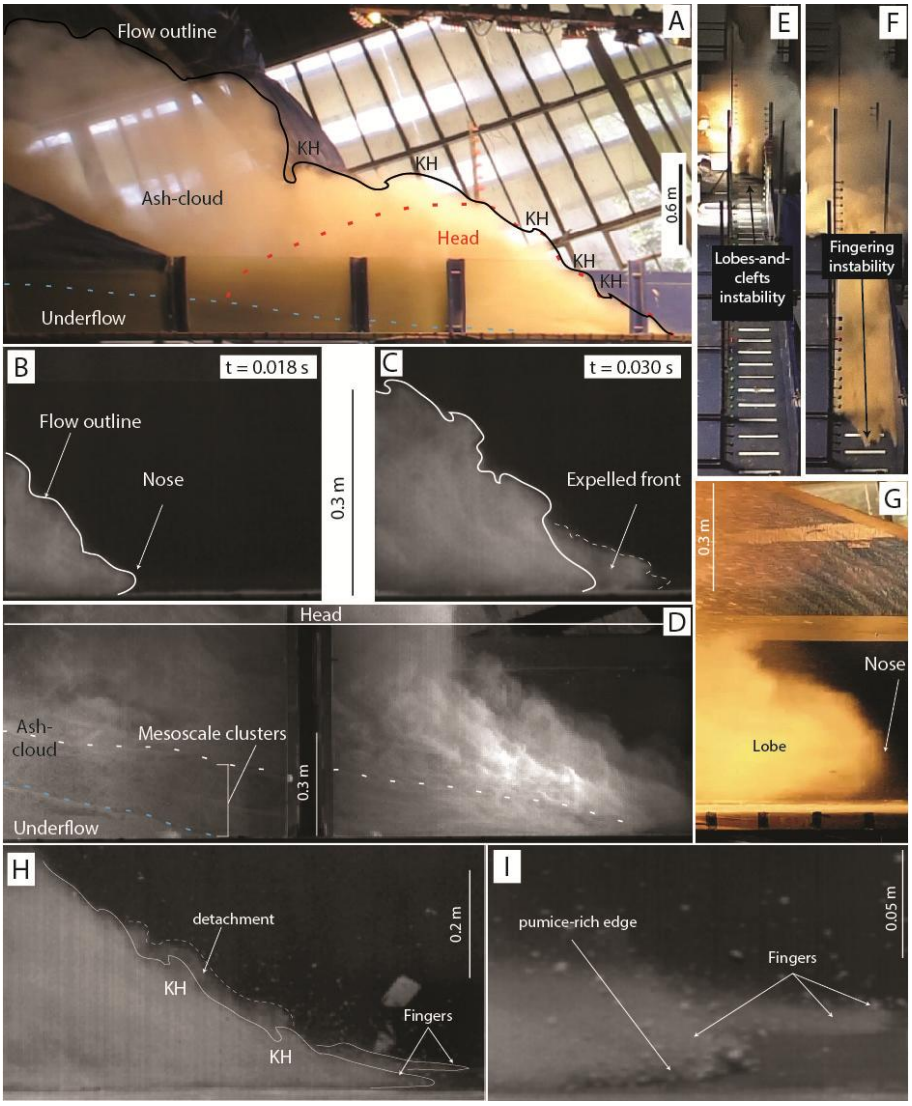

Fig. 4.3. Photographs of various aspects portion and processes occurring within the head of experimental currents. A: Sideview photograph showing the nearly semi-elliptical head shape with a wedge front. Note Kelvin-Helmholtz instabilities that grew in size up current. Dashed and solid lines indicate the different outlines of the ash-cloud, underflow and head. B: Close-up photograph of the snout of the head, which developed a small elevated nose. C: Photograph of the same front after 0.012 sec (after B) that depicts a transient expelled flow front. D: Picture of the internal structure of the flow head shows three zones: the lowermost one is the underflow, separated by a sharp interphase from the intermediate concentrated zone where mesoscales structures develop. Particles gather in clusters of dendritic pattern. E: Frontal view of the flow in the proximal area showing lobes-and-clefts instabilities. F: Flow front develop finger instabilities in the medial and distal area. G: Cross-section through a lobe developed nose. H: Close-up photographs showing a cross section through the flow front with finger instabilities. Note the thin <1cm thick fingers. I: Finger instabilities can transport large particles (pumices) at the front.

The boundary of the rear of the head towards the ash-cloud body is demarked by a prominent trough in particle concentration. This occurred behind the concentration maximum associated with the passage of the central part of the head (Fig. 4.5 B-D). At a static observer position, the concentration trough passed earlier at larger heights. This demonstrates that the head-body boundary is curved downwards in an upstream direction.

Ash-cloud body. The body of the ash-cloud moved on top of the underflow. Particle and gas phases appeared better mixed than in the head. However, fine dendritic mesoscale clusters and the migration and concentration of particles within larger eddies were also observed, particularly in the leading section of the body and its lower half (Fig. 4.4B–D). Some of these structures were associated with the propagation of higher-density pulses through the body (Fig. 4.4A and 4.5). These pulses occurred at frequencies of 0.1 to 0.5 seconds, caused local acceleration and could be traced downstream, but their origin remains unclear (Fig. 4.5B-D). The upper boundary of the body towards the ash-cloud wake was associated with a marked decline in particle concentration and strong shear. This induced numerous K-H at the body-wake interface, with the instabilities growing upwards into the wake and detaching frequently from the body (Fig. 4.5B-D). Only much later (c. 8 sec), when the head had reached its full runout length and the underflow was deposited, did K-H grow to be larger in size. This caused large-scale advection that mixed the diluted body and wake regions and caused the ascent of billows from the co-ignimbrite ash-cloud up to c. 8 m.

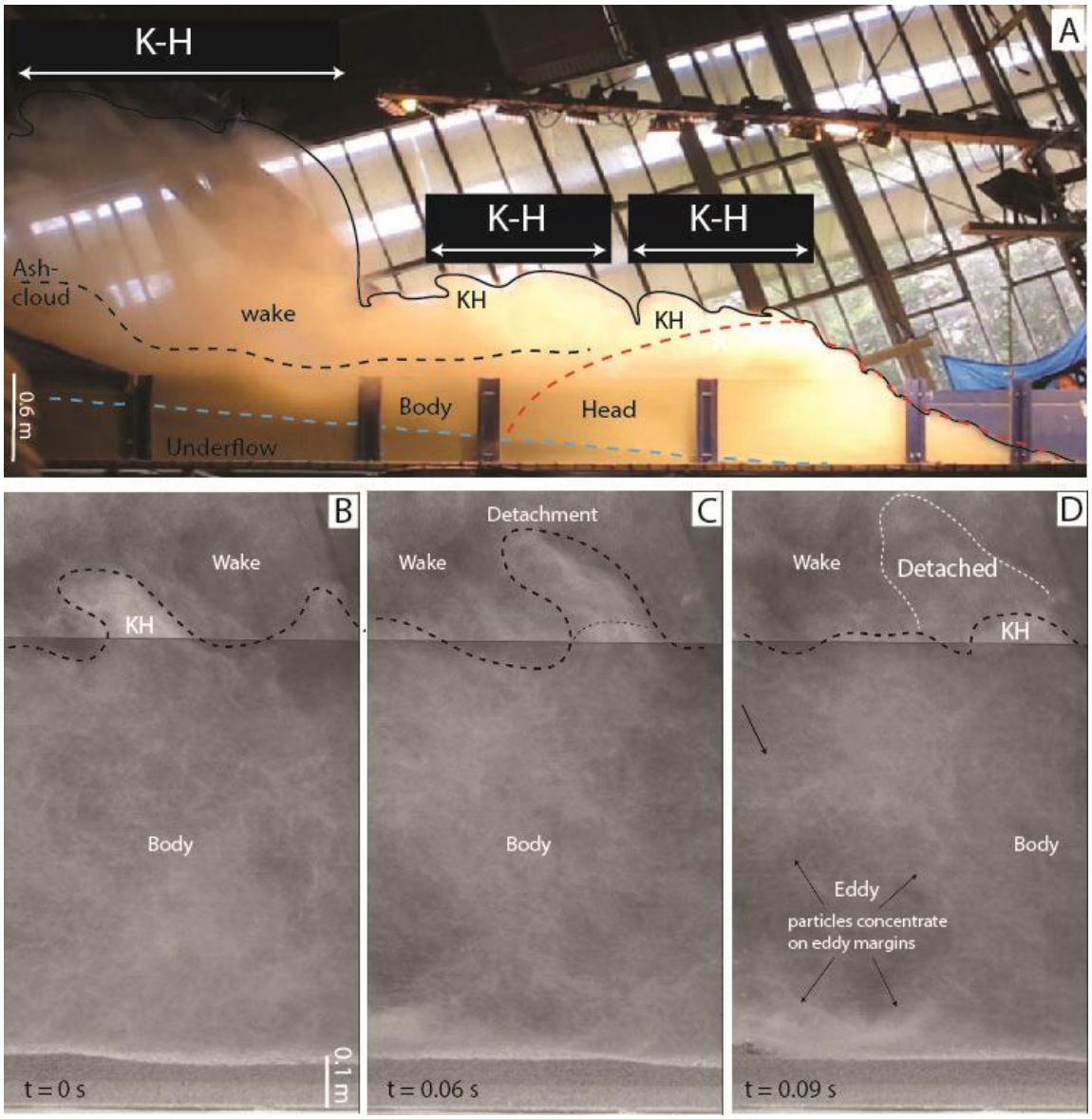

Fig. 4.4. Photographs illustrating main processes occurring within the body and wake of the ash-cloud. A: Large Kelvin-Helmholtz instabilities form in the wake and can have a size scaled with the layer thickness. Formation of the wake occurs through the first vortex located in the middle of the head. B-D: Sequence of photographs showing the instabilities forming along the wake-body interface, and the breakdown of KH instabilities that feed the wake from the ash-cloud. Note also the eddy passing through with particles that locally migrated towards its margin.

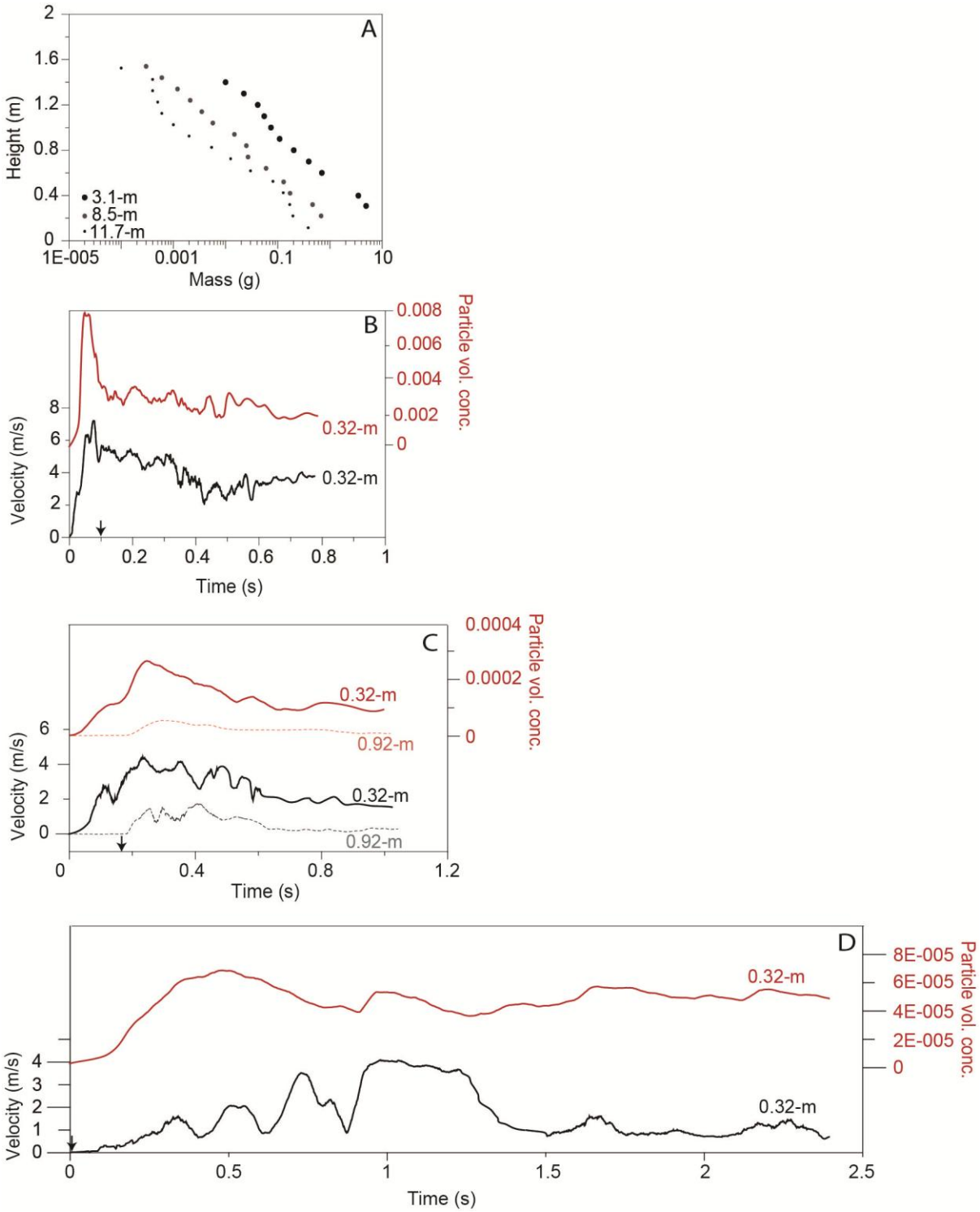

Fig. 4.5. Height-variant dynamics. A: Height-variant mass transported in the ash-cloud and captured by samplers at three locations (3.1, 8.5 and 11.7 m from source). B: Time-variant velocity (black line) and concentration (red line) at 0.32 m of height at 3.1 m of distance from source. C: Time-variant velocity and concentration at 0.32 and 0.92 m of height at 8.5 m from source. D: Time-variant velocity and concentration at 0.32 and 0.92 m of height at 11.7 m from source.

4.3.2. Fluid dynamic characteristics of PDC regions

Before delving deeper into the details of the internal flow structure, let us first elucidate through non-dimensional numbers the principal (depth-averaged) fluid mechanical characteristics of the main flow regions and their transitions. Here I consider the temporal variations in the bulk Reynolds number *Re***, the densimetric Froude number *Fr'*, and the entrainment coefficient α of the passing current at three observer locations.

Unsurprisingly, the underflow and ash-cloud regions, due to their strong differences in particle volumetric concentration, contrast markedly in bulk current behaviour. While the underflow obeys mildly transient turbulence and close to laminar transport with Reynolds numbers ranging from 7–18, the ash-cloud is fully turbulent with *Re*** well in excess of 10^4. The underflow is always subcritical with the maximum Froude number values of 0.99 only reached in its thin frontal region. By contrast, Froude numbers in the ash-cloud are supercritical to critical, ranging between values of 1–4.2. However, in the ash-cloud, the head, body and wake region have their own unique characteristics in terms of the three non-dimensional products (Fig. 4.6).

The head is the flow region with the largest vertical and longitudinal variation in turbulence. This can be qualitatively assessed through measurements of maximum eddy sizes in vorticity plots obtained by PIV. These measurements show that the smallest (maximum) eddy sizes of generally <0.1 m occur in the frontal and lowermost part of the head; intermediate (maximum) eddy sizes between 0.1–0.3 m characterise the central and upper part of the head; and larger eddies of 0.3–0.5 m are only abundant in the large K-H instabilities in the rear of the head transitioning to the wake. Eddy sizes in the body are less variable, but show systematic vertical variation. Intermediate (maximum) eddy sizes (0.1–0.3 m) dominate in the lower part of the body, while in its upper part they typically range between 0.3–0.5 m. By

contrast, the ash-cloud wake shows the largest (maximum) eddies with sizes in excess of 0.5 m and approaching maxima of c.1.5 m.

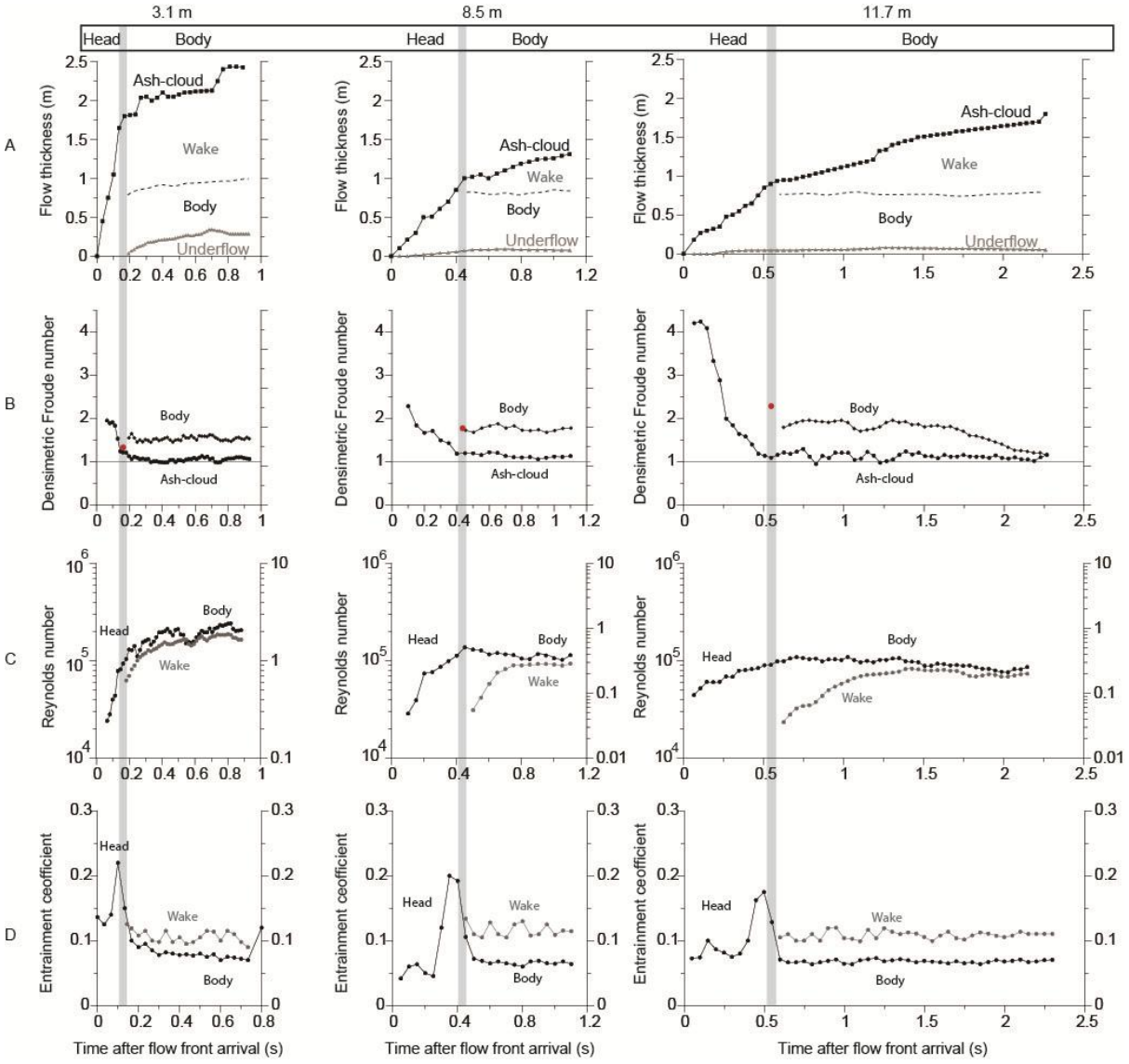

Fig. 4.6. Time-variant fluid dynamics of the flow at the three observer locations. A: Time-variant wake, body, and underflow upper interfaces at the three observer locations. B: Densimetric Froude number of the total ash-cloud and body at the three observer locations. C: Reynolds number of the head, wake and body at the three observer locations. D: Entrainment coefficients of the head, wake and body at the three observer locations. Note the grey bar that highlights the transition zone where the wake is created.

These qualitative observations of turbulence are in agreement with temporal changes of the depth-averaged bulk Reynolds number. During passage of the front of the head, *Re*** strongly increases from lower 10^4 to above 2×10^5, approaching a maximum during passage of rear of the head (Fig. 4.6C). During passage of the body, *Re*** remains relatively time-invariant and high. The ash-cloud wake shows similar values of *Re*** as the body, but their origin is somewhat different. High *Re*** in the body are associated with high velocities and moderate particle concentrations (leading to moderate values in bulk dynamic viscosity), while similar values of *Re*** in the low-concentration wake (implying a low bulk dynamic viscosity) are due to lower depth-averaged velocities than those in the body below.

The head is characterised by high and strongly time-variant Froude numbers (Fig. 4.6B). The highest and strongly supercritical values are associated with the passage of the frontal part of the head encompassing the nose and fingering instabilities. During passage of progressively thicker parts of the leading head (at the top of which regular K-H billows occur) Froude numbers decline rapidly. However, these remain supercritical and Froude numbers only approach values of ~1.2 during passage of the rear of the head. Behind the head, Froude numbers in the ash-cloud are characteristically time-invariant ranging between 1.1 and 1.3.

Some periodic variation in *Fr'* is seen at the distal observer location and is associated with the passage of larger eddies in the wake. Froude numbers calculated for the ash-cloud body region (only) also show relative time-invariance, but higher (supercritical) values than the depth-averaged ash-cloud (body and wake) of between 1.5–1.9.

The entrainment coefficient also varies strongly during passage of different ash-cloud regions (Fig. 4.6D). The frontal part of the head has moderately low entrainment coefficients typically between 0.04 and 0.08. Only in proximal reaches, where lobes-and-cleft instabilities occur, does entrainment increase to values between 0.12–0.14. Entrainment increases sharply

in the rear of the head associated with the large K-H billows with maximum values of α up to 0.22. In the body, entrainment coefficients are low (0.05–0.1) and characteristically time-invariant and a sharp decline in α marks the head-body boundary. By contrast, entrainment coefficients for the ash-cloud wake are high (0.1–0.14).

These observations confirm previous measurements of entrainment into PDC-analogue gravity currents in that entrainment is highly variable within the ash-cloud (Turner, 1986; Parker et al., 1987; Wells et al., 2010; Andrews, 2014). Consequently, semi-empirical relationships between the bulk Froude number and bulk current entrainment (e.g. Parker et al., 1987) cannot fully describe the complexity of entrainment processes. In particular, entrainment into the supercritical leading part of the head is lower than predicted by these laws, while entrainment into the rear of the head is substantially higher than the theoretical maximum value of 0.1 (c.f. Wells et al., 2010).

4.3.3 Coupled motion between underflow and ash-cloud regions

In our experiments, the ash-cloud region is not a simple gravity current with a no-slip basal boundary. Instead, it travels on top of an already fast moving dense underflow. To better understand the underflow/ash-cloud system, I characterised the kinematics of both regions.

After the initial segregation into ash-cloud and underflow regions, the front of the underflow initially lagged behind the front of the head. Subsequently, however, the underflow front migrated towards and eventually caught up with the head front (e.g. Figs. 4.2B and 4.7A). During the vast majority of flow passage along the three observer locations, the depth-averaged velocities in the underflow were considerably larger than the depth-averaged velocities in the ash cloud above (Fig. 4.7B). Only much later, when the air-cushion at the base of the underflow, which drives its high mobility, broke down (see also Lube and Breard

et al. 2015), was this behaviour reversed and the ash-cloud velocity exceeded underflow velocities.

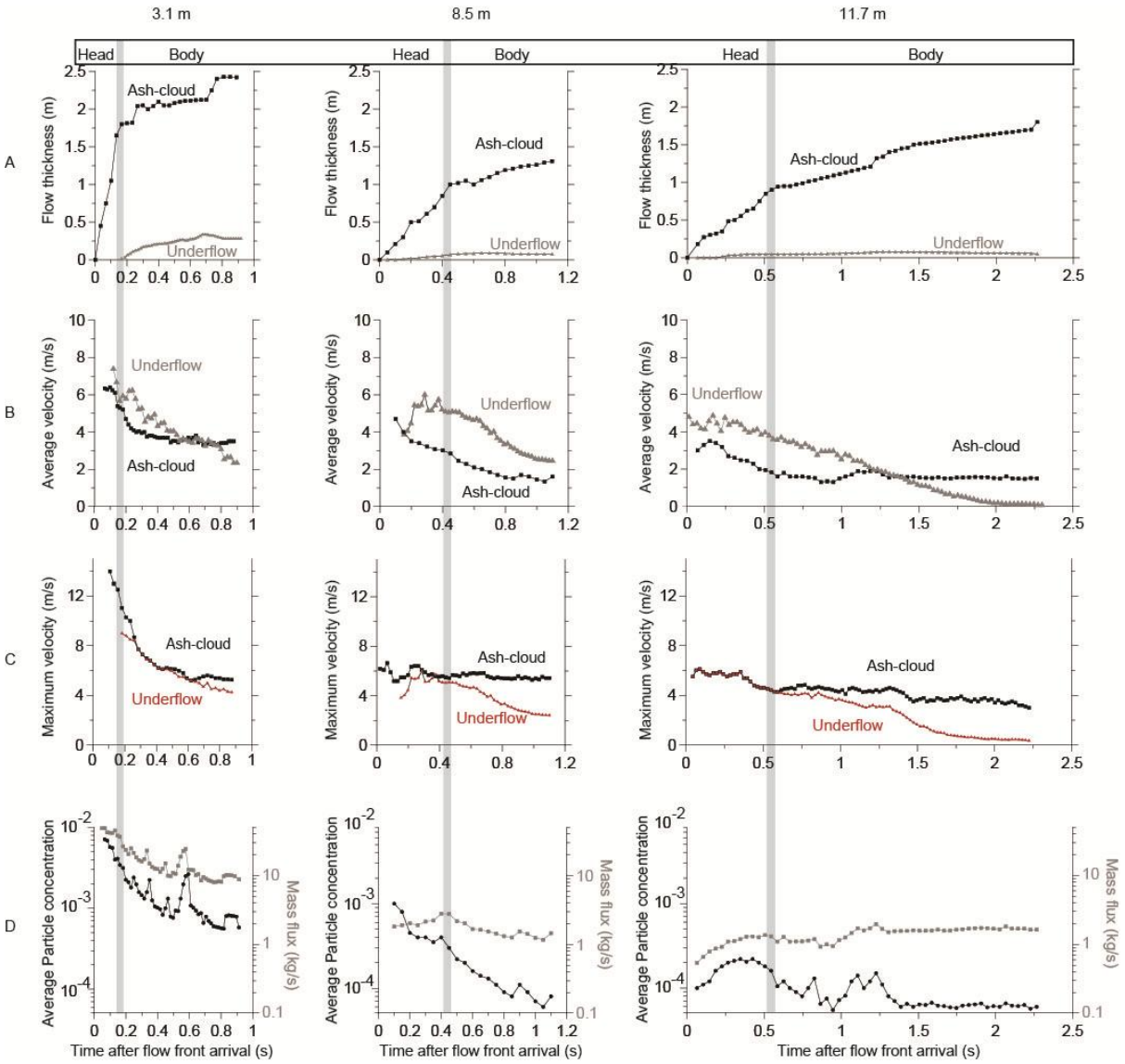

Fig. 4.7. Depth-averaged flow kinematics of the ash-cloud and underflow. A: Time-variant wake, body, and underflow upper interfaces at the three observer locations at 3.1, 8.5 and 11.7 m. B: Time-variant average velocity of the ash-cloud (black) and underflow (grey). C: Maximum velocity value within ash-cloud and underflow. D: Depth-averaged particle concentration of the ash-cloud and underflow and depth-averaged mass-flux.

The velocity differential between underflow and ash-cloud regions results in three main regimes of coupling and traction behaviour. These regimes can be defined by comparing the time-variant maximum flow velocities of the underflow U_{U_max} and the ash-cloud U_{A_max} (Fig.

4.7C). The maximum velocity of the underflow always occurs at its top and hence at the boundary to the ash-cloud region, while the location of the maximum velocity of the ash-cloud is variable in the three coupling regimes.

Regime 1. $U_{U\_max} = 0$ and $U_{A\_max} > 0$. This condition occurs in the frontal part of the head when the underflow still lags behind the head front and traction occurs between the substrate and the ash-cloud (Fig. 4.7C, supplementary Fig. 4.2). In this region, the head always slips across the solid flow boundary; i.e. basal flow velocities were greater than zero. The same condition also occurs much later when the underflow has stopped (Fig. 4.7C). In this latter situation, the head and body regions are travelling on top of a rigid substrate and strong traction without slip occurs at the lower flow boundary.

Regime 2. $U_{U\_max} = U_{A\_max}$. This condition occurs proximally for a significant proportion of the passage of the body, and further downstream for most or the entire duration of the passage of the head (Fig. 4.7C). In this regime, underflow and ash-cloud regions are firmly kinematically coupled.

Regime 3. $U_{U\_max} < U_{A\_max}$ and $U_{U\_max} > 0$. This condition characterises most of the passage time of the body and lasts up until rapid aggradation of the underflow deposit (Fig. 4.7C). In this regime, strong traction develops at the underflow/ash-cloud interface.

The coupling and traction regimes 1–3 are not rigidly associated with a particular PDC flow region and transitions between regimes can occur. For instance, the underflow typically comprises surface waves that travel faster than the bulk underflow. If these pass a static observer location in regime 3, they can cause brief transitioning into regime 2. Thus, in real-world flows propagating over complex topography, transitions between regimes 2 and 3 can occur frequently during topography-controlled acceleration of the underflow. Topography-

controlled deceleration will cause the slipping frontal part of the head to race ahead of the underflow, resulting in a spatially extended regime 1.

4.3.4 The internal flow structure

The presence of an underflow beneath the ash-cloud and the relative motion between these two regions has a strong effect on the flow-internal velocity and density structure. The velocity and density structure differs in several aspects from that of dilute gravity currents (e.g. Kneller et al., 1999; Kneller and Buckee, 2000). Vertical velocity profiles in classical gravity currents consist of an inner region in contact with the lower flow boundary, with a zero (no-slip) velocity at the base and a positive velocity gradient, and an outer region with a negative velocity gradient (Altinakar et al., 1996). The inner region with high shear due to traction with the lower flow boundary can be envisaged as a turbulent boundary layer of the current. The height of the maximum velocity at the boundary between the inner and outer regions decreases with increasing Froude number. In subcritical gravity currents, vertical density profiles take a so-called two-layer form with a lower part of high and relatively height-invariant density, and an upper region where density is strongly (and approximately logarithmically) decreasing upwards (Britter and Simpson, 1978; Simpson and Britter, 1979a; Sequeiros et al., 2010; Sequeiros, 2012a). At supercritical conditions, flow density in the lower part changes to a Rouseian form with density increasing exponentially downwards towards the lower flow boundary (e.g. García, 1994).

In our experiments, similar velocity and density profiles as in dilute gravity currents occur only at a late stage (under coupling and traction regime 1); i.e. when the front has reached its maximum runout distance and the underflow as stopped completely (Fig. 4.8A and B at time "D"). At all other times, and hence characteristic for the overall flow transport, velocity and

concentration profiles depart from the above described forms and vary strongly dependent on the type of coupling and traction regime.

Regime 1. $U_{U\_max} = 0$ and $U_{A\_max} > 0$ in the head. In the supercritical head, the velocity profiles have a characteristic high boundary velocity with the substrate, and consist of a thin inner region with a positive velocity gradient and broad outer region with a negative velocity gradient (Appendix 4.3). Concentration profiles take a two-layer form (usually only found in subcritical gravity currents) with a lower relatively height-invariant and high concentration part and an upper part of strongly upwards decreasing concentration (supplementary Fig. 4.2).

Regime 2. $U_{U\_max} = U_{A\_max}$. Because the height of U_{U_max} always coincides with the top of the underflow, the maximum overall flow velocity in regime 2 occurs at or very near the boundary between underflow and ash-cloud. The smooth velocity gradient across the underflow/ash-cloud interface implies nearly perfect kinematic coupling and extremely low traction (Fig. 4.8A at time "A"). This indicates also low friction at this interface, further exemplified through very low velocity gradients (or shear) across the interface. Concentration profiles in regime 2 show a strong decrease at the underflow/ash-cloud boundary. Above the boundary, concentration profiles in the ash-cloud have a similar ("two-layer") form as in the head situation of regime 1 (Fig. 4.8B at time "A"). Because of the absence of an inner region of positive velocity gradient in the ash-cloud, the underflow essentially becomes the boundary layer of the flow.

Typically, there is a brief time (or short region) before regime 2, where U_{A_max} is slightly higher than U_{A_max}. Here the ash-cloud, due to its low friction with the underflow, slips swiftly along the low-friction boundary. We suggest that this behaviour results in the local frontal accelerations and the formation of the fingering instabilities described above.

Regime 3. $U_{U\_max} < U_{A\_max}$ and $U_{U\_max} > 0$. In this regime, strong traction develops at the underflow/ash-cloud interface as illustrated by a rapid decline in velocity immediately above the interface (Fig. 4.8A at times "B" and "C"). Above, the velocity profile in the ash-cloud shows an inner region with a positive velocity gradient towards the velocity maximum, and an outer region of upward declining velocity. Similarly to regime 2, vertical concentration profiles in regime 3 show a "two-layer" form with a lower part (c. lower third to half of body) of relatively height-invariant or only slightly upwards decreasing concentration, and an upper part of strongly decreasing concentration (Fig. 8B at times "B" and "C"). The interface between the body and wake regions is characterised by a marked decrease in concentration over a few centimetres and by a switch from predominantly downward motion (body) to predominant upward motion (wake) (Fig. 4.8A at times "B" and "C").

4.3.5 Distribution of dynamic pressure inside experimental PDCs

The measured velocity and density time-series data lend themselves to 'image' the distribution of destructive dynamic pressures inside the current (Fig. 4.8B). The underflow constitutes the 'most destructive' flow region with dynamic pressures of 10^2–10^3 Pa. The ash-cloud shows a vertical and longitudinal zoning in dynamic pressure with values ranging from less than 1 Pa to 10^2 Pa. In proximal regions during initial acceleration, maximum dynamic pressures in the ash-cloud reach values of several kilopascals.

In the head and the leading part of the body, a broad high pressure zone (10^1–10^2 Pa) occupies roughly the lower third of the ash-cloud. Within this zone, maximum pressures occur during passage of the central part of the head (c. 0.1–0.4 sec). However, this is followed by two additional high-pressure regions during passage of the rear of the head (c. 0.55–0.8 sec) and the frontal part of the body (c. 1.05–1.3 sec). These are associated with

local increases in velocity and particle concentration, respectively. The succession of several pulses of high dynamic pressure, separated by periods of lower pressure, could have important implications for the interpretation of PDC damage potential. For instance, the successive weakening and consequent failure of infrastructure hit by several pulses of dynamic pressure could be as high (or potentially exceed) the damage potential of a faster and/or more concentrated current that only has a single pressure high.

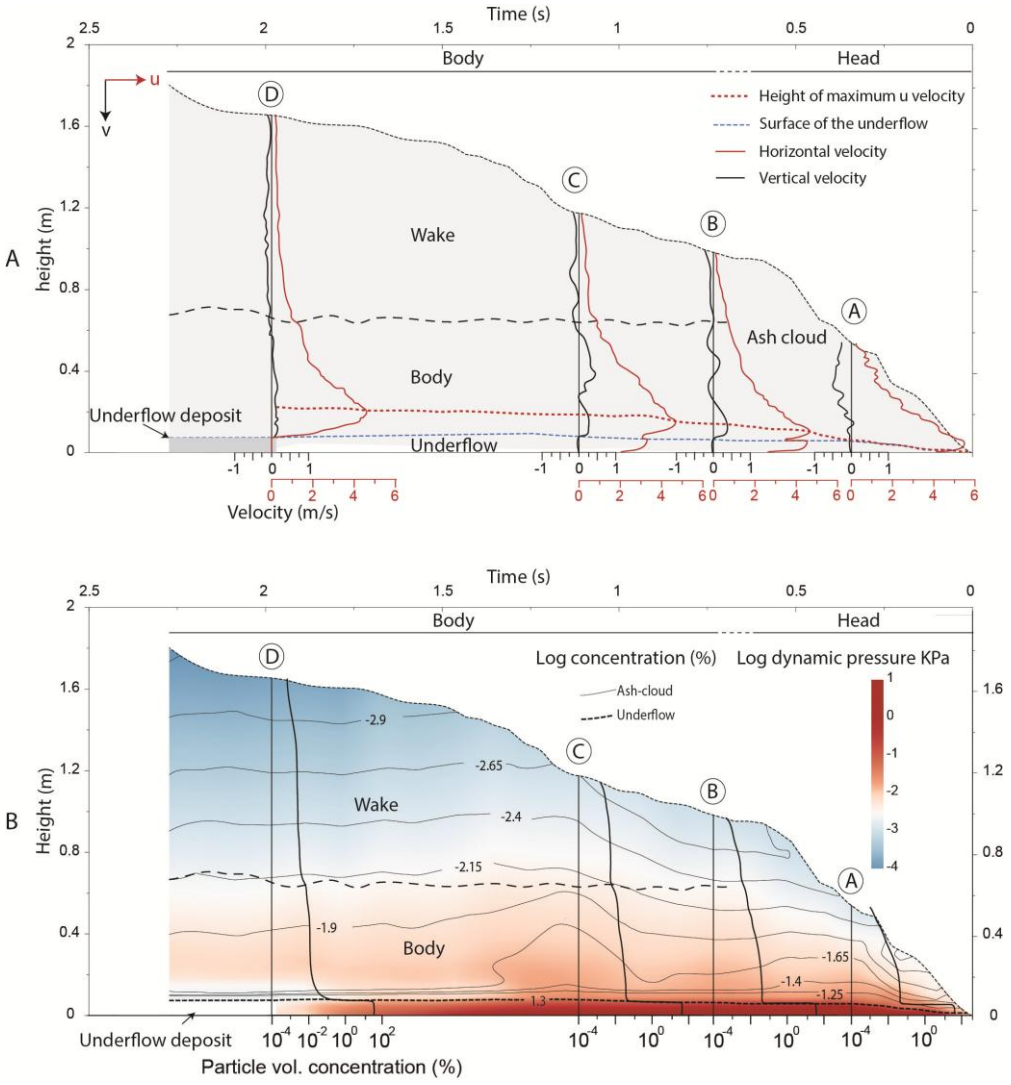

Fig. 4.8. Vertical distribution of densities and velocities at 11.7 m. A: Vertical velocity profiles of the vertical (black component) and horizontal component (red). B: Logarithmic concentration isolines and dynamic pressure map. Vertical concentration profiles are indicated in black. Note the three pulses of dynamic pressures. The first two are within the head, while the last occurs rearwards of the head.

4.3.6 Multiphase transport

Finally, I take a closer look into the characteristics of gas-particle transport regimes in the PDC ash-cloud region. These can be characterised through the Stokes number and the Stability number (Burgisser and Bergantz, 2002). The Stokes number is a measure of coupling between solid and fluid phases, and compares two time-scales of turbulent transport; the response time of particles forced by unsteady motion, and the time-scale of fluid rotation within an eddy. It is defined as:

$$S_T = \frac{U_T \Delta U_i}{g\delta}$$

where U_T is the terminal fall velocity, ΔU_i is the eddy rotation velocity, g gravitational acceleration and δ is the eddy diameter. Generally, $S_T < 1$ implies coupled transport and $S_T > 1$ uncoupled motion between particles and fluid. The Stability number is a measure of the residence time of particles within an eddy and it is used to evaluate the tendency of particles to either remain in turbulent suspension or sediment downwards. The Stability number is defined as the ratio of the theoretical terminal particle fall velocity and the maximum eddy rotational speed as:

$$\Sigma_T = \frac{U_T}{\Delta U_i}$$

Generally, $\Sigma_T < 1$ defines suspension and $\Sigma_T > 1$ defines sedimentation.

In combination, Stokes and Stability numbers define five main regimes of contrasting turbulent gas-particle transport and Burgisser and Bergantz (2002) demarcated the tentative boundaries between them: (I) $S_T \geq 1$ and $\Sigma_T < 3.16$ defines the intermediately turbulent regime associated with the development of mesoscale clusters and/or with particles unrolling

from eddies or migrating to eddy peripheries resulting in strongly asymmetric transport of decoupled and coupled particles; (II) for $S_T < 1$ and $\Sigma_T \geq 0.3$, the flow is within the fully turbulent regime characterised by turbulent sedimentation of particles resulting in fast sedimentation of heavy particles due to centrifugal forces in eddies and delayed sedimentation of lighter particles caught in vorticies; (III) for S_T 0.1–1 and Σ_T 0.1–0.3, the flow enters the fully turbulent regime, which is transient between turbulent sedimentation and homogeneous suspension; (IV) with $S_T < 0.1$ and $\Sigma_T < 0.3$, the flow is within the fully turbulent regime characterised by homogeneous and well-coupled particles and gas phases; and (V) when $S_T > 1$ and $\Sigma_T \geq 3.16$, the flow is within the fall regime of fully decoupled particle motion where sedimentation of particles is dominant.

For experiments with a variety of channel slopes (9–19°) and at the three different observer locations (3.1 m, 8.5 m and 11.7 m from source), I used the grain-size distribution of flow samples (supplementary Fig. 4.1) and estimates of δ, ΔU_i and U_T to compute pairs of Stokes and Stability numbers at regular height and time intervals in the passing ash-cloud.

As anticipated from bulk flow scaling analyses (Lube et al. 2015), the ash-cloud occupies a wide field of transport regimes (Fig. 4.9). This shows a roughly positive correlation between Stokes and Stability numbers across the turbulent gas-particle transport (TGPT) regimes I-IV of fully coupled to partially coupled and suspended to turbulently sedimenting transport. However, along the entire runout length, fully decoupled transport of the postulated TGPT fall regime does not occur for any broad grain-size distribution transported. Only rarely observed isolated large pumices falling as ballistics through the mixture satisfy this condition.

The head shows the greatest variety in TGPT behaviour across regimes I–IV (Fig. 4.9A). These regimes are strongly vertically zoned from TGPT I at the base with abundant dendritic mesoscale clusters through TGPT IV in the upper head region with fully-coupled transport

(Fig. 4.10B). In regime I, the reduced particle drag in mesoscale turbulence leads to extreme sedimentation rates that feed the frontal part of the underflow (Breard et al. 2015). Proximally, regime I can occupy at least one third of the depth of the ash-cloud, but with subsequent sedimentation and dilution downstream, this zone shrinks and finally disappears in distal reaches (Fig. 4.10C).

The ash-cloud body shows a considerably narrower range of TGPT regimes than the head (Fig. 9B). This includes a thin zone above the underflow of turbulent sedimentation (TGPT II), above a broad zone of transient transport (TGPT III), which occupies the majority of the body depth (Fig. 10B and C). Homogeneous fully coupled gas-particle transport (TGPT IV) only occurs close to the body/wake boundary. Overall this makes the body a very stable zone of turbulent gas-particle transport, where particles settling out of turbulent suspension are much slower than in the head.

Particles in the ash-cloud wake are almost solely transported in homogeneous suspensions with well-coupled gas and particle phases (TGPT IV; Fig. 9C and 10B and C). The small size and narrow range of transported particle sizes in the wake favours this regime and stems from constant feeding through Kelvin Helmholtz instabilities from the rear of the head and the upper part of the body.

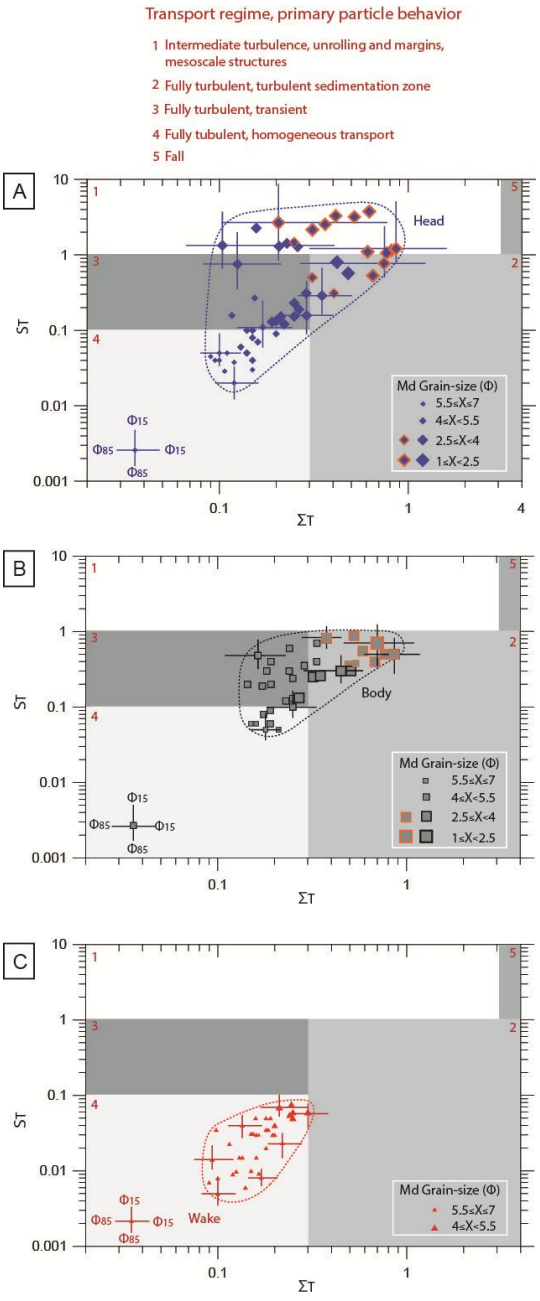

Fig. 4.9. Transport regimes for the head, body and wake in experimental flows. Stokes (ST) and Stability ΣT non-dimensional numbers of the local median grain-size transported within the head (A), body (B) and wake (C). ST and ΣT describe the degree of coupling of the solid and gas and also the particle residence time within largest eddies respectively. Median grain-size is indicated by the size of the symbols. Symbols with an orange rim represent near-bed measurements in the lower 5-10% of the total flow thickness. Arrows indicate the 15th and 85th percentiles of the distribution. Fields from 1 to 5 are indicated in shades of grey with red numbers referring to respective transport regimes described atop the figure.

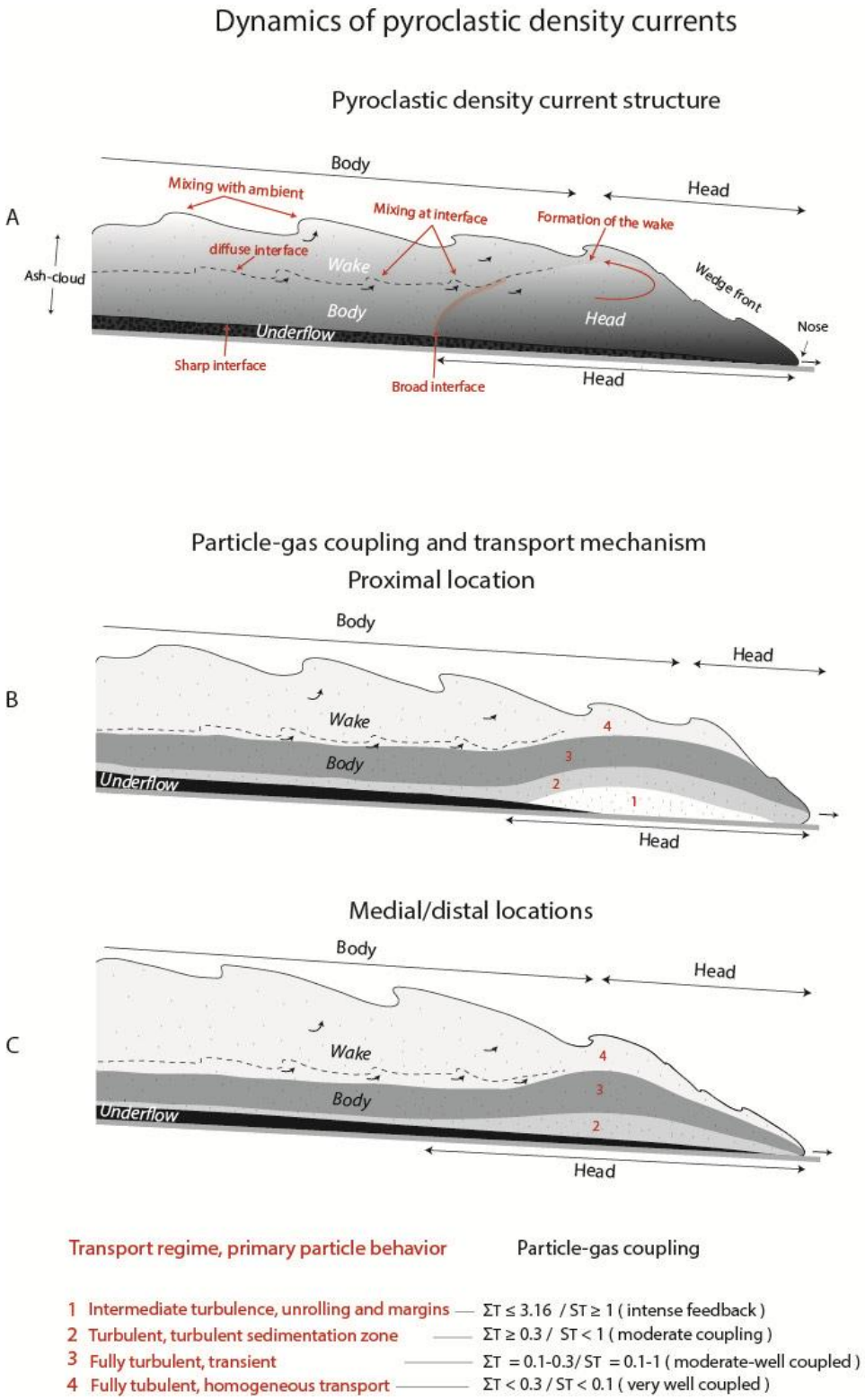

Fig. 4.10. Schematic diagram of PDC vertical and longitudinal structure. A: Generalized structure of a PDC with underflow and ash-cloud with highlight on the form and formation of the head, body and wake zones. B: Particle transport regimes in proximal PDCs, where the underflow lags behind the front. C: Particle transport regimes in medial and distal PDCs where the underflow is well present inside the head of the ash-cloud. Note the lengthening of the head and evolution of the front shape.

4.4. Discussion

4.4.1. The PDC structure

The large-scale outer features of our experimental PDCs with the occurrence of the ash-cloud head, body and wake regions are broadly similar to that of dilute gravity currents. The internal structure, in addition and largely due to the presence of an underflow, differs strongly from the dilute gravity current end-member analogue.

The non-turbulent/turbulent boundary between the underflow and ash-cloud regions is characterised by a strong reduction in particle concentration by 2–3 orders of magnitude. This bipartite vertical structure is characteristic for the flow evolution from proximal to distal reaches, and a hypothesized natural spectrum or continuous vertical gradation of particle concentration within PDCs (c.f. Branney and Kokelaar, 2002) does not occur. However, for a significant proportion of the flow, and unlike the speculation in earlier bipartite PDC models, the concentration boundary does not act as a strong rheological boundary. Particularly in the head and frontal body regions, this is signified through smooth velocity profiles across the dense/dilute boundary with extremely low shear. This implies low interfacial friction contrasting with a highly viscous and dissipative boundary assumed in current PDC multiphase models (e.g. Esposti Ongaro et al., 2012). Part of the reason for the smooth rheological boundary may reside in the ultra-low friction of the underflow (Lube and Breard et al., 2015) bordering against a possibly also low-friction regime in the lower ash-cloud above. This is suggested through observation of large amounts of air entrapped in the lowermost ash-cloud, which becomes buried by extremely fast settling particles in mesoscale clusters (see also Breard et al. 2015).

4.4.2. Coupled underflow/ash-cloud motion

The coupled motion of underflow and ash-cloud regions controls the velocity and density structure of the ash-cloud to depart strongly from measured and theoretical laws of dilute gravity currents. I have demonstrated the existence of four principle forms of vertical velocity profiles and two different forms of density profiles, which are dependent on the degree of coupling and traction between the ash-cloud and underflow regions.

The effects of coupling are strongest during regime 2 of perfect kinematic coupling of the underflow with the head and frontal body regions. Here the underflow becomes the boundary layer of the PDC and a (classic) inner turbulent boundary layer in the ash-cloud disappears. This coupled motion of the ash-cloud on top of a fast moving carrier current allows the head to propagate as a thin and fast (supercritical) flow. However, this occurs without the strong entrainment expected from a normal supercritical gravity current because the high-shear, high-turbulent, and hence highly entraining, inner boundary layer is non-existent. I call this behaviour *forced super-criticality*. I also suggest that the underlying coupling mechanism becomes a second important driver of PDC motion in addition to the density contrast between the ash-cloud and the ambient air. This process also offers a different view onto the hazard potential of natural PDCs where supercritical fronts are often observed. Current PDC models based on a dilute gravity current analogy predict that supercritical flow conditions lead to strong entrainment, consequently strong dilution and low runout distances resulting in spatially restricted damage potential (e.g. Bursik and Woods, 1996). Quite the opposite will occur in forced supercritical PDCs, where moderate entrainment delays sedimentation and dilution to allow fast and long flowing currents with a significant sediment cargo and hence high dynamic pressure to endure.

During passage of the body, when moderate traction between underflow and ash-cloud regions develops (regime 3), the still strong coupling only allows for a relatively thin turbulent boundary layer to develop in the ash-cloud. Together with the wake shielding entrainment of ambient air into the body, this maintains (forced) super-criticality in the body for most of the flow duration.

4.4.3. Gas-particle transport

The great majority of mass transport in PDCs occurs in the underflow. Qualitative models of column-collapse derived PDCs envisage a process of 'deflation' by which a dilute current can continuously sediment its basal underflow over its entire runout length (Wohletz and Sheridan, 1979). In our experiments, the main process of mass transfer from the ash-cloud onto the underflow is through fast sedimentation of mesoscale clusters in TGPT regime I. This regime is favoured in fast currents under high particle concentrations. It thus occurs predominantly proximally and immediately after 'eruption-column' impact, where the expanding ash-cloud has concentrations that range between 10^{-1}–10^{0} vol%. Because of the strong reduction of particle drag in mesoscale clusters, sedimentation rates are very high with particle settling velocities approaching the theoretical terminal fall velocity in pure air (Fig 3D, see also Breard et al. 2015). In medial and distal reaches, high sedimentation rates through fast settling mesoscale structures only occur in the lower head and lower frontal part of the body. Breard et al. (2015) has demonstrated that this leads to the continuous growth of the frontal underflow during PDC runout.

Burgisser and Bergantz (2002) hypothesized that underflows accrete by the settling of fully decoupled particles in the TGPT fall regime V, but this is unlikely. The median grain-size diameter of underflow deposits can vary from approximately 125 µm to 8 mm (Walker,

1983). However, fully decoupled settling of particles of this size-range requires very low flow velocities; i.e. 0.7–1 m s^{-1} (for ash-sized particles) or 8–12 m s^{-1} (for lapilli). These velocities are clearly too low for typical PDC speeds in proximal to medial reaches.

However, fully decoupled settling at realistic PDC flow velocities is likely to occur for block-sized particles (e.g. 25–40 m s^{-1} for particles with diameters of 64 mm). I suggest that this process is likely to contribute to the formation of coarse-grained lag-breccia deposits of PDCs. Thus, the median grain-size of lag-breccia deposits could be used to estimate local PDC velocities.

The type and range of gas-particle transport regimes differs strongly between the segregated PDC regions. As a result, each region transports a different and limited range of particle sizes and densities. This leads to strong contrasts in the deposition time-scales and grain-size distributions emplaced by each PDC region (Breard et al., 2015). The ash-cloud head is the main driver of the spatial separation of particles with different settling characteristics and it thereby also controls the mass transfer from the head into underflow and wake regions.

The efficiency of this spatial separation of particles is largely controlled by the high velocity of the head and its kinematic coupling with the underflow. The high velocity results in a strong transport capacity for a broad range of particle grain-sizes and densities. Often, the Stokes and Stability numbers of the fine tail of the grain-size distribution fall into a different transport regime than the corresponding values for the coarse tail (Fig. 9A). This implies a local co-existence of different gas-particle transport regimes (in particular TGPT I, II and III). Fine-ash particles that are relatively well-coupled with the gas phase remain transported inside individual eddies for long times. Coarser and heavier particles efficiently migrate to the outer and lower eddy peripheries, where they will tend to unroll from eddy margins to settle into lower, more intensely downward settling and generally less well-coupled regions.

The kinematic coupling of the head with the underflow facilitates the particle separation process on a large scale. Like a conveyer belt, the coupling constitutes a major driver for the large, anticlockwise-rotating head vortex, which revolves much more vigorously than in a dilute gravity current with no-slip. The vortex rotation dictates the large-scale gas-particle transport paths and repeatedly circulates particles through all four TGPT regimes. In the lower part of the head (TGPT I), sedimentation of a wide range of grain-sizes in fast settling mesoscale clusters onto the top of the underflow accelerates the head dilution. Further up, where TGPT II dominates, turbulent settling of heavy particles will be fast-tracked, while settling of lighter particles is delayed because they remain caught in eddies, where they may endure subsequent vortex rotations. Multiple vortex rotations thus "sieve' particles in eddies by settling characteristics. This results in eddies with an increasingly narrower and finer grain-size distribution that eventually separate from the head in large K-H instabilities to feed the ash-cloud wake.

4.5. Conclusion

Large-scale PDC experiments of particles and gas show major differences in internal structure and gas-particle transport to dilute gravity currents. Fast proximal sedimentation of an underflow through mesoscale clusters creates a strong density interface between underflow and ash-cloud regions that sustain long flow runout. This contrasts with the previous hypothesis of a continuous spectrum between dense and dilute end-member flow regimes. Kinematic coupling between the underflow and ash-cloud region strongly controls the velocity and density structure of the ash-cloud and leads to forced super-criticality of the ash-cloud. The experiments demonstrate the existence of a previously hypothesized wide

range of gas-particle transport behaviours that span from poorly coupled, fast-sedimenting regimes to homogeneously coupled and long-suspended regimes.

4.6. Supplementary material

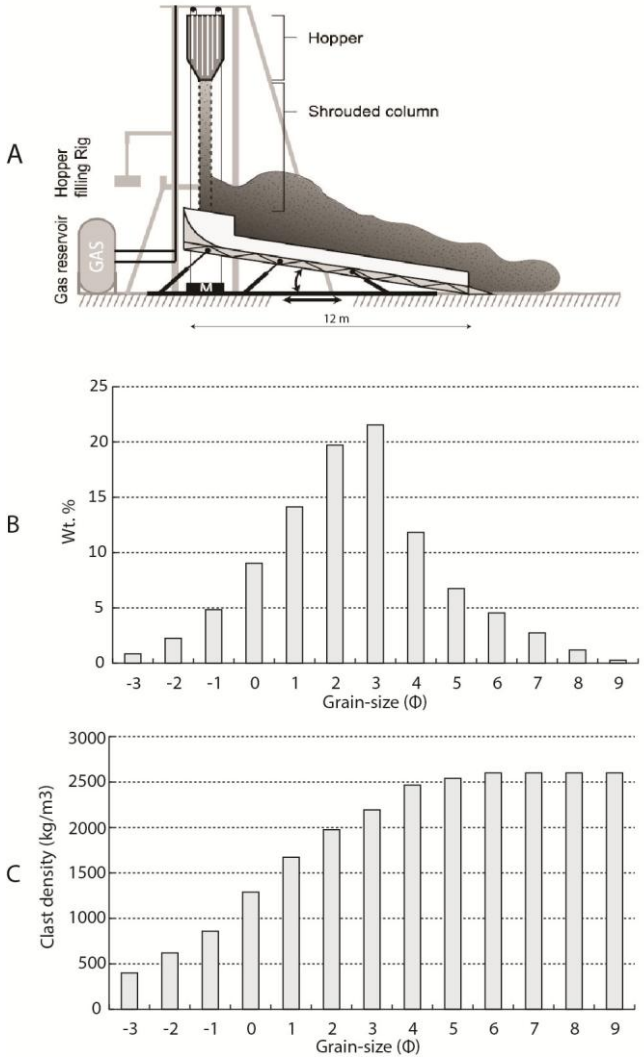

Supplementary Fig. 4.1. Experimental setup and grain-size characteristics. A: Sketch of PELE setup. Note that in experiments presented in this paper, no Supplementary gas was added to the mixture. B: Unimodal grain-size distribution of the initial mixture. C: Density distribution of the experimental mixture.

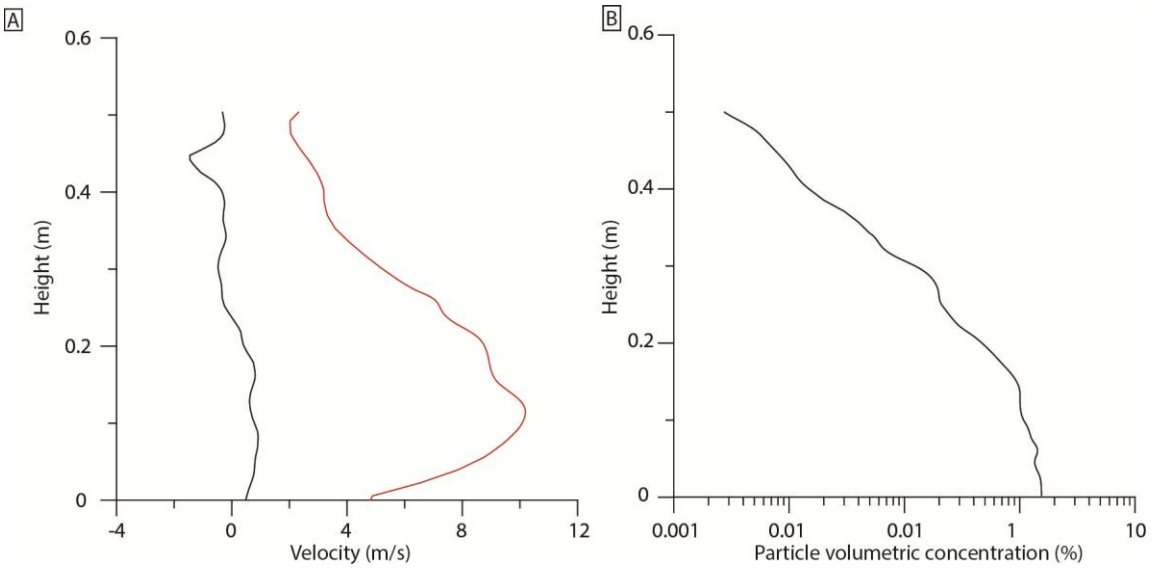

Supplementary Fig. 4.2. Velocity and concentration profile in the frontal part of the head prior arrival of the underflow at 3.1 m from source. A: Horizontal and Vertical velocity profiles (black and red lines respectively). B: Concentration profile.

Parameter	Nature	PELE
Particle diameter (m)	10^{-6}–10^{-1}	10^{-6}–10^{-2}
Particle density (kg m^{-3})	300–2600	300–2600
Fluid density (kg m^{-3})	0.6–1.25	1-1.25
Dynamic viscosity of the carrier phase (kg m^{-1} s^{-1})	$1x10^{-5}$–$4x10^{-3}$	$1x10^{-5}$–$5x10^{-3}$
Flow velocity (m s^{-1})	10–200	<2–20
Reynolds number $Re = \frac{\rho U L}{\mu}$	$1x10^{4}$–$6.7x10^{9}$	$1.5x10^{4}$–$2x10^{6}$
Stokes number $S_T = \frac{1}{f}\frac{\Delta\rho D^2}{18\mu}\frac{\Delta U}{\delta}$	$1.1x10^{-3}$–$9.7x10^{7}$	$7.4x10^{-5}$–$4.6x10^{4}$
Stability number $\Sigma_T = \frac{S_T}{Fr^2} = \frac{\tau_v g}{f\Delta U} = \frac{U_T}{\Delta U}$	$2.8x10^{-6}$–$9.7x10^{9}$	$7.1x10^{-7}$–$4.6x10^{5}$
Particle Froude number $Fr = \frac{U}{\left[(\rho_p - \rho_g)gD\right]^{0.5}}$	0.1–20	0.3–10
Richardson number $Ri = \frac{(\rho - \rho_o)gH}{\rho_o U^2}$	$2x10^{-4}$(-$5x10^{0}$*) – $1.1x10^{1}$	$1x10^{-3}$–$4.5x10^{1}$

Supplementary Table 4.1. Bulk flow scaling of natural dilute PDCs (Burgisser and Bergantz, 2005) and PELE experimental currents. Where U and L are characteristic velocity and length scales of the flow. μ corresponds to the dynamic viscosity of the flow. ρ is the mixture density. ρ is the flow density and ρ_o is the ambient medium density. D is the particle diameter. * Estimates of the range of negative values of the Richardson number corresponding to hot PDCs with buoyancy reversal is based on the study of volcanic plume (Carazzo et al., 2015) and PDCs (Dufek, 2016).

Parameter	Nature	PELE
Particle diameter (m)	10^{-6}–10^{-1}	10^{-6}–10^{-2}
Particle density (kg m^{-3})	300–2600	300–2600
Fluid density (kg m^{-3})	0.6–1.25	1-1.25
Particle volumetric concentration	30–60 %	40–60 %
Dynamic viscosity of the fluid (kg m^{-1}s^{-1})	1x10^{-5}–4x10^{-5}	1x10^{-5}–3x10^{-5}
Underflow velocity (m s^{-1})	10-30	<2–15
Bagnold number	1x10^{-2}–1x10^{2}	1x10^{0}–1x10^{2}
$Ba = \frac{c^* \rho_p \dot{\gamma} D^2}{\mu_g}$		
With $c^* = \left[c^{\frac{1}{3}}/(c_0{}^{\frac{1}{3}} - c^{\frac{1}{3}})\right]^{1/2}$		
Darcy number	1x10^{2}–1x10^{4}	1x10^{0}–1x10^{3}
$Da = \frac{\rho_g}{\rho_s}\frac{D^2}{Re_p kc}$		
Froude number	1.6–9.6	1.5–6.2
$Fr = \frac{U}{\left[(\rho_p - \rho_g)gD\right]^{0.5}}$		
Savage number	1x10^{-9}–1x10^{-7}	1x10^{-6}–1x10^{-5}
$Sa = \frac{\rho_p \dot{\gamma} D^2}{(\rho_p - \rho_g)gh_c}$		

Supplementary Table 4.2. Underflow scaling of natural PDCs (Roche et al., 2012) and PELE experimental currents. Where ρ_p and ρ_g the particle and gas density, $\dot{\gamma}$ the shear rate, μ_g the gas dynamic viscosity, D the particle diameter, h_c the current height, g the acceleration of gravity. c denotes the flow concentration during propagation, c_o is the maximum concentration at loose packing, γ is the shear rate. $\underline{k}$ is the permeability of the granular medium. Re_p is the particle Reynolds number defined as follows: $Re_p = 2DU\rho_s / \mu$.

Chapter 5 – Dynamics of the PDC frontal region – The influence of underflow and ash-cloud interactions on the head kinematics and structure

Chapter contents

This Chapter is based on a paper submitted to Journal of Geophysical Research.

Participating authors:

Eric C. P. Breard (designed and undertook the experiments, collected and analysed the data, interpreted them and wrote the manuscript).

Gert Lube (conducted experiments with ECPB, manuscript editing and discussion)

Chapter 5 – Dynamics of the PDC frontal region – the influence of underflow and ash-cloud interactions on the head kinematics and structure

5.1 Introduction

Pyroclastic density currents are gravity-driven hot gas-particle flows that are able to inundate and bury wide areas (Druitt, 1998; Sulpizio and Dellino, 2008). The lethal character of these flows results from high temperatures and high-dynamic pressures (Valentine, 1998; Baxter et al., 2005) that makes it impossible to either measure or observe the flows internally (Sulpizio et al., 2014). Uncertainties about the internal velocity and density stratification prevent direct estimates of the destruction potential of PDCs. Instead, researchers are reliant upon assumptions of the density and dynamic pressure from destruction patterns to infer the internal flow dynamics. However, these estimates cannot be verified because of the lack of direct measurements (Dellino et al., 2008; Jenkins et al., 2013).

Our knowledge of the dynamics of PDCs has developed considerably with understanding of the physics of dilute and fully turbulent gravity currents (Dade and Huppert, 1995; Dade and Huppert, 1996; Bursik and Woods, 1996). Gravity currents have been widely studied in laboratory experiments through continuous (Britter and Simpson, 1978; García and Parsons, 1996; Cenedece and Adduce, 2008; Sequeiros et al., 2009b; Gerber, 2011) and instantaneous (Huppert and Simpson, 1980; Hacker et al., 1996; Marino et al., 2005; Lombardi et al., 2015) releases of a fluid into another "ambient" fluid of lower density. In these situations, the horizontal difference in buoyancy of the two contacting fluids is the main driving force for the motion into opposite directions (Hallworth et al., 1993; Shin et al., 2004; Zhu et al., 2006).

Based on detailed observations and measurements of these experimental gravity currents, a strong foundation of analytical, empirical and numerical models was established to quantify their structure and runout dynamics (e.g. Simpson 1982; Huppert 2006). A great success of these models has been in their application to predicting a wide range of natural gravity currents, including turbidity currents (Parker et al., 1987; Cantero et al., 2012), snow avalanches (Rastello and Hopfinger, 2004), atmospheric currents (Simpson, 1982), and pyroclastic density currents (Sparks et al., 1978a; Dade and Huppert, 1996).

Pyroclastic density currents are arguably the most complex gravity currents of all because of the extremely wide range of particle sizes, bulk flow densities and velocities they encompass (Sparks, 1976; Fisher, 1979; Druitt, 1998). Traditionally, the occurrence of two main types of PDC deposits with contrasting deposit geometries and sedimentary characteristics has led to the inference of a two end-member transport regime (Freundt and Bursik, 1998; Wohletz, 1998; Freundt et al., 2000), where the end-members are described known as dilute PDCs (also pyroclastic surges) and concentrated PDCs (also called pyroclastic flows). Dilute PDCs with bulk concentrations of typically less than one volume percent are thought to share strong structural and behavioural similarity with dilute gravity currents, including a strong, but continuous vertical stratification in density and velocity (Valentine, 1987). Concentrated PDCs are known to be composed of a basal underflow of high bulk density (with typical volume fractions of particles relative to air above one and up to several tens of percent) and an overriding dilute ash-cloud (with a bulk concentration of typically much less than one percent). However, no direct observations exist on how the underflow and ash-cloud regions are structurally linked, and whether and how they interact during PDC transport (Branney and Kokelaar, 2002). Current theoretical models conceptualise either a continuous gradation in density between ash-cloud and underflow, or the existence of a strong internal boundary between the two regions with major jumps in density, rheology and turbulence (Doyle et al.,

2010; Dufek et al., 2015). Recent, large-scale experiments that synthesized concentrated PDCs with basal underflow and overriding ash-cloud regions have offered further insights into this problem. These experiments demonstrated that a continuous vertical density stratification from the dilute upper ash-cloud to the dense underflow is absent. Instead, a marked internal interface separates the two regions and is characterised by strong jumps in flow density, turbulence intensity and the dominant type of gas-particle interaction (Chapters 3 and 4). Furthermore, it was demonstrated that there are four principle forms of vertical velocity profiles, which are dependent on the degree of coupling and related traction between the ash-cloud and underflow regions (Chapter 4).

The current chapter aims at gaining further insights on the interaction between underflow and ash-cloud regions through large-scale experiments. In particular, I aim at answering the following questions: what are the qualitative and quantitative effects of the underflow on the frontal velocity of PDCs and what are the similarities and differences of the internal head geometry and structure compared with other gravity currents?

5.2. Methods

5.2.1 Producing PDC in large-scale experiments

Experimental pyroclastic density currents were generated by column collapse at the eruption generator PELE (fully described in Lube et al., 2015). Located inside a disused boiler house at Massey University (NZ), PELE is an experimental setup that synthesizes PDCs scaled from dense to dilute end-members (supplementary Tables 5.1 and 5.2). Experiments involved the release of 1.5 tonnes of natural pyroclastic material collected from the AD 232 ignimbrite near Taupo. The experimental volcanic mixture was a blend of two different deposits of the AD 232 Taupo Ignimbrite (Hogg et al., 2012). The mixture had a unimodal grain-size

distribution with a median diameter of ~250 µm, an average clast density of 1950 kg m^{-3}, and contained 10 wt.% of very fine ash material (particles <63 µm) (supplementary Fig. 5.1).

Particle-gas suspensions were released from a hopper and accelerated during free fall down a shrouded vertical section before collapsing onto an instrumented channel section. After collapse, the mixture formed a density current that flowed along the inclinable, 12 m long, 0.5 m wide and 0.6 m high rectangular channel section composed of one side of glass windows. After 12 m of runout, flows propagated further onto an unconfined, horizontal runout section that extended outside the boiler house (Fig. 5.1). All experiments were conducted at ambient temperature of c.15 ° Celsius. Please see Lube et al. (2015) for a detailed description of the experimental set-up, including the experimental control of initial and boundary conditions.

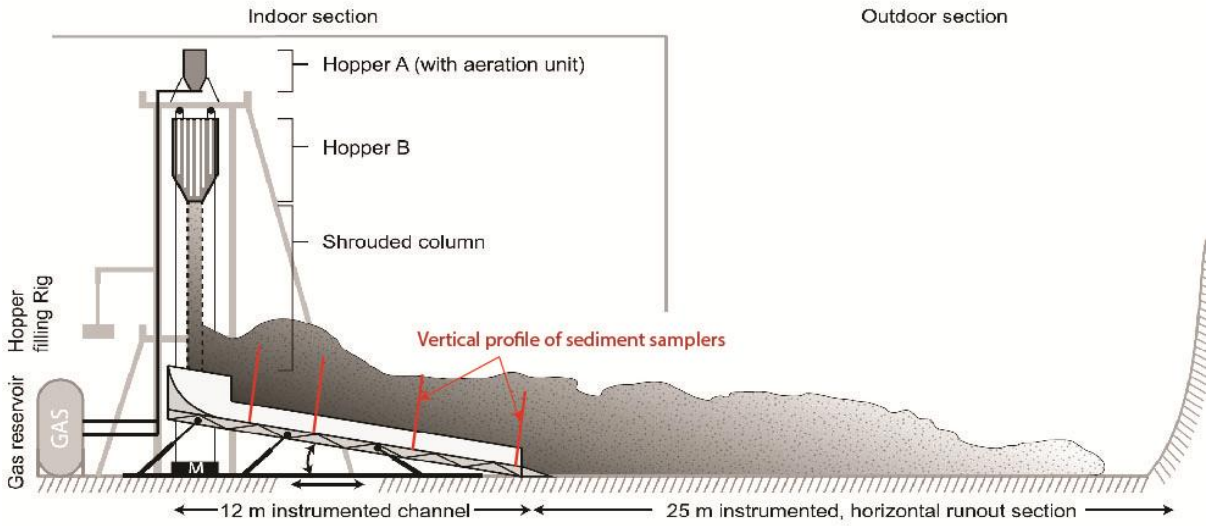

Fig. 5.1. Large-scale experimental setup and location of the sediment samplers at 3.1, 5.4, 8.5 and 11.7 m from source. Note that the experiment presented in this chapter only involved the large hopper B.

While the grain-size distribution of the initial mixture and the hopper discharge rate (=890 kg s^{-1}) were invariant for all experiments, the channel inclination and the drop height were varied. The initial and boundary experimental conditions are summarized in Table 5.1. By

varying the channel inclination (9–19°) and the drop height on which the impact velocity (2.5–5 m) and concentration are dependent, a range of velocities of 7–10 m s^{-1} and particle volume concentrations (7.5–10.7 vol.%) at impact with the channel were reached (Lube et al., 2015). A further set of experiments involved keeping the drop height constant while the inclination of the channel was varied. Note that due to the time-consuming nature and complexity of the large-scale experiments, the number of experiments that were undertaken was limited and the ranges of the initial conditions were chosen accordingly.

The present study focuses on the observation and measurement of the flow head region in the first 12 m of runout of the experimental PDCs. Over this runout length, measurements of the outer shape and the internal structure of the gravity current head were obtained to determine how these components of the PDC are related.

Experiment #	**Channel inclination (°)**	**Drop height (m)**	**Impact velocity (m s^{-1})**	**Particle concentration at impact (vol.%)**
1	9	5	9.8	7.5
2	9	2.5	7	10.7
3	15	4	8.8	8.4
4	15	2.5	7	10.7
5	19	3	7.5	9.7
6	19	2.5	7	10.7

Table 5.1. Experimental variables and resulting initial flow conditions at impact for the six different experiments. Impact velocities were measured from high-speed video footage, while the impact particle concentrations were estimated following the method of Lube et al., (2015).

5.2.2 Sensors and analytical methods

The experimental PDCs were recorded from a wide range of viewing angles with 2 high-speed cameras shooting at 600-1000 frames per second, and 4 other cameras recording the flow passage at 24-240 frames per second.

Vertical velocity profiles of the experimental currents at various runout distances along the channel (3.1 m, 10.4 m , 11.7 m) were computed from high-speed videos via particle-image-velocimetry (PIV) using the software PIVlab (Thielicke and Stamhuis 2014). These profiles included both the dense underflow and dilute ash-cloud parts of the flows. Prior to the image analysis, raw images were filtered to enhance the PIV (Stamhuis, 2006) with contrast-limited adaptive histogram equalization and the Wiener denoise algorithm implemented in PIVlab.

Vertical particle concentration profiles of the ash-cloud were also obtained at these runout distances using an optical method. This method makes use of an empirical relationship between the local median gray-scale of high-speed images and the local particles volume concentration. The validity of the empirical relationship and the minimum range of quantifiable concentrations (c. 10^{-5}–10^{1} %) were confirmed through direct measurements of the time-variant mixture density (Chapters 2 and 4). The empirical relationship takes the form of a power law, where the concentration C_p is obtained from the median gray-scale Md(gray) from the following law: $C_p = a x Md(gray)^k$ with *a* being an experimentally determined constant of $5x10^{-8}$, while *k* is dependent on the background illumination and requires calibration. The calibration of the *k* value is described as follows. After the experiment, the time-integrated sediment mass m_m captured by passive flow samplers was weighted. By measuring, at the height of the sampler, the time-variant velocity and median gray-scale (which can be converted into a concentration C_p ($C_p = a x Md(gray)^k$) using an assumed value of *k*), the

integration of the mass flow rate between the arrival of the flow at t_0 and the final stage at t_f gives an estimated mass in the sampler equivalent to m_e:

$$\int_{t_0}^{t_f} v * A * C_p * \rho_p = mass\ of\ sediment\ collected\ in\ sampler = m_e$$

where the particle solid density is ρ_p, the particle volume concentration is C_p, the sampler area is A and the velocity v. The exponent "k" is initially unknown, but it is determined by fitting the estimated mass m_e obtained through integration of the mass flow rate to the measured sediment mass m_m.

In order to test the accuracy of this method, I used time-variant measurements of the median grayscale (converted into particle concentrations) and velocity to obtain an estimate of the mass that was deposited in the tubes and found a very good agreement of 89–95% between the estimates and direct measurements of particle concentration.

Measurements of the head geometry and flow front velocity. The head geometry was measured from side-view images that first involved the manual correction of the distortion of the image with Adobe Photoshop® and subsequent measurements of the head length and height with Adobe Illustrator®.

Measurements of the position of the ash-cloud front as a function of time were collected from a combination of views (frontal and side-views) obtained from all cameras. Measurements of the time-variant position of the front of the underflow were derived from intermediate-speed and high-speed close-up shots that provided a visualization of the thin front.

5.3. Results

5.3.1 Outer flow kinematics

5.3.1.1 Outer appearance of experimental flows

Upon impact, the pyroclastic mixture accelerated, expanded and reached velocity maxima (of up to 25 m s^{-1}) during the proximal c. 2 m of runout. Over this distance, the mixture also rapidly segregated into a basal underflow and an overriding ash-cloud. The ash-cloud can be divided into head, body and wake regions (see Chapter 4 for definition of the different regions; Fig. 5.2A). Experimental PDCs synthesized with the initial parameters listed in Table 5.1 were always composed of an underflow and an ash-cloud (Fig. 5.2A and B). In all experiments, excluding experiment #2, the underflow and ash-cloud parts of the experimental flows propagated further than our observation window of 12 m. In experiment #2, with the lowest slope and initial drop height, the underflow came to a halt after c. 10 m of runout whereas the ash-cloud flowed farther.

The head is the most dynamic portion of the ash-cloud where the highest velocities were measured and where intense mass transfer occurred by feeding of the underflow front and the wake (See chapters 3 and 4). At the rear of the head, successive detachments of large anti-clockwise-rotating vortices led to the formation of the wake. The boundary between the head and the body was gradual rather than sharp and marked by a downstream decrease of the (depth-averaged) velocity to a relatively constant value (See Chapter 4).

The most prominent variable feature of the ash-cloud head was its outer shape, which ranged from a classical bulbous shape with a well-defined nose (Fig. 5.2C) to a wedge-shaped form with the near absence of a definable nose (Fig. 5.2B). This variation in shape appeared to be strongly related to the presence and position of the underflow within the ash-cloud head. A

wedge-shaped front formed solely when the underflow was located inside the head, whereas the head formed a bulbous front with a well-defined nose when devoid of underflow (Fig. 5.2B and C). Interestingly, natural PDCs also display both types of head shape (Fig. 5.2D and E).

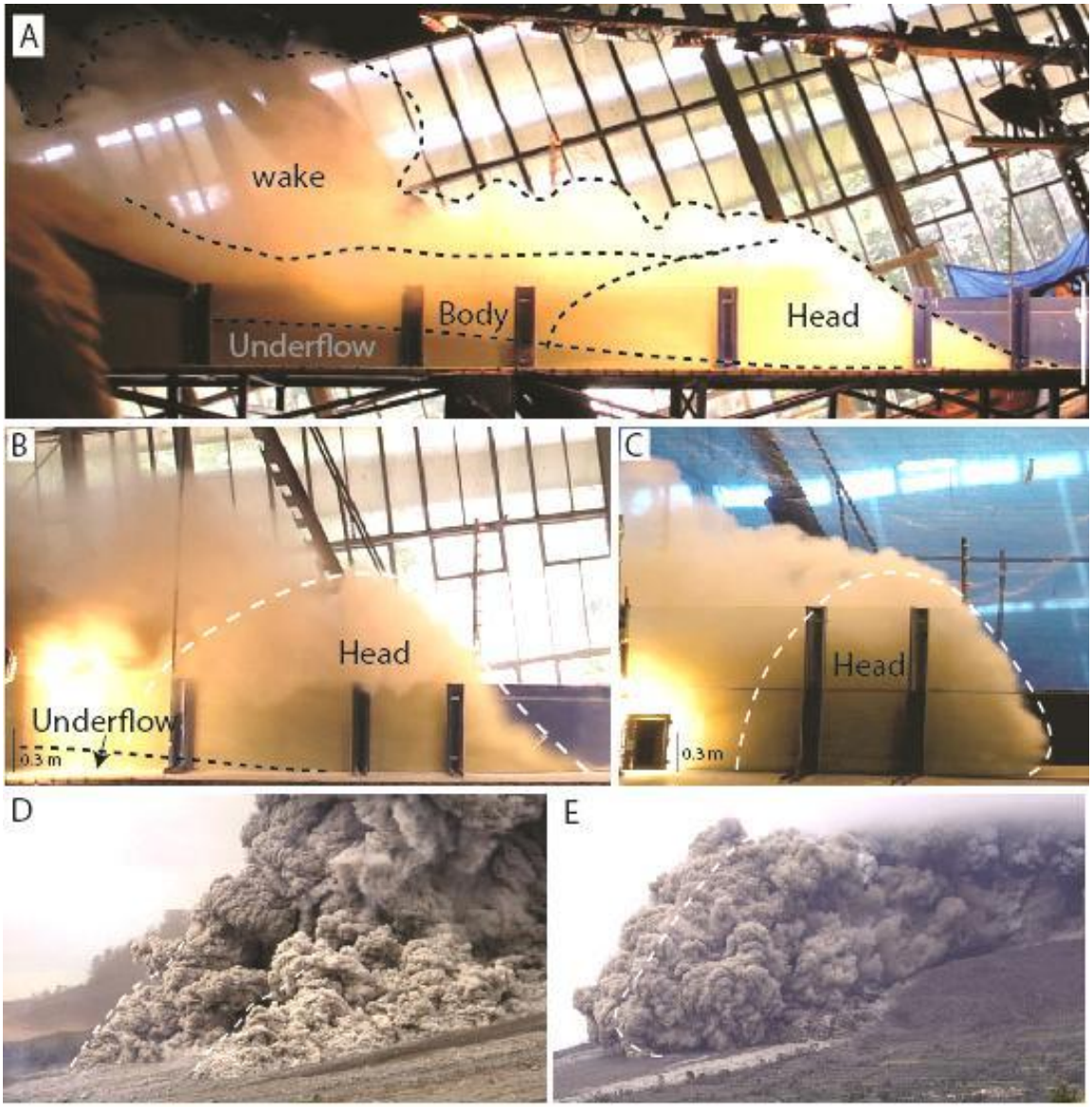

Fig. 5.2. Images of the experimental flows and photographs of natural PDCs. A: The PDC is composed of an ash-cloud head, body and wake overriding a concentrated underflow. Note the different shapes of the head. B: Experiment where a wedge-shaped front developed in the ash-cloud head. C: Experiment where the ash-cloud front took a bulbous shape. D: PDC with a well-developed wedge front at Sinabung volcano. Courtesy of Marc Szeglat. E: PDC with a bulbous front at Sinabung volcano, Indonesia. Courtesy of Bracken.

5.3.1.2 Kinematics data of the flow front

All experiments displayed similar overall behaviour of the flow front kinematics: a brief phase of initial acceleration after impact with the channel was followed by a phase of deceleration until the final stop. The most proximal measurements of the flow front velocity in the acceleration phase obtained at 2.5 m from source were 200–250% higher than the impact velocity. For a given slope, higher impact velocities led to higher velocities in the acceleration phase (Fig. 5.3). Furthermore, flows initiated over variable slopes, but with similar drop heights (=2.5 m) showed an inverse relationship of the velocity maximum during the acceleration phase and slope. After initial acceleration, flow front velocities declined strongly between 2–3 m from the impact point. Downstream of 2–3 m, further deceleration occurred, but at a lower rate.

Experiments on a 9° slope formed flows whose deceleration behaviours varied considerably with variable initial conditions. Flow front kinematic data of experiment #2 (drop height = 2.5 m) showed a stronger deceleration than for experiment #1 (drop height = 5). On a 15° slope for two experiments with different drop heights (=2.5 and 4m, experiments #3 and #4) the velocity maxima obtained during the initial acceleration phase also varied strongly by c. 4 m s^{-1} (Fig. 5.3A). The downstream deceleration behaviour, however was very similar for these experiments #3 and #4 (Fig. 5.3B). On the 19° slope, a small range of impact velocities (2.5–3 m) produced a narrow range of velocity maxima during the acceleration phase as well as very similar deceleration behaviours (Fig. 5.3C).

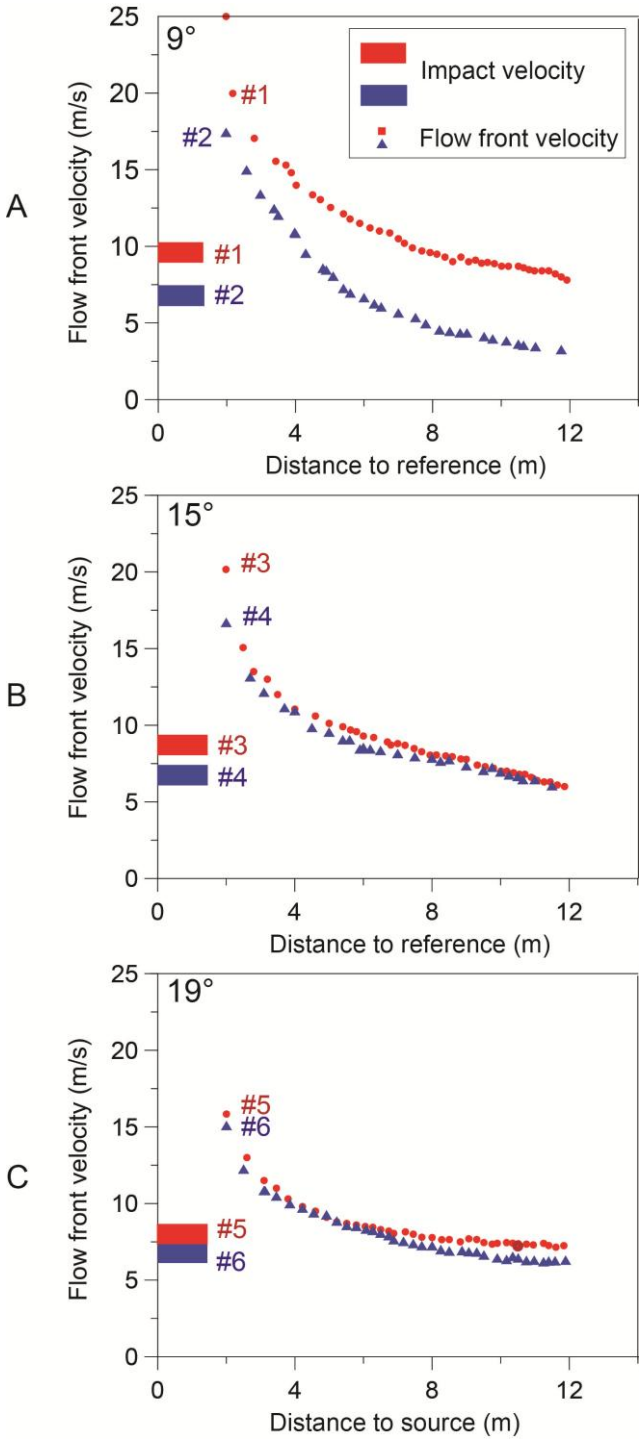

Fig. 5.3. Kinematic of the flow front. A: Flow front velocity on slopes of 19°, 15° (B) and 9° (C). Symbols for the different experimental runs (see number of experiment and experimental conditions in Table 5.1) are indicated by an insert in figure 5.3.A.

5.3.1.3 Kinematic data of the ash-cloud and underflow

The velocity of the underflow for the three experiments never exceeded the impact velocity (Fig. 5.4A–C), but instead declined nearly linearly with distance. The deceleration of the underflow front was high on the 9° slope in experiment #2 where the underflow stopped at 10 m from source (Fig. 5.4E), whereas the underflow decelerated more slowly in experiments on the 15° and 19° slopes (Fig. 5.4F and G). On the 15° and 19° slopes (#4 and 5#), the underflow decelerated slower than the ash-cloud, so that the underflow was faster than the ash-cloud after c.10 m of runout. On the 9° slope (#2) the ash-cloud was always faster than the fast decelerating underflow.

As a result of the difference in the deceleration rate of the ash-cloud and underflows, the relative position of the ash-cloud and underflow fronts varied with distance. The experiments may thus be grouped into three different scenarios: i) In experiment #2, the distance between the underflow and ash-cloud fronts increased over time (Fig. 5.4D). ii) In experiment #4 the distance between underflow and ash-cloud fronts remained relatively constant over the initial 12 m of runout (Fig. 5.4E). iii) In experiment # 5 the distance between underflow and ash-cloud fronts decreased over time and reached 0 at c. 11 m from source (Fig. 5.4F).

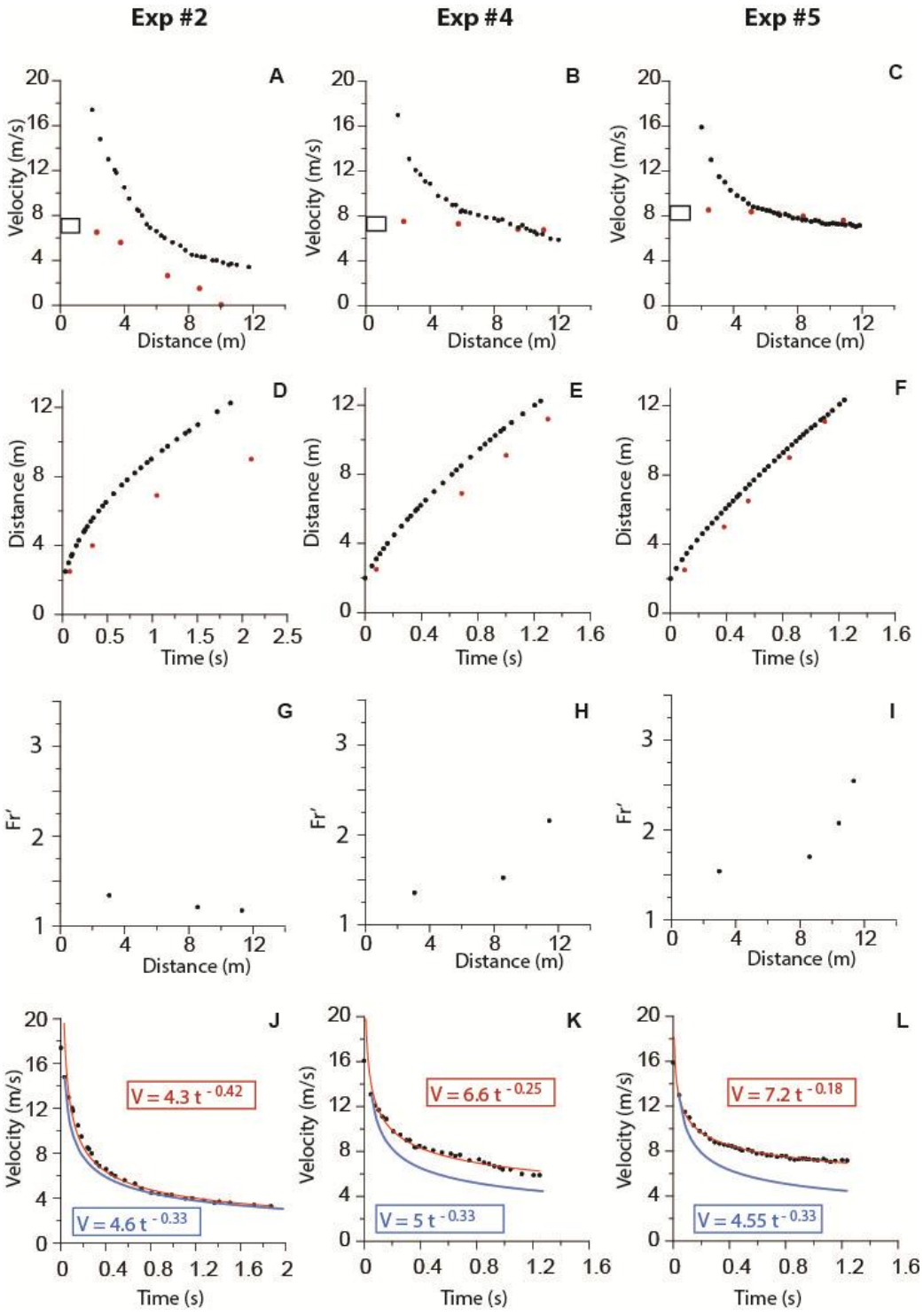

Fig. 5.4. Ash-cloud and underflow kinematics. A–C: Velocity of the ash-cloud front (black dots) and underflow (red dots) versus distance from source. D–F: Position of the ash-cloud (black) and underflow (red) fronts versus time. G–I: Densimetric Froude number Fr' of the head at different observation points along the channel. J–L: Velocity of the ash-cloud front with time. The red curve is a best fit regression, whereas the blue curve is the theoretical fit of the flow front velocity of planar gravity currents assuming a constant densimetric Froude number (Huppert and Simpson, 1980).

5.3.1.4 Densimetric Froude number of the ash-cloud head

The non-dimensional densimetric head Froude number, Fr', is the ratio of flow inertial to buoyancy forces, calculated as follows:

$$Fr' = \frac{Uf}{\sqrt{\frac{g(\rho-\rho_o)}{\rho_o} h\, cos(\theta)}} \qquad (5.1)$$

Cos θ accounts for the effect of the slope θ (Wells et al. 2010). *Uf* is the flow front velocity, ρ and ρ_o are the flow and ambient density respectively. *h* is the height of the ash-cloud over which the density is averaged. The location of the maximum height is found by locating the formation of the wake (concentration profile jump as seen in Chapter 4). From that point upstream the flow thickness increases, whereas downstream, the flow thickness decreases. θ is the slope angle to the horizontal. ρ was taken as the depth averaged density in the middle of the head, where *h* is at a maximum .

The densimetric Froude number (Fr') of the ash-cloud head was time-variant and spanned a range of 1 to 2.5 (Fig. 5.4). In experiment #2 the ash-cloud tended to a critical behaviour, where Fr' decreased from 1.4 to 1.2. In experiments #4 and #5, the ash-cloud head had a supercritical-Fr', that increased with distance from values of 1.3–1.5 to 2.2–3.

The asymptotic deceleration behaviour of dilute gravity currents is well known and predicted by the balance of inertial and buoyancy forces during the *inertial phase* (Fr'~1, Huppert and Simpson, 1980). During the inertial phase, the time-variant front velocity of planar gravity currents scales with time t as $t^{-1/3}$. Our experimental data was compared to the theoretical power law proposed by Huppert and Simpson (1980). For experiment #2, the fit is relatively close to the theoretical asymptotic deceleration law from c. 8 m from source onwards. This distance corresponds to the runout position downstream of which the underflow left the ash-cloud head due to a rapid deceleration (Fig. 5.4J). In contrast, for experiment #4 (Fig. 5.4K),

the data shows a much slower deceleration of the ash-cloud over time than predicted for dilute gravity currents. This trend is even more pronounced for experiment #5 (Fig. 5.4L).

The deviation of the experimental data in experiment #4 and #5 suggest that the flow front velocity is not controlled by a unique Fr' of ~1 but rather dictated by the presence of the underflow in the ash-cloud head. In fact, the three scenarios (#2, #4 and #5) indicate that the ash-cloud dynamics is strongly influenced by the relative velocities and respective positions of the ash-cloud and underflow fronts.

5.3.1.5 Outer shape of the ash-cloud head

Boundary velocity

As observed in the kinematic data (Fig. 5.4), the deceleration of the ash-cloud head is influenced by the underflow when the underflow is present in the head. In this case, the effect of the moving underflow on the head is explored by defining a non-dimensional expression of the velocity at the lower ash-cloud boundary, noted *A*, as follows:

$$A = \frac{1}{Uf}\ U_U \frac{2*L_{1/2}-X}{2*L_{1/2}} \qquad (5.2)$$

With U_U as the underflow front velocity, Uf as the ash-cloud front velocity, $2L_{1/2}$ as the total length of the head and X as the distance separating the underflow and ash-cloud front. In our experiments, the non-dimensional boundary velocity A ranges from values of 0 to 1. A decreases with an increasing distance between underflow and ash-cloud fronts, and it increases when the ratio of underflow to ash-cloud front velocities decreases. Note that the velocity at the lower ash-cloud boundary (and the non-dimensional boundary velocity A) should not be mistaken for slip. The ash-cloud did not slip above the underflow, but the

underflow motion provided an initial velocity (at the interface) to the ash-cloud that is called here 'boundary velocity'.

Interestingly, experimental data of A against the head densimetric Froude number collapses onto a universal curve for all explored ranges and combinations of substrate slopes θ, U_f, U_U and X. The data is well-described by a logarithmic fit of the form: $A = 1.3 \ln(Fr') - 0.1$ (Fig. 5.5). This suggests that the boundary velocity at the base of the ash-cloud is the main control on the densimetric head Froude number.

Head aspect ratio

The head geometry was characterized by an aspect ratio, which is defined by the ratio of the ash-cloud head maximum height (H) and distance (parallel to the slope) of this point in the flow front, $L_{1/2}$ (Figs. 5.5A and B). The aspect ratio R is equal to $H/2L_{1/2}$. Experimental data shows a clear dependence of the head aspect ratio to the densimetric Froude number (Fig. 5.5D). All experimental data fall upon the same trend that describes nearly linearly the lengthening of the head as Fr' increases. All data collapses upon a universal curve regardless of the slope inclination.

For comparison with the present study, available data from the literature of saline and turbidity gravity currents on slope <20° were also plotted and this shows a good overlap with data from the present study. Flows propagating under a critical regime ($Fr' \leq 1$) exhibit a constant head geometry with $H/2L_{1/2}$ equal to ~0.45–0.5, whereas supercritical flows ($Fr' > 1$) display a linear dependence of the head aspect ratio to the densimetric Froude number.

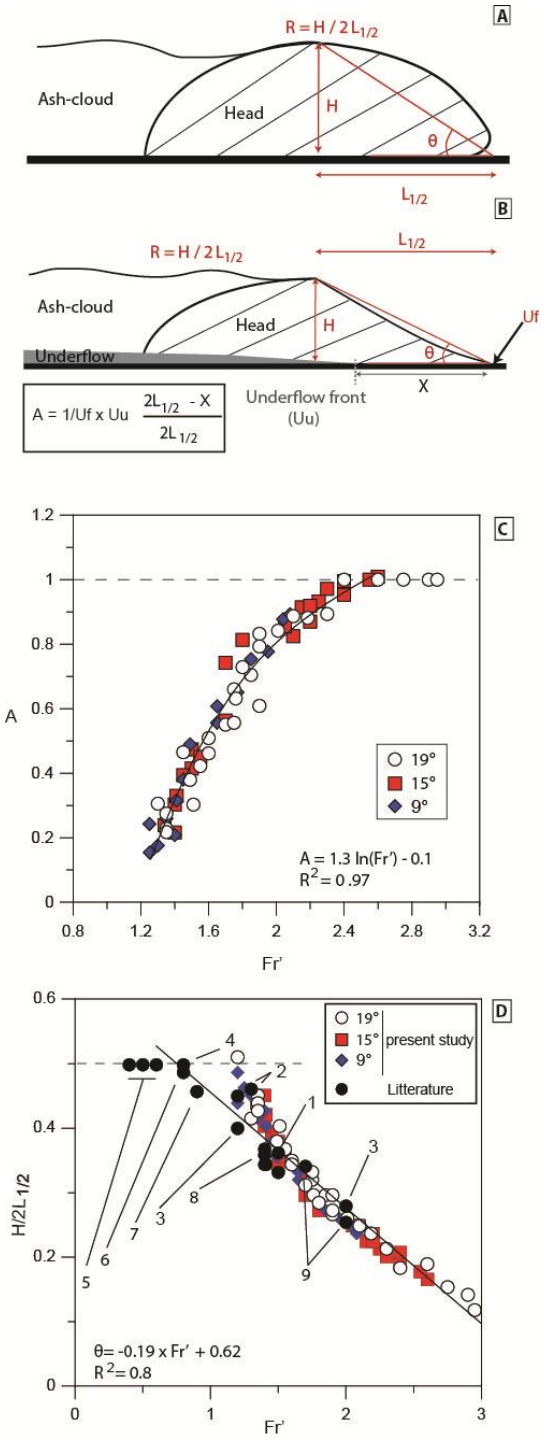

Fig. 5.5. Variation of the head geometry and the non-dimensional lower boundary velocity of the ash-cloud as a function of the densimetric head Froude number. A and B: Definition of the head ratio R is defined as equal to $H/2L_{1/2}$. Definition of the parameter noted A as the non-dimensional velocity at the lower ash-cloud boundary. C: Plot of A against the densimetric head Froude number. D: Plot of R against the densimetric Froude number (Fr') of the head. Data from the literature are from (1) Britter and Linden, 1980; (2) Simpson and Britter, 1979; (3) Sequeiros et al., 2010; (4) Maxworthy and Nokes, 2007; (5) Hacker et al., 1996; (6) Marino et al., 2005; (7) Nogueira et al., 2013; (8) Shin et al., 2004; (9) Gladstone et al., 2004.

5.3.2 Inner flow kinematics

5.3.2.1 Internal velocity through the head region

Vertical velocity profiles through dilute and fully turbulent gravity currents are characterised by an inner region of upward increasing velocity and an outer region towards the ambient fluid where velocity is decreasing upwards. Analogous to turbulent wall jets, the variation of velocity with height can be well approximated by two different mathematical relationships (Altinakar, 1996). In the inner region, velocity increases logarithmically with height from a value of zero (no-slip boundary condition) towards a maximum value U_p at the height H_p, where shear vanishes, which is typically expressed in the following form:

$$U(z) = u^* \left[8.48 + 5.75\, log\left(\frac{z}{K}\right)\right] \qquad (5.3) \qquad \text{(Allen, 1970)}$$

Equation 3 is typically referred to as the law of the Wall (Allen, 1970), with u^* being the shear velocity, z the height and K is the average size of the roughness elements of the substrate underneath the gravity current.

The outer region depicts a near-Gaussian upward decrease of velocity from the height H_p of maximum velocity U_p, which is well described by the following expression:

$$u(z) = U_p * exp\left[-\alpha\left(\frac{z-Hp}{H-Hp}\right)^m\right] \qquad (5.4) \qquad \text{(Altinakar et al. 1996)}$$

Equation (4) is often called the turbulent wall jet law (Altinakar, 1996). The parameter α controls how curved the velocity profile is in the outer region, while the parameter m controls how rapidly the velocity declines above the height H_p.

In our experimental PDCs, the head of the ash-cloud is characterized by a basal velocity in excess of zero. This velocity condition at the boundary arises downstream of the front of the underflow due to true slip with the non-moving substrate and upstream of the front of the moving underflow as a relative slip due to the non-zero velocity at the top of the underflow

(Fig. 5.6A). In order to test how well the law of the Wall approximates our experimental data its form needs to be adapted to account for the velocity at the lower boundary as follows:

$$u(z) = u_{boundary} + u^* \left[8.48 + 5.75\, log\left(\frac{z}{K}\right)\right] \qquad (5.5)$$

Where $u_{boundary}$ is the velocity at the base of the ash-cloud where z = 0 by definition. While the law of the Wall was modified to try to fit our experimental data, the Turbulent Wall Jet law of the outer region was kept similar to the original definition of Eq.(5.4).

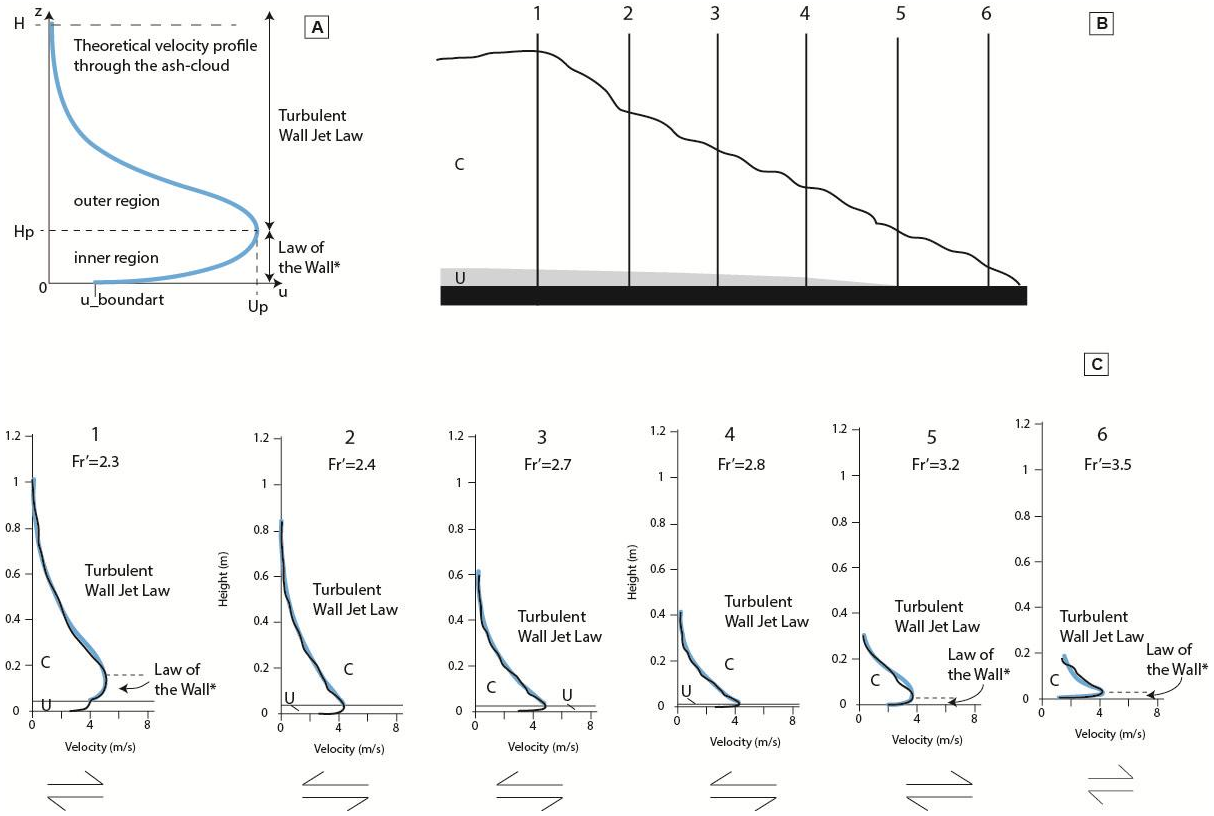

Fig. 5.6. Velocity profile through the head. A: Idealized velocity profile composed of an inner region where the modified law of the Wall noted with "*" is applied and an outer region where the velocity is described by the Turbulent Wall Jet from the height Hp upward. B: Sketch of the 6 velocity profiles through the head. Note that they are time-variant profiles. C: 6 velocity profiles and associated densimetric Froude number. The ash-cloud noted "C" is delimited from the underflow noted "U" by a thin vertical line. The black line corresponds to the measurements whereas the blue line corresponds to the theoretical fit built from either the combination of the modified law of the Wall and Turbulent Wall Jet or solely the Turbulent Wall Jet. The dashed line separates the inner and outer region of the velocity profile within the ash-cloud. The symbol underneath each velocity profile depicts the direction of the traction at the ash-cloud/underflow interface. When the upper arrow points forward (to the right), the ash-cloud induces traction at its lower boundary, whereas the opposite symbol where the upper arrow points to the left indicate that the underflow imposes traction on the ash-cloud.

Vertical velocity profiles through the head from the front to its central portion show strong variation with regards to the presence of the underflow and various traction regimes that occur (Fig. 5.6). Velocity profiles downstream of the front of the underflow (= head front) are composed of an inner and an outer region fitted well by Eq.(5.4) and Eq.(5.5) when taking into account the boundary velocity. In profiles #5 and #6 (Fig. 5.6C), traction at the ash-cloud base acts upon the substrate in the absence of the underflow and formed the tractional regime 1 defined in Chapter 4. Upstream of the front of the underflow towards the middle of the head, (profiles #2, #3 and #4, Fig. 5.6C), the maximum velocity of the ash-cloud is located at the interface between the underflow and ash-cloud. Smooth velocity profiles across this interface show strong kinematic coupling between underflow and ash-cloud regions (the tractional regime 2 defined in Chapter 4). An inner region of upward increasing velocity was non-existent, and the velocity profile of the ash-cloud can be described by the turbulent wall jet law alone. In the middle of the head (profile #1, Fig. 5.6C), the ash-cloud develops traction (tractional regime 3) at the interface with the underflow leading to the formation of an inner region, whose height-variant velocity structure can be well fitted to the modified Law of the Wall (Eq. 5.5). Above, vertical velocity profiles in the outer region are well described by the Turbulent Wall Jet Law.

The complexity of the wedge of the ash-cloud is also indicated by the variability of the densimetric Froude number (Fr') which increases from the middle of the head forward from values of 2.3 to 3.5. Because of the definition of the Fr' (Eq.5.1) and its interdependence on the height, the variations of the Fr' across the head found were not surprising.

5.3.2.2 Vertical velocity and concentration structure in the middle of the head

In the middle of the head, vertical velocity profiles can be approximated by the modified Law of the Wall for the inner region and the classic Turbulent Wall Jet Law for the outer region

(Eqs. 5.4 and 5.5, Fig. 5.7A). The concentration profile was also composed of two parts: a constant lower part where the concentration was maxima and equals to *Cc* and an upper part above a height *Hc*, where the turbulent jet law of the concentration was applied and described the upward near-gaussian decrease in velocity (Altinakar et al., 1996; Fig. 5.7B). The concentration law was approximated by a constant from the lower ash-cloud boundary up to the height Hc, above which the concentration profile took the following form:

$$C(z) = Cc * exp\left[-\lambda\left(\frac{z-Hc}{H-Hc}\right)^{\beta}\right] \qquad (6) \qquad \text{(Altinakar et al., 1996)}$$

The fitted parameters λ and β describe respectively the degree of "concavity" of the curve and how rapid the change of concentration is above the maximum.

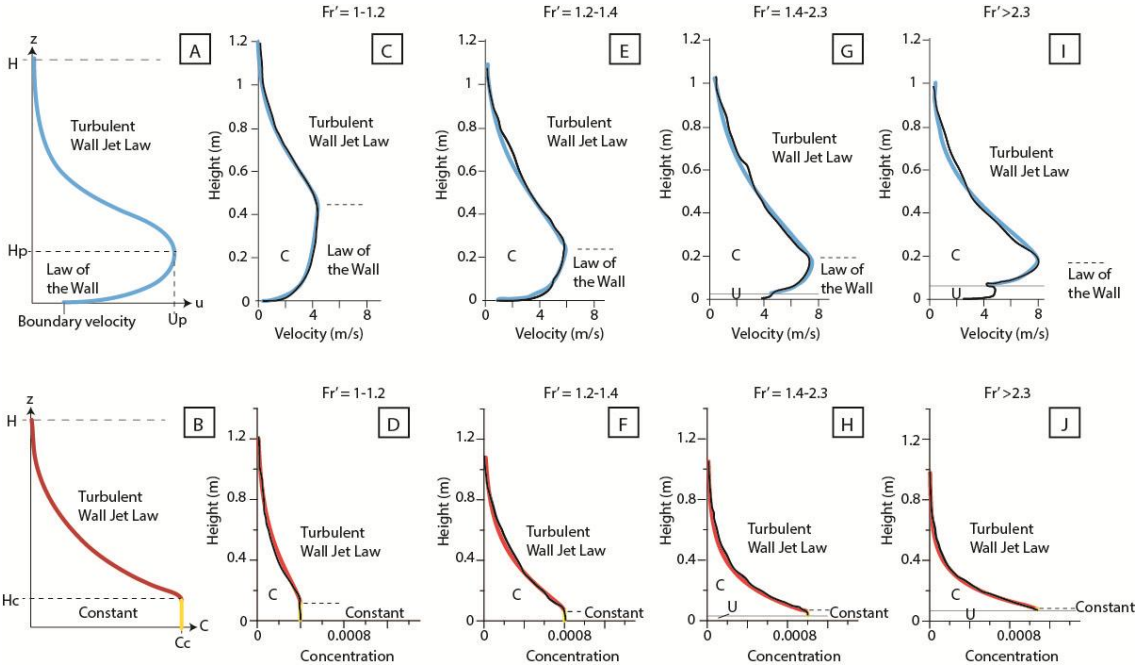

Fig. 5.7. Idealized velocity and concentration profile with theoretical laws describing the velocity and concentration of the ash-cloud (B). Thick blue and red/yellow lines represent the velocity (C, E, G and I) and concentration law respectively (D, F, H and J), whereas the black lines represent the experimental data. Law of the wall has been plotted from the lower ash-cloud boundary up to the height of maximum velocity (inner region). The turbulent wall jet law (Altinakar et al., 1996) has been plotted as an approximation of the outer velocity region of the ash-cloud while the inner region has been approximated with the law of the wall following the Von Karman approach (Allen 1970; Altinakar et al., 1996). Similarly, the concentration law follows the description of Altinakar et al. (1996) for turbulent wall jet in red while in yellow is the portion of the concentration that is nearly constant.

Analysis of the vertical velocity and concentration profiles at the middle of the head as a function of the densimetric head Froude number (Fig. 5.7C–J), revealed distinct profiles. For all experimentally determined values of Fr', the middle of the head displayed a velocity profile composed of an inner region with a velocity-boundary condition fitted well by Eq.(5.4) and an outer region, which can be described by Eq. (5.5) (Figs. 5.7C, E, G, I). Most notably, the shape of the velocity profile varied with respect to the Fr'. As Fr' increased, the inner region was shortened. Subsequently, the concentration profiles showed similar overall structures for all phases. They were composed of a lower small inner region where the concentration is constant and a larger outer region where the concentration decreased exponentially upward. Predictions of vertical concentration profiles from the Eq.(5.6) were in good agreement with the data (Figs. 5.7D, F, H and J). Similarly to the velocity profiles, the concentration profiles displayed a shape that systematically changed with the head Froude number, inasmuch as the thickness of the inner region with constant concentration decreased with increasing Fr'.

5.4. Discussion

5.4.1 Kinematic coupling of underflow and ash-cloud

The series of experiments that were undertaken that involved varying initial impact velocity, initial particle concentration at impact and slope angle have produced currents composed of an underflow and an ash-cloud, where the head of the ash-cloud was always moving in a supercritical regime (Fr'>1).

The relative position of the underflow with regards to the ash-cloud comprises two end-members. The first end-member characterizes currents in which the ash-cloud head was devoid of a basal underflow and shows strong similarity with dilute gravity currents.

Specifically, the flow front velocity was markedly controlled by the balance of inertial and buoyancy forces, where the densimetric Froude number of the head is near unity (Fr'~1–1.2) and approximately constant with runout distance. The other end-member characterises flows where the underflow had migrated to the front of the ash-cloud and ash-cloud and underflow fronts moved at similar velocities. In the second case, there was a very intense kinematic coupling imposed by the underflow onto the ash-cloud. This resulted in highly variable and supercritical Froude numbers of the overriding ash-cloud over distance. Both end-members encompass the spectrum of coupling behaviours between the ash-cloud and underflow, where intermediate coupling behaviours of the ash-cloud to the underflow occurred when the underflow front was within the ash-cloud head but both fronts were spatially separated.

Thus the experiments illuminated the role of the underflow upon ash-cloud kinematics, by demonstrating that the moving underflow provided a non-zero boundary velocity to the lower ash-cloud boundary, which induced supercriticality. Subsequently, kinematic coupling of the ash-cloud with the underflow lowered the shear stress at the ash-cloud boundary, therefore changing the velocity and concentration structures.

5.4.2 Interdependence of the head vertical structure to the Froude number

Relationships between the velocity and concentration structures with the Fr' can be assessed through four non-dimensional ratios of the maximum velocity (*Up/u_avg*), maximum concentration (*Cc/C_avg*), height of the inner boundary layer of the velocity profile (*Hp/H*) and height of the inner boundary layer of the concentration profile (*Hc/H*) (Fig. 5.7A–D). All four non-dimensional ratios are related to the head Fr' by power laws. This suggests that high degrees of coupling between the ash-cloud and underflow regions (Fr'>>1) led to the reduction of the shear stress near the ash-cloud/underflow interface and subsequent shrinking

of the inner boundary layer of both velocity and concentration profiles. This process was accompanied by the strongly delayed deceleration of the ash-cloud head and by an increase in particle concentration of the ash-cloud near its base.

The interdependence of the internal structure to the Fr' is not peculiar to experimental pyroclastic density currents. Similar behaviour has been reported in saline and turbidity gravity currents (Fig. 5.8; Sequeiros et al., 2010). However, these gravity currents did not involve an underflow, nor did they involve noticeable velocity at the lower flow boundary. In their case, supercritical regimes were obtained under the conditions of smooth substrate roughness, high slopes and high inertia of the current (Sequeiros et al., 2010). Consequently, the empirical laws (Fig. 5.8) that were derived from the present study differ partially from those found in non-slipping saline gravity currents and turbidity currents. In particular, the inner region of the concentration profile where the concentration is constant in supercritical flows with non-zero velocity boundary conditions is higher than for supercritical currents with no-slip boundary conditions. This may be due to the low friction and low shear of the lower ash-cloud boundary when propagating on top of a moving underflow.

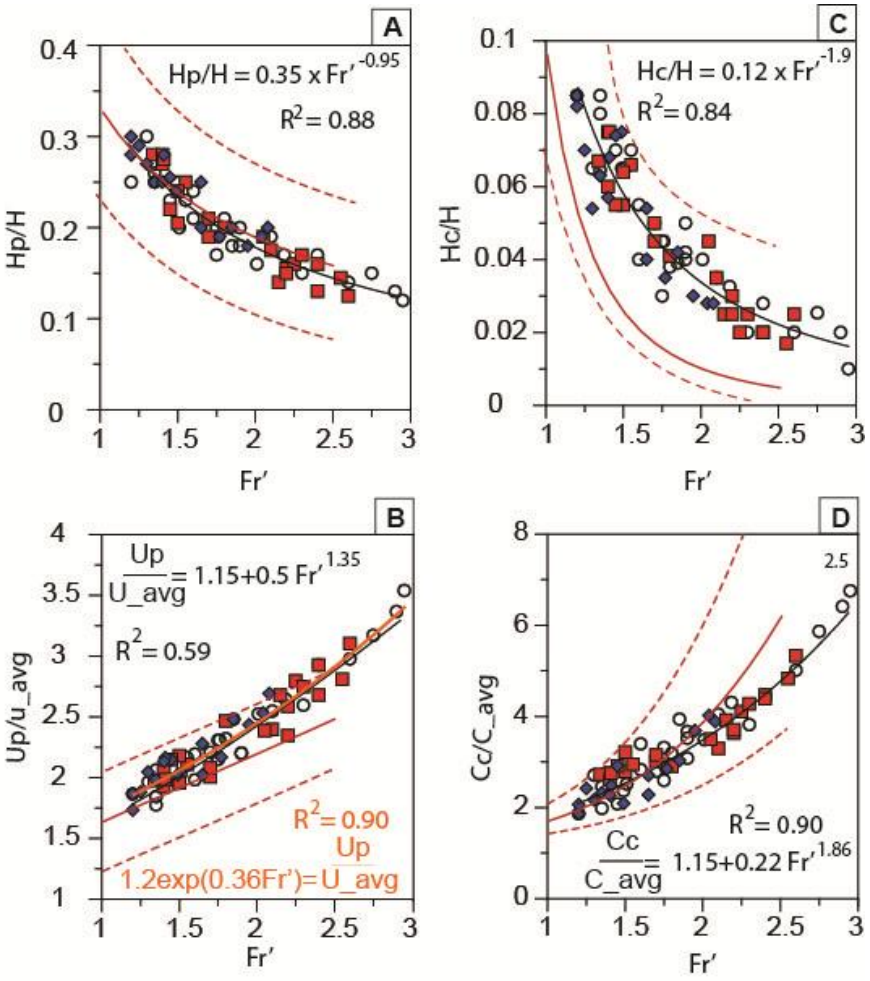

Fig. 5.8. Velocity and concentration profiles versus the ash-cloud head densimetric Froude number. A: Ratio of the maximum flow height over the maximum height (Hp/H) of the head as a function of the Froude number. B: Maximum velocity over the depth-averaged velocity (Up/U_avg) as a function of the Froude number of the head. C: Height of the deflection point in the concentration profile over the total head height (Hc/H) as a function of the Froude number (Fr'). D: Ratio of the maximum concentration over the depth-averaged concentration (Cc/C_avg) in the middle of the head (where H was measured). The black lines are the fits to the data of the present study, with the equation and corresponding R^2 indicated. The red solid lines are the fits to saline and turbidity currents combined by Sequeiros et al. (2010), with the red dashed lines that encompass all data spread around the fits. The orange solid line in B and respective equation and R^2 represent the alternative best fit to the ash-cloud data of the present study.

The outer regions of the velocity and concentration profiles were relatively well described by existing Turbulent Wall Jet Law identified by Altinakar et al. (1996), whereas the inner region of the velocity profiles required accounting for the non-zero boundary velocity in the adapted form of the law of the Wall. Moreover, the inner region of the concentration profile depicted a constant value. This suggests that shear-induced mixing disrupted the stratification near the lower flow interface. This case characterizes the phases where the ash-cloud is

partially coupled to the underflow. Efficient coupling between the ash-cloud and underflow led to the active shrinking of the inner region of the concentration profile.

5.4.3 Forced supercriticality and head shape – comparison with other gravity currents

Commonly, the densimetric Froude number of gravity currents is assumed to be ~1 (Huppert and Simpson, 1980; Huppert 2006). However, under certain initial and boundary conditions such as high slopes, smoothness of the substrate and high inertia, gravity currents can become supercritical (Fr'>1) (Sequeiros et al., 2009a; Sequeiros et al., 2009b; Sequeiros et al., 2010; Sequeiros, 2012b). Our results add the development of a velocity at the lower boundary as another cause for an imbalance of inertial and buoyancy forces. Velocity boundary conditions can develop at the lower boundary of PDC ash-clouds due to the presence of a moving underflow. This forces the supercritical behaviour of the ash-cloud head by lowering the basal shear stress. Therefore, the term forced-supercriticality used here describes the behaviour of the ash-cloud moving atop an underflow. This excess of inertia promotes the longitudinal growth of the head relative to its height. The effect of the supercriticality on the lengthening of the head is not clearly mentioned in the literature. The most common ratio reported in published studies characterizing the head was found to be the aspect ratio of height over length and most studies produced flows with Fr' <1.2. This may be attributed to the difficulty of producing flows with high inertia; in fact less than 10% of published studies produced supercritical gravity currents. The most common reported value of the aspect ratio (R) of the head ranges between 0.4 and 0.5 (Nogueira et al., 2013). While critical currents tend to form a head with aspect ratios of ~0.4–0.5, supercritical currents show variable head aspect ratio <<0.5 that are governed by the internal velocity and concentration structures that are intrinsically dictated by the Froude number.

5.4.4 Implication of the underflow-ash-cloud coupling on PDC hazards

Results of the study of concentrated PDCs in large-scale experiments highlight the major role of the underflow upon the ash-cloud head kinematics and internal structure. Realistic predictions of the ash-cloud behaviour cannot be achieved without a good prediction of the underflow kinematics. This requires better knowledge of the rheology of underflows in concentrated PDCs.

Forced-supercriticality due to development of a non-zero velocity at the lower ash-cloud boundary has a number of implications. Beyond delaying deceleration of the ash-cloud, the maximum velocity and concentration increases and their respective heights are lowered. Thus, the highest dynamic pressures develop at lower heights than for subcritical currents, and therefore closer to the typical height of man-made infrastructures, such as buildings, power lines and bridges. The kinematic coupling of the underflow and ash-cloud needs to be accounted for in hazard models to better predict the destruction pattern of PDCs.

Predicting the runout of an ash-cloud is difficult when dealing with examples where an underflow is present, because models restricted to the underflow (e.g. Titan2D, Patra et al., 2005) cannot predict the full behaviour of these complex flows. Two layer models would be required to account for kinematic coupling between the dense underflow and dilute ash-cloud. However, current models so far do not account for the kinematic coupling between the two layers (Doyle et al., 2010), thus they underestimate the runout and destruction potential of these flows. By way of example, because Doyle et al. (2008) did not account for the ash-cloud coupling, they envisaged cases where the ash-cloud could terminate, while the underflow would continue to propagate. Furthermore, they also envisaged a case wherein the ash-cloud and underflow would terminate at the same location. None of these cases are really plausible. The first case is unlikely, because the underflow can catch up with the ash-cloud

front and if accelerating, would actively enhance the supercritical behaviour of the upper cloud rather than separate from it. Therefore, the fast underflow would be perfectly coupled with the ash-cloud and increase by multiple times its maximum velocity and runout. The lack of consideration of such effects results in underprediction of the ash-cloud extent and hazard. The second case envisaged is also unlikely, because when the underflow comes to rest, the ash-cloud would propagate further, as long as its density is greater than the ambient air and a Froude number near unity. In our experiments, while the underflow commonly came to rest after c.16 m from source, the ash-cloud continued to move until ~25 m, where it became buoyant.

Finally, the Froude number of the ash-cloud is often assumed to be constant and ~1 for dilute PDCs and also for the ash-cloud of concentrated PDCs. Such input is used as a closure for numerical models (Dade and Huppert, 1996; Dufek and Manga, 2008), whereas experiments revealed that the Froude number of ash-clouds can be variable and supercritical.

5.5 Conclusions

The coupling between the underflow and the ash-cloud affects the dynamics of the ash-cloud head in different ways. A velocity develops at the lower ash-cloud boundary and is provided by the moving underflow. Subsequently, at the interface between the ash-cloud and underflow, kinematic coupling yields reduction of the shear stress. Vertical velocity and concentration profiles change because of the new boundary conditions. The inner regions of the velocity and concentration profiles can fully disappear and the ash-cloud accelerates while becoming more dense near its base, which lead to the forced-supercriticality of the ash-cloud ($Fr'>1$). As a result, heads of ash-clouds with underflows decelerate slower than classic dilute gravity currents (Fig. 5.9).

The forced-supercriticality of the ash-cloud is dependent on the location of the moving underflow, which affects the velocity, concentration structures and the shape of the head. When the underflow front is located within the head, the ash-cloud head adopts a wedge shape that is dictated by the densimetric head Froude number. Therefore, the supercriticality of the ash-cloud forced by the underflow affects the inner and outer structure of the ash-cloud head as well as its kinematics.

The presence of a velocity boundary condition is added to other known processes such as high inertia (i.e high eruption rate), low roughness and high slopes that can lead to supercritical Fr' of gravity currents. Despite the evident differences of the carrier fluid between volcanic gas-particle flows and saline/turbidity currents, their inner and outer structures respond in a similar manner to the degree of criticality of the head, with minor differences attributed to the origin of their supercritical behaviour.

The present study concludes that forced-supercritical ash-cloud heads are potentially very hazardous and that modelling of their behaviours requires an accurate knowledge of the underflow dynamics.

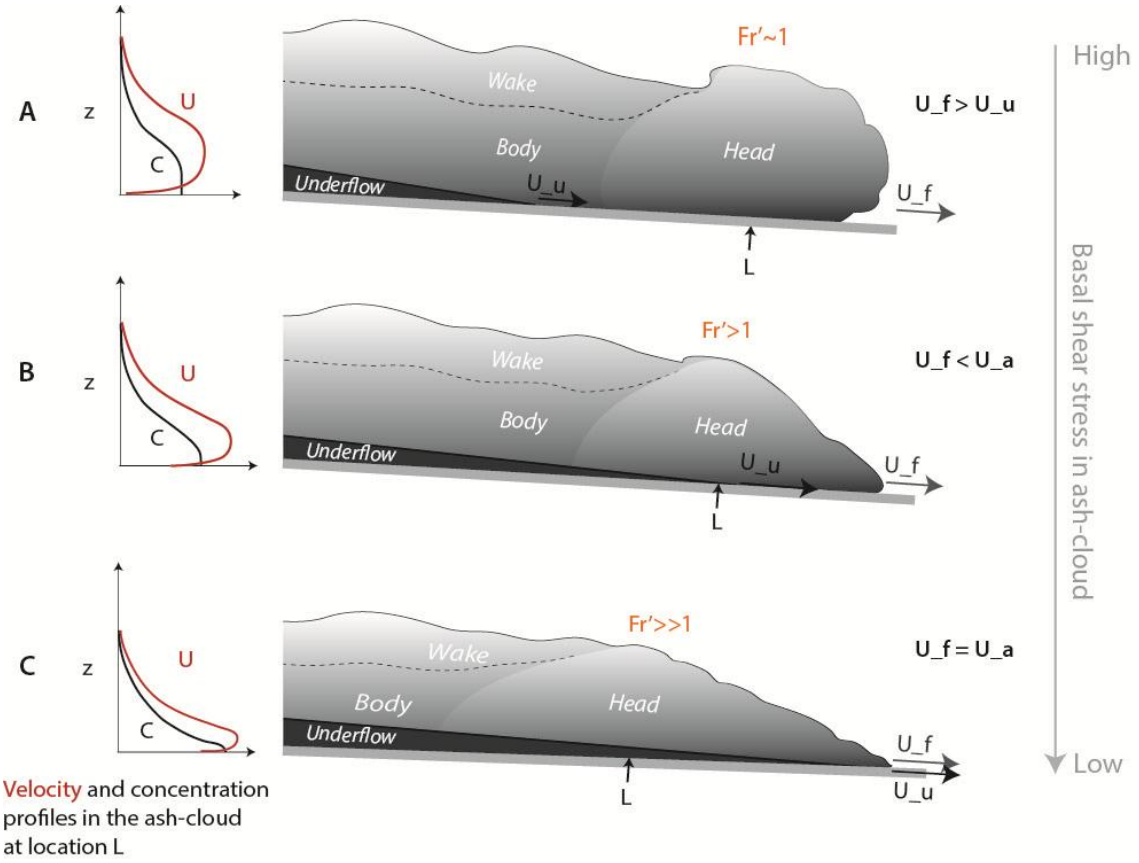

Fig. 5.9. Schematic diagram of the ash-cloud forced to a supercritical behaviour by the underflow. The diagrams show the penetration from A to C of the underflow within the ash-cloud and subsequent effects upon the ash-cloud head internal and outer structures. A: The underflow is lagging behind the ash-cloud head. The velocity of the ash-cloud front U_f is greater than the underflow front velocity U_u. Velocity and concentration profiles through the middle of the head depict a thick inner boundary layer. Note the head of the ash-cloud with an aspect ratio Height/Length ~0.5. The head densimetric Froude number Fr' is near 1. B: The underflow front is within the ash-cloud head. The underflow is faster than the ash-cloud and provides a velocity in the lower ash-cloud head, which affects the internal velocity and concentration profiles. The inner region of both velocity and concentration profiles shrinks while the underflow densifies near the lower boundary and accelerates. Coupling between underflow and ash-cloud yields the forced-supercriticality of the ash-cloud where Fr' of the head is >1. C: Similar to B, but the underflow and ash-cloud fronts are "merged". While the relative higher mobility of the underflow leads to scenarios from A to C, the reverse is also possible (C to A), where the underflow would slow down faster than the ash-cloud (for instance on shallow slopes) and the latter would "decouple" from the underflow and behave as a dilute gravity current with Fr'~1.

5.6 Supplementary material

Parameter	Nature	PELE
Particle diameter (m)	10^{-6}–10^{-1}	10^{-6}–10^{-2}
Particle density (kg m^{-3})	300–2600	300–2600
Fluid density (kg m^{-3})	0.6–1.25	1-1.25
Dynamic viscosity of the carrier phase (kg m^{-1} s^{-1})	1x10^{-5}–4x10^{-3}	1x10^{-5}–5x10^{-3}
Flow velocity (m s^{-1})	10–200	<2–20
Reynolds number $Re = \frac{\rho U L}{\mu}$	1x10^{4}–6.7x10^{9}	1.5x10^{4}–2x10^{6}
Stokes number $S_T = \frac{1}{f}\frac{\Delta\rho d^2}{18\mu}\frac{\Delta U}{\delta}$	1.1x10^{-3}–9.7x10^{7}	7.4x10^{-5}–4.6x10^{4}
Stability number $\Sigma_T = \frac{S_T}{Fr^2} = \frac{\tau_v g}{f\Delta U} = \frac{U_T}{\Delta U}$	2.8x10^{-6}–9.7x10^{9}	7.1x10^{-7}–4.6x10^{5}
Particle Froude number $Fr = \frac{U}{\left[(\rho_p - \rho_g)gD\right]^{0.5}}$	0.1–20	0.3–10
Richardson number $Ri = \frac{(\rho - \rho_o)gH}{\rho_o U^2}$	2x10^{-4}–1.1x10^{1}	1x10^{-3}–4.5x10^{1}

Supplementary Table 5.1. Bulk flow scaling of natural dilute PDCs (Burgisser and Bergantz, 2005) and PELE experimental currents. Where U and L are characteristic velocity and length scales of the flow. μ corresponds to the dynamic viscosity of the flow. ρ is the mixture density. ρ is the flow density and ρ_o is the ambient medium density. D is the particle diameter.

Parameter	Nature	PELE
Particle diameter (m)	10^{-6}–10^{-1}	10^{-6}–10^{-2}
Particle density (kg m^{-3})	300–2600	300–2600
Fluid density (kg m^{-3})	0.6–1.25	1-1.25
Particle volumetric concentration	30–60 %	40–60 %
Dynamic viscosity of the fluid (kg m^{-1} s^{-1})	$1x10^{-5}$–$4x10^{-5}$	$1x10^{-5}$–$3x10^{-5}$
Underflow velocity (m s^{-1})	10-30	<2–15
Bagnold number	$1x10^{-2}$–$1x10^{2}$	$1x10^{0}$–$1x10^{2}$
$Ba = \frac{c^* \rho_p \dot{\gamma} D^2}{\mu_g}$		
With $c^* = \left[c^{\frac{1}{3}}/(c_0{}^{\frac{1}{3}} - c^{\frac{1}{3}})\right]^{1/2}$		
Darcy number	$1x10^{2}$–$1x10^{4}$	$1x10^{0}$–$1x10^{3}$
$Da = \frac{\rho_g}{\rho_s}\frac{D^2}{Re_p kc}$		
Froude number	1.6–9.6	1.5–6.2
$Fr = \frac{U}{\left[(\rho_p - \rho_g)gD\right]^{0.5}}$		
Savage number	$1x10^{-9}$–$1x10^{-7}$	$1x10^{-6}$–$1x10^{-5}$
$Sa = \frac{\rho_p \dot{\gamma} D^2}{(\rho_p - \rho_g)gh_c}$		

Supplementary Table 5.2. Underflow scaling of natural PDCs (Roche et al., 2012) and PELE experimental currents. Where ρ_p and ρ_g the particle and gas density, $\dot{\gamma}$ the shear rate, μ_g the gas dynamic viscosity, D the particle diameter, h_c the current height, g the acceleration of gravity. c denotes the flow concentration during propagation, c_o is the maximum concentration at loose packing, γ is the shear rate. $\underline{k}$ is the permeability of the granular medium. Re_p is the particle Reynolds number defined as follows: $Re_p = 2DU\rho_s / \mu$.

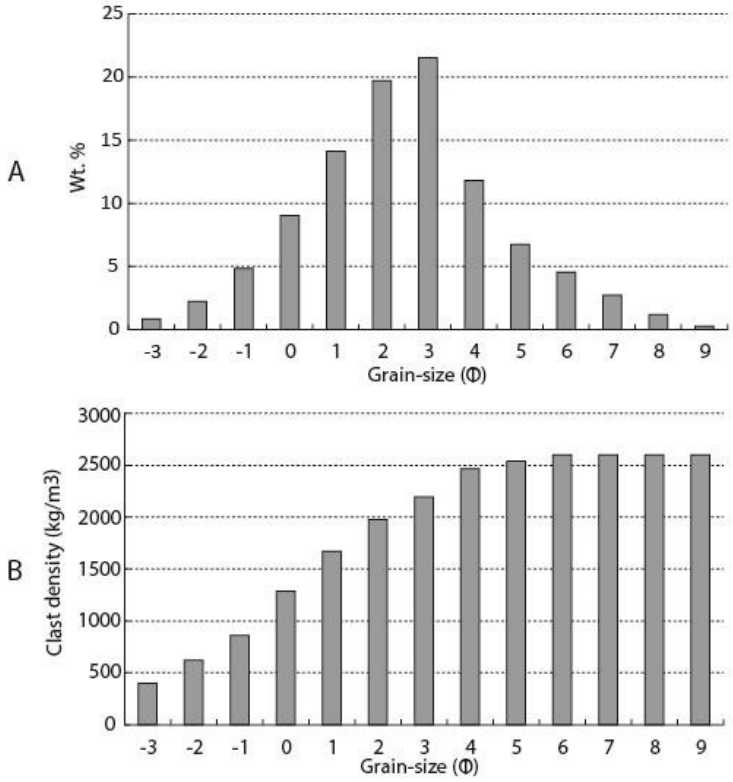

Supplementary Fig. 5.1. A: Unimodal grain-size distribution of the initial mixture. B: Particle density distribution of the experimental mixture with respect to grain-size.

Picture of the Te Maari vent from the Tongariro Crossing, with the eruptive fissure degassing.

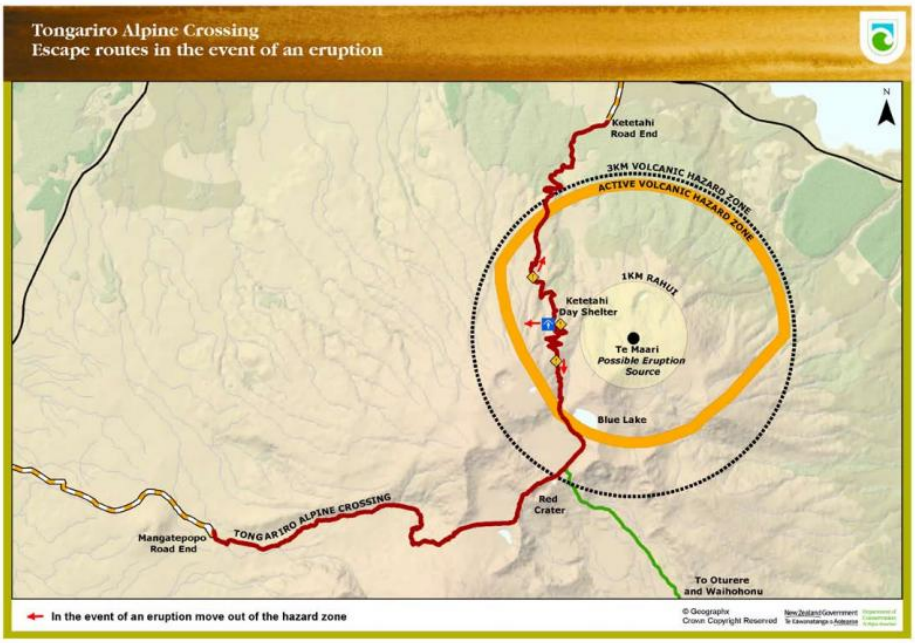

Te Maari Active Volcanic Hazard Zone based upon the present study, Department of Conservation.

Chapter 6 - Using the spatial distribution and lithology of ballistic blocks to interpret eruption sequence and dynamics: August 6 2012 Upper Te Maari eruption

Chapter contents

This Chapter is based on a published paper:

Breard, E.C.P., Lube, G., Cronin, S.J., Fitzgerald, R., Kennedy, B., Scheu, B., Montanaro, C., White, J.D.L., Tost, M., Procter, J.N. and Moebis, A., 2014. Using the spatial distribution and lithology of ballistic blocks to interpret eruption sequence and dynamics: August 6 2012 Upper Te Maari eruption, New Zealand. *Journal of Volcanology and Geothermal Research*.

Participating authors:

Eric C. P. Breard (Field work, manuscript development, data analysis, manuscript writing and editing).

Gert Lube (Field work, manuscript editing and discussion)

Shane J. Cronin (Field work, manuscript editing and discussion)

Rebecca Fitzgerald (Discussion)

Ben Kennedy (Discussion)

Bettina Scheu (Field work)

Cristian Montanaro (Field work)

James D. L. White (Discussion)

Manuela Tost (Field work)

Jon Procter (Discussion)

Anja Moebis (Discussion)

Chapter 6 – Using the spatial distribution and lithology of ballistic blocks to interpret eruption sequence and dynamics: August 6 2012 Upper Te Maari eruption

6.1 Introduction

Volcanic ballistic projectiles produced during explosive eruptions impose a great hazard for areas within 1–2 km of an eruptive vent (Sparks et al., 1997). Ballistic clasts can be of any origin and have an average diameter exceeding a few centimetres. Generally, these are ejected from an eruption vent on nearly parabolic trajectories. The size and mass distribution is important for determining hazard, but these features along with lithology are also important for interpreting eruption dynamics, such as depth and mechanisms of explosion. In addition, ballistic projectile trajectories can be used to approximate the initial velocity of any simultaneously occurring multiphase flow such as a dilute pyroclastic density current (Fagents and Wilson, 1993). Several models have been proposed to reproduce ballistic trajectories from sustained eruptions (Sparks et al., 1997), or single-pulse events, such as vulcanian activity (Self et al., 1980; Fagents and Wilson, 1993; Waitt et al., 1995; Goto et al., 2001; Alatorre-Ibargueengoitia and Delgado-Granados, 2006; de'Michieli Vitturi et al., 2010). In these studies, a number of factors were shown to modify ballistic fragment dispersal, including: whether explosions are magmatic, phreatomagmatic, or hydrothermal; the explosion depth; the mechanism of explosive impulse; and crater morphology. Here I map and interpret the distribution and properties of ballistic blocks to examine the mechanisms and predominant directionality behind a sudden-onset, but short-lived eruption from the Upper Te Maari vent on the northern flanks of Mt. Tongariro (Fig. 6.1).

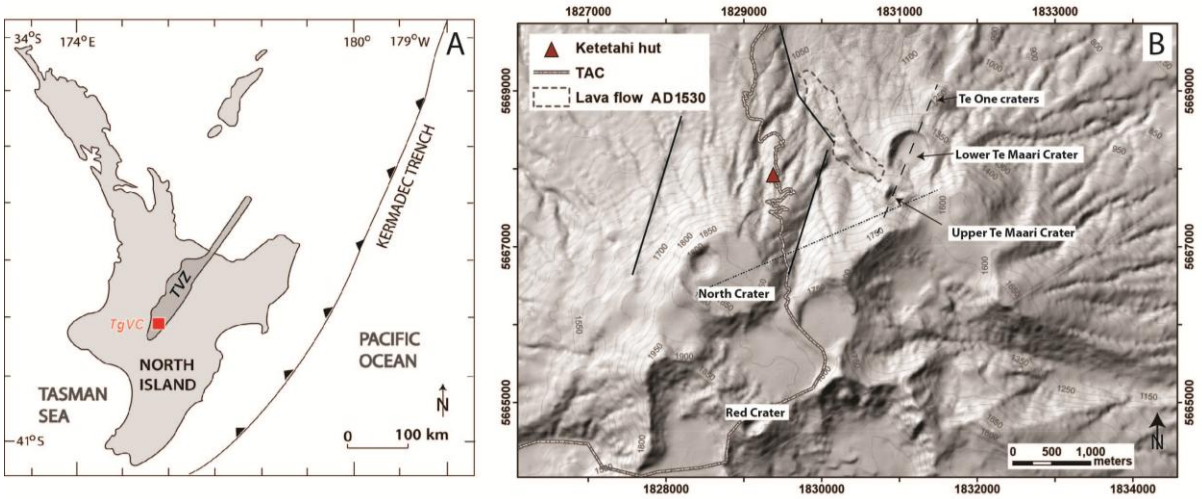

Fig. 6.1. Location of Upper Te Maari Crater. A: Map of North Island (New Zealand) showing the position of the Tongariro Volcanic Centre (TgVC) and the Taupo Volcanic Zone (TVZ). B: DEM of the northern portion of Mt Tongariro with the main volcanic features marked. Solid lines show the regional normal fault trend; the dotted line represents the alignment of vents that is almost parallel to the regional fault trend. The pointed line represents the possible extension mapped in North crater to the Upper Te Maari Crater.

This explosive hydrothermal eruption although driven by magmatic gas, ejected exclusively non-juvenile material. It produced at least two laterally directed, cool (<100 °C) PDCs towards the east and west (Lube et al., 2014), as well as a 7.8 km-high eruptive plume (Pardo et al., 2014). Ballistic impacts severely damaged the Tongariro Alpine Crossing (TAC, ~18,000 visitors per year, Jolly et al., 2014) that passes as close as 1.2 km west of the Upper Te Maari Crater. The lack of data characterizing Tongariro ballistic hazards prompted immediate surveys of the August 6 impact craters using ground and airborne mapping techniques.

I present an interpretation of the conditions and vent location(s) responsible for producing the spatial distributions of ballistic blocks from the hydrothermal eruption. I also describe the distribution of lithologies ejected and correlate them to new proximal exposures of the vent area. These observations allow interpretation of the geology of the source region and I postulate the mechanisms for explosive energy release. Further, the most complete subset of

ballistic block and impact-crater data is used to approximate the kinematic and geometric characteristics of the westerly-directed explosion.

6.1.1 Tongariro Volcano and the 6 August 2012 Te Maari eruption

Tongariro volcano forms part of the Tongariro Volcanic Centre (Cole et al., 1986) in the Central North Island of New Zealand at the southern end of the Taupo Volcanic Zone (Fig. 6.1A). This long-lived andesitic volcano is composed of multiple overlapping cone and crater systems, which have intermittently erupted since ~300 ka (Gamble et al., 2003). Several stages of large-scale explosive plinian eruptive activity have occurred since 50 ka (Hobden et al., 1999). In the post c. A.D. 1860 historical record, eruptions are known only from Ngauruhoe, and Upper Te Maari Crater of Tongariro (Topping, 1974). The Upper Te Maari Crater is an inconspicuous feature located on the northern flank of the sprawling Tongariro edifice (Fig. 6.1B). It is named after a local Maori Chief who died after an eruption from it in 1868. Lava flows dated at c. 1530 from this area show that it has been an intermittently active vent for around 500 years (Topping, 1974). Observed eruptions from this area also occurred in 1892 and 1896–1897, involving repeated explosions of similar scale, including ballistics and occasionally widely dispersed fine ash fall (Hill, 1893; Hill, 1897). In the most recent eruption at 23:49:06 (GMT + 12) on 6 August 2012 (Jolly et al., 2014b) , a collapse from the hydrothermally altered Upper Te Maari produced a debris avalanche (Fig. 6.1; Procter et al., 2014). A short while later, at 23:52:20 (GMT + 12) a >60 s eruption occurred from the Upper Te Maari area (Jolly et al., 2014b) that produced laterally directed explosions and PDCs (Lube et al., 2014). Based on a lack of any confirmed juvenile component in the lithic ash (Pardo et al., 2014a), the eruption was most likely caused by a rapid decompression of the pre-existing hydrothermal system (Rowlands et al., 2005). Eye-witnesses 7 km NNE of the eruption site, reported three brief explosions with eruption clouds, including ballistic trails, directed sequentially to the east (at angles exceeding 45° to horizontal), then west at a lower

angle (<45°) and finally vertically, resulting in an ash plume. Bright light was reported, which could indicate lightning associated with the plume. The lack of obvious vegetation charring by ballistic clasts, and their derivation from country rock indicates dominantly low temperatures. A ~5 km^2 ballistic impact field was formed during the eruption, covering the Tongariro Alpine Crossing walkway (1.2 km from Upper Te Maari at its closest point), along with the Ketetahi Hut (1.4 km from source; Fig. 6.1).

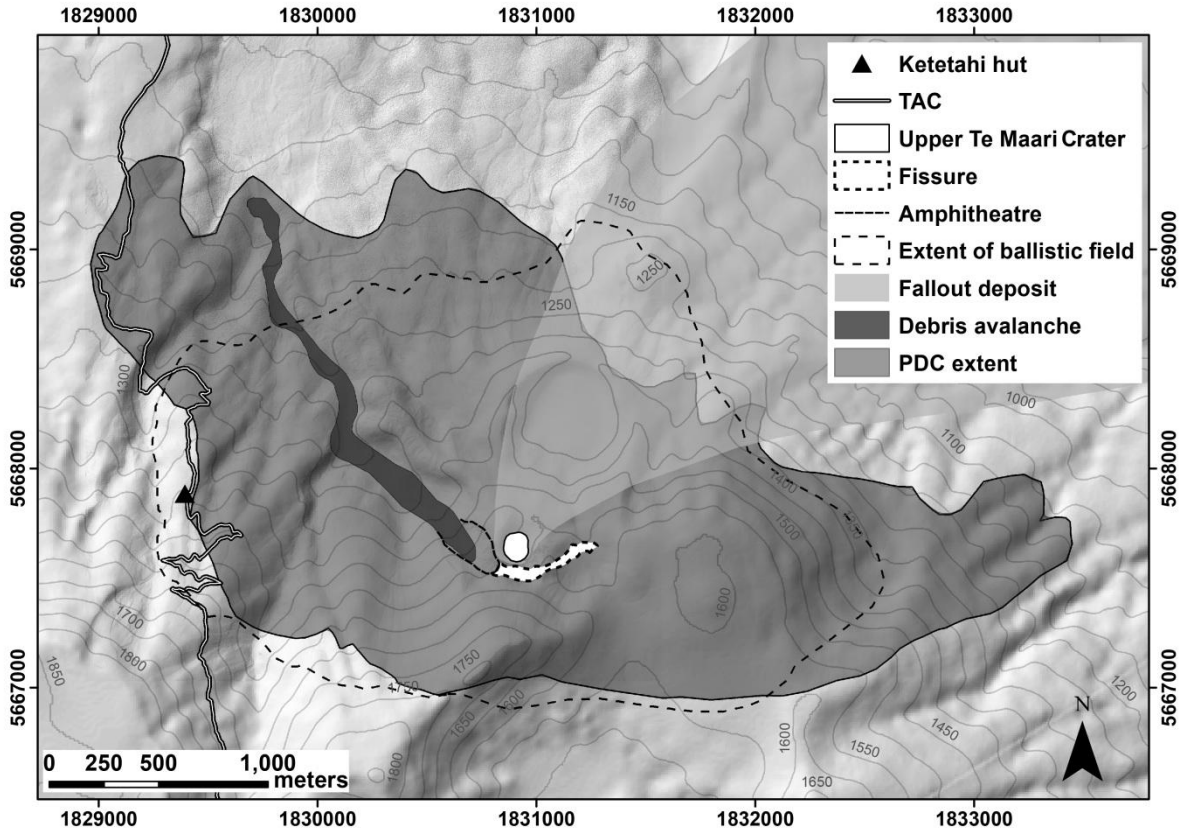

Fig. 6.2. Distribution of the eruption units of the 6 August 2012 Upper Te Maari eruption on top of a LiDAR DEM and 10_m DEM. I notice that the maximum extent of the PDC deposit and ballistic field are in similar directions NW and E of Upper Te Maari Crater. The coordinate system is NZTM2000. (TAC= Tongariro Alpine Crossing).

6.2 Methods

6.2.1 Mapping

The spatial distribution of ballistic craters of the 6 August 2012 eruption was characterized using three approaches:

(1) Locating fresh impact structures using >300 photographs taken from multiple helicopter fly-overs, beginning within 12 h of the eruption and continuing through the following two weeks.

(2) Identifying fresh craters using high-resolution orthophotographs from low-elevation flights taken in November 2012.

(3) Systematic field transects across the impacted area, beginning in September 2012, with site-by-site measurements of crater diameter and, where possible, diameters and for blocks of <50 kg, their mass.

In an area where recent historical eruptions of similar style have occurred, the immediate-post event photographs were essential for distinguishing new ballistic particle impact craters from older ones. In up to half of the impact craters examined in the field, multiple blocks with differing lithologies were found. Some of these were obviously exposed from the substrate regolith. To ensure that only the lithologies of August 6 projectiles were described, sites with a single obvious block or broken block of the same lithology were concentrated upon. Crater size and recognition varied with soil strength. On the AD 1530 lava flow, few craters were identified, but the ballistic clasts could be distinguished from the lava by their contrasting lithology and freshly broken nature. On this lava flow, ballistic clasts were located by ground mapping, with clast diameters and lithology used to generate equivalent hypothetical crater diameters based on clast size and density relationships as described below.

Recognizing ballistic projectile impact craters was also difficult for small features and on steep slopes. Craters <1.5 m-diameter seen on orthophotos were easily confused with other erosional patterns on vegetated slopes, or erosion-smoothed older craters. Hence, to ensure reliability in the measurements, only those with a minimum diameter of 2.5 m were categorized. The resulting map of impact craters >2.5 m in diameter comprises 2215 craters. The spatial-density of features was calculated via the "Kernel Density" tool within ArcGIS v. 10.1, with a similar process used for maps of crater size distribution.

Systematic transects radiating outward from Upper Te Maari Crater were carried out to characterize 150 impact craters in terms of diameter and depth, substrate characteristics, and thickness of PDC deposits inside and outside the crater. For roughly 30% of these craters, the corresponding ballistic block (or fragments of it) was found. In these cases, the three principal block axes were measured, those less than 50 kg weighed, and sub-samples of the main lithotypes collected. Bulk densities of the sampled clasts were measured using a MICROMERITICS Geopyc 1360 Envelope Density apparatus. The explosion source region was also described and samples collected from a 45 m-high new section exposed by the headwall of a new landslide.

6.2.2 Ballistic modelling

I used the "Eject!" (Mastin, 2001) ballistic model to determine a range of angles and initial velocities that best matched the western field of ballistic blocks (Table 6.1).

Speed of tailwind (m s-1)	Thermal lapse rate (°C/km)	Temperature at sea level (°C)	Elevation of takeoff point (m)	Block diameter (m)	Drag coefficient	Average density (kg m-3)	Block shape	Reduce drag distance (*rd*) (m)
1.5	6.5	10	1540	0.4-0.5	1	2200	Sphere	400

Table 6. 1. Initial parameters used in the Eject! ballistic model.

The calculation assumes that ballistic blocks are launched from a fixed position and with a given velocity and angle. A constant drag coefficient (CD= 1) was applied, consistent with experimental and numerical studies (Alatorre-Ibargueengoitia and Delgado-Granados, 2006; de'Michieli Vitturi et al., 2010). Ballistic blocks are initially partially coupled with a gas-laden jet as they are propelled and accelerated. They rapidly decouple from the gas stream due to high drag. Farther outward, the gas-jet decelerates and decays, and blocks become the fastest-moving elements (de'Michieli Vitturi et al., 2010). To use Eject!, a minimum distance of coupling between ballistic block and gas jet was assumed at 400 m, based on comparable vulcanian explosions.

The initial trajectory of the ballistic blocks is controlled by the expansion direction of the jet. Size and density of blocks are two parameters that largely influence the ballistic pathway. Accordingly, I focused our modelling approach on craters with a narrow range of sizes and density (Table 6.1). I defined an empirical relationship between crater size and block diameter for the main block lithology, which has a narrow range in density as measured in the laboratory. Thus, a small range of ballistic densities and size values was applied to the Eject! model.

By examining a single traverse through the ballistic field and using the empirical relationship between crater size and block diameter, I can approximate the best fit (velocity/angle) for the greatest extent of ballistic impact. The calculated initial velocities were related to corresponding block sizes and densities and used to determine the optimal launch angle for generating the observed impact density distribution along an axis to the west of Upper Te Maari. To compare the results of a simple ballistic model, such as Eject! to those from a complex jet coupled model, such as that from de'Michieli Vitturi et al. (2010), initial

velocities of ballistic blocks in Eject! may be amplified by over 30%. Hence any initial velocities calculated via this modelling approach will be overestimates for the Te Maari case.

In a stratified atmosphere, the optimal launch angle of ballistics is close to 45° if launching and landing elevations are similar. For vertical jets from a crater, launch angles of <45° are unlikely, because of the conduit and vent confinement (de'Michieli Vitturi et al., 2010). Large-scale experiments on maar-diatreme volcanism have demonstrated that very shallow explosions partially eject material at launch angles of <45°, and confirm that explosions at depth tend to focus the ejected material into an upward jet (Taddeucci et al., 2013). In the case of a lateral explosion, ballistics can be launched at very shallow angles (Belousov et al., 2007), and jet expansion directions (burst phase) can be reconstructed from ballistic trajectories.

6.3 Results

6.3.1 Geology of the fissure area

Upper Te Maari Crater is formed by pyroclastic deposits that overlie and abut a blocky andesitic lava flow thought to be ~AD 1530 in age (based on dendrochronology; Topping, 1974) (Fig. 6.2). The 6 August 2012 eruption produced an amphitheatre-like depression and a c.430 m-long fissure created by a landslide and excavation respectively (Figs. 6.2 D & 6.3). The fissure occurs up-slope of the Upper Te Maari Crater and widens to the west where the landslide started. It cuts through previous zones of weakness (Figs. 6.1B and 6.3C), which align with pre-existing fractures in the North Crater. The fissure comprises two parts, the widest and deepest portion slopes toward the west, while over a saddle, a narrower, shallower fissure portion has its base inclined ENE (Table 6.2).

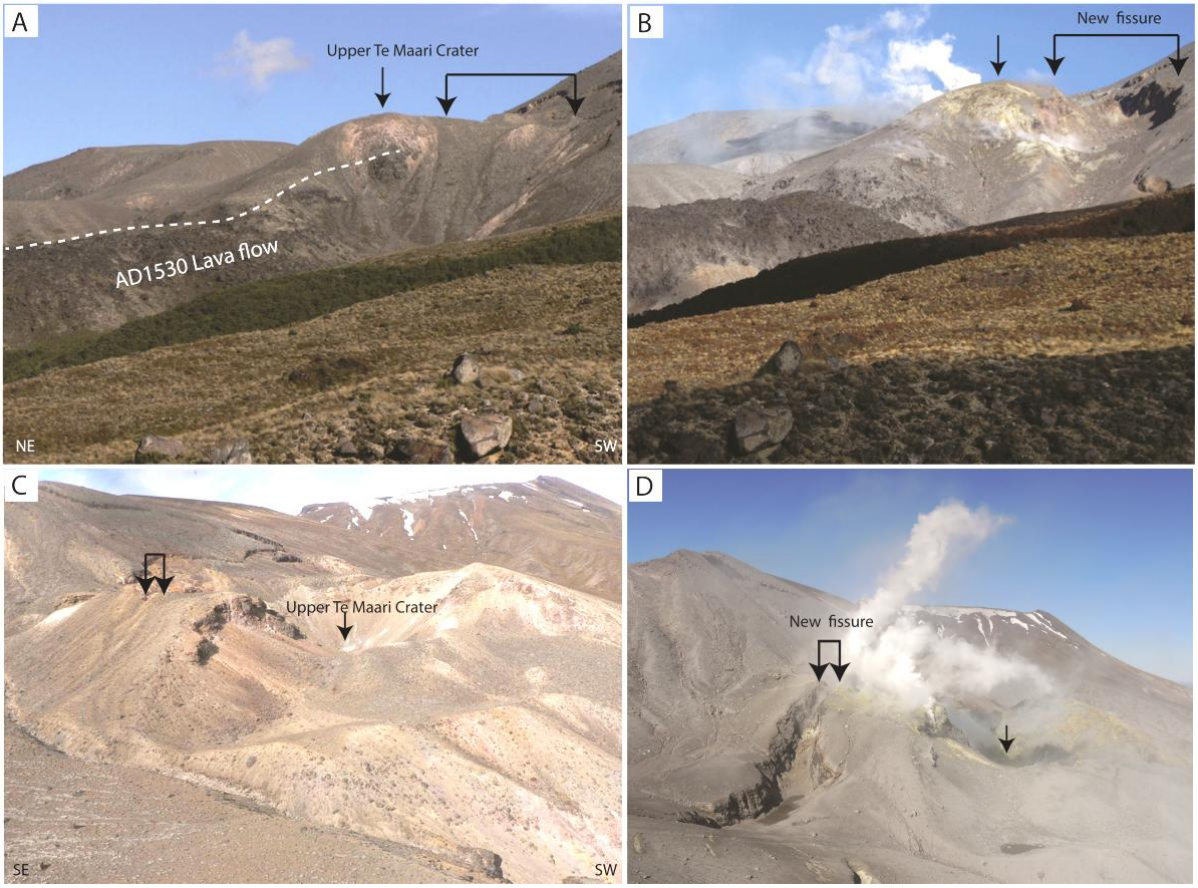

Fig. 6.3. Comparison of the Upper Te Maari Crater area before and after the eruption. A: The crater from the Tongariro Alpine Crossing in January 2009. B: View in November 2012 showing the western, broader part of the fissure (>50m wide). Note that the crater is still intact. C: The Upper Te Maari Crater view from the east in January 2009. D: Post eruption view showing the new eastern part of the fissure. The two linked arrows show the position of the junction between the western and eastern fissure at its narrowest (10 m) and shallowest part (10 m).

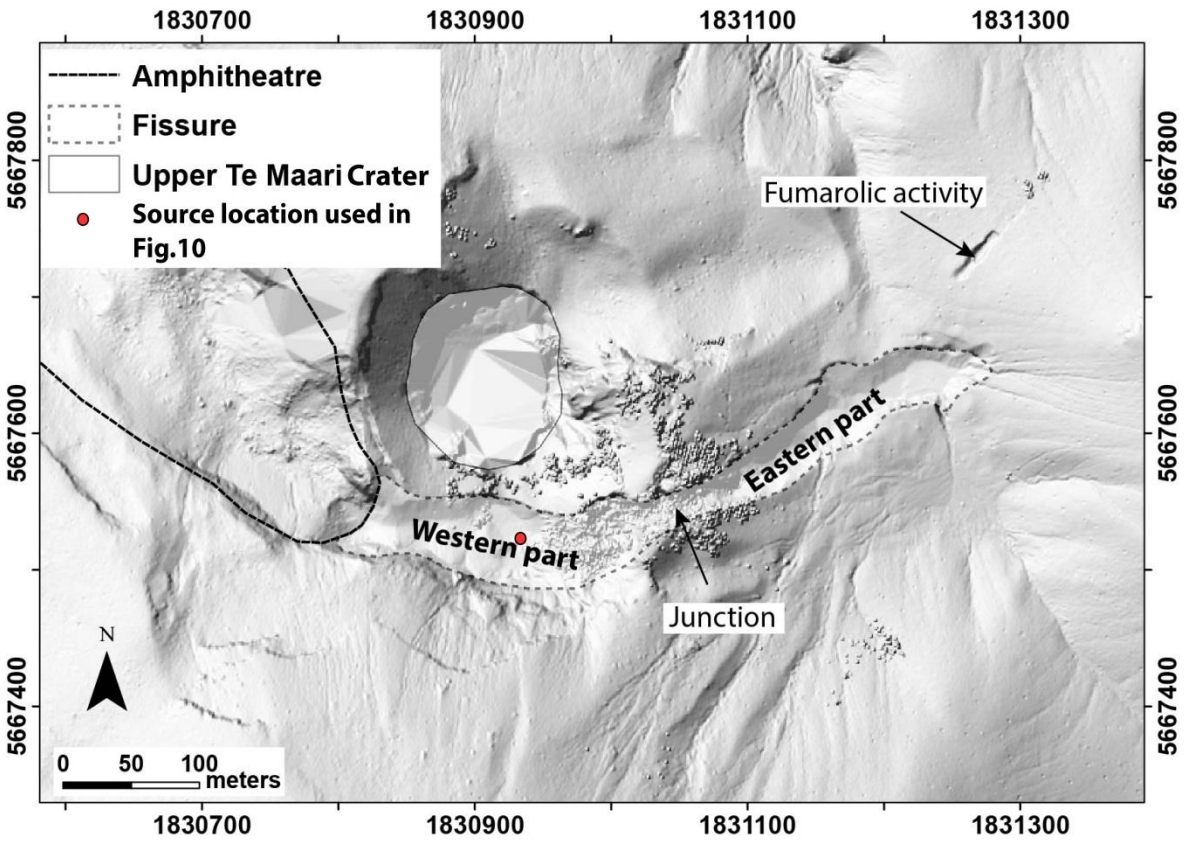

Fig. 6.4. Post-eruption Digital Elevation Model (DEM) based on LiDAR data of the fissure and Upper Te Maari crater area. The junction represents the narrowest and shallowest point of the fissure and delimits the eastern and western parts as shown on Fig. 6.3B.

Fissure	**Western part**	**Eastern part**
Direction	N282 W	N23 E
Length (m)	220	210
Max/Min (average) width (m)	10-60 (45)	10-40 (30)
Average depth (m)	19.5	16.4
Pre/post eruption volume difference (m^3)	200 100	148 200
Total volume of surge deposit (m^3)	*348 300*	

Table 6.2. Characteristics of the eastern and western fissures. Western and eastern PDC deposit volumes after Lube et al. (2014) are presented for comparison.

At the saddle between the eastern and western fissures (Fig. 6.3B and B′), pre-eruption deposits are in situ at the base of the fissure. Lithologies exposed on the eastern 10–20 m deep walls include several m-thick breccias and diamictons (Fig. 6.3A and B). The deposits are generally poorly sorted, and polylithic proximal pyroclastic units including dense and scoriacious blocks up to 1 m-diameter are observed up to 20 m below the pre-eruption

surface. Most lithologies are highly altered. In the western part of the fissure, many of the units are completely or partly altered hydrothermally and replaced by horizontally and vertically discontinuous zones (5 m thick by 30 m long) of hydrothermal clays. Original textures are observable, but clasts and matrix are often completely replaced. The western fissure is underlain by agglutinates that enclose dense blocks and agglomerates found at 0–30 m and c. 20–30 m below the pre-eruption surface, respectively (Fig. 6.5C, D and D′). They are formed by a mostly dark grayish breccia having sub-angular to angular lithic clasts within a fine-grained pale gray to dark gray matrix (Fig. 6.5E and E′). The gray matrix is compact and quite homogeneous fine-medium ash. Color changes (whitish, gray, reddish, beige, greenish) are attributed to a varying degree of alteration and/or secondary mineralization. Furthermore, blocks fallen from a zone of distinctive color contrast in the fissure walls show a discontinuous highly altered layer, 60 to 70 cm thick, made up of sub-rounded to angular altered clasts in a dense and inhomogeneous clay rich matrix separating two types of breccia (Fig. 6.5F). The breccias are composed of mostly lapilli-sized, highly altered, sub-rounded dense clasts in a gray fine and clay-rich matrix and show decreasing alteration with distance away from the highly altered layer, resulting in a finer matrix close to the contact with a color change from gray to greenish gray.

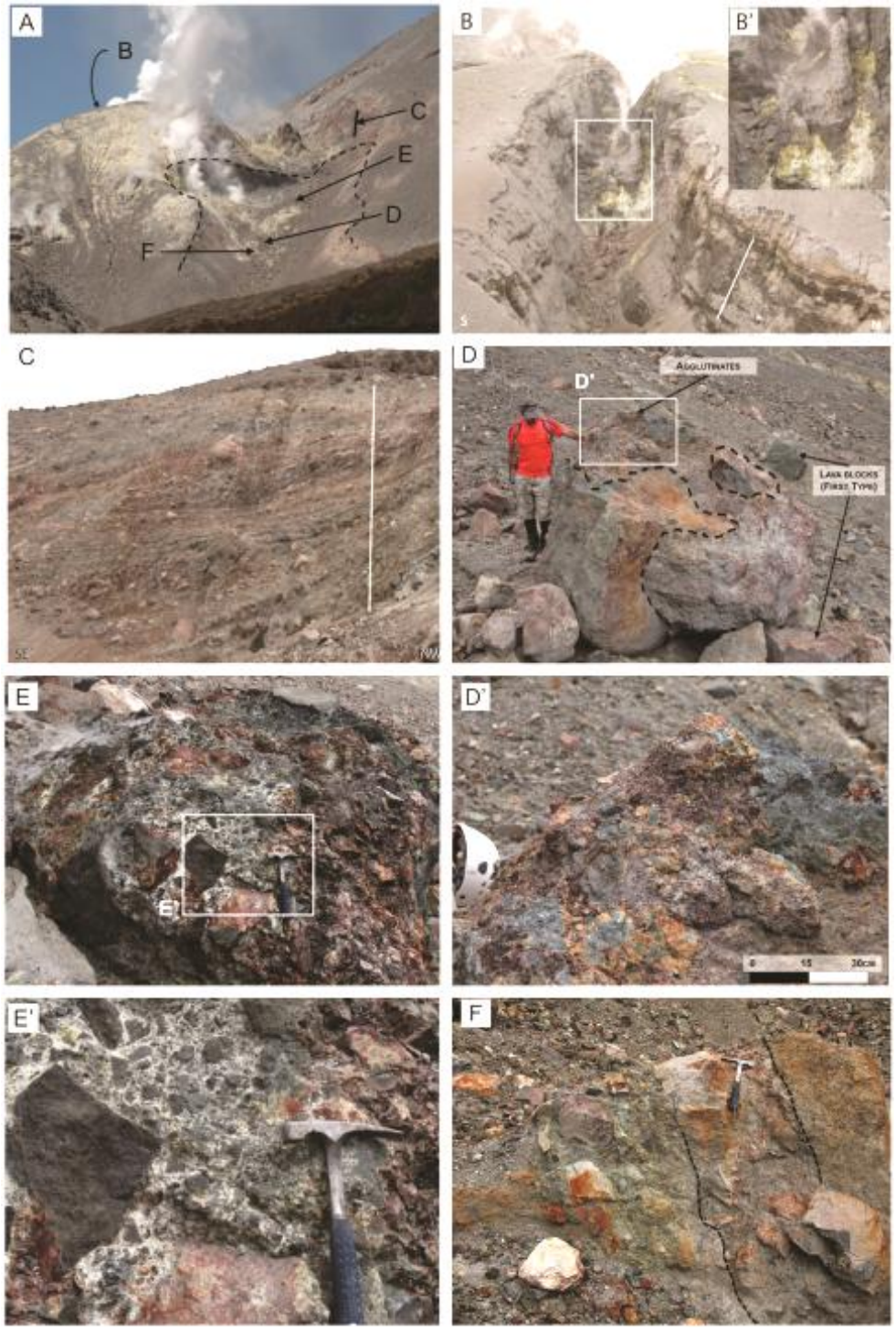

Fig. 6.5. A: View of the western fissure, A: Delineation of amphitheater (dashed line) created by the landslide (see Procter et al., 2014) and end points of section B,C and the blocks D,E, F described in the text. B: Eastern part of the fissure with exposures of the same stratigraphy as in A. The two white lines are 5 m long. B′: Closer look at the bottom of the junction between fissures. C: Stratigraphic section along the western fissure composed of a succession of proximal PDCs and fallout deposits. D–D′: Underlying, and in the background, single blocks of lava (first type) are present. Second type of block visible on the landslide amphitheater, corresponding to agglutinates attached to dense lava blocks (delineated by dashed line). E–E′: Breccia (third type of block) made by angular lithic in a compacted fine-grained matrix composing the base of the fissure. F: Block with a discontinuous highly altered zone (delineated by dashed line) separating two type of breccia.

6.3.2 Ballistic crater distribution

More than 2215 impact craters with a short-axis larger than 2.5 m were mapped in this study (Fig. 6.6A). Craters were classified by diameter into three classes: 1) 2.5–3.5m, 2) 3.5–4.5m, and 3) >4.5m. There is no obvious grading of crater sizes with distance (Fig. 6.6B). For example, the Tongariro Alpine Crossing, while located in the outer margin of the western ballistic field, has impact craters spanning the full range of observed crater diameters (<1 m to >10 m). No large craters were found within 200 m of the vent area. Many large blocks lie on the surface and in the PDC deposit in this proximal range; they were supplied by small rock falls from the crater surrounding walls and deposited with the PDCs respectively.

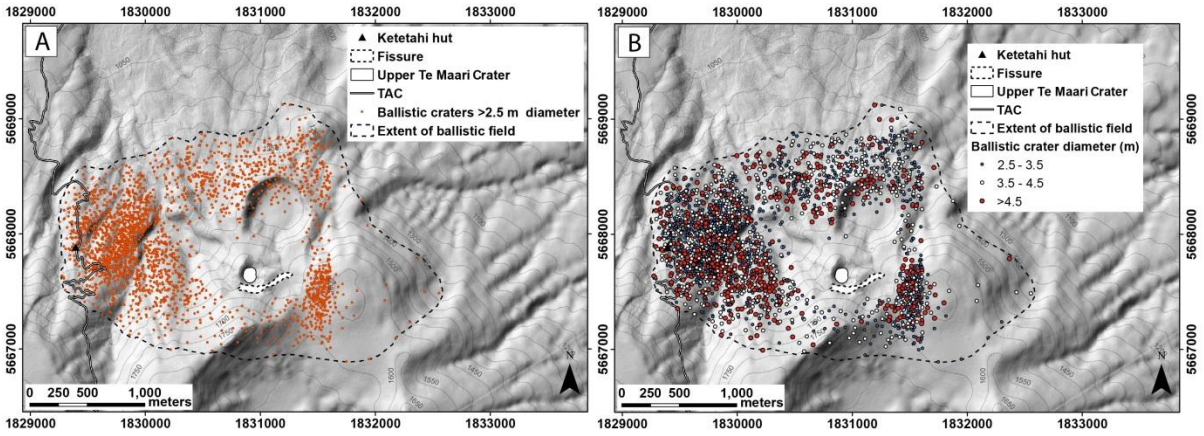

Fig. 6.6. A: Distribution of all >2.5 m size craters in the ballistic field. B: Crater size distribution: 2.5–3.5 m, 3.5–4.5 m and >4.5 m.

The 5.1 km^2 ballistic-impact field extends farthest to the WNW (1.7 km), is narrowest to the south (0.75 km) and intermediate towards the east and north (1.4 and 1.5 km, respectively). This gives the field a rough E–W oriented elliptical form (Fig. 6.2). The entire field shows an average spatial impact density of c.450 craters/km^2. The highest spatial densities (Fig. 6.7A) are in two distinct zones west and east of the vent area. In both areas, impact densities reach values six times higher than the average background density. A threshold of 2050 craters/km^2 was used to distinguish the eastern and western high-density zones from the background

spatial density. The western locus with crater densities up to 3450 craters/km^2, is centered ~1180 m WNW from the crater/fissure source area and shows a NNE elongate elliptical form. The eastern density locus (up to 2750 craters/km2) is similarly shaped, oriented N–S and centered ~600 m from the vent at a higher elevation. Each high-density area spans an azimuth range of 40–45°. The full lateral extent of the eastern zone is not as well defined as that in the west, because it extends beyond the range of the high-resolution orthophotograph. Nonetheless, the margins were walked out, including the most distal >2.5 m craters. Density maps for the <4.5 m crater-size classes clearly depict the western and eastern high-density loci, showing that the impact concentration occurs independent of crater size (Fig. 6B–D). A frequency analysis of all impact craters >2.5 m shows a unimodal distribution with a mode at 3.25 m, well above the truncation at 2.5 m.

6.3.3 Ballistic craters and block lithologies

In the western and eastern ballistic fields, PDC deposits are slightly thicker inside the craters, and both massive-textured and stratified PDC units are preserved (Fig. 6.8A and B). East and west of the vent, PDC deposits mantle 75% of the ballistic craters (Fig. 6.8A and C). Ballistic blocks were either preserved within their craters (Fig. 6.8D), shattered and scattered (Fig. 6.8E), buried, or missing (Fig. 6.8A). In the proximal area, large clasts are predominantly found without craters, but often syn-depositional with the massive PDC deposit (Fig. 6.8F; Lube et al., 2014).

In the north, however, impact craters often show a disturbed PDC stratigraphy that is also thinner than PDC deposits outside the craters. This indicates that, at a distance exceeding ~200 m from the vent, at least in the east and west fans, ballistic craters were created prior to PDC deposition.

Half craters are almost perfectly circular in plan shape with a diameter ratio (Dr) of maximum vs. minimum axis <1.1. Elliptical craters, with Dr >1.1 are usually found on steep leeward-facing slopes (in respect to eruptive source location). Elongate craters that are poorly covered by the PDC deposit often display a rim of ejecta with an elliptic shape that reflects the low impact angle of the block.

Ballistic blocks from craters of >2.5 m-diameter were classified into four lithological groups: 1. high-density clasts (d_{avg} = 2.4 g cm^{-3}) composed of angular, poorly vesicular, porphyritic andesitic lava (Fig. 6.9A and B) some of which has rims or partial coatings of agglutinate (Fig. 6.9B); 2: low-density andesitic scoria or highly vesicular lava (c. 1.3 g cm^{-3}) (Fig. 6.9D and E); 3. intermediate-density blocks of breccia, agglomerate or agglutinate (c. 2.1 g cm^{-3}); which are commonly heterolithologic, containing angular to rounded block or lapilli clasts of varying textures incorporated in firm ash-rich matrix or alternatively within welded agglomerate (Fig. 6.9G–I); the latter clast-types have variable degrees of alteration, with pyrite and chalcopyrite crystals and sulphur filling cracks (e.g. Fig. 6.9G); and 4. intermediate-density blocks of poorly vesicular columnar-jointed lava (c. 2.1 g cm^{-3}),which are angular and the least altered of the four lithofacies (Fig. 6.9J and K). Clast types 1, 2 and 3 have been found in fresh exposures of the Upper Te Maari area inside the eastern and western fissure areas (Fig. 6.5C and D). Blocks of type 1 are uniformly dispersed over all the ballistic impact area (Fig. 6.9C), type 2 clasts are present, but less common outside the west and eastern fields and type 3 clasts are restricted within primarily the western field (Fig. 6.9F and J). Type 4 clasts are only found in proximal to medial areas (within 1.2 km of the vent) and although sparse, form a roughly circular distribution (Fig. 6.9M). Overall, lithotype 1 is the most common and types 3 and 4 are the rarest (Table 6.3).

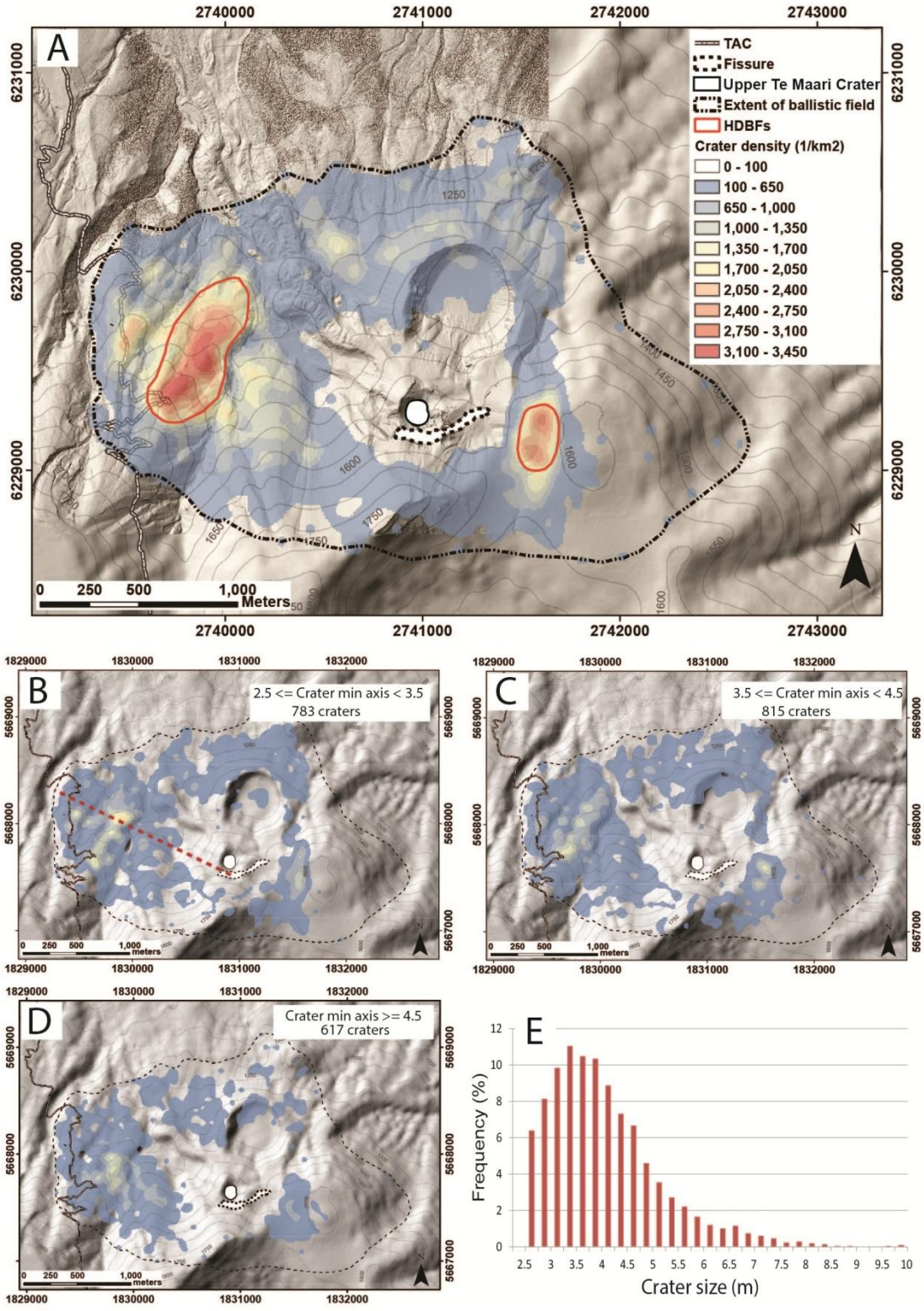

Fig. 6.7. Distribution of ballistic impact craters of various size classes. A: All craters ≥2.5 m, the background density is 450 craters/km2 and the red-outlined areas (HDBF) are the loci of highest spatial density. B: Craters between 2.5 and 3.5 m. The red dotted line defines the profile shown in Fig. 6.10. C: Craters between 3.5 and 4.5 m. D: Craters ≥4.5 m. E: Crater size distribution.

Fig. 6.8. Impact craters: A: A 6m diameter crater within the high-density western part of the ballistic field. A′: PDC deposit covering the crater, scale in cm. B: 3 m-wide crater in the eastern high-density impact area. B′: PDC deposit (massive and stratified layer) inside and beside the crater. C: 2 m-wide crater in the northern ballistic field. C′: Very thin laminated ash cover. D: 4 m ballistic crater with preserved block (circled) outside of the PDC inundation area WNW of the crater. E: Scattered ballistics blocks (highlighted) in a 4 m-wide crater in the western deposit area. F: Block deposited during the PDC emplacement. The Block impacted the massive PDC layer and is covered by the stratified layer. The flow direction (left to right) is indicating by the thinning of the top PDC layer behind the block.

Lithotype	West high density field (%)	Eastern high density field (%)	Northern field (%)
1 - Lava	62	53	90
2 - Scoria	25	43	0
3 - Breccia/agglutinate	8	0	0
4 – Fresh lava	5	4	10

Table 6.3. Proportions of different lithologies within and outside the eastern and western high-density impact area and the northern impact field.

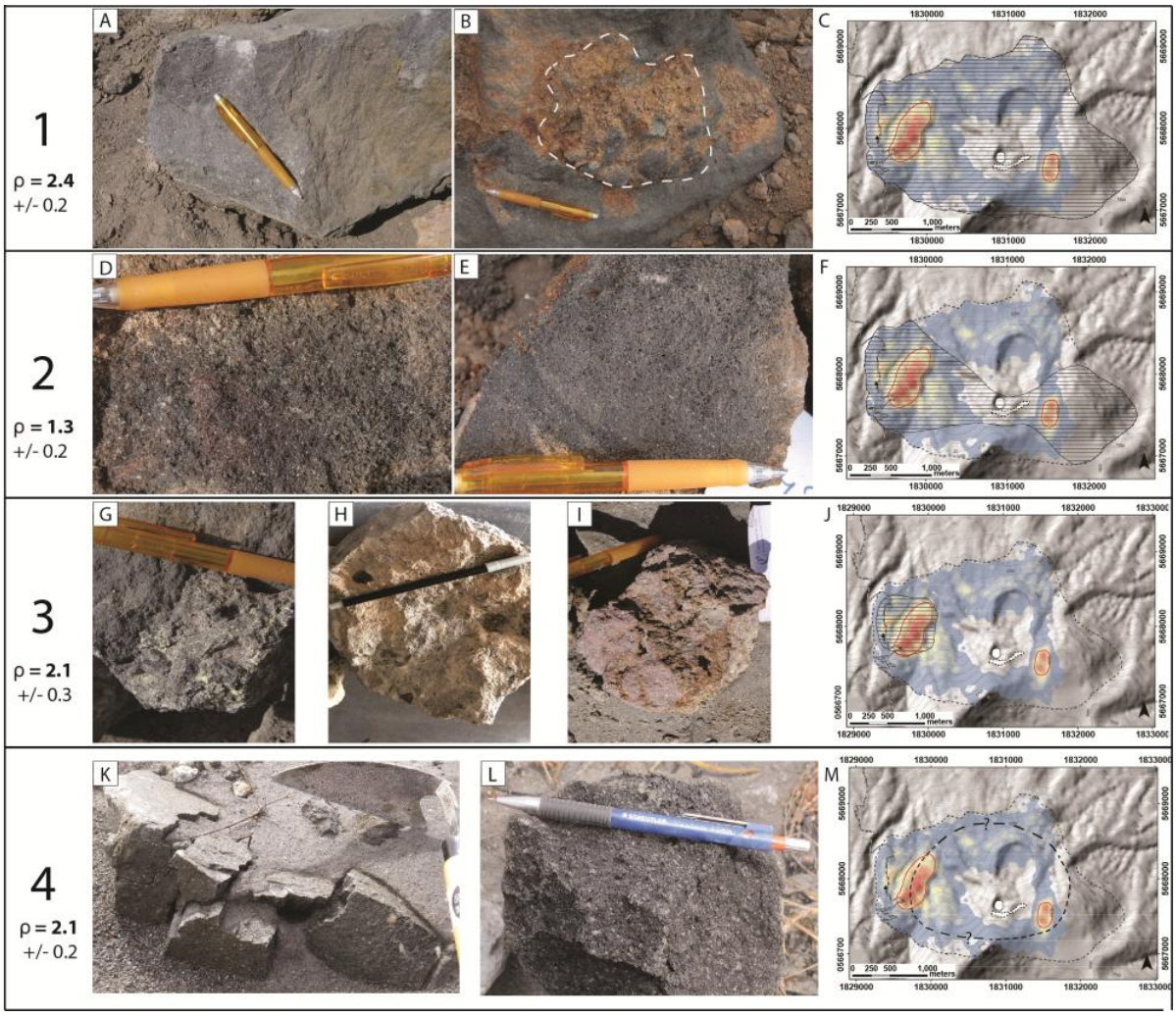

Fig. 6.9. Lithologies, densities and distribution of the four classes of ballistic blocks (densities in g/cm3). Stripped lines represent the area where ballistic lithology types were found (C, F, J and M). Block type 1 is made up of dense lava (A and B), sometimes with attached agglutinate (B; circled by dotted line). Type 2 blocks are vesicular scoria or vesicular lava fragments (C and D). Type 3 clasts include breccias, agglomerates and agglutinate blocks (G, H and I), that can be hydrothermally altered (G), or oxidized (I). Type 4 blocks are porphyritic, angular, poorly vesicular, often columnar jointed and fresh to poorly altered andesitic lava (Fig. K and L).

6.3.4 Estimation of launch-angles of the western ballistic field

The calculation of preferred launch angles for ballistics blocks was estimated for the westerly-directed explosion, for which the ballistic impact dataset is most complete. I make the simplifying assumption that the eruption source was a point source located at the centre of the western fissure zone (Fig. 6.4). A profile of topography and crater-density from the model source through the western high-density impact zone is displayed in Fig. 6.10B.

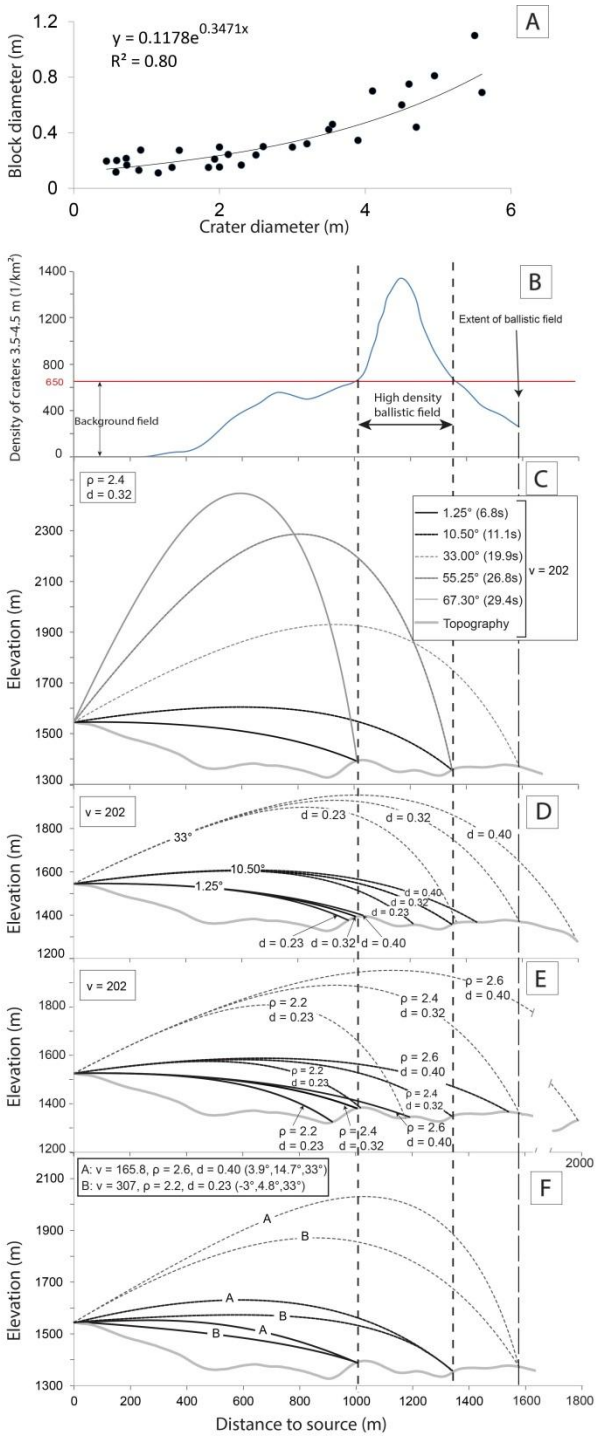

Fig. 6.10. Calculated possible ballistic trajectories for the range of block sizes and density seen in the western high impact density zone using Eject! (Mastin, 2001). A: Relationship of crater diameter to type 1 block-diameter. B: Crater density profile on the westerly traverse (Fig. 6.7B) for 2.5–3.5 m diameter craters, showing the limits of the high-density zone (>650 craters m^{-2}) between 1010 and 1350m from source. C: Calculation for velocities "v"=202 m s^{-1} of the optimal angle 33° for blocks of 0.32m of diameter with a density 2.4 g cm^{-3} and estimates of launch angle to reach the high density zone. D: Estimation of shallow angle trajectories for a range of observed block diameters (0.23–0.4 m) using initial parameters from panel C. E: Effect of the range of density and block diameter on trajectories using launch angles and velocity from panel C. F: Estimation of the range in velocities (165.8–307 m s^{-1}) explaining the range of ballistics found in 2.5–3.5 m diameter-craters along the topographic profile.

In order to yield useful estimates of the predominant geometry of the western explosion, I only use a narrow sub-set of clast densities and sizes. I focused on the most common Type 1 lithology (~60% of the ballistics in the western field; Table 6.3), which have a density of 2.4 ± 0.2 g cm^{-3}. The relationship between crater diameter and Type 1 block diameter approximately follows an exponential law (Fig. 6.10A). The uncertainty in this relationship varies with crater size. However, the fit is very good for craters of 2.5–3.5 m, which also includes the mode of the ballistic crater-size distributions at 3.25 m (Fig. 6.7E). Following this power law, the modal crater diameter corresponds to a Type 1 clast size of 0.32 m. An assumption of randomly distributed craters of 2.5–3.5 m size (related to Type 1 blocks) is supported by the results of transect studies by Fitzgerald et al. (2014), which show that there is no size grading within block lithology class with distance in the western ballistic field.

The most distal craters in the 2.5–3.5 m diameter range are 1600 m from source, on the same bearing as the western high-density zone (Fig. 6.7B). Thus I can assume that craters of the farthest and high density ballistic zone are related. Hence craters of the distal area represent the optimal launch angle of 33° to the horizontal. The optimal launch angle varies from the ideal angle of 45° because of the difference in elevation of the source and landing positions. Using a density of 2.4 g cm^{-3}, a 0.32 m block size and an ejection angle of 33°, a velocity of 202 m s^{-1} is required for the block to reach the maximum observed extent of the western field at 1600 m from source (Fig. 6.10C). Using this velocity, and the above clast properties, I determined the two ballistic launch angles that yield trajectories towards the proximal and distal ends of the Western high-density field (1000 m and 1350 m from source, respectively). These two angles define the geometry of the central portion of the western explosive jet, but I note that outside this core, a lower-density halo of ballistic blocks was probably also ejected on wider angles. In this case, two optimal solutions for the ejection angles can be obtained: a shallow blast, between 1.25 and 10.50°, or a high-angle jet, between 55.25 and 67.30°. The

high-angle solution implies a ballistic travel time to 1000 m of ~27 s (or >35 s if a velocity correction after de'Michieli Vitturi et al. (2010) is taken into account). The stratigraphy shows that ballistic clasts landed before PDC deposition. As ballistics and PDC-producing blasts are initially coupled, this implies a maximum average PDC velocity of ~37 m s^{-1}. However, minimum PDC velocities 1000 m from source were independently estimated at 60–70 m s^{-1} (Lube et al., 2014). Thus the high-angle jet solution is unlikely. By contrast, the very shallow launch angle option implies much lower ballistic travel times, down to 6.8 s (Fig. 6.10C) giving enough time for ballistic cratering to occur before PDC deposition. The shallow launch angles and an initial velocity of 202 m s^{-1} would produce final impact angles of between 26° and 68° (predicted by Eject! model), in agreement with field observations of asymmetric impact crater rims and frequently observed bounced impactors.

I also investigated the effects of block density and size on the ballistic trajectory. For instance, blocks of 0.23 m to 0.4 m diameter (corresponding to crater diameters of 2.5 m and 3.5 m, respectively) at initial velocities of 202 m s^{-1}, and ejection angles of 1.25 to 10.50° would fall in a zone from 960 m to 1450 m from the vent (Fig. 6.10D), This result agrees with the distribution of the high-density field. At the optimal launching angle, 0.4 m blocks would reach a distance of 1800 m, slightly outside the ballistic field limits. If clast density is taken into account, the effect is larger (Fig. 6.10E), with high-density clasts (2.6 g cm^{-3}) of 0.4m in diameter at the optimum launching angle theoretically reaching c. 2 km. This suggests that a single initial velocity for all ballistics cannot explain the distribution of the different block sizes and densities observed in the western ballistic field. This is not surprising because the effectiveness of gas–particle coupling in the initial burst will vary spatially and temporally and is related to the particle size and density. Also, our field observations show that blocks inside Upper Te Maari Crater do not start from a single point source as assumed here. Further assumptions made in the Eject! calculation such as uniform

clast drag coefficients and clast shapes also oversimplify the natural process. However, there are insufficient data to characterize these starting conditions with more precision at this stage. I explored the range of launch angles and velocities leading to the 1D distribution of ballistic craters (2.5–3.5 m diameter) along the western transverse (Fig. 6.10A) using boundaries of the high-density zone, with observed block-property limits (0.23 m, 2.2 g $cm^{-3}$and 0.4 m, 2.6 g cm^{-3}). This leads to a range of combinations of velocities and launching angles. Matching the above defined boundaries of the high-density zone (1000 m to 1350 m), yields velocities between 165 and 310 m s^{-1} (Fig. 6.10F) and launch angles between −3° to 15°. The absolute values of initial velocities are probably overestimated, because the Eject! model approach neglects any acceleration and deceleration processes during initial block coupling with the gas–particle mixture (de'Michieli Vitturi et al., 2010). Hence true velocities may be ~30% lower, 120–215 m s^{-1}.

6.4 Discussion

6.4.1 Crater distribution

Ideal ballistic clast-distributions from vertical jets are circular. High spatial densities concentric around a vent thus indicate a dominantly steep launch-angle for ballistics (>45°), which are generally associated with an eruption column (e.g., de'Michieli Vitturi et al., 2010). For laterally directed explosions, more complex ballistic clast distributions are found, but with concentrated zones in the direction of blast (Alvarado et al., 2006). Ballistic block deposition in a fan-shape was reported from a single strombolian burst at Stromboli volcano (Gurioli et al., 2013), and from steam eruptions produced by decompression of hydrothermal systems, such as the 2007 Ruapehu eruption (Kilgour et al., 2010). In the latter case, surtseyan jets produced small-scale PDCs and ballistic blocks that were deposited in similar

directions from the vent over similar areas. Large lateral eruptions (blasts) such as the ~1150 BP Sugar Bowl deposit at Mount St Helens, USA (Mullineaux and Crandell, 1981), or the September 1996 blast of Soufrière Hills volcano yielded a narrow radial distribution of ballistic blocks (Branney and Kokelaar, 2002). The May 1980 Mount St Helens, USA blast involved multiple explosions directed at shallow take-off angles (average 30°, Belousov et al., 2007). Such cases have observed (e.g., Voight, 1981) or modeled shallow ballistic trajectories (Esposti Ongaro et al., 2005).

By comparison with these examples, the 6 August 2012 Upper Te Maari hydrothermal system explosion produced complex ballistic impact patterns whose spatial density distribution can be best explained by three partially overlapping fields or fans of impacts. The western and eastern fans are characterized by high-spatial densities of impacts focused on a narrow lateral spread (<45°) centered c. 1180 and 600 m from the source area, respectively. These relate to the first two blasts witnessed by observers of the eruption. The third explosion was apparently sub-vertical with an angle to the north, in association with the short-lived ash plume. Upper Te Maari Crater is clearly opened to the north; this asymmetry may explain a sub-vertical directed explosion northward (Sung-Wook Kim, unpublished results). Ballistic clasts associated with the third explosion phase mantled the two earlier fans as well as being distributed in the northern sector.

The east and west fan-shaped distributions of ballistic impact craters are likely due to a lateral jetting mechanism, which also generated PDCs in both of these directions (Lube et al., 2014). The spatial limits of the western high-density zone, with ballistic clast properties constrained by craters 2.5–3.5 m in diameter, were most likely controlled by preferential ejection of ballistic blocks at angles between −3 to 15° to the horizontal. This is the most likely central concentrated portion of the westward jet, but ballistic blocks may have been also ejected at higher launch angles given the lateral gradational boundaries of the high-density field. Even

when considering the significant effects of variable density and block size on possible ballistic trajectory, there is a strong likelihood of low-angle launch of most ballistic blocks with variable initial velocities depending on the efficiency of their coupling with the expanding explosive jet. The relatively large diameter of ballistic craters compared to the small size of the blocks (ratio of ~10) may be related to the soft/friable nature of the substratum most of which is composed of non-compacted, soft, pumice-rich, Taupo Ignimbrite, capped by a firmer brown weathered andesitic ash-sourced topsoil. Even though the clasts were apparently launched at shallow angles, only 30% of the Upper Te Maari ballistic blocks created elongate craters (diameter ratio > 1.1) on the stoss sides of ridges. However, 70% of craters on the lee sides of ridges are elongate. The slope, thus, had an important influence on crater ellipticity, by increasing or decreasing the local impact angle onto the landing surface. Another effect of the topography is shown by the enhancement of bouncing of blocks out of their craters on lee sides of ridges.

6.4.2 Eruption source

Spatial distribution and clustering of ballistics have been used to localize the approximate position of the eruptive vents, e.g., of the Minoan eruption from Santorini Caldera (Pfeiffer, 2001), a maar in Italy (Buttinelli et al., 2011), or the late 18th century eruption of Kīlauea caldera in Hawai'I (Swanson et al., 2012). Eye-witness and geophysical observations of the 6 August 2012 Te Maari eruption help explain the types of events and their timing, but do not give precise details about the accurate source. The Type 3 ballistic blocks (agglutinate and hydrothermally altered block and lapilli tuff) found only in the western fan of ballistic impacts were clearly derived from the beds of similar lithology now exposed in the western part of the fissure, within and surrounding the headwall of the landslide that preceded this eruption. This lithology also occurs commonly within the debris avalanche deposit. The Type

2 clasts were found in the proximal vent area as well as in the western and eastern fan-shaped ballistic field. Because of the absence of such block lithology on the southern or northern areas, I relate them to the fissure area. The Type 1 ballistic clasts are typical of the entire Upper Te Maari area and are hence not diagnostic of any particular vent site. Type 4 blocks are the most confined, within a roughly concentric distribution and are also the freshest type of clast found. This may suggest that these blocks were erupted from the Upper Te Maari vent where they could have been derived from a lava plug or part of the AD 1530 lava flow disrupted during vent clearing.

The most likely low take-off angle of the blocks making up the high density western ballistic impact area shows that the vent location was most probably the landslide headwall area. Sourcing these from the main Upper Te Maari Crater would require high ejection angles and thus travel times that are too long in relation to the PDC passage and deposition. The mechanism for low-angle ballistic clast ejection in the Upper Te Maari eruption probably involves lateral or directed explosion of a particle-laden mixture (a volcanic jet or blast). Initially, volcanic blasts have a narrow cone shape that expands laterally, at times influenced by conduit geometry. A vertical jet transforms into a column, where the flow maintains its initial direction when buoyancy becomes the driving mechanism. Lateral blasts, however, depart from the initial impulse direction (burst phase) after a few seconds because of the drag and gravity (collapse phase) and can spread in a broader area of up to 180° (Kieffer, 1984; Buttinelli et al., 2011). At Upper Te Maari, directed volcanic jets probably resulted from the explosive release of pressurized hydrothermal fluids following landslide unroofing of part of the hydrothermal system. These blasts entrained and accelerated lithic material from the fissure area during the burst phase, including large blocks that later decoupled as ballistics. Stratigraphic position shows that for both the east- and west-directed explosions, the associated ballistics landed prior to PDC arrival. In contrast, the third explosion from the

Upper Te Maari vent created a sub-vertical explosion with associated ballistics ejected during initial vent clearing with a slight northward component.

Acoustic data of the August 6 Upper Te Maari eruption suggest that 4 explosions occurred in rapid succession within less than 20 s (Jolly et al., 2014). A rough estimate of the relative explosion energy based on infrasound data of the four explosions yields: 20% (explosive phase 1); 5% (explosive phase 2); 50% (explosive phase 3); 20% (explosive phase 4). Eyewitness accounts and the ballistic data presented here give evidence for only three large explosion events. These are likely related to the infrasound events 1, 3 and 4. The second, smallest event may also have ejected ballistics, but it is not recognizable in our data.

In the Upper Te Maari eruption the collapse and landslide destabilized part of the hydrothermal system by unloading. There was a delay of 3min and 12 s (Jolly et al., 2014) before explosive eruption that may reflect the process of fracture formation through capping deposits that sealed the system at depth. According to a witness, the eastern explosion occurred at a high angle, possibly with its orientation and the long eastern fissure representing a pre-existing weakness (Fig. 6.11). The low-angle western explosion was likely strongly influenced by the newly formed landslide headwall scarp which might have reflected the explosion from roughly flat-lying beds exposed in the base of the headwall area.

6.5 Conclusions

Ballistic blocks were produced by at least three of the brief explosive phases of the August 6 2012 Upper Te Maari hydrothermal eruption. The first phase was a short-lived eastward-directed explosion, jetting particles on ballistic trajectories of N45° to create an impact fan to the east, with a high spatial-density zone of ballistic impacts concentrated c. 600 m from the source (Fig. 6.11B and B′). The narrow, focused explosion (on a <45° horizontal arc) was

caused by escape of overpressured hydrothermal fluids through a pre-existing weakness in the form of a long cross-slope crack or pre-existing fault immediately upslope and east of the Upper Te Maari Crater (Figs. 6.1B and 6.3C). This first event was apparently triggered by rapid destabilization of the Upper Te Maari hydrothermal system following a landslide from the western flank of the Crater (Fig. 6.11A). Immediately following the east-directed explosion, a similar, but larger explosion was generated from the westward-facing landslide scarp (Fig. 6.11C). This explosion initiated in flat-lying cemented breccias and tuffs was directed westward with very low (<15°) take-off angles, probably influenced by the geometry of the landslide headwall. The westward-directed ballistic block fan is the only area that includes blocks with a distinctive tuff and breccia lithology, matching that exposed in the new landslide scarp. These blocks travelled up to 1600 m, but formed a zone of very high spatial impact intensity between 1000 and 1350 m from source (Fig. 6.11C′). Following the two laterally directed events, a third sub-vertical explosion occurred from within the main Upper Te Maari Crater producing a concentric rain of large ballistic particles as well as a weak ash plume (Fig. 6.11D and D′).

The small eruption thus involved three phases from three separate vent areas. The eastern and western jets were associated the production of low-temperature PDCs, that arrived in the western high-density impact area a few seconds after ballistic impact craters were formed. After the eruption, large changes around the vent area included a fissure-like feature extending north of and upslope of the Upper Te Maari Crater (Fig. 6.3). The origin of this was initially unclear, but ballistic clast lithologies allowed identification of the source for the largest western explosion. Similarly the eastern jet, characterized by Type 1 and 2 lithologies, was identified as coming from a new eastern arm of the fissure, located along a previously visible lineation, possibly marking an old fault system.

Through detailed measurements of ballistic blocks on the western fan, the geometry of the initial western jet was reconstructed. It appears to have had a predominant horizontal radial expansion of 40–45° and launch angles for ballistic blocks between –3 to 15° relative to horizontal. Such focusing produced startlingly long-range impacts, with heavy concentrations of blocks landing in tightly focused areas. As a result, low-angle hydrothermal blasts should be included in regular hazard assessments of all areas where hydrothermal or vulcanian explosions occur through layered, altered and fault-traversed volcaniclastic strata.

Landslide failure planes, and old fissures and fault lines can amplify the focus and directionality of hydrothermal explosions. In the case of the 6 August 2012 eruption, the main explosion was directed towards the most vulnerable and populous area possible in the region, the Tongariro Alpine Crossing and the Ketetahi Hut. The present geomorphology of the Upper Te Maari Crater area, with a deep westward-facing amphitheatre, makes westward focusing likely for any future eruptions and explosive jetting through its hydrothermal system.

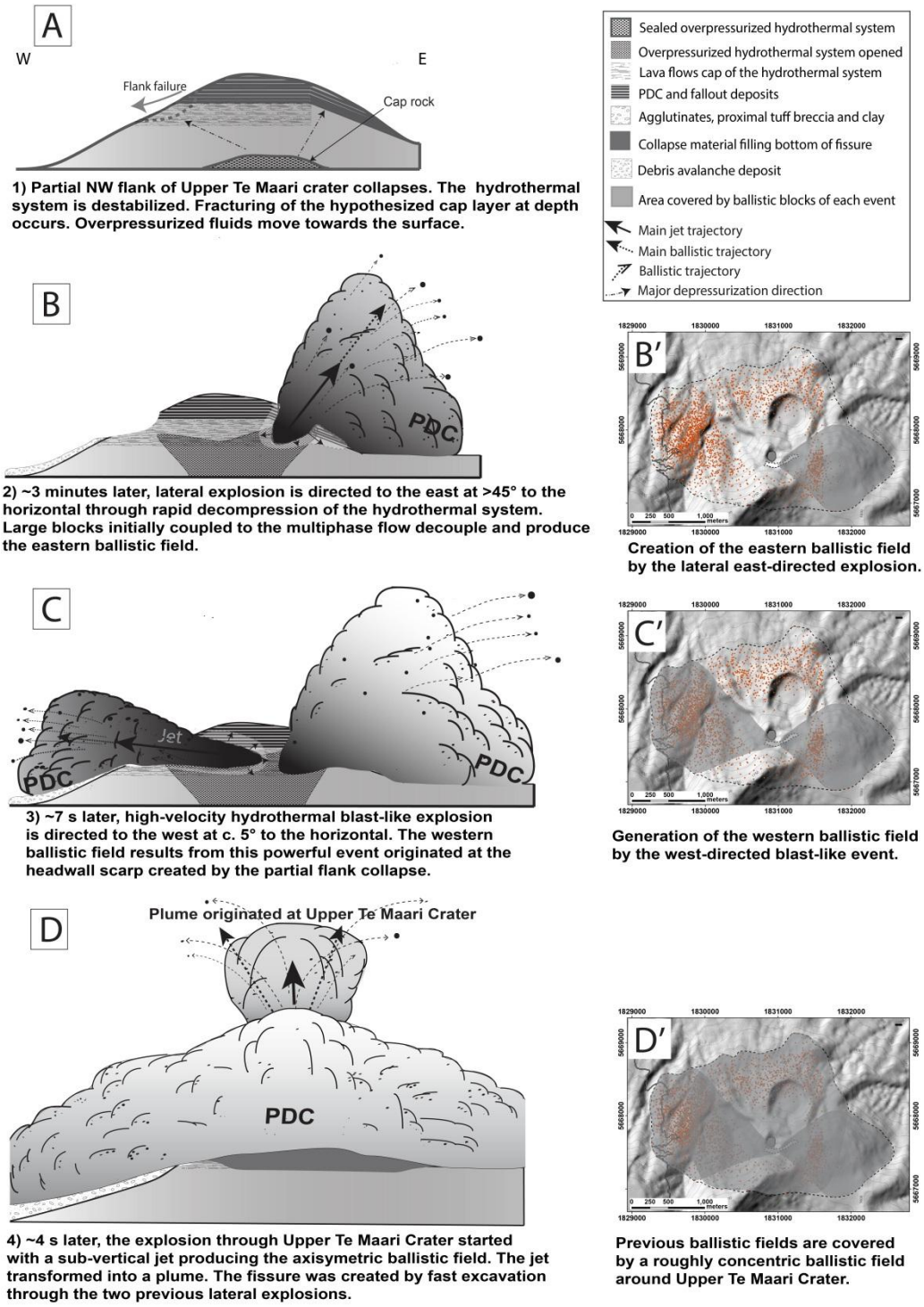

Fig. 6.11. Model for the 6 August 2012 eruption of Upper Te Maari. After destabilization of the hydrothermal system (A), three main explosions (B–D) produced distinct ballistic fields partially overlapping (B′–D′). Not to scale.

Chapter 7 – Transport and deposition processes of the hydrothermal blast of the 6 August 2012 Te Maari eruption, Mt. Tongariro

Chapter contents

This Chapter is based on a published paper:

Eric C.P. Breard, Gert Lube, Shane J. Cronin, Greg A. Valentine. 2015. Transport and deposition processes of the hydrothermal blast of the 6 August 2012 Te Maari eruption, Mt. Tongariro. *Bulletin of Volcanology*.

Participating authors:

Eric C. P. Breard (Field work, manuscript development, data analysis, manuscript writing and editing).

Gert Lube (Field work, manuscript editing and discussion)

Shane J. Cronin (Manuscript editing and discussion)

Greg A. Valentine (Manuscript editing and discussion)

Chapter 7 – Transport and deposition processes of the hydrothermal blast of the 6 August 2012 Te Maari eruption, Mt. Tongariro

7.1 Introduction

Volcanic lateral blasts result from powerful, laterally directed explosions that transform into the most mobile and hazardous type of pyroclastic density currents known on Earth relative to their volume. They occur during the rapid unloading of lava domes (e.g. Montserrat in 1997, Druitt and Kokelaar 2002; Mt. Lamington in 1951, Belousova et al., 2011), flank collapses exposing cryptodomes (e.g. the 1980 blast of Mount St Helens, Lipman and Mullineaux, 1981; Bezymianny in 1956, Gorshkov, 1959; Belousov 1996; Belousov et al., 2007), and also during rapid unloading of hydrothermal systems (e.g. Bandai in 1888, Glicken and Nakamura, 1988; Fujinawa et al., 2008; Tongariro in 2012, Lube et al., 2014). Our understanding of lateral blast dynamics is based on a combination of direct observations of the Mount St Helens blast in 1980 (e.g. Voight, 1981), detailed field studies of blast deposits (Fisher, 1990; Druitt, 1992; Belousov 1996; Sparks et al., 2002; Voight et al., 2002), and theoretical models and numerical simulations (Bursik et al., 1998; Esposti Ongaro et al., 2008; Esposti Ongaro et al., 2011). An early model of laterally directed explosions (Kieffer, 1981) considered high-velocity (>300 m s-1) nozzle flows, producing under-expanded jets. More-recent, numerical multiphase flow models suggested that these Mach disk phenomena probably do not occur (Ongaro et al., 2011; Ongaro et al., 2008; 2012). Instead, blast-related destruction patterns are better explained by the spatial partitioning of internal dynamic pressures. Following these recent computational studies, volcanic blasts are now believed to evolve through three main stages: the **burst,** a decompression stage during which the magma is fragmented simultaneously with the passage of a decompression wave. A multiphase

mixture of gas, juvenile and lithic particles accelerates. This is followed by gravitational **collapse** of the mixture which is denser than the surrounding atmosphere, to form a ground-hugging current. The final stage is the development of a stratified **pyroclastic density current** (PDC) the dynamics of which are dominated by interaction with topographic obstacles, turbulent diffusion, segregation and sedimentation of particles (Belousov et al., 2007). Velocities of such currents in more recent multiphase models (e.g. Ongaro et al., 2011; Ongaro 2012) are typically <180 m s^{-1} for the MSH blast, much lower than predicted by the earlier nozzle flow hypothesis (i.e. >300 m s^{-1}). Despite this, however, the mixture may locally reach supersonic velocities. The hazard and damage potential of such flows is related to the particle carried within them and to their high dynamic pressures (Valentine, 1998; Baxter et al., 2005).

The relative infrequency of blasts means that many aspects of their transport and deposition remain controversial (Belousov et al., 2007; Cronin et al., 2013; Komorowski et al., 2013). Here I present new information from a low volume, end-member, hydrothermal blast deposit from Mt. Tongariro. I document the sedimentary facies architecture of these well-preserved PDC deposits and use proximal-to-distal facies changes along the main blast axis to interpret the PDC transport and deposition processes. I also discuss the interaction of the flow with topography and document the associated deposit bedforms.

PDC deposit of the August 6 2012 Upper Te Maari crater eruption

On the night of August 6 2012, a partial collapse of the western flank of Upper Te Maari crater (Tongariro Volcanic Center, New Zealand, Fig. 7.1A) triggered a c. 20 second-long series of four hydrothermal explosions of the partially sealed and pressurized hydrothermal system below the volcano (Jolly et al., 2014; Lube et al., 2014). The first three explosions

excavated a 430 m-long, up to 65 m-wide and 30 m-deep fissure, immediately south of Upper Te Maari crater, and generated directed low-temperature pyroclastic density current (Fig. 7.1B and C).

Initial stratigraphic and sedimentary work on the PDC deposits showed that these are exclusively composed of non-juvenile clasts, and that they display similarities to magmatic blasts and blast-like surges, despite the relatively small scale of the event and its low emplacement temperatures (Efford et al., 2014; Lube et al., 2014). Within the first c. 8 seconds of the eruption, two easterly-directed particle-laden jets associated with the initial two explosions excavated the eastern part of the fissure. These were immediately followed by the third and largest, 4-8 seconds long explosion that excavated the western part of the fissure and which produced a shallow inclined jet to the WNW (Breard et al., 2014; Lube et al., 2014). The collapses of the three jets fed a pyroclastic density currents that spread radially outwards from the fissure to inundate a 6.1 km^2 area of rugged ridge and valley terrain. Due to the directionality of the explosions, the resulting 340,000 m^3 PDC deposit exhibits a strong WNW-E asymmetry with the longest runout distances towards the WNW (2.6 km) and E (2.5 km), the shortest runout to the south (0.5 km) and intermediate runout to the north (1.6 km). The geometry of deposit isopachs and the zones of largest PDC damage parallel the asymmetric deposit fingerprint and highlight the major blast axis to the east and WNW (Fig. 7.1B). Here I focus on analysis of PDC deposits emplaced along the main WNW axis of the directed PDCs.

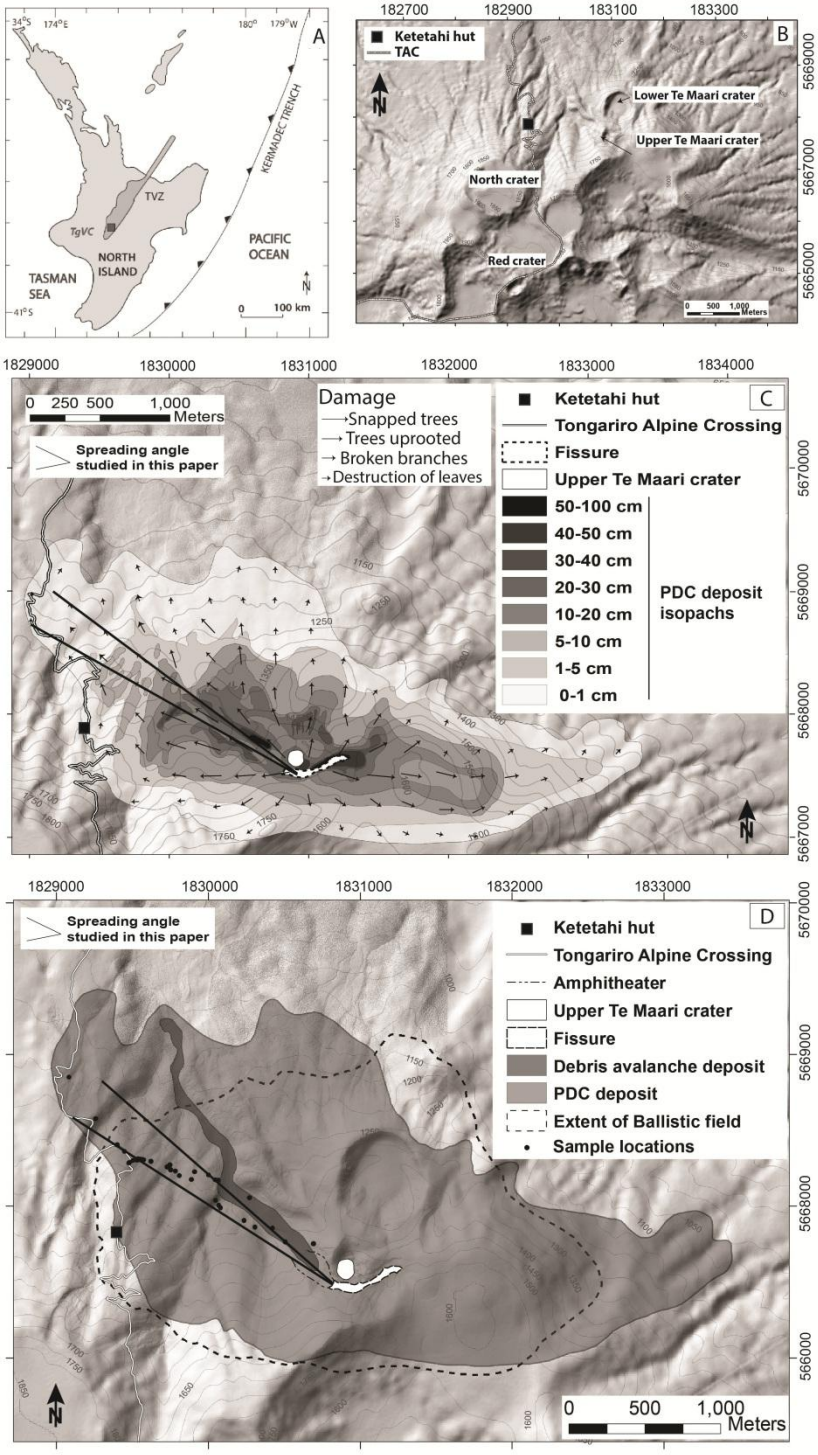

Fig. 7.1. A: Location of the Tongariro Volcanic Center (TgVC) in the Taupo Volcanic Zone (TVZ) of New Zealand. B: Location of the Upper Te Maari crater in the TgVC. C: Isopach map of the PDC deposit and flow directionality and damages (modified from Lube et al., 2014). D: Distribution of the eruption units of the 6 August 2012 Te Maari eruption (modified from Breard et al., 2014). The black line indicates the sampling transect along the main spreading axis for the WNW blast.

7.2 Methods

7.2.1 Characterizing the PDC deposit along the WNW sector

Along the main WNW blast axis (Fig. 7.1C), excavated profiles were described on a mm-scale, and bulk samples of individual PDC depositional units were taken for granulometric analysis. To characterize large-scale thickness variations of the bulk deposit and individual depositional units, average thicknesses were computed from measurements of at least 20 dissected beds at each location. The overall dune dimensions were also measured. Samples were sieved to 500 μm, and finer fractions were analyzed with a laser particle size analyzer. The void ratio (E) of the PDC deposit was estimated after quantification of the clast density for eight full-Φ grain-size fractions with a Micromeritics GeoPyc® 1360 Envelope Density Analyzer (for bulk density) and a Quantachrome He Ultrapycnometer 1000® (for grain skeletal density). In order to characterize the settling velocity of clasts of different size fractions, the shape factor (Ψ) was measured from high-resolution digital photographs of -3 to 3 Φ grain-size fractions, following the methods of Dellino et al. (2005).

7.2.2 Total grain-size distribution

PDC deposit grain-size and thickness data from 24 sample locations along the WNW blast axis were integrated to yield a total grain-size distribution (see supplementary material in section 7.5). In addition, the grain-size distribution of ballistics (co-generated with the explosions, but deposited independently from the PDC; e.g. Breard et al. (2014) over the transect was calculated by integrating the ballistic grain-size, number density and clast density data reported in Breard et al. (2014) and Fitzgerald et al. (2014)). Estimates of both components were combined to characterize the total composition of the blast cloud at origin.

7.3 Results

7.3.1 General characteristics and stratigraphy

Topography.

The topography and the substrate surface roughness were highly variable along the 2600 m long WNW blast-axis (Fig. 7.2). In the proximal c. 1000 m, the axis runs from the western boundary of the eruption fissure along the valley course of the SE headwaters of the Mangatipua stream. Here it contained a proximal, steep (30˚) section, with a major break in slope at c. 400 m from source, after which the slope angles became generally less than 5˚ until c. 1000 m. The remaining profile to 2500 m included a series of seven 20-80 m high ridges and interjacent gullies oriented roughly perpendicular to the blast axis. Up to 1000 m, an unvegetated surface with surface clasts c. 0.4 m to c. 5 m diameter was present on top of a debris-avalanche deposit, emplaced only minutes before the PDC (Procter et al., 2014). Beyond 1000 m, the surface had patchy vegetation, with up to 0.5 m-high tussock grass on ridge tops and dense scrubland with 1.5-3 m-high bushes in valleys.

Overall deposit architecture.

Longitudinally, the PDC deposit can be subdivided into three main intergrading sedimentary facies (Fig. 7.2A). In proximal reaches, 0–1000 m from source, the deposit was a massive, sand- to gravel-rich facies. This was characterized by a strong lateral thickness variation of up to 150 cm over 25 m showing thick, wedge-shaped deposits with steeply dipping (up to 45°) surfaces at the valley margins and in front of large boulders, and thin, planar deposits along the central valley axis. This facies represented 40% of the total volume and 10% of the inundated area. In medial reaches, c. 1000–1700 m from source, dune-bedded ash-rich deposits occurred. This zone makes up 55% of the total volume and 30% of the deposition

area. In distal zones, >1700 m from source, a thin blanket of weakly wavy- to planar-bedded ash-rich deposits occurred. This zone included ~5% of the volume and 60% of the total deposit footprint.

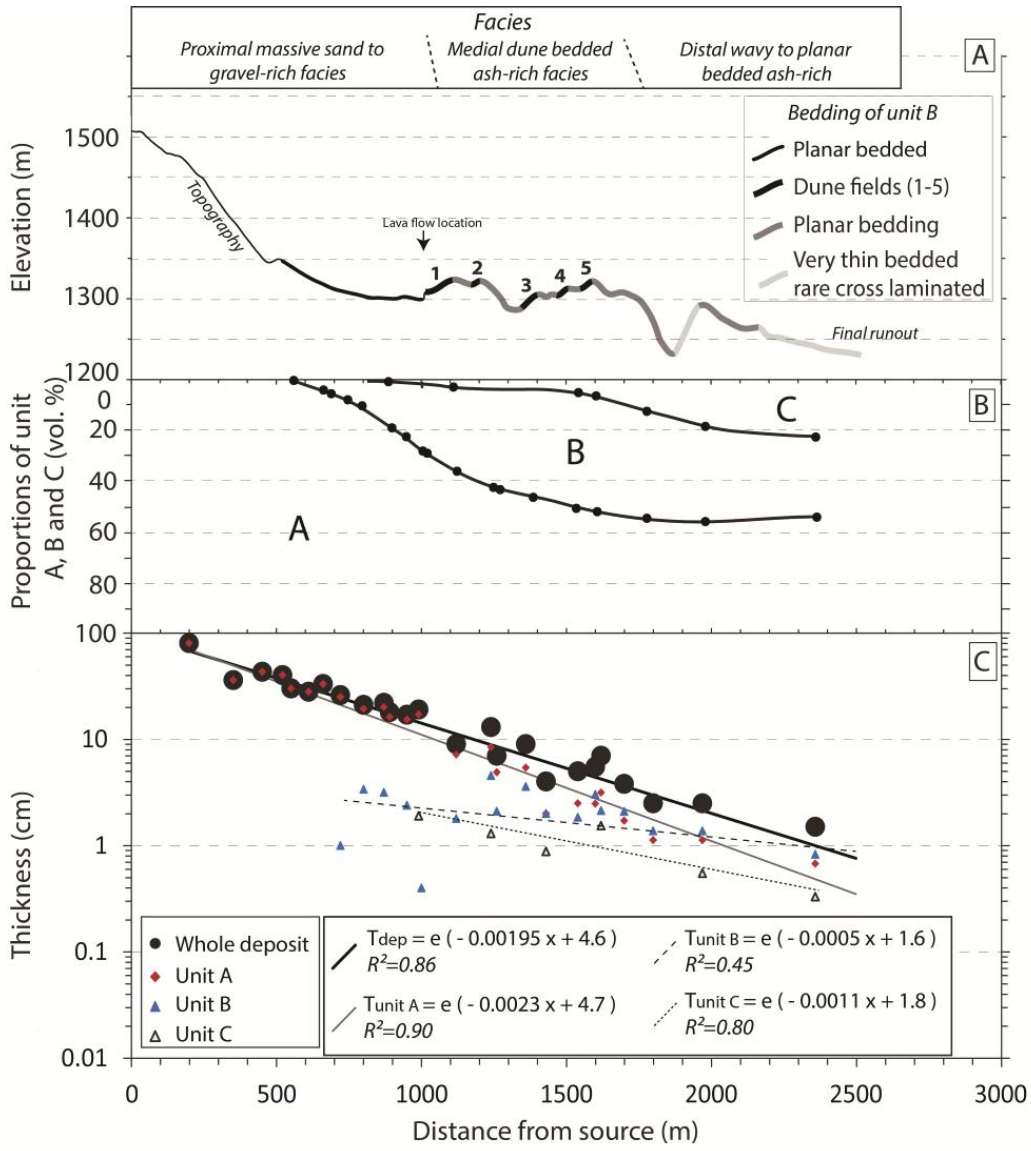

Fig. 7.2. Topographic profile along the main WNW PDC axis with the distribution of the main depositional facies and the locations of large dune fields also shown. B: Relative proportions of units A, B and C against distance from source. C: Deposit thickness against distance from source. Black, grey and dotted lines are exponential fits of the form e^{ax+b}.

Stratigraphy.

The PDC deposits showed a clear tripartite and overall upward fining sequence: a lower coarse-grained and mostly massive unit A, a middle finer-grained, stratified and dune-bedded unit B and an upper fines-rich and laminated unit C. In the proximal sand- to gravel-rich facies, unit A comprised at least 80% of the total deposit thickness. In the medial dune-bedded region, the proportions of units B and C increase to c. 40% and c. 10%, respectively. In the distal areas, the proportion of unit A remains 40-50%, unit B makes up ~30%, and unit C >20% (Fig. 7.2B).

Unit A: The lower contact of unit A was always sharp, and in the first 1500 m, erosive, with entrained vegetation, soil and lithic fragments deposited in the lower part of unit A. This massive to slightly normally graded unit was, proximally, a very coarse-grained, fines-depleted, clast-supported breccia characterized by a clast imbrication in its lower third (Figs. 7.3A and A'). Laterally over 1000 m, the unit became finer-grained, with fewer blocks, and greater matrix content (Figs. 7.3B and B'). At distances of 1000 to 1700 m, the unit became dominated by medium ash and it also developed crude cm-scale stratification in its upper third, while its lower two-thirds was massive to slightly normally graded (Fig. 7.3C and C'). Beyond 1700 m, the deposit was crudely stratified (Fig. 7.3D and D').

Unit B: Up to ~500 m of runout, the PDC deposit was only composed of unit A. At distances of 500-1000 m, unit A was overlain, in sharp contact, by a 1 to 3 cm stratified, coarse-ash-rich unit B (Fig. 7.3B'). The deposit showed wavy bedding into 8-10 coarse- and medium-ash bed sets that generally fined upwards. At distances of 1000-1700 m, unit B overlaid unit A with an erosive, scoured contact (Fig. 7.3C'). The unit reached thicknesses of 5 cm and comprised 8-10 individually upward fining beds of coarse to fine ash. Cross- and plane-

parallel bedding occurs and dune bedforms were well developed on the stoss sides of ridges. The maximum-clast size was <1 cm in diameter. At distances of 1700-2500 m, unit B was entirely composed of medium to fine ash that compose mm to sub-mm thin laminae and the lower contact to unit A becomes markedly less erosive and in places gradational (Fig. 7.3D'). While unit C displays a sub-parallel and millimetre to sub-millimetre lamination in the distal area, locally, centimetre-scale undulations and small lenses of coarser particles intercalated within laminae were observed.

Unit C: At distances of 700 m onwards, unit B was sharply blanketed by the indurated pale gray, weakly normally graded, moderately- to well-sorted, fine-laminated ash unit C (Figs. 7.3B to D'). The deposit grain-size fined overall with distance, although the very fine ash content of unit C was greater closer to source. This unit was generally planar-laminated and rarely undulatory-laminated in the proximal zone with a weakly erosive lower contact. The number of lamina that could be counted ranged between 10 and 15. Rare accretionary lapilli were also present.

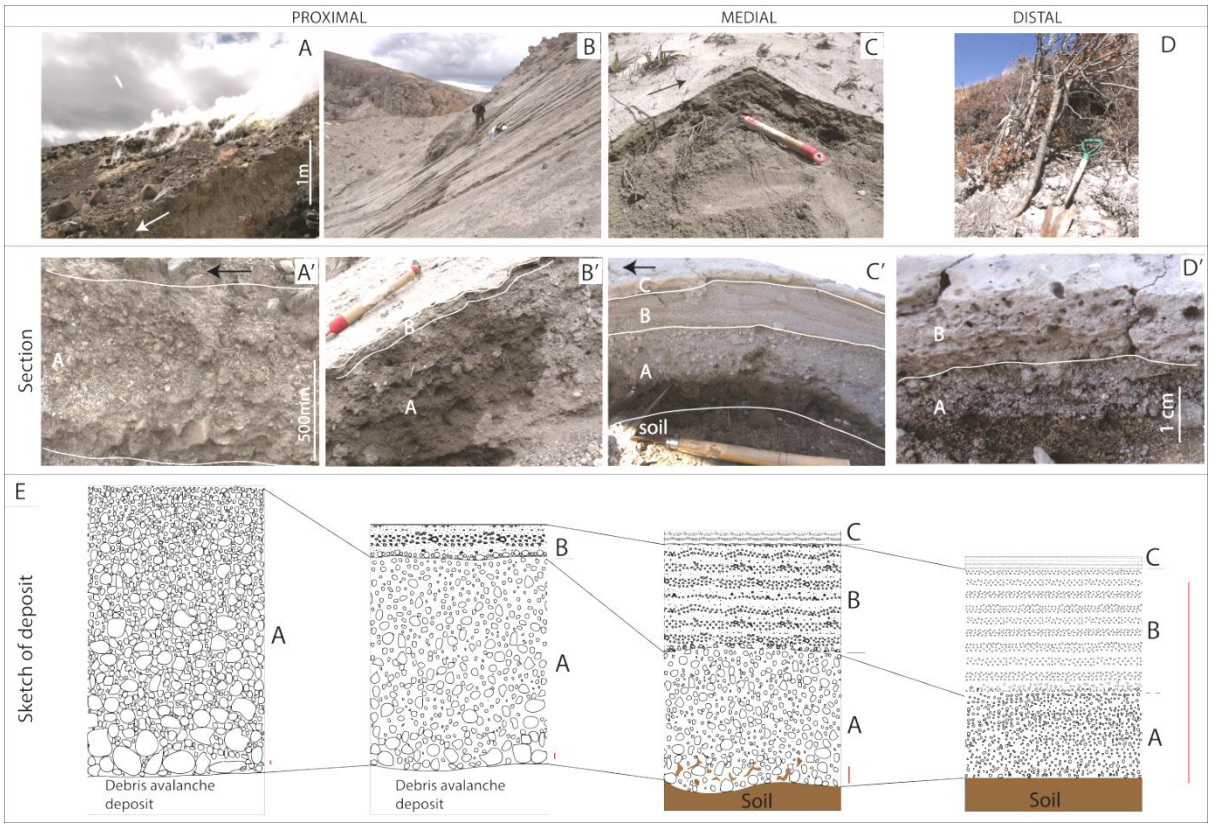

Fig. 7.3. A, B and A', B': Proximal tuff breccia facies of unit A. C and C': PDC deposit forming a dune and section through the tripartite deposit. D and D': In the distal zone, the PDC deposit is often plastered onto obstacles and is composed of unit A, B and C, with the latter being poorly preserved. E: Proximal-to-distal stratigraphic section of the Tongariro hydrothermal blast. The red line represents 2cm of length. Note different vertical scales on bar charts.

Deposit thinning.

Despite a variable topography along the WNW blast axis, a clear pattern of deposit thinning with respect to distance was apparent. The entire deposit (units A-C), as well as unit A, thins strongly from c. 100 cm at 200 m from source to less than 1 cm at 2500 m runout length (Fig. 7.2C). Locally averaged thickness/ distance data are well described by thinning laws of the form:

$$T = e^{ax+b} \qquad (7.1)$$

where *e* is the Euler constant and *x* is the radial distance from source (Wohletz and Sheridan, 1979). Dune-bedded unit B showed a distinctively smaller range in locally averaged thickness from c. 5 cm down to 0.5 cm but a greater spreading of the thickness data that result

in a poor exponential fit (Fig. 7.2C). Thickness maxima for unit B did not occur in proximal exposures, but in the largest dune fields at intermediate runout lengths of c. 1200 to 1400 m. From c. 1600 m, thicknesses of unit B became slightly larger than those of unit A. Unit C displays a clear thinning trend.

7.3.2 Granulometry

Total grain-size distribution.

The total grain-size distributions for units A, B, C and the PDC as a whole were estimated from the complete dataset of grain-size distributions from samples collected along the WNW blast axis (Fig. 7.4). The coarse-grained unit A makes up 74% of the entire PDC deposit volume (Table 6.1), while unit B makes up 20% and C 6%. The estimated total grain-size distribution of unit A is very poorly sorted and polymodal, with modes at -3.5, 1.5 and 2.5Φ (Fig. 7.4A). Unit B displays a well-sorted and weakly bimodal distribution with a main mode at 1.5Φ and a minor mode at 6Φ (Fig. 7.4B). The total grain-size distribution of unit C is well sorted and mesokurtic, with a mode at 1.5Φ (Fig. 7.4C). For the entire deposit along the blast axis, the grain-size distribution is bimodal with the main mode at 2.5Φ and the minor mode at -3.5Φ (Fig. 7.4E).

The total ballistic grain-size distribution is much coarser, overlapping with unit A only in the -7Φ class size (Fig. 7.4D). Previous detailed studies of ballistic blocks ejected by the WNW-directed blast (Breard et al. 2014; Fitzgerald et al. 2014) allowed for the first time the quantification of the proportion of material expelled in the blast, which travelled either as ballistics or inside the PDC. By comparing the total volume of ballistics ejected, as estimated by Fitzgerald et al. (2014), and the volume deposited by the PDC, I estimate that ballistics

comprise only 0.1% of the total blast mass, indicating that only a small fraction of the ejected material travelled separately from the PDC.

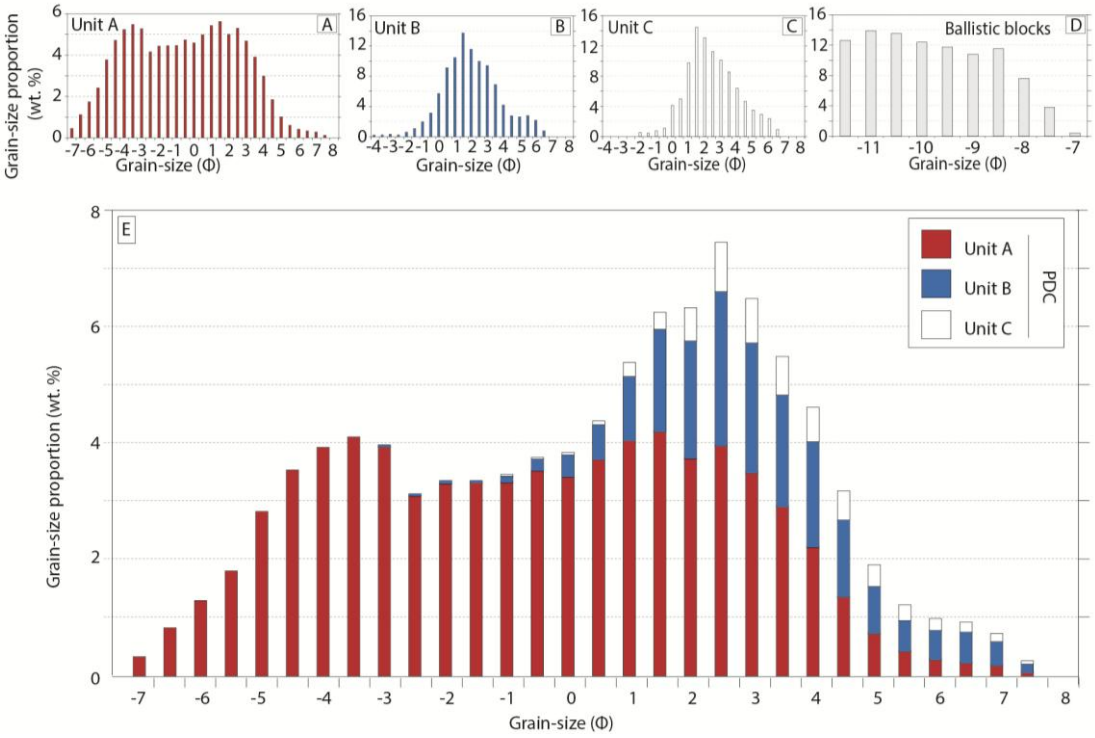

Fig. 7.4. A–C: Integrated grain-size distribution of units A, B and C. D: Grain-size distribution of the ballistic blocks. E: Total grain-size distribution of the PDC.

Unit A.

Unit A showed the strongest lateral facies changes, with the most pronounced trend in a sorting versus median diameter plot, where the two parameters have a strongly linear relationship (Fig. 7.5A). Grain-size distributions of unit A systematically change from proximally polymodal and very fine-skewed (SkI = 0.45) forms to distally unimodal and coarse-skewed (SkI = -0.12) forms (Fig. 7.5C). Over the 2500 m transect sorting improves considerably with sorting coefficients decreasing from >3Φ to <1Φ (Fig. 7.5B). This was accompanied by a strong downstream decrease in the median diameter from medium lapilli to medium ash. Note that proximally (0-700 m) the median grain-size parameter appears quasi constant, while it decreases at a greater rate over 700 m from source. Similarly, the largest

diameter clasts of unit A strongly decreased from 150 mm to 0.5 mm along the transect (Fig. 7.6A). Unlike the other grain-size parameters, the largest diameter shows an abrupt decrease from 60 to 10 mm at 1000 m from source, related to the PDC passing over the first of eight successive ridges. This partial blocking of the current effectively removed medium lapilli and larger-sized clasts, which were absent from units A, B and C farther downstream. Overall, the unit A displayed a coarse-tail grading. This is well-illustrated by the systematic decrease of the lapilli and block fraction from 70 to 0 wt.% and the anti-correlated increase of the fine to coarse ash fraction from c. 25 to 95 wt.% over the first 1700 m runout distance (Fig. 7.6B and C). The very fine-ash content remained largely unchanged at <10 wt.% and only increased sharply to >20 wt.% in the distal wavy to planar bedded ash-rich facies (Fig. 7.6D).

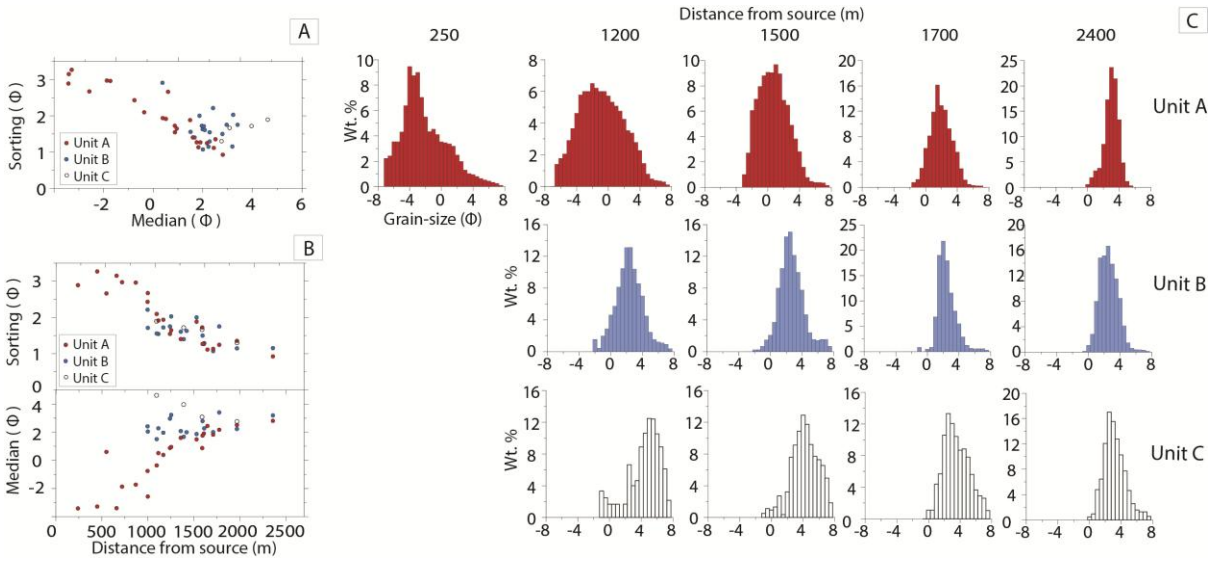

Fig. 7.5. The grain-size median diameter MdΦ versus sorting σΦ of units A, B and C. B: Grain-size sorting σΦ and median diameter MdΦ of the three units against distance from source. C: Examples of grain-size frequency (>-1Φ = lapilli blocks; 4≥ X >1Φ = medium and coarse ash; >4Φ = fine ash) histograms for units A, B and C at different distances from source. Note different vertical scales on bar charts.

Unit B.

Samples of unit B with similar median diameters as unit A are generally better sorted than the basal unit. While the spread in sorting coefficients of both units is comparable, unit B samples show no clear relationship between the median and sorting grain-size parameters

(Fig. 7.5A). The polymodal grain-size distributions of unit B are characterized by a main mode at 1.5Φ (Fig. 7.5C) and, unlike unit A, distributions only change slightly downstream due to distribution grading. In fact two different trends can be observed in plots of various grain-size parameters against distance. Unit B samples collected from topographically similar locations (e.g. in large dune fields at the upstream side of ridges) show subtle, but systematic downstream improvement in sorting, a decrease in the median diameter and lapilli fraction, and an increase in the fine to coarse ash fractions from 1000 to 2700 m (Fig. 7.5B and 8.6B and C). These large-scale longitudinal trends, however, are overprinted by strong variations in grain-size distribution in relation to local changes in topography and surface roughness. The fraction of very fine ash varied by more than 30 wt.% over tens of meters at strong topographic changes (especially in the direction and magnitude of slope inclination), and at changes of substrate roughness (e.g., deposition in front of large boulders or over local patches of dense vegetation; Fig. 7.6D). The interplay between large-scale and local scale variations explains the apparent scatter in grain-size data of unit B. However, I also noted that the largest diameter is largely unaffected by local changes in the depositional environment and decreases monotonically over the runout length from c. 5 mm to < 1 mm (Fig. 7.6A). Interestingly, and in contrast to unit A (see above), this trend is not altered by flow blocking at the first ridge at 1000 m.

Unit C.

Similar to unit B, unit C samples have polymodal distributions with the main mode at 1.5Φ; however, unit C is enriched in very fine ash. Interesting downstream trends also occur in the grain-size data of unit C, although there are only a few samples available. In contrast to units A and B, the median diameter of the uppermost unit slightly increases with runout distance, along with a weak improvement in sorting of the grain-size distribution (Fig. 7.5C). This

coarsening occurs through a strong depletion in very fine ash and subtle increases in the relative proportions of lapilli to fine-ash fractions.

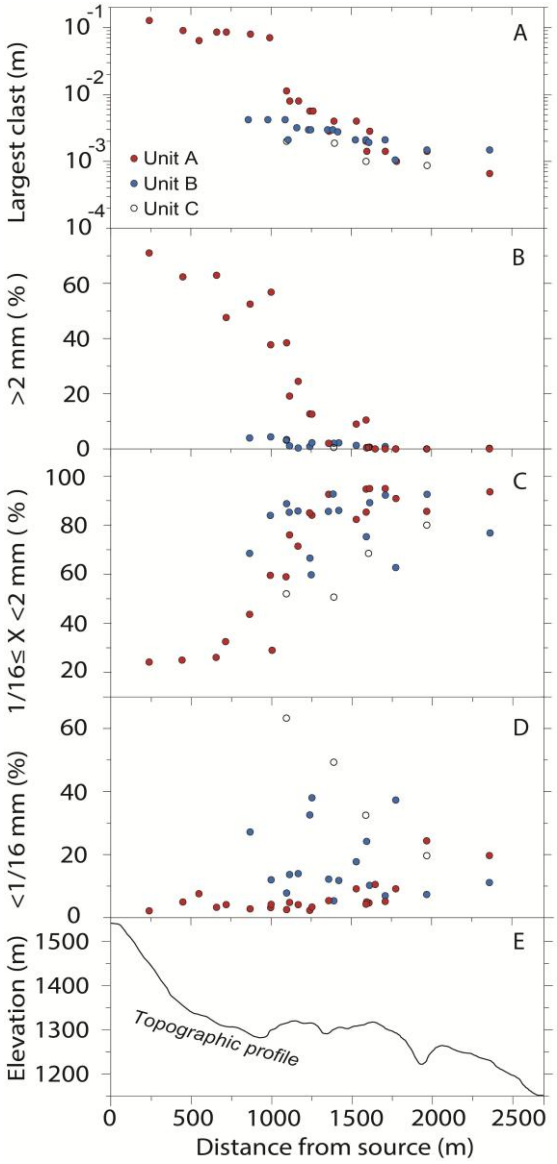

Fig. 7.6. Largest clast diameter in each unit versus distance (A). B-D: Weight percentage of different grain-size fractions against distance in unit A, B and C. E: Topographic profile along the main flow axis.

Sedimentation of units A and B.

To better understand the downstream deposition pattern of the first emplaced massive unit A and the subsequently deposited stratified unit B I computed for both units and different runout distances the absolute mass of each grain-size class emplaced over a unit area. Bursik

et al. (1998) introduced this method to distinguish deposition of concentrated PDCs (with no clear dependence of sedimentation (mass/area) data of each grain-size versus distance) and dilute fully turbulent currents, for which case they suggested sedimentation *S* to follow an exponential law of the form:

$$S = S_o\, e^{-\beta x} \quad (7.2)$$

where S_o is the amount of sediment at x_o=0, x is the distance from a reference location in m, which here is the source, and β is the sedimentation gradient in m^{-1}. In this formulation, the value of *S* is intrinsically related to the overall grain-size distribution and downstream deposit thickness variation, while the sedimentation gradient β is independent of unit thicknesses. Example sedimentation plots for selected full phi grain-size classes from fine ash to medium lapilli are shown in Figure 7.7.

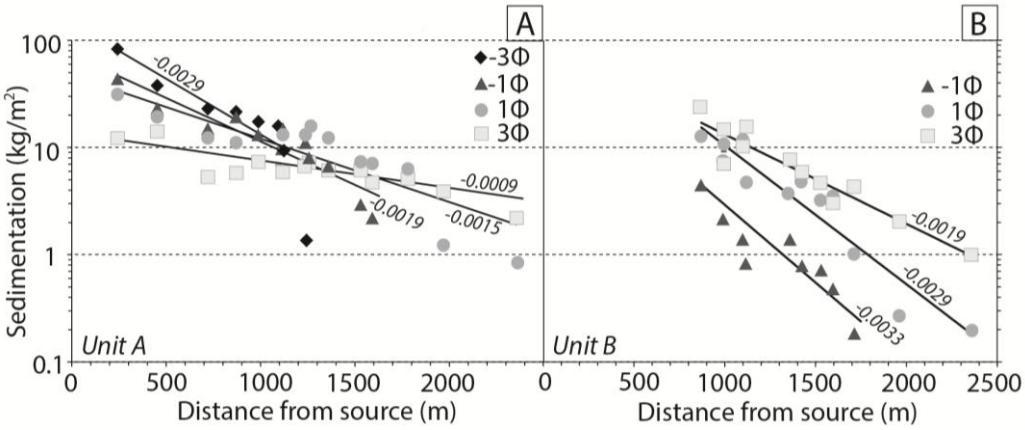

Fig. 7.7. Deposit mass per unit area of individual full-phi size classes of units A and B against distance from source. Only a few grain-sizes are shown for clarity. Exponential sedimentation laws of the form $e^{-\beta x}$ are fitted to the data of each grain-size class for unit A (Fig. 7A) and unit B (Fig. 7B). The value of the slope coefficient β or sedimentation gradient is shown for each fit.

Units A and B follow exponential sedimentation trends that can be approximated by best fits of the form of equation 2. Note that Unit A shows more dispersion of the data around the trend than unit B. As expected for deposition from a turbulent suspension, the sedimentation gradient β systematically increases with grain-size. *En masse* deposition from a concentrated current would result in a horizontal fit for each grain-size, which is not observed. The

systematic loss of the coarsest grain-sizes is clearly depicted by the depletion of fractions -3Φ and -1Φ at 1250 and 1600 m, respectively, in unit A (Fig. 7.7A). Similarly, clasts of the -1Φ fraction in unit B disappear at 1700 m (Fig. 7.7B). For each grain-size class the sedimentation gradient of unit B is significantly larger (and approximately double) than that of unit A. This indicates that the sediment transport capacity of the part of the PDC emplacing unit A was higher than that of the trailing and/or waning flow proportion depositing unit B.

7.3.3 Local facies variations

Interaction with topography.

Aside from the systematic broad-scale facies changes described above, abrupt local variations in grain-size characteristics, bedforms and unit thicknesses occurred due to changes in substrate roughness and topography, especially in relation to sub-perpendicular ridges and valleys. Across ridges, the deposit displayed systematic bedform changes (Seen in Fig. 7.2A). From 1000-1600 m, dunes were ubiquitous on the stoss-flank of the ridge (Figs. 8.8A' and B), but generally less well developed bedforms, with planar to weak wavy bedforms and rare cross-bedding, occurred on the lee-flanks (Fig. 7.8C). Stoss-side deposits were usually twice the thickness of lee side ones, and the deposit thickened in topographic lows and thinned at the top of ridges. In areas >1600 m from source, beds formed dunes on the stoss sides and they were planar-bedded on the lee sides. In regions of dense scrub <1300 m from source, bushes generally survived the passing of the flow, but the deposit was much thinner and finer-grained than in nearby unvegetated areas and the tripartite deposit structure was absent. Between trees, unit B displayed a weaker stratification than elsewhere (Fig. 7.8D).

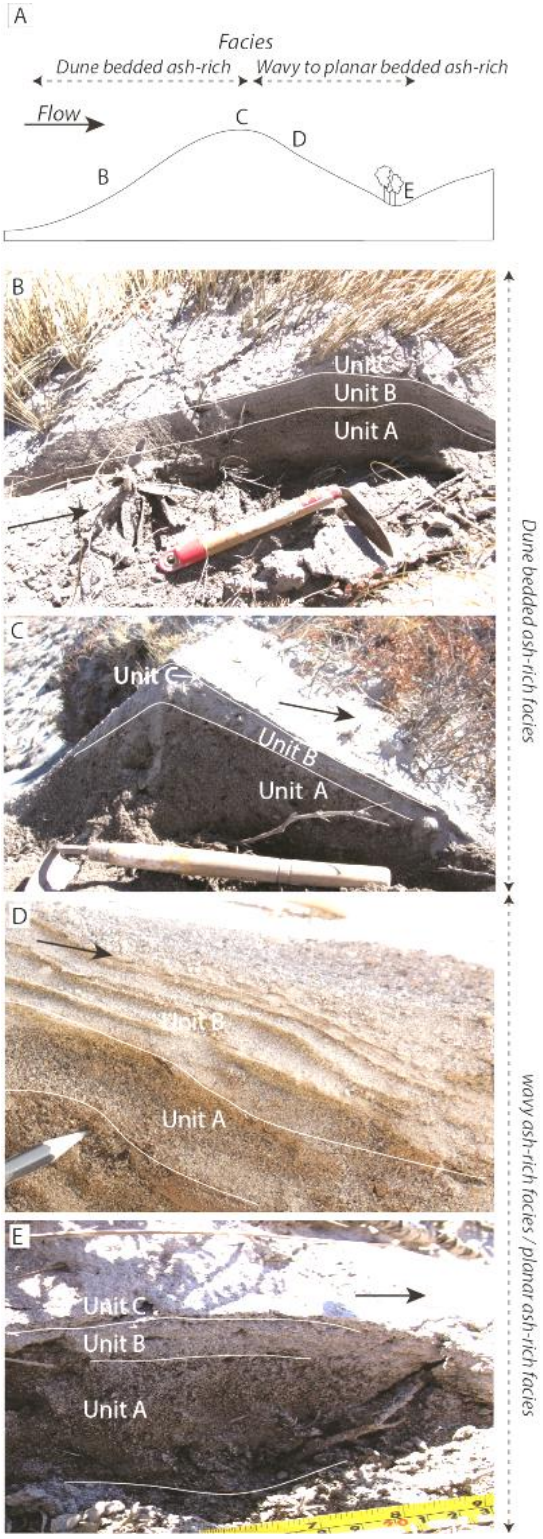

Fig. 7.8. Strong change in PDC deposit facies across a 40 m high ridge at 1200 m from source. A: Overview sketch of different sampling locations across the ridge. B: Dune bedform which nucleated around vegetation and characterized by a rounded crest and shallow slopes; C: Dune bedform on the ridge crest that shows a lee length longer than the stoss length and high dip of the slopes: D: 5cm thick deposit sequence with highly erosive lower contact of unit A and B. While unit A is massive, unit B is stratified with undulatory beds that display small scale thickness variations. Thin unit C is very fine laminated; E: 8 cm thick tripartite PDC sequence composed of the unit A which is vegetation rich at its base, a planar stratified unit B and laminated unit C.

Dune bedforms. Dunes occurred commonly on the stoss sides of substrate ridges (Figs. 7.8A). The dunes often formed on substrate irregularities and obstacles, such as grass or blocks (Fig. 7.8B and C). The dune bedforms were primarily formed by unit B deposits, and were composed of stratified beds of ash and lapilli with sharp contacts. The beds were lenticular, thickened on the stoss side, and thinned towards the crest and lee side, sometimes disappearing altogether. At places, the dunes exhibited wake cross-bedding, grading up- and down-flow into undulatory and planar laminated facies.

Dunes showed an asymmetric geometry (Figs. 7.8B) that suggests dominant stoss-side aggradation, but had rounded crests displaying both downstream and upstream crest migration in any one location. The dunes usually showed a gentle and longer stoss side than their lee side. With increasing distance from source, dunes became increasingly asymmetrical and, although they thinned with distance, their slope angles became steeper, displaying low to intermediate dip angles (10–30°) relative to the ground surface. Rare crest climb angles as high as 45° are observed. The wavelengths and thicknesses of the dunes decreased exponentially with respect to distance (Fig. 7.9A and B).

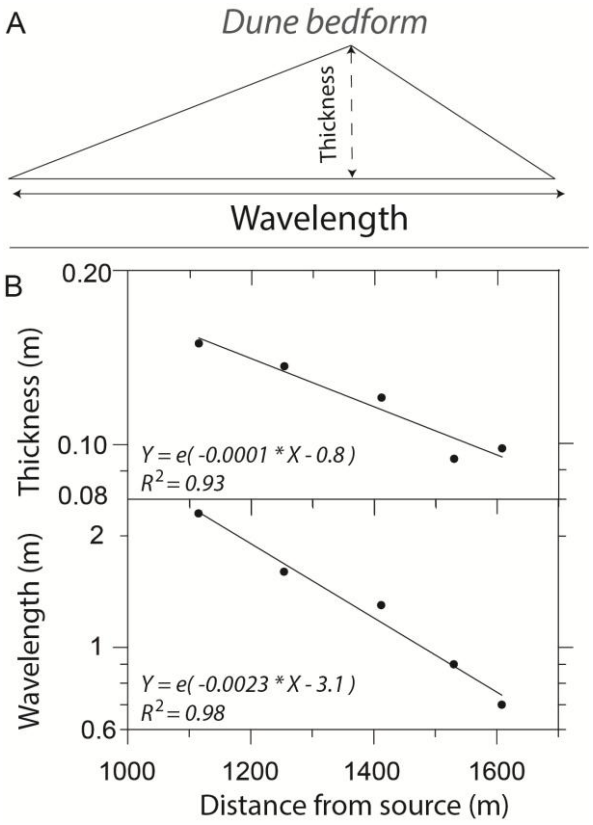

Fig. 7.9. A: Geometric parameters of dune bedforms measured in the field. B: Average thickness and wavelength of the dunes in each dune field against distance. Exponential fits to the data and the square misfits (R^2) are also shown.

Vertical obstacle. The lava ridge at 1000 m from source locally blocked the lowermost 15 m of the flow and provided an opportunity to test two contrasting models for the transport and deposition of the PDC. The complete PDC deposit sequence of unit A, B and C was found at the base (0.245 m-thick) and at the top (0.017 m-thick) of the obstacle (Fig. 7.10A and B). However, the characteristics of unit A changed significantly from the base to the top section. This included decreases in thickness (0.20 to 0.015 m), maximum clast diameters (-6.5 to -2.5 Φ), median diameter (-0.9 to 1.2 Φ) and an increase in the fraction of very fine ash (c. 10 to 3 wt.%).

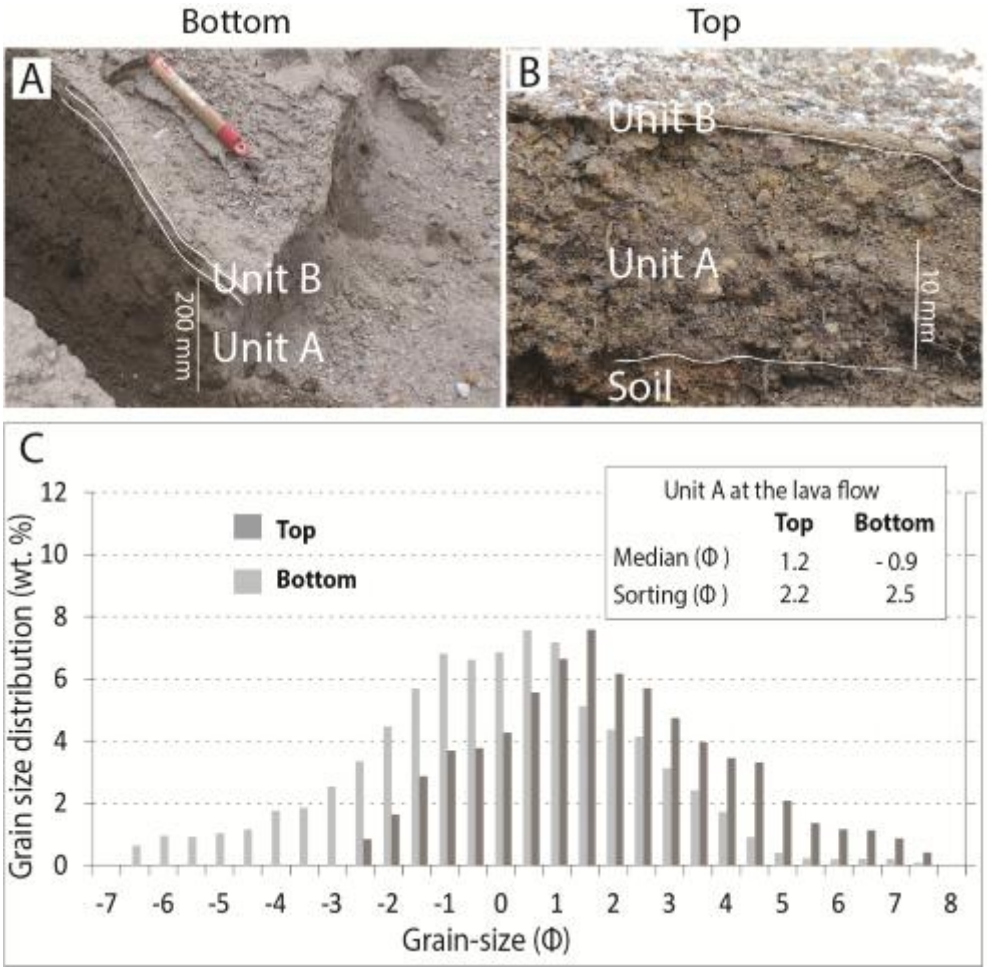

Fig. 7.10. Cross-sections of the PDC deposit at the bottom (A) and the top of the lava ridge at 1000 m from source (B). C: Grain-size distribution of unit A at the bottom and at the top of the lava flow with grain-size median and sorting parameters.

Dynamic pressure estimate from trees knocked down

At 1200 m from source, the flow knocked down dead Toatoa pine trees (Phyllocladus genus) that were delimbed prior the eruption. Trees have an ultimate strength in tension of σ_{ult} = 51 MPa and an assumed drag coefficient C_D =1.1 that Clarke and Voight (2000) demonstrated to be a valid assumption. I use dimension data from the largest snapped and delimbed tree for the estimation of the PDC dynamic pressure thus approximated as a pole. The largest tree (h = 4.1 m, r = 0.05 m) was broken at 60 cm from the base (h_o=3.5 m). The dynamic pressure

required to knock down the tree which is conceptualized as a solid uniform pole is defined by:

$$P_{dyn} = \frac{\pi \sigma_{ult} r^2}{4 {h_0}^2 C_D} \quad \text{(Clarke and Voight, 2000)} \qquad (7.3)$$

The equivalent height-averaged dynamic pressure resulting is 7 kPa. The dynamic pressure must have equalled or exceeded this value at some instant.

7.4 Discussion

7.4.1 General interpretation

The overall structure of the PDC deposit, such as the exponential thinning of individual units and overall deposit, the systematic repetition of the tripartite sequence on all obstacles, the dunes' bedform geometry, including the progressive loss of finer clast sizes from the propagating blast along its WNW axis, is characteristic of a deposit produced by a turbulent PDC. After the initial burst phase, pyroclasts rapidly organized themselves into a vertically stratified current that developed a high concentration at the base and was progressively more dilute upward. A highly energetic flow is able to transport a large range of clast sizes; however, with distance the flow loses its competence to transport the larger clasts, and they are segregated towards the base. The flowing mixture becomes better sorted and finer grained with time (and with distance), resulting in a decrease of the median grain-size of the deposited mixture. A proximal-to-distal PDC-facies change suggests a decreasing sedimentation rate of the suspended load with increasing distance and at a given location, which is related to the progressive dilution and fining of the flow with time.

7.4.2 Architecture of the PDC deposit

Units A, B and C were deposited by diachronous deposition (Branney and Kokelaar, 2002). Unit A was present from source outward but units B and C only occur at distances of >500 m, and >700 m, respectively. The inferred depochrons (also separated by erosional unconformities) coincide with a lithofacies change between the units: massive (unit A) to stratified (unit B), and stratified to finely laminated (unit C). This reflects the temporal evolution of the blast flow that deposited each unit under different regimes.

The open-work texture of the proximal facies of unit A suggests a very rapidly emplacement (Druitt 1992). Proximally, large clasts were not supported or entrained into the flowing mixture and settled by fallout from suspended-laod, inducing an upward motion of gas and fine particles, which thereby became depleted in the deposit (Middleton, 1967; Allen, 1982; Middleton and Neal, 1989). Rapid sedimentation allowed only weakly tractive conditions for the clasts from a "moderate to dense suspension" (Druitt, 1992), in which turbulence near the base was damped because of the high concentration, and steep concentration gradient, of particles near the base, inhibiting flow separation behind obstacles and producing a unit with few bedforms (Allen and Leeder, 1980). The over-thickening of the massive sand- to gravel-rich unit A at stoss sides of obstacles is consistent with the particles having experienced little lateral movement in the depositional system (up to 10 m) before final deposition. Rapid sedimentation of the largest clasts resulted in depletion of the flow in coarse clasts through longitudinal coarse-tail grading. In contrast to the Mount St Helens blast (Druitt 1992), rapid sedimentation did not produce a basal zone thick enough to be able to detach from the flow and drain into valleys. After rapid and proximal loss of its coarsest load, reduced sedimentation rates and the overall finer grain size allowed deposition of the matrix-supported facies of unit A in medial to distal reaches.

After the rapid deposition of unit A, gradually, finer particles were able to saltate and roll at the flow base and were deposited when a critical threshold was reached. The bedload started to be deposited under a traction-dominated regime to produce unit B. Both grain-by-grain and dilute depositional regimes are suggested to explain the dune-bedded sedimentation features within unit B, with each lamina possibly recording the passage of a large eddy (Andrews and Manga, 2012). The contrast of depositional regimes dominated by rapid-suspension sedimentation to that dominated by traction was recorded by a sharp boundary between units A and B up to c. 1500 m from source. This boundary also reflects a time brief gap separating deposition of the two units. At distances exceeding c. 1500 m of runout, the contact between unit A and B is often gradational which indicates an increasingly transitional deposition regime of unit A from rapid-suspension sedimentation to traction. An important feature displayed by the PDC deposit is the increasing relative abundance of unit B and C with distance over unit A that is indicative of a waxing of organized traction of the particles at the substrate.

Unit B is composed of alternating coarse- and fine-grained laminae that reflect the unsteadiness of the flow-boundary zone dominated by either tractional or grain by grain deposition behaviour (Sulpizio et al., 2014). The occurrence of coarse-grained laminae is typical of a traction-carpet sedimentation where coarse grains are moved by shear stress exerted by the overriding dilute cloud while the finer grained laminae are related to the fallout of particles with the absence of traction at the bed (Branney and Kokelaar, 2002; Sulpizio et al., 2007a). The draping of the PDC deposit by unit C is related to a late stage deposition from a slow moving and moderately turbulent flow that deposited particles grain-by-grain.

Topographic changes affected the deposition dynamics of the PDC. The most noticeable observations were obtained across the hilly field (1000-1800m), where thicknesses of individual units decreased by half between stoss and lee side of a ridge. Rapid changes in slope angles induced systematic variations of the lithofacies, with dune-bedded facies on the stoss side and planar facies commonly deposited on the lee sides. This feature can be explained by a rapid increase of the near-bed shear stress, which was able to suppress the formation of undulatory bedforms when the flow accelerated on the lee side of a ridge (Dade, 2003).

Unit B deposits show classic features of pyroclastic surge deposits, such as thin bedding and abundant sandwave structures (Sohn and Chough 1989; Chough and Sohn 1990; Wohletz 1998). I observed an exponential decay of the dune bedforms' lengths and wavelengths with distance from source. The decay of dune lengths with distance to source were similarly documented at Taal volcano (Fisher and Waters, 1970), Laacher See (Schmincke et al., 1973), Ubehebe (Crow and Fisher, 1973), El Chichón (Sigurdsson et al., 1987), and Mount St Helens (Druitt 1992).

7.4.3 Bottom-and-top deposit at the lava flow obstacle

The natural 15 m high wall created by the lava flow blocked particles below and led to an overthickening of the deposit at the base of the wall. Nonetheless, the portion of the flow above the wall was able to surmount the obstacle. Similar blocking of a PDC by a vertical obstacle has been interpreted in various locations worldwide (Branney and Kokelaar, 2002; Sulpizio and Dellino, 2008; Jeon et al., 2011).

One potential interpretation of the bottom-top relationship is that coarsest clasts were transported in a "traction carpet" at the base of the flow by shear stress (Sohn, 1997), while

finer particles were transported by turbulence in a suspension (Branney and Kokelaar, 2002). In this case, the deposit would reflect the blocking of coarse particles by the lava ridge and the surmounting of wall by the fines, for which transport is favoured at a higher level inside the flow. With this interpretation I would expect that the PDC deposit would be composed of a massive coarse unit at the base and a fine laminated or stratified unit at the top (Jeon et al., 2011). However, at Tongariro I noted that the sequence of massive-to-stratified sequence of units (A and B) was repeated even on top of a large obstacle. This is similar to the blast deposit at Mount St. Helens, where the layered stratigraphy of the deposit was likewise preserved at small scales on top of obstacles, such as large tree stumps, as well as on open ground (Fisher, 1990). This strongly suggests that emplacement of unit A at Tongariro was undertaken by rapid-suspension sedimentation, as inferred for larger blast deposits (Druitt, 1992; Belousov et al., 2007). The differences in grain-sizes and thicknesses of unit A at the base versus the top of the vertical obstacle record vertical differences in the abundance and size of clasts in the turbulent transport system, which rapidly sedimented to form the deposit.

7.4.4 Grain-size distribution within the PDC

The grain-size distribution of the deposit at a given location is indirectly related to that of the flowing mixture. Differences of lithofacies and inferred depositional regimes between units A and B discussed in the previous section are related to differences of grain-size distributions. Unit A is at all distances coarser than the upper units B and C and shows enrichment in blocks and coarse lapilli in the total grain-size distribution.

Proximally (0–700 m), various grain-size parameters such as the median grain-size diameter and the maximum clast size show very little change over distance that can reflect the grain-size distribution supplied by the explosion. The largest blocks that travelled with the PDC

never exceeded 0.13 m in size and the relatively constant maximum grain-size deposited in unit A is consistent with this observation. Proximally, one could envisage the coarse-tail grading effect to be delayed for multiple reasons: 1) the blast had not yet collapsed into the PDC phase, and large particles were deposited rapidly without sorting by clast size, 2) the downslope topography increased the flow velocity, thus particles were transported farther.

The median diameter and sorting coefficient of the deposit started to change markedly beyond 700-1000 m from source. This distance corresponds to a transition from a relatively smooth, concave upward slope to a series of flow-oblique ridges. It also marks the transition zone from the massive sand- and gravel-rich facies to the medial dune-bedded ash-rich facies, and the occurrence of units B and C in the deposition sequence. The change in topography accelerated deposition of the coarsest clasts. It did not, however, change the overall deposition pattern, with the rate of mass deposition following a uniform exponential decay function from source to terminus. The lack of flow channelization by topographic obstacles (50-20 m high in the medial area) indicates that the flow had a much greater thickness than the ridge heights (Valentine, 1987; Walker et al., 1995). However, the c.80 m high final ridge located at c.2000 m from source partially blocked the lower part of the flow, which intensively deposited the particulate load against the stoss side of the ridge.

The mass of particles transported in the flow decreased overall exponentially with distance as expected for a turbulent suspension. Data suggest that the deposition regimes of units A and B are somewhat independent from another and that the particle transport capacity in the evolving PDC was decaying both downstream and with time.

7.4.5 Longitudinal PDC zoning

PDC deposits with strongly upward-fining sequences, with systematic downstream decays in deposit thickness, median diameter and sorting coefficients and the replacement of high-energy bedforms by subsequently lower energy ones are characteristic of many documented surge and blasts deposits (e.g. Fisher et al., 1980; Sigurdsson et al., 1987; Lajoie et al., 1989; Fisher, 1990; Druitt, 1992; Belousov, 1996; Yamamoto et al., 1999; Sulpizio et al., 2007a; Fujinawa et al., 2008). Each vertical section documented along the WNW blast axis can be envisaged as a series of snapshots characterizing the passage and deposition of the evolving and progressing flow. Our model envisages that the passage of a strongly vertically stratified current is manifested in the internal normal grading of unit A and individual bedsets in unit B, and that the strong lithofacies changes from one unit to another (as well as erosional unconformities in-between) are related to a strong longitudinal zoning of the density current. For a longitudinally zoned current, the occurrence of longitudinally correlated unconformities and depositional units (here units A, B and C) reflect the passage of different parts (or zones) of the density current, while downstream changes in the characteristics of the unconformities and grain-size distributions of each unit reflect the evolution of each zone through progressive deposition.

For the 2012 Tongariro PDCs I envisage that the zoned flow structure progressively developed in the first 1000 m of runout as units A, B and C were produced by diachronous deposition. Each zone inside the flow deposited the particulate load under different regimes, hence producing different lithofacies (Figs. 7.11A and B). The first portion of the flow that arrived at any site eroded the substrate and did not leave a deposit trace. At some distance behind the front, the PDC transporting a very poorly sorted mixture of particles deposited the massive unit A by rapid-suspension sedimentation. The second unconformity and the strong lithofacies change indicate a time gap before initiation of deposition from a second zone at a

given site, with the incoming zone transporting a better sorted mixture of finer particles that were transported in a portion of the flow moving at much lower velocities than the portion depositing unit A. Pulsatory deposition of unit B under a traction-dominated regime generated a distinctly stratified unit. The last and slowest-advancing zone deposited the finest particles at a very slow rate under weakly tractive conditions (Fig. 7.12A). Differences of lithofacies from bottom to top of the PDC deposit at any location reflect an abrupt decrease of sedimentation rate between each unit (Fig. 7.12B). A result of the longitudinal zoning is that at any location, the overall flow dilutes and slows down with time as demonstrated by numerical modelling (Esposti Ongaro et al., 2012; Doronzo and Dellino, 2014).

The large heterogeneity between the two zones depositing units A and B lessened with respect to distance as the frontal zone diluted rapidly and lost the coarsest clasts. Hence, at distances exceeding c. 1500 m, the early-time and intermediate-time parts of the current tended to transport similar grain-size distributions so that deposition of unit A graded into deposition of unit B in the distal area. I note that our qualitative model does not explicitly link the longitudinal zones of erosion and deposition to the structure of a density current (e.g. including a head, body and tail). While such links seem plausible to the authors they cannot be concluded from deposit characteristics alone.

7.4.6 Density stratification of the blast current

A longstanding goal in physical volcanology is to quantitatively relate sedimentary characteristics of PDC deposits to the dynamic properties of the flow that emplaced them. One approach taken is that of describing the vertical density and velocity stratification in a fully turbulent and dilute PDC using the so-called law of the Wall (e.g. Valentine, 1987; Dellino et al., 2004). However, thus far this method remains unsatisfactory as it involves a

number of very strong assumptions to close the set of governing equations of this law (e.g. estimating depth-averaged particle concentration by approximating the PDC as a static fluid (Lajoie et al., 1989; Clarke and Voight, 2000; Dellino and La Volpe, 2000; Doronzo and Dellino, 2013) arbitrarily choosing a reference height in the PDC for which absolute particle concentration can be constrained (i.e. Dellino et al., 2008). In the following I suggest a simple method that allows some aspects of the vertical density stratification of PDCs to be inferred without these strong assumptions.

At 1000 m from source, the PDC flowed against a 15 m vertical lava wall and deposited the tripartite sequence of units A, B and C at the bottom and at the top. In the below, subscript 1 refers to the base of the wall and subscript 2 refers to the top of the wall. Unit A had a deposit thickness d_1 of 0.2 m just upstream the lava flow and a thickness d_2 of 0.015 m on top of the obstacle.

Deposit thickness can be expressed as the product of sedimentation rate *S*, and sedimentation time *t*, and for the lava wall location I can write the ratio d_1/d_2 as follows:

$$d_1/d_2 = (S_1t_1) / (S_2t_2) \qquad (7.4)$$

If *S* is measured by an average concentration *C* of particles in the current above the two depositional sites, multiplied by average settling velocity *w* of suspended particles:

$$d_1/d_2 = (C_1w_1t_1) / (C_2w_2t_2) \qquad (7.5)$$

If I assume that the sedimentation durations are the same at both bottom and top of wall, the ratio of deposit thickness equals:

$$d_1/d_2 = (C_1w_1) / (C_2w_2) \qquad (7.6)$$

Both concentrations C_1 and C_2 represent the time- and depth-averaged concentration of the PDC during deposition of unit A at the foot of the wall (i.e., from ground level to top of current), and at the top of the wall (from wall top to top of current).

Using the ratio of the deposit thicknesses and the settling velocities at the base and top of wall, I compute the ratio of the concentrations:

$$C_1/C_2 = d_1w_2/d_2w_1 \qquad (7.7)$$

This approximates the ratio of average concentrations C_1 and C_2 during deposition of unit A. Here I estimate a plausible range of settling velocity using the median particle size and maximum clast size at the base of the wall and at the top of the wall (for w_1, w_2, respectively).

The settling velocity, w, of particles through a fluid is described as follows (Dellino et al., 2005) :

$$w = \frac{1.2065\mu\left(\frac{D^3 g\left(\rho_S-\rho_f\right)\rho_f\Psi^{1.6}}{\mu^2}\right)^{0.5206}}{d\rho_f} \qquad (7.8)$$

where Ψ is the shape factor, ρ_s is the particle density, ρ_f is the fluid density, d is the particle diameter, μ is the gas dynamic viscosity and D the particle diameter. Note that I aimed to determine the ratio of settling velocities; hence, I can use a fluid density of clear air at 100^o and average elevation of 1300 m a.s.l (i.e. 0.8 kg m^{-3}), a measured shape factor of 0.5, and a dynamic viscosity of 2.3 x 10^{-5}. When using the median particle diameter (D_1 = -0.9 and D_2 = 1.2 Φ), I calculate from Eq.(7.8) that w_1 equals 6 m s^{-1} and w_2 is 2.6 m s^{-1}, which give a ratio C_1/C_2 = 31. With the maximum clast diameters (D_1 = -6.5 to D_1 = -2.5 Φ) as an input into Eq.(7.8), w_1 equals 46 m s^{-1} and w_2 is 9 m s^{-1} resulting in C_1/C_2 = 68. This simple model suggests that on average 97-98.5% of the PDC mass was transported in the lowermost 15 m of the flow at the distance where it encountered the lava wall. This result suggests that the

hydrothermal blast was strongly density-stratified as hypothesized for dilute and turbulent PDCs (Valentine, 1987; Branney and Kokelaar, 2002; Sulpizio et al., 2014).

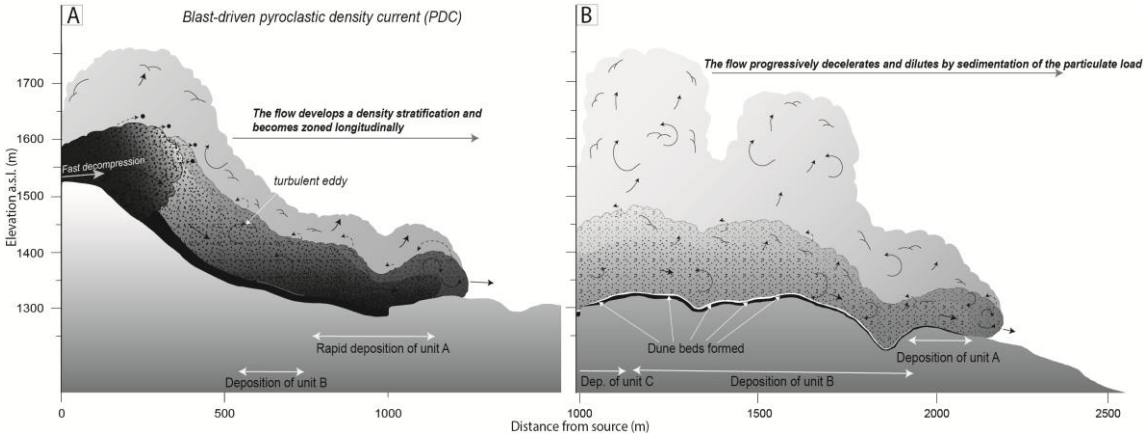

Fig. 7.11. Cartoons of the blast evolution with distance at Tongariro. After the burst phase, the pyroclastic mixture rapidly collapses and develops vertical and longitudinal density stratifications. Rapid deposition leads to the formation of unit A (A). At 500 m from source, a second unit B is deposited from the slower and more dilute zone of the flow (A). Dune bedforms are generated regularly on the stoss sides of five ridges located along the main flow axis. For illustrative purposes, unit A and B are represented in black and white respectively.

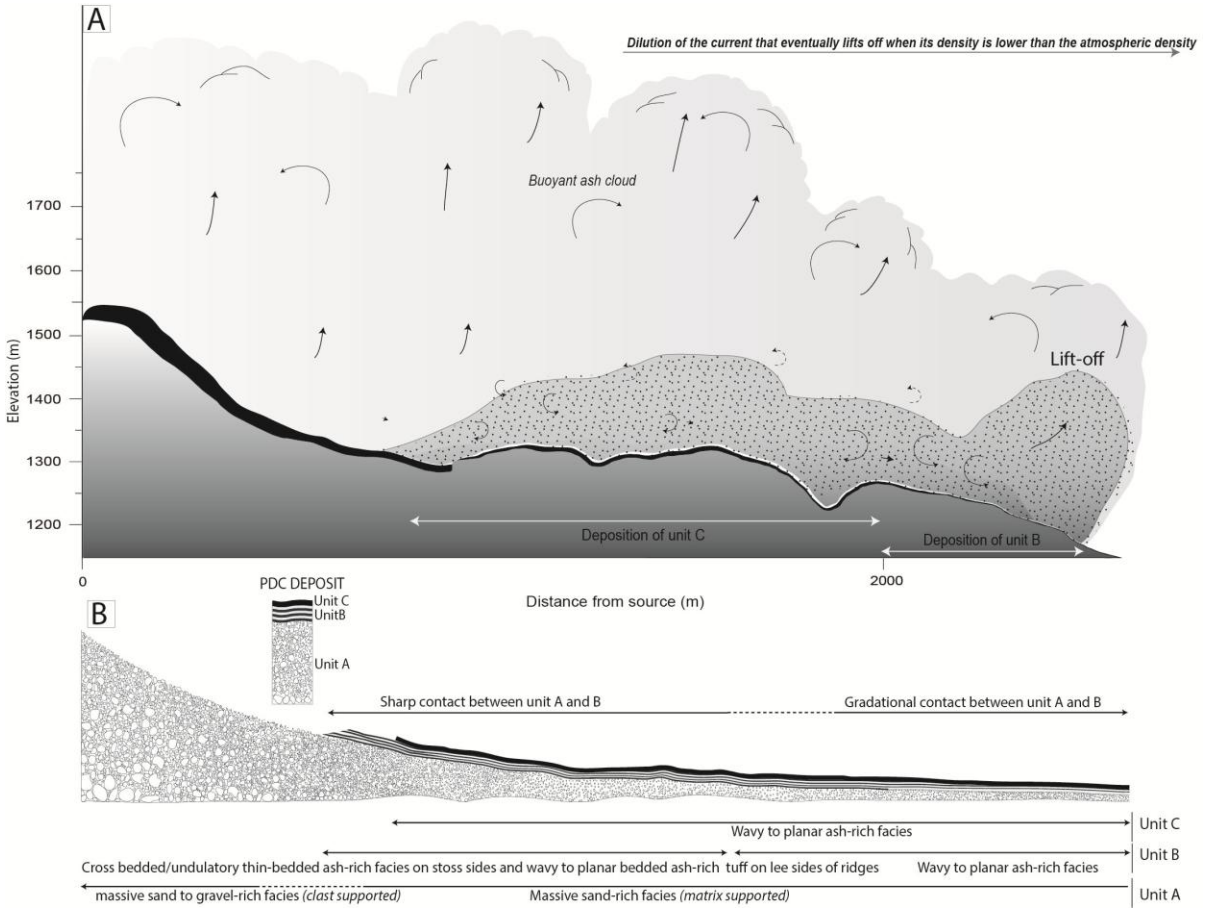

Fig. 7.12. Cartoons of the blast evolution with distance and longitudinal deposit facies variations at Tongariro. A: The thin unit C veneers the two other units. At ~2400–2500 m from source, the flow becomes buoyant and reaches its final runout. For illustrative purposes, unit A and B are represented in black and white respectively. B: Longitudinal facies change of the PDC deposit.

7.5 Conclusions

The PDC deposit produced by the 2012 Upper Te Maari eruption is related to a laterally directed hydrothermal blast produced by sudden decompression of the hydrothermal system. The multiphase mixture collapsed and flowed as a stratified PDC that easily overwhelmed topographic highs and lifted off when the bulk flow density was reduced to atmospheric density around 2500 m from source. The PDC progressively became longitudinally zoned in the proximal area and first deposited some of its particulate load as unit A. Later on, the slower moving, waning flow deposited unit B, and unit C. Hence the tri-partite PDC deposit

reflects the temporal and spatial evolution of the flow structure. Integration of the PDC deposit allowed us to calculate the total blast distribution, which was used to reconstruct the evolution of the flow composition with distance. Our analysis shows that at distances < 1500 m there was a distinct longitudinal grain-size zoning in the flow, and that at a distance >1500 m from source, the flow, when depositing unit A and B, had roughly similar grain-size distributions (signalling the decay of the zonal structure).

The flow rapidly deposited massive unit A by suspension-sedimentation. This was followed by a brief period of non-deposition until the flow velocity decreased and reached a certain threshold allowing rolling/saltation processes to become dominant. This marked the starting point for deposition of unit B under a traction-dominated regime. As a result, the two units are separated by a sharp boundary. At distances greater than 1500 m, the boundary between unit A and B becomes rather gradational and this reflects the progressive longitudinal homogenization of the flow. In the distal zone, deposition of unit A transitioned continuously to deposition of B.

Owing to the low thickness of the deposits, deposit of blasts like this are generally poorly preserved. However, due to the extreme ability of blast flows to surmount topographic obstacles and their very great mobility, hydrothermal blasts should be included on many hazards maps of stratovolcanoes all around the world.

7.6 Supplementary material: Method for estimation of the total blast grain-size distribution

The total grain-size distribution was computed for each PDC unit (A, B and C) and ballistic grain-size distributions using a total of 24 sampling locations inside a 5˚ fan bracketing the WNW axis (Fig. 7.1D). An axisymmetric geometry was chosen because of the radial spreads of both the PDC flow directionality vectors (Lube et al., 2014; Fig. 7.1C) and the ballistic block fans (Breard et al., 2014), and because along the WNW axis significant drainage and channelling into topographic lows and deviations from the axisymmetric spreading trend is absent (Lube et al., 2014). PDC deposit grain-size distributions are those introduced in this paper, while ballistic grain-size distributions are those reported in Breard et al. (2014) and Fitzgerald et al. (2014).

The volume of ballistic blocks was estimated as follows:

1) I mapped ballistic craters in the 5˚ fan and obtained a crater-size distribution.

2) I found an empirical law that relate block and crater diameters (supplementary Fig. 7.1).

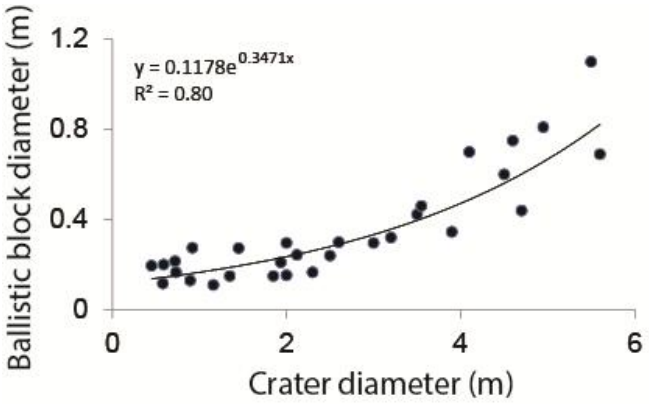

Supplementary Fig. 7.1. Crater diameter versus ballistic block diameter

1) Ballistic blocks were approximated as spheres, allowing us to estimate the total volume of ballistics from the block-size distribution within the fan.

The integration of each grain-size fraction of the PDC deposit was done as follows:

1) I numerically integrated the particle volumetric concentration C of a given size fraction (for a given unit X) noted "$_i$" with distance "x" from source: $Ci\ (unit\ X) = \frac{1}{r} * \int_{x=0}^{r} f(C_i)\ dx$, where *r* is the final flow runout.

2) The arc length, *s*, with distance is given by: $s_x = \frac{\theta * \pi}{180}$*x , where θ is the spreading angle (5˚) in degrees.

3) C_i of each unit can then be rewritten as:

$$Ci\ (unit\ X) = \frac{1}{A_{PDC}} \int_{x=0}^{r} f(C_i) * s_x\ dx$$

where the area of the deposit (A_{PDC}) in the fan is expressed as follows: $A_{PDC} = \frac{0.5\theta\pi}{180} r^2$.

By calculating the C_i for all fractions, I obtained the grain-size distribution of the 3 units. The total distribution of the PDC has been calculated using the respective volume of each unit A, B and C. The volume of a certain unit X ($V_{unit\ X}$) is estimated from the area of the fan and from the thickness of the unit $T_{unit\ X}$:

$$V_{unit\ X} = A_{PDC}\ \frac{1}{r} \int_{x=0}^{r} T_{unit\ X}\ dx$$

$$Ci\ (PDC) = \frac{Ci(unit\ A)\ V_{unit\ A} + Ci(unit\ B)\ V_{unit\ B} + Ci(unit\ C)\ V_{unit\ C}}{V_{PDC}}$$

The full distribution of the blast was estimated from combining total distributions of A, B, C and ballistic blocks. Fine ash, which lifted off as a co-ignimbrite plume was neglected in the calculation, as the fallout had been deposited at further distances.

Chapter 8 – Synthesis and conclusions

Chapter contents

Chapter 8 – Synthesis and conclusions

8.1 Synthesis

PDCs are the most deadly volcanic processes known to humankind (Druitt, 1998; Branney and Kokelaar, 2002, Sulpizio et al., 2014). The reasons for this lie in their ability to travel long distances at high speed and to sweep across landscapes to devastate everything in their path. Many unknowns remain about the internal structure and transport mechanisms of PDCs. Owing to their lethal character, internal observations and measurements cannot be obtained directly. Thus, highly sought-after validation datasets to test and advance numerical PDC hazard models are currently absent. This makes forecasts of PDC runout and damage behaviour for volcanic hazard assessments and planning extremely challenging. This thesis ties in with the recent trend of large-scale experiments as a way to synthesize the dynamics of PDCs under highly controllable conditions that obey scaled similitude to real-world flows, and that allow for quantitative observations and measurements in safety. Through the most thoroughly scaled and largest PDC experiments carried out to date, this work provided first quantitative views into the internal structure and transport processes of these dangerous flows. Direct measurements of the synthesized PDCs are introduced as a new key to characterize the enigmatic structure and gas-particle transport processes of PDCs, and to link these to the PDC runout dynamics and hazard potential.

The large-scale experimental facility PELE in New Zealand enables the synthesis of PDCs by ‘eruption column collapse’ of a mixture of natural pyroclastic material and air (Lube et al., 2015). The present work focused on the experimental study of concentrated PDCs, which are composed of a basal underflow of high particle concentration and a dilute overriding ash-cloud. To decipher the flow properties of these PDC-analogue currents, visual observations

from high-speed video recordings were combined with measurements of the flows' velocity, density and turbulence fields along with additional observations of the flow and deposit grain-size characteristics. From systematic series of experiments, wherein the initial velocity, particle concentration and flow boundary conditions were varied, the outer and inner structures of the PDC were defined and correlated to the degree of turbulence and to the degree of criticality of the flow. The investigations shed light onto a number of hitherto poorly understood processes in PDCs, including the nature of gas-particle interaction and transport, the entrainment of ambient air into the advancing currents, as well as the dynamic coupling and the exchanges of mass and momentum between different PDC flow regions. Furthermore, a field study was conducted at Tongariro volcano, New Zealand, as part of this thesis to investigate the recent and hazardous 2012 hydrothermal eruption of Upper Te Maari crater. The study involved the mapping of the distribution of ballistic craters, mapping of the spatial distribution of the PDC facies deposits and their detailed sedimentological analysis along the main flow axis. The combined ballistic and PDC study provided insights into the proximal-to-distal transport and emplacement dynamics of laterally-directed explosions.

The experimental study successfully synthesized well-scaled PDC-analogue flows of volcanic particles and air, which comprised the long-theorized dense basal underflow and dilute upper ash-cloud regions. This provided quantitative evidence for the co-existence and first direct observations of fully turbulent, dilute and non-turbulent to mildly turbulent, concentrated PDC transport regimes. In experiments, the mildly turbulent concentrated regime represents 95-99% of the total mass of the flow. Both dilute and concentrated regimes are linked by a zone of intermediate concentration and turbulence wherein **mesoscale turbulence structures** form. These structures are characterized by the clustering of particles and have their own specific settling behaviour, which defies the common understanding of

particle settling and sedimentation in dilute PDCs and PDC ash-cloud regions. The extremely rapid settling of particles in the intermediate regime actively contributes to the feeding of the front of the underflow from the ash-cloud. This hitherto unrecognized process yields very effective transfers of mass and momentum between ash-cloud and underflow regions.

The recognition of gas-particle transport regimes at intermediate concentration and turbulence intensity adds complexity to previous conceptual models of the vertical stratification in concentrated PDCs. Simple bipartite models (e.g. Doyle et al., 2008), which envisage a marked boundary between dense, granular-type underflows and very dilute, fully turbulent ash-clouds, do not capture the effective exchanges of mass and momentum through the intermediate regime. These models will underestimate mass and momentum increases of the underflow particularly in proximal to intermediate runout reaches, where the intermediate regime characterizes a significant proportion of the ash-cloud thickness. Such models would also falsely predict the density stratification in ash-clouds and consequently the development of dynamic pressure in PDC ash-cloud regions. On the other hand, models that envisage a continuous vertical density stratification from upper dilute to basal dense regimes include the occurrence of gas-particle transport at intermediate particle concentrations (e.g. Branney and Kokelaar, 2002). However, the experiments show that the upper and lower boundaries of the intermediate regime are characterized by marked jumps in density and turbulence intensity, contradicting with a model of gradual continuous stratification. Such models would also falsely predict the vertical mass distribution, the height-variant flow rheology and damage potential due to dynamic pressure. A next generation of computational PDC flow models needs to account for and resolve mesoscale turbulence in order to successfully forecast PDC runout and damage potentials.

The study shows that in concentrated PDC-analogue flows, wherein an **underflow** and an ash-cloud have formed, the current possesses an outer structure broadly similar to dilute gravity currents, as the ash-cloud is composed of **head**, **body** and **wake** regions. Conversely, the inner structure can be markedly different from a dilute gravity current through the presence of an underflow, and its ability to control the vertical velocity and density stratification. In fact, through strong kinematic coupling, the underflow largely controls the frontal velocity and geometry of the advancing PDC and ash-cloud regions, and simple analytical gravity current models fail to predict the runout behaviour.

The present work provided direct observations and measurements characterizing the nature of gas-particle transport regimes in the PDC ash-cloud region. Importantly, these data showed that the common assumption in PDC models of well-mixed and fully coupled gas and particle phases in the PDC ash-cloud is inadequate. Instead, the experiments confirmed a previously theoretically predicted wide spectrum of gas-particle interactions, which ranges from **fully coupled** and **poorly-coupled** to **non-coupled** regimes (Burgisser and Bergantz, 2002). Differences between the theoretical prediction and the experimental measurements include the intense feeding of the underflow from the ash-cloud through the "mesoscale regime" of poorly-coupled gas-particle interactions instead of the previously theorized "fall regime" of uncoupled gas-particle motion. Furthermore, individual PDC regions (underflow, head, body and wake) have their own specific range of gas-particle transport regimes, which control the grain sizes transported within each zone over space and time. These results have strong implications for the correct description of gas-particle interaction in state-of-the-art numerical multiphase models.

Detailed studies of proximal-to-distal PDC deposits are extremely rare. Therefore, the study of the pristine Tongariro blast deposits provided new observations and the derivation of a qualitative sedimentation flow model. The tripartite deposit architecture that characterizes the blast deposit and the longitudinal facies variations in each depositional unit directly are here inferred and reflect a longitudinally zoned flow structure. In the proposed model, each zone within the flow is envisaged to transport clasts of a specific grain-size range and to deposit them under a narrow range of deposition mechanisms. Similarities between the facies and architecture of the hydrothermal blast deposit from Tongariro and deposits of magmatic blast and surges described elsewhere suggest that the emplacement model developed from this study could be applied to interpret the deposits of a wide range of dilute PDCs.

8.2 Specific findings

8.2.1 Gas-particle transport in PDCs at intermediate concentration and turbulence intensity

The intermediate regime that vertically links concentrated and fully dilute PDC transport regimes is characterized by the abundance of mesoscale structures that originate from the clustering of particles in either bands or dendritic patterns when intense feedback between gas and particles occur (Stokes number approaches or exceeds 1). These structures form favourably in high particle-concentration ash-clouds (>1 vol. %) and are prominently developed in the lower portion of the ash-cloud head and front of the body in proximal distances from source. In experiments, the appearance of such a regime is only short-lived because of the extremely high settling velocities that characterize the particle clusters.

When the intermediate regime exists, velocity and concentration profiles may diverge from the Rouseian form. However, when the intermediate zone vanishes, the concentration and

velocity structure of the ash-cloud can be described by a modified version of the Rouseian approach that takes into account the boundary velocity.

8.2.2 Tractional interaction between PDC underflow and ash-cloud regions

There is little known about the possible coupling between the ash-cloud and the underlying underflow. However, the experiments provided the first measurements and views into this complex process. The study has shown that kinematic coupling between the underflow and ash-cloud exists and can be further classified into three tractional regimes.

In the first regime, the ash-cloud rides ahead of the underflow on the substrate with a boundary velocity. A similar configuration also occurs after deposition of the underflow, where the ash-cloud propagates atop the underflow deposit, but with a no-slip boundary condition. In this regime, the maximum velocity height in the ash-cloud sits far from the lower ash-cloud boundary and traction develops at the base of the ash-cloud.

In regime 2, the ash-cloud is “perfectly” coupled to the underflow, and the maximum velocity of the ash-cloud occurs at the interface with the underflow, which suggests that the maximum velocity of the ash-cloud is dictated by the underflow dynamics. This regime occurs dominantly in the head of the ash-cloud and is characterized by an absence of traction at the underflow/ash-cloud interface.

Regime 3 occurs for most of the flow passage and forms when the ash-cloud is partially coupled with the underflow. In this regime, the ash-cloud develops traction at the

underflow/ash-cloud interface and the maximum velocity height in the ash-cloud is located above the interface with the underflow.

Experiments have shown that the ash-cloud does not passively travel atop the moving underflow; instead, the underflow constantly affects the dynamics of the overriding ash-cloud.

8.2.3 Forced-supercriticality – how interaction between underflow and ash-cloud regions leads to supercritical flow

In the PDC head, the strong kinematic coupling between underflow and ash-cloud regions leads to a significant reduction of the shear stress at the base of the ash-cloud. This has several implications: the thickness of the inner boundary layer, which forms in turbulent wall-bounded flows due to friction with the static substrate, is strongly reduced and can disappear in the frontal part of the head. A lower part of the ash-cloud characterized by the highest and relatively height-invariant particle concentrations shrinks also. The kinematic coupling between the underflow and ash-cloud regions creates a strong momentum transfer upwards. This prevents the usual equilibration of inertial and gravitational forces known to occur in dilute turbulent gravity currents. As a consequence, the PDC head lengthens to move as a fast and thin, supercritical current with densimetric Froude numbers typically in excess of 1.2 and up to maximum values of 3. This forced supercriticality is due to a strongly delayed deceleration of the ash-cloud atop a fast moving underflow and supersedes other effects known to induce supercritical flow in natural dilute gravity currents (e.g. high slopes, smooth substrates and high initial inertia). This implies that the runout behaviour of the PDC head is not primarily driven by its difference in buoyancy with the ambient air. Instead the motion of the fast underflow dictates the PDC head dynamics for as long as the underflow penetrates

the PDC head region. This way, supercritical ash-clouds, characterized by relatively high values of maximum velocity and flow density that occur at relatively low flow levels, can exist at large distances from volcanoes and lead to unexpectedly high values of potentially destructive dynamic pressures.

8.2.4 Entrainment of ambient air

Entrainment of the ambient air within the flow occurs dominantly through Kelvin-Helmholtz (K-H) instabilities. The entrainment coefficient is at its peak in the middle of the head and can locally reach values of 0.2–0.3, whereas values of 0.05–0.1 are typically observed in the wake and body of the ash-cloud. Surprisingly, there is no clear relationship between the Froude number and the entrainment coefficient. In fact, when the ash-cloud head is highly inertial ($Fr>>1$), a shallow wedge-shaped front develops wherein entrainment is limited.

8.2.5 Head vortex

The ash-cloud head is composed of a large anti-clockwise vortex, which actively dictates the behaviour of particles within the head. While particles trapped in the mesoscale clusters are only weakly influenced by the large vortex, other particles better coupled with the dusty gas can be fast tracked and their deposition is delayed by further entrainment higher up in the current. The finest particles transported in the well-coupled regime follow the motion of the large vortex and can be fed into the wake when they reach the upper part of the flow, where large K-H instabilities detach from the head. While proximally the head transports a wide range of particles, over time depletion of the coarsest particles by sedimentation contributes to a progressive narrowing of the grain-size transported and subsequent range of gas-transport regimes.

8.2.6 Hydrothermal blast: PDC

The 2012 hydrothermal eruption of Tongariro volcano generated highly mobile blast-derived pyroclastic density currents. Along the main flowing axis, proximal-to-distal sedimentary structures and grain-size data suggest emplacement of the fining upward tripartite depositional sequence (massive, stratified and laminated) under a dilute turbulent PDC that was longitudinally zoned. Prior emplacement models of similar deposit architecture envisaged the particles composing the massive layer to be transported in a concentrated layer at the base of the current whereas particles deposited in the stratified and laminated units are thought to be transported in the upper dilute suspension (i.e. Dellino et al., 2008). Instead, at Tongariro, the grain-size data and presence of the massive unit atop decameter high obstacles suggest that particles were transported by suspension and deposited very rapidly. After deposition of the massive unit, the flow velocity waned and the stratified unit was deposited by a traction-dominated regime, which was followed by deposition of the top laminated unit grain by grain from the waning current. Therefore, the tripartite deposit sequence reflects the temporal and spatial evolution of the PDC structure. Similarities between the deposit architecture at Tongariro and magmatic blast and surge deposits elsewhere suggest that the longitudinal zoning may be a common feature of PDCs.

8.2.7 Hydrothermal blast: ballistics

During the 2012 hydrothermal eruption of Upper Te Maari, explosions expelled thousands of ballistics that impacted an area of 5.1 km^2. While particles of diameter <7Φ were dominantly transported in the blast-derived PDC, those ≥7Φ were preferentially ejected as ballistics that travelled ahead and through the PDC. These were focused in lateral zones, reflecting the direction and angle of the source explosion. Inverse modelling of ballistic trajectories showed that the initial ejection velocity of the westward explosion was ~200 m s^{-1} at a low angle of

c.6° above the horizontal. The westward explosion was the largest and most hazardous event of this eruption, which directly impacted the popular Tongariro Alpine Crossing.

8.2.8 Hypothesized similarities between experimental PDCs and the Tongariro blast.

Owing to the presence of an underflow beneath the ash-cloud in PELE experimental PDCs (chapter 3–5 in this thesis), the experimental flows differ significantly from the Tongariro blast, which instead has strong similarities with the "surge" run presented in Lube et al. (2015). As demonstrated in chapters 4 and 5, the presence of an underflow modifies the external (i.e. flow shape) and internal structure (i.e. velocity, concentration), as well as the fluid dynamics (i.e. degree of criticality), of the ash-cloud. Nevertheless, I hypothesize that some of the processes discovered from PELE large-scale experiments may have also occurred during the transport and emplacement of the blast at Tongariro:

1) *Mesoscale turbulence structures.* Mesoscale turbulence structures, which form by particle clustering, have been observed experimentally and their effective reduction of particle-drag demonstrated. Similar particle clustering processes likely occurred in the blast, where the absence of a moving underflow would result in an inner sheared boundary layer, thus preventing the formation of clusters in a dendritic pattern. Instead, particle clusters would have formed as bands, oriented parallel to the shear. The reduction of the particle drag due to clustering could thus increase settling velocities of the particles (transported in clusters) and favour their rapid emplacement as a massive layer. While the abundance of mesoscale clusters is positively correlated to the particle volumetric concentration (Chen, 2016), clusters formed in experiments even at low particle concentrations (<0.1vol.%). These observations confirm the importance of mesoscale clusters in polydispersed mixtures, where they have far more influence than in monodispersed fluidized bed. In the latter case, mesoscale clusters commonly do not affect the settling behaviour of particles for solid concentrations <~1 vol.%

(Chen, 2016). As demonstrated at Tongariro, the hydrothermal blast was composed of a wide range of particles (from a few microns to a few decimetres in diameter), supporting the hypothesis that mesoscale turbulence structures developed.

2) *The flow structure*. In PELE experimental flows, I showed evidence of zoning within the ash-cloud into head, body and wake regions, each characterized by a range of gas-particle transport regimes. Similar regions likely formed in the Tongariro blast, and could support the inferred longitudinal zoning of the blast. Although there are differences between the ash-clouds of the concentrated experimental PDCs and the natural blast, the results of the experiments could help to qualitatively describe the zoning of the blast's and its temporal evolution.

The rear of the head and frontal body regions were the most concentrated areas of the experimental ash-clouds, making the corresponding regions in the Tongariro blast the most likely locations for the formation of mesoscale clusters and subsequent deposition of a massive layer (layer A), due to their rapid settling. Rearward of the highly concentrated zone of the body, particles were probably transported by a smaller range of gas-particle transport regimes, thus reducing the range of grain-sizes transported and emplaced the stratified layer B. Furthermore, segregation of the very fine particles (well-coupled with the gas) by detachment of the large head vortex in Kelvin-Helmholtz instabilities likely fed the wake. From this region, the finest particles were deposited in the laminated layer C during the final propagation stage of the low energy current.

The temporal evolution of a zoned flow (i.e. heterogeneous, with highly concentrated zones and a wide range of transported grain-sizes) is dictated by the "particle control" and "gas control" principles (Chen, 2016). The "particle control" principle means that particles tend to minimize their gravitational potential energy. Large particles have greater potential energy

than smaller particles and will tend to lose it rapidly due to poor coupling with the gas and rapid settling. The “gas control” principle signifies that gas tends to minimize the resistance around particles, which yields the formation of a path of minimum-resistance and the concentration of particles in clusters. Hence, concentrated regions of a heterogeneous flow have much greater suspended transport energy and will decrease it faster (through settling of mesoscale clusters) than other less concentrated zones. These processes tend to homogenize PDCs.

As exhibited in experiments, over time, the velocity and particle volumetric concentration gradients between regions of the Tongariro blast must have decreased, yielding increasing homogeneity and the waning of the longitudinal zonation.

8.3 Future perspectives

From the present thesis, further questions have been asked:

- **Temperature**

The effects of temperature on the dynamics of the ash-cloud and underflow need to be examined. Hot ash-clouds are expected to be of lower mobility as the effect of the gas’s density will increase its potential for buoyant lift-off. Entrainment of the ambient air may be different to cold flows. Furthermore, the friction weakening mechanism in concentrated underflows (Lube and Breard et al., *in review*), due to the formation of a basal air-cushion zone, would also be enhanced.

- **Unsteadiness and duration**

Experiments presented in this thesis were restricted to short-lived steady column collapses, wherein discharge durations never exceeded 10–30% of the time required for the flow to reach its final runout. Also, natural eruptions are not only composed of single pulses, but are instead collapses of volcanic eruption columns, which can last for minutes or longer or be characterized by multiple pulses. Consequently, unsteadiness at source and longer column collapse durations exceeding the runout time of the flow by orders of magnitude could be investigated in order to explore to what degree the PDC structure discovered from short-lived flows is valid, and what the possible effects are on the transport and deposition dynamics of the currents.

- **Topographic barriers**

The effects of confinement, valley bends, as well as topographic barriers, are required to be better understood. Furthering our knowledge of the complex interactions of the flows with their environment would allow for better predictions of their behaviour in complex terrain. The study of the Tongariro blast illuminated the possibility to derive simplified estimates of the internal flow stratification from the interaction of the flow with a vertical wall. Systematic large-scale experiments modelling the interaction of a dilute PDC with a vertical obstacle could provide a validated quantitative model to derive internal flow dynamics from deposit characteristics.

- **Validation dataset**

The combination of large-scale experiments and numerical models would be an important next step to test and advance current computational PDC hazard models. Validation datasets required to calibrate multiphase models and simpler numerical models could be derived from large-scale experiments. A thorough validation study would identify the limits of our current constitutive descriptions of gas-particle dynamics and could bring new descriptions of poorly known gas-particle systems.

- **Tripartite deposit facies**

The tripartite deposit facies recognized as a result of the longitudinal zoning of the parent current in blasts could be explored experimentally. Preliminary results from large-scale experiments on dilute end-members suggest that the zoning exists in analogue flows, but further work is needed to correlate the parent flow dynamics to the deposit with regards, for instance, to the overall structure of the ash-cloud (head, body and wake).

References

Abdurachman, E.K., Bourdier, J.L. and Voight, B., 2000. Nuees ardentes of 22 November 1994 at Merapi Volcano, Java, Indonesia. Journal of Volcanology and Geothermal Research, 100(1-4): 345-361.

Agrawal, K., Loezos, P.N., Syamlal, M. and Sundaresan, S., 2001. The role of meso-scale structures in rapid gas-solid flows. J. Fluid Mech(445): 151-185.

Alatorre-Ibargueengoitia, M.A. and Delgado-Granados, H., 2006. Experimental determination of drag coefficient for volcanic materials; calibration and application of a model to Popocatepetl Volcano (Mexico) ballistic projectiles. Geophysical Research Letters, 33(11): 5-5, L11302.

Alidibirov, M. and Dingwell, D.B., 1996. Magma fragmentation by rapid decompression. Nature (London), 380(6570): 146-148.

Allen, J.R.L., 1970. Physical Processes of Sedimentation. Elsevier, New York.

Allen, J.R.L., 1982. Sedimentary structures. Their character and physical basis. Volume II, Elsevier, Amsterdam, 663 pp.

Allen, J.R.L., 1984. Sedimentary structures: Their character and Physical Basis. Elsevier, Amsterdam.

Allen, J.R.L. and Leeder, M.R., 1980. Criteria for the instability of upper-stage plane beds. Sedimentology, 27(2): 209-217.

Altinakar, M.S., Graf, W.H. and Hopfinger, E.J., 1996. Flow structure in turbidity currents. J. Hydraul. Res.(34): 713-718.

Alvarado, G.E., Soto, G.J., Schmincke, H.U., Bolge, L.L. and Sumita, M., 2006. The 1968 andesitic lateral blast eruption at Arenal Volcano, Costa Rica. Journal of Volcanology and Geothermal Research, 157(1-3): 9-33.

Andreotti, B., Forterre, Y. and Pouliquen, O., 2013. Granular media: between fluid and solid. Cambridge, New York.

Andrews, B.J., 2014. Dispersal and air entrainment in unconfined dilute pyroclastic density currents. Bulletin of Volcanology, 76(9): 1-14.

Andrews, B.J. and Manga, M., 2011. Effects of topography on pyroclastic density current runout and formation of coignimbrites. Geology, 39(12): 1099-1102.

Andrews, B.J. and Manga, M., 2012. Experimental study of turbulence, sedimentation, and coignimbrite mass partitioning in dilute pyroclastic density currents. Journal of Volcanology and Geothermal Research, 225-226: 30-44.

Aramaki, S. and Ui, T., 1966. The Aira and Ata pyroclastic flows and related caldera and depressions in southern Kyushu, Japan. Bulletin of Volcanology, 29: 29-47.

Bacon, C.R., 1987. Mount Mazama and Crater Lake Caldera, Oregon. In: M.L. Hill (Editor), Cordilleran Section of the Geological Society of America. Geol. Soc. Am., Boulder, CO, United States, pp. 301-306.

Bagnold, R.A., 1954. Experiments on a gravity-free dispersion of large solid spheres in a Newtonian fluid under shear. Proc. Royal Soc., London, A, 225: 49-63.

Bagnold, R.A., 1956. The flow of cohesionless grains in fluid. Philosophical Transactions of the Royal Society of London(A249): 235-297.

Bagnold, R.A., 1973. The nature of saltation and of 'bed-load' transport in water. Proc. Royal Soc., London(A332): 473-504.

Balmforth, N.J. and Kerswell , R.R., 2005. Granular collapse in two dimensions. Journal of Fluid Mechanics, 538: 399-428.

Baxter, P.J., Aspinall, W.P., Neri, A., Zuccaro, G., Spence, R.J.S., Cioni, R. and Woo, G., 2008. Emergency planning and mitigation at Vesuvius; a new evidence-based approach. Journal of Volcanology and Geothermal Research, 178(3): 454-473.

Baxter, P.J., Boyle, R., Cole, P., Neri, A., Spence, R. and Zuccaro, G., 2005. The impacts of pyroclastic surges on buildings at the eruption of the Soufriere Hills volcano, Montserrat. Bulletin of Volcanology, 67(4): 292-313.

Baxter, P.J., Neri, A. and Todesco, M., 1998. Physical modelling and human survival in pyroclastic flows. Natural Hazards, 17(2): 163-176.

Belousov, A., 1996. Deposits of the 30 March 1956 directed blast at Bezymianny Volcano, Kamchatka, Russia. Bulletin of Volcanology, 57(8): 649-662.

Belousov, A., Behncke, B. and Belousova, M., 2011. Generation of pyroclastic flows by explosive interaction of lava flows with ice/water-saturated substrate. Journal of Volcanology and Geothermal Research, 202(1–2): 60-72.

Belousov, A., Voight, B. and Belousova, M., 2007. Directed blasts and blast-generated pyroclastic density currents: A comparison of the Bezymianny 1956, Mount St Helens 1980, and Soufriere Hills, Montserrat 1997 eruptions and deposits. Bulletin of Volcanology, 69(7): 701-740.

Belousov, A.B. and Belousova, M.G., 2000. Deposits and sequence of Bezymyannyy Volcano eruption on March 30, 1956; directed blast deposits

Otlozheniya i posledovatel'nost' sobytiy izverzheniya vulkana Bezymyannyy 30 marta 1956 goda (Kamchatka); otlozheniya napravlennogo vzryva. Vulkanologiya i Seysmologiya, 2000(2): 3-17.

Belousova, M., Belousov, A., Patia, H. and Hoblitt, R.P., 2011. The january 21, 1951 blast of mount lamington in Papua New Guinea: sequence of events and characteristics of the deposits. American Geophysical Union Fall Meeting, 2011: Abstract V51F-2567.

Berton, G., Delannay, R., Richard, P., Taberlet, N. and Valance, A., 2003. Two-dimensional inclined chute flows: Transverse motion and segregation. Physical Review E, 68(5): 051303.

Bonnecaze, R.T., Huppert, H.E. and Lister, J.R., 1993. Particle-driven gravity currents. Journal of Fluid Mechanics, 250: 339-369.

Boudon, G. and Lajoie, J., 1989. The 1902 Peleean deposits in the Fort Cemetery of St. Pierre, Martinique; a model for the accumulation of turbulent nuees ardentes. Journal of Volcanology and Geothermal Research, 38(1-2): 113-129.

Bourdier, J.L. and Abdurachmann, E.K., 2001. Decoupling of small-volume pyroclastic flows and related hazards at Merapi Volcano, Indonesia. Bulletin of Volcanology, 63(5): 309-325.

Branney, M. and Kokelaar, P., 2002. Pyroclastic density currents and the sedimentation of ignimbrites. Geological Society Publishing House, Bath, United Kingdom, 143 pp.

Branney, M.J. and Kokelaar, P., 1992. A reappraisal of ignimbrite emplacement; progressive aggradation and changes from particulate to non-particulate flow during emplacement of high-grade ignimbrite. Bulletin of Volcanology, 54(6): 504-520.

Branney, M.J. and Kokelaar, P., 1997. Giant bed from a sustained catastrophic density current flowing over topography; Acatlan ignimbrite, Mexico. Geology (Boulder), 25(2): 115-118.

Breard, E.C.P., Lube, G., Cronin, S.J., Fitzgerald, R., Kennedy, B., Scheu, B., Montanaro, C., White, J.D.L., Tost, M., Procter, J.N. and Moebis, A., 2014. Using the spatial distribution and lithology of ballistic blocks to interpret eruption sequence and dynamics: August 6 2012 Upper Te Maari eruption, New Zealand. Journal of Volcanology and Geothermal Research(0).

Breard, E.C.P., Lube, G., Cronin, S.J. and Valentine, G.A., 2015. Transport and deposition processes of the hydrothermal blast of the 6 August 2012 Te Maari eruption, Mt. Tongariro. Bulletin of Volcanology, 77(11): 1-18.

Breard, E.C.P., Lube, G., Jones, J.R., Dufek, J., J., C.S., Valentine, G.A. and Moebis, A., In Review. Revealing the internal structure of pyroclastic flows. Nature Geoscience.

Britter, R.E. and Linden, P.F., 1980. The motion of the front of a gravity current travelling down an incline. Journal of Fluid Mechanics, 99(03): 531-543.

Britter, R.E. and Simpson, J.E., 1978. Experiments on the dynamics of a gravity current head. Journal of Fluid Mechanics, 88(02): 223-240.

Brown, M.C., 1962. Nuees ardentes and fluidization. American Journal of Science, 260(6): 467-470.

Brown, R.J. and Andrews, G.D.M., 2015. Chapter 36 - Deposits of Pyroclastic Density Currents. In: H. Sigurdsson (Editor), The Encyclopedia of Volcanoes (Second Edition). Academic Press, Amsterdam, pp. 631-648.

Brown, R.J. and Branney, M.J., 2004. Event-stratigraphy of a caldera-forming ignimbrite eruption on Tenerife: the 273ka Poris Formation. Bulletin of Volcanology, 66(5): 392-416.

Brown, R.J. and Branney, M.J., 2013. Internal flow variations and diachronous sedimentation within extensive, sustained, density-stratified pyroclastic density currents flowing down gentle slopes, as revealed by the internal architectures of ignimbrites on Tenerife. Bulletin of Volcanology, 75(7): 1-24.

Burgisser, A., 2005. Physical volcanology of the 2,050 bp caldera-forming eruption of Okmok volcano, Alaska. Bulletin of Volcanology, 67(6): 497-525.

Burgisser, A. and Bergantz, G.W., 2002. Reconciling pyroclastic flow and surge: the multiphase physics of pyroclastic density currents. Earth and Planetary Science Letters, 202(2): 405-418.

Burgisser, A., Bergantz, G.W. and Breidenthal, R.E., 2005. Addressing complexity in laboratory experiments: the scaling of dilute multiphase flows in magmatic systems. Journal of Volcanology and Geothermal Research, 141(3-4): 245-265.

Bursik, M.I., 1989. Effects of the drag force on the rise height of particles in the gas-thrust region of volcanic eruption columns. Geophysical Research Letters, 16(5): 441-444.

Bursik, M.I., Kurbatov, A.V., Sheridan, M.F. and Woods, A.W., 1998. Transport and deposition in the May 18, 1980, Mount St. Helens blast flow. Geology, 26(2): 155-158.

Bursik, M.I. and Woods, A.W., 1996. The dynamics and thermodynamics of large ash flows. Bulletin of Volcanology, 58(2-3): 175-193.

Buttinelli, M., Rita, D., Cremisini, C. and Cimarelli, C., 2011. Deep explosive focal depths during maar forming magmatic-hydrothermal eruption: Baccano Crater, Central Italy. Bulletin of Volcanology, 73(7): 899-915.

Cagnoli, B. and Manga, M., 2004. Granular mass flows and Coulomb's friction in shear cell experiments: Implications for geophysical flows. Journal of Geophysical Research: Earth Surface, 109(F4): n/a-n/a.

Cagnoli, B. and Manga, M., 2005. Vertical segregation in granular mass flows: A shear cell study. Geophysical Research Letters, 32(10): n/a-n/a.

Calder, E.S., Cole, P.D., Dade, W.B., Druitt, T.H., Hoblitt, R.P., Huppert, H.E., Ritchie, L., Sparks, R.S.J. and Young, S.R., 1999. Mobility of pyroclastic flows and surges at the Soufriere Hills Volcano, Montserrat. Geophysical Research Letters, 26(5): 537-540.

Calder, E.S., Lavallée, Y., Kendrick, J.E. and Bernstein, M., 2015. Chapter 18 - Lava Dome Eruptions. In: H. Sigurdsson (Editor), The Encyclopedia of Volcanoes (Second Edition). Academic Press, Amsterdam, pp. 343-362.

Calder, E.S., Sparks, R.S.J. and Gardeweg, M.C., 2000. Erosion, transport and segregation of pumice and lithic clasts in pyroclastic flows inferred from ignimbrite at Lascar Volcano, Chile. Journal of Volcanology and Geothermal Research, 104(1-4): 201-235.

Campbell, C.S., 1990. Rapid granular flows. Ann. Rev. Fluid Mech., 22: 57-92.

Campbell, C.S. and Brennen, C.E., 1985. Cumputer-simulation of granular shear flows. Journal of Fluid Mechanics(151): 167-188.

Cantero, M.I., Cantelli, A., Pirmez, C., Balachandar, S., Mohrig, D., Hickson, T.A., Yeh, T.-h., Naruse, H. and Parker, G., 2012. Emplacement of massive turbidites linked to extinction of turbulence in turbidity currents. Nature Geoscience, 5(1): 42-45.

Carazzo, G., Kaminski, E. and Tait, S., 2015. The timing and intensity of column collapse during explosive volcanic eruptions. Earth and Planetary Science Letters, 411: 208-217.

Carey, S., Sigurdsson, H., Mandeville, C. and Bronto, S., 1996. Pyroclastic flows and surges over water; an example from the 1883 Krakatau eruption. Bulletin of Volcanology, 57(7): 493-511.

Carey, S.N., 1991. Transport and deposition of tephra by pyroclastic flows and surges. In: Fisher, R.V. and Smith, G.A. (Eds), Sedimentation in volcanic settings, SEPM, Special Publications. 45.

Carey, S.N., Sigurdsson, H. and Sparks, R.S.J., 1988. Experimental studies of particle-laden plumes. Journal of Geophysical Research, 93(B12): 15-15,328.

Cas, R.A.F., Wright, H.M.N., Folkes, C.B., Lesti, C., Porreca, M., Giordano, G., Viramonte, J.G. and Cashman, K., 2011. The flow dynamics of an extremely large volume pyroclastic flow, the 2.08-Ma Cerro Galan ignimbrite, NW Argentina, and comparison with other flow types. Bulletin of Volcanology, 73(10): 1583-1609.

Cas, R.A.F. and Wright, J.V., 1987. Volcanic successions: modern and ancient. A geological approach to processes, products and successions. Allen and Unwin, London, UK.

Cashman, K.V. and Scheu, B., 2015. Chapter 25 - Magmatic Fragmentation. In: H. Sigurdsson (Editor), The Encyclopedia of Volcanoes (Second Edition). Academic Press, Amsterdam, pp. 459-471.

Cashman, K.V. and Sparks, R.J., 2013. How volcanoes work: A 25 year perspective. Bulletin of the Geological Society of America, 125(5-6): 664-690.

Cenedece, C. and Adduce, C., 2008. Mixing in a density-driven current flowing down a slope in a rotating fluid. Journal of Fluid Mechanics, 604: 369-388.

Charbonnier, S.J. and Gertisser, R., 2009. Numerical simulations of block-and-ash flows using the Titan2D flow model; examples from the 2006 eruption of Merapi Volcano, Java, Indonesia. Bulletin of Volcanology, 71(8): 953-959.

Charbonnier, S.J. and Gertisser, R., 2011. Deposit architecture and dynamics of the 2006 block-and-ash flows of Merapi Volcano, Java, Indonesia. Sedimentology, 58(6): 1573-1612.

Chedeville, C. and Roche, O., 2014. Autofluidization of pyroclastic flows propagating on rough substrates as shown by laboratory experiments. Journal of Geophysical Research: Solid Earth, 119(3): 1764-1776.

Chough, S.K. and Sohn, Y.K., 1990. Depositional mechanics and sequences of base surges, Songaksan tuff ring, Cheju Island, Korea. Sedimentology, 37(6): 1115-1135.

Choux, C.M. and Druitt, T.H., 2002. Analogue study of particle segregation in pyroclastic density currents, with implications for the emplacement mechanisms of large ignimbrites. Sedimentology, 49(5): 907-928.

Clarke, A.B. and Voight, B., 2000. Pyroclastic current dynamic pressure from aerodynamics of tree or pole blow-down. Journal of Volcanology and Geothermal Research, 100(1-4): 395-412.

Clarke, A.B., Voight, B., Neri, A. and Macedonio, G., 2002. Transient dynamics of vulcanian explosions and column collapse. Nature, 415(6874): 897-901.

Cole, P.D., Calder, E.S., Druitt, T.H., Hoblitt, R., Robertson, R., Sparks, R.S.J. and Young, S.R., 1998. Pyroclastic flows generated by gravitational instability of the 1996–97 Lava Dome of Soufriere Hills Volcano, Montserrat. Geophysical Research Letters, 25(18): 3425-3428.

Cole, P.D., Calder, E.S., Sparks, R.S.J., Clarke, A.B., Druitt, T.H., Young, S.R., Herd, R.A., Harford, C.L. and Norton, G.E., 2002. Deposits from dome-collapse and fountain-collapse pyroclastic flows at Soufriere Hills Volcano, Montserrat. Memoirs of the Geological Society of London, 21: 231-262.

Cronin, S.J., Lube, G., Dayudi, D.S., Sumarti, S., Subrandiyo, S. and Surono, 2013. Insights into the October–November 2010 Gunung Merapi eruption (Central Java, Indonesia) from the stratigraphy, volume and characteristics of its pyroclastic deposits. Journal of Volcanology and Geothermal Research, 261: 244-259.

Crowe, B.M. and Fisher, R.V., 1973. Sedimentary Structures in Base-Surge Deposits with Special Reference to Cross-Bedding, Ubehebe Craters, Death Valley, California. Geological Society of America Bulletin, 84(2): 663-681.

da Cruz, F., Emam, S., Prochnow, M., Roux J.-N. and Chevoir, F., 2005. Rheophysics of dense granular materials: Discrete simulation of plane shear flows. Physical Review E(72): 021309.

Dade, B.W. and Huppert, H.E., 1995. Runout and fine-sediment deposits of axisymmetric turbidity currents. J Geophys Res, 100: 18597-18609.

Dade, B.W. and Huppert , H.E., 1998. Long runout rockfalls. Geology(26): 612-615.

Dade, W.B., 2003. The emplacement of low-aspect ratio ignimbrites by turbulent parent flows. Journal of Geophysical Research, 108(B4): 9.

Dade, W.B. and Huppert, H.E., 1996. Emplacement of the Taupo ignimbrite by a dilute turbulent flow. Nature, 381(6582): 509-512.

Dartevelle, S., 2003. Numerical and granulometric approaches to geophysical granular flows, Ph.D. dissertation thesis, Dep. of Geol. and Min. Eng., Mich. Technol. Univ., Houghton.

Dartevelle, S., 2004. Numerical modeling of geophysical granular flows: 1. A comprehensive approach to granular rheologies and geophysical multiphase flows. Geochemistry, Geophysics, Geosystems, 5(8): n/a-n/a.

Dartevelle, S., Rose, W.I., Stix, J., Kelfoun, K. and Vallance, J.W., 2004. Numerical modeling of geophysical granular flows; 2, Computer simulations of plinian clouds and pyroclastic flows and surges. Geochemistry, Geophysics, Geosystems - G3, 5(8): 36.

de'Michieli Vitturi, M., Neri, A., Esposti Ongaro, T., Lo Savio, S. and Boschi, E., 2010. Lagrangian modeling of large volcanic particles; application to Vulcanian explosions. Journal of Geophysical Research, 115(B8): 0-Citation B08206.

Delannay, R., Louge, M., Richard, P., Taberlet, N. and Valance, A., 2007. Towards a theoretical picture of dense granular flows down inclines. Nat Mater, 6(2): 99-108.

Delinger, R.P., 1987. A model for generation of ash clouds by pyroclastic flows, with application to the 1980 eruptions at Mount St. Helens. Journal of Geophysical Research(B93): 10284-10298.

Dellino, P., Dioguardi, F., Mele, D., D'Addabbo, M., Zimanowski, B., Buettner, R., Doronzo, D.M., Sonder, I., Sulpizio, R., Durig, T. and La Volpe, L., 2014. Volcanic jets,

plumes, and collapsing fountains; evidence from large-scale experiments, with particular emphasis on the entrainment rate. Bulletin of Volcanology, 76(6): 1-18.

Dellino, P., Isaia, R. and Veneruso, M., 2004. Turbulent boundary layer shear flows as an approximation of base surges at Campi Flegrei (southern Italy). Journal of Volcanology and Geothermal Research, 133(1-4): 211-228.

Dellino, P. and La Volpe, L., 2000. Structures and grain size distribution in surge deposits as a tool for modelling the dynamics of dilute pyroclastic density currents at La Fossa di Vulcano (Aeolian Islands, Italy). Journal of Volcanology and Geothermal Research, 96(1-2): 57-78.

Dellino, P., Mele, D., Bonasia, R., Braia, G., La Volpe, L. and Sulpizio, R., 2005. The analysis of the influence of pumice shape on its terminal velocity. Geophysical Research Letters, 32(21): 4.

Dellino, P., Mele, D., Sulpizio, R., La Volpe, L. and Braia, G., 2008. A method for the calculation of the impact parameters of dilute pyroclastic density currents based on deposit particle characteristics. Journal of Geophysical Research, 113(B7): 0-Citation B07206.

Dellino, P., Zimanowski, B., Buttner, R., La Volpe, L., Mele, D. and Sulpizio, R., 2007. Large-scale experiments on the mechanics of pyroclastic flows: Design, engineering, and first results. Journal of Geophysical Research B: Solid Earth, 112(4).

Dimotakis, P.E. and Catrakis, H.J., 1999. Turbulence, fractals, and mixing. In: Chate, H., Villermaux, E., Chomaz, J.-M. (Eds.), Mixing, Chaos and Turbulence. . NATO ASI Series B: Physics,, 373: 59- 144.

Dobran, F., Neri, A. and Macedonio, G., 1993. Numerical simulation of collapsing volcanic columns. Journal of Geophysical Research: Solid Earth, 98(B3): 4231-4259.

Doronzo, D.M., de Tullio, M.D., Dellino, P. and Pascazio, G., 2011. Numerical simulation of pyroclastic density currents using locally refined Cartesian grids. Computers & Fluids, 44(1): 56-67.

Doronzo, D.M. and Dellino, P., 2011. Interaction between pyroclastic density currents and buildings: Numerical simulation and first experiments. Earth and Planetary Science Letters, 310(3-4): 286-292.

Doronzo, D.M. and Dellino, P., 2013. Hydraulics of subaqueous ash flows as deduced from their deposits; 2, Water entrainment, sedimentation, and deposition, with implications on pyroclastic density current deposit emplacement. Journal of Volcanology and Geothermal Research, 258: 176-186.

Doronzo, D.M. and Dellino, P., 2014. Pyroclastic density currents and local topography as seen with the conveyer model. Journal of Volcanology and Geothermal Research, 278-279: 25-39.

Douillet, G.A., Pacheco, D.A., Kueppers, U., Letort, J., Tsang-Hin-Sun, E., Bustillos, J., Hall, M., Ramon, P. and Dingwell, D.B., 2013. Dune bedforms produced by dilute pyroclastic density currents from the August 2006 eruption of Tungurahua volcano, Ecuador. Bulletin of Volcanology, 75(11): 1-20.

Douillet, G.A., Rasmussen, K.R., Kueppers, U., Lo Castro, D., Merrison, J.P., Iversen, J.J. and Dingwell, D.B., 2014. Saltation threshold for pyroclasts at various bedslopes: Wind tunnel measurements. Journal of Volcanology and Geothermal Research, 278–279(0): 14-24.

Doyle, E.E., Hogg, A.J., Mader, H.M. and Sparks, R.S.J., 2008. Modeling dense pyroclastic basal flows from collapsing columns. Geophysical Research Letters, 35(4): n/a-n/a.

Doyle, E.E., Hogg, A.J., Mader, H.M. and Sparks, R.S.J., 2010. A two-layer model for the evolution and propagation of dense and dilute regions of pyroclastic currents. Journal of Volcanology and Geothermal Research, 190(3-4): 365-378.

Drescher, A., 1992. On the Criteria For Mass Flow Hoppers. Powder Technology, 95: 143-151.

Druitt, T.H., 1992. Emplacement of the 18 May 1980, lateral blast deposit ENE of Mount St. Helens, Washington. Bulletin of Volcanology, 54(7): 554-572.

Druitt, T.H., 1998. Pyroclastic density currents. Geological Society Special Publication(145): 145-182.

Druitt, T.H., 2014. New insights into the initiation and venting of the Bronze-Age eruption of Santorini (Greece), from component analysis. Bulletin of Volcanology, 76(2): 1-21.

Druitt, T.H., Avard, G., Bruni, G., Lettieri, P. and Maez, F., 2007. Gas retention in fine-grained pyroclastic flow materials at high temperatures. Bulletin of Volcanology, 69(8): 881-901.

Druitt, T.H., Bruni, G., Lettieri, P. and Yates, J.G., 2004. The fluidization behaviour of ignimbrite at high temperature and with mechanical agitation. Geophysical Research Letters, 31(2).

Druitt, T.H. and Kokelaar, B.P., 2002. The eruption of Soufrière Hills volcano, Montserrat, from 1995 to 1999. Geol Soc London Memoir 21, 845 pp.

Dufek, J., 2016. The Fluid Mechanics of Pyroclastic Density Currents. In: S.H. Davis and P. Moin (Editors), Annual Review of Fluid Mechanics, Vol 48. Annual Review of Fluid Mechanics. Annual Reviews, Palo Alto, pp. 459-485.

Dufek, J. and Bergantz, G.W., 2005. Transient two-dimensional dynamics in the upper conduit of a rhyolitic eruption; a comparison of closure models for the granular stress. Journal of Volcanology and Geothermal Research, 143(1-3): 113-132.

Dufek, J. and Bergantz, G.W., 2007a. Dynamics and deposits generated by the Kos Plateau Tuff eruption; controls of basal particle loss on pyroclastic flow transport. Geochemistry, Geophysics, Geosystems - G3, 8(12): Citation Q12007.

Dufek, J. and Bergantz, G.W., 2007b. Dynamics and deposits generated by the Kos Plateau Tuff eruption; controls of basal particle loss on pyroclastic flow transport. Geochemistry, Geophysics, Geosystems - G (super 3), 8(12).

Dufek, J. and Bergantz, G.W., 2007c. Suspended load and bed-load transport of particle-laden gravity currents: The role of particle-bed interaction. Theoretical and Computational Fluid Dynamics, 21(2): 119-145.

Dufek, J., Bergantz, G.W., Ubertini, L., Manciola, P., Casadei, S. and Grimaldi, S., 2007. Modeling the dynamics of turbulent multiphase gravity currents; the importance of geologically diverse boundary conditions. International Union of Geodesy and Geophysics General Assembly = Union Geodesique et Geophysique Internationale Comptes Rendus de la ...Assemblee Generale, 24: Abstract 74.

Dufek, J., Esposti Ongaro, T. and Roche, O., 2015. Chapter 35 - Pyroclastic Density Currents: Processes and Models. In: H. Sigurdsson (Editor), The Encyclopedia of Volcanoes (Second Edition). Academic Press, Amsterdam, pp. 617-629.

Dufek, J. and Manga, M., 2008. In situ production of ash in pyroclastic flows. Journal of Geophysical Research, 113(B9): Citation B09207.

Efford, J.T., Bylsma, R.J., Clarkson, B.D., Pittari, A., Mauriohooho, K. and Moon, V.G., 2014. Vegetation dieback as a proxy for temperature within a wet pyroclastic density current: A novel experiment and observations from the 6th of August 2012 Tongariro eruption. Journal of Volcanology and Geothermal Research(0).

Einstein, H. and Chien, N., 1955. Effects of heavy sediment concentration near the bed on velocity and sediment distribution. US Army Corps of Engineers, Misouri River Division, Sedimentology Series(8): 1-76.

Ellison, T.H. and Turner, J.S., 1959. Turbulent entrainment in stratified flows. Journal of Fluid Mechanics, 6(03): 423-448.

Esposti Ongaro, T., Clarke, A.B., Neri, A., Voight, B. and Widiwijayanti, C., 2008. Fluid dynamics of the 1997 Boxing Day volcanic blast on Montserrat, West Indies. J. Geophys. Res, 113.

Esposti Ongaro, T., Clarke, A.B., Voight, B., Neri, A. and Widiwijayanti, C., 2012. Multiphase flow dynamics of pyroclastic density currents during the May 18, 1980 lateral blast of Mount St. Helens. Journal of Geophysical Research, 117(B6): B06208.

Esposti Ongaro, T., Widiwijayanti, C., Clarke, A.B., Voight, B. and Neri, A., 2011. Multiphase-flow numerical modeling of the 18 May 1980 lateral blast at Mount St. Helens, USA. Geology, 39(6): 535-538.

Esposti Ongaro, T.E., Clarke, A.B., Neri, A., Voight, B., Widiwijayanti, C. and Anonymous, 2005. A new high-performance 3D multiphase flow code to simulate volcanic blasts and pyroclastic density currents; example from the Boxing Day event, Montserrat. Eos, Transactions, American Geophysical Union, 86(52, Suppl.): Abstract V31D-0645.

Fagents, S.A. and Wilson, L., 1993. Explosive volcanic eruptions; VII, The ranges of pyroclasts ejected in transient volcanic explosions. Geophysical Journal International, 113(2): 359-370.

Fink, J.H., 1990. Lava Flows and Domes New York.

Fink, J.H. and Kieffer, S.W., 1993. Estimate of pyroclastic flow velocities resulting from explosive decompression of lava domes. Nature (London), 363(6430): 612-615.

Fisher, R.V., 1966. Mechanism of deposition from pyroclastic flows. Am. J. Sci., 264: 350-366.

Fisher, R.V., 1979. Models of pyroclastic surges and pyroclastic flows. Journal of Volcanology and Geothermal Research, 6(3-4): 305-318.

Fisher, R.V., 1990. Transport and deposition of a pyroclastic surge across an area of high relief; the 18 May 1980 eruption of Mount St. Helens, Washington. Geological Society of America Bulletin, 102(8): 1038-1054.

Fisher, R.V., 1995. Decoupling of pyroclastic currents; hazards assessments. Journal of Volcanology and Geothermal Research, 66(1-4): 257-263.

Fisher, R.V., Schmincke, H.-U. and van den Bogaard, P., 1983. Origin and emplacement of a pyroclastic flow and surge unit at Laacher See, Germany. Journal of Volcanology and Geothermal Research, 17(1-4): 375-392.

Fisher, R.V. and Schmincke, H.U., 1984. Pyroclastic rocks. Springer-Verlag, Berlin, West Germany, xiv+472 pp.

Fisher, R.V., Smith, A.L. and Roobol, M.J., 1980. Destruction of St. Pierre, Martinique, by ash-cloud surges, May 8 and 20, 1902. Geology (Boulder), 8(10): 472-476.

Fisher, R.V. and Waters, A.C., 1970. Base surge bed forms in maar volcanoes. American Journal of Science, 268(2): 157-180.

Fitzgerald, R.H., Tsunematsu, K., Kennedy, B.M., Breard, E.C.P., Lube, G., Wilson, T.M., Jolly, A.D., Pawson, J., Rosenberg, M.D. and Cronin, S.J., 2014. The application of a calibrated 3D ballistic trajectory model to ballistic hazard assessments at Upper Te Maari, Tongariro. Journal of Volcanology and Geothermal Research, 286(0): 248-262.

Francis, P.W. and Baker, M.C.W., 1977. Mobility of pyroclastic flows. Nature, 270(5633): 164-165.

Freundt, A., 2003. Entrance of hot pyroclastic flows into the sea; experimental observations. Bulletin of Volcanology, 65(2-3): 144-164.

Freundt, A. and Bursik, M., 1998. Pyroclastic flow transport mechanisms. Developments in Volcanology: 173-245.

Freundt, A., Wilson, C.J.N. and Carey, S.N., 2000. Ignimbrites and block-and-ash flow deposits. In: H. Sigurdsson, B.F. Houghton, S.R. McNutt, H. Rymer, J. Stix and R.D. Ballard (Editors), Encyclopedia of volcanoes. Academic Press, San Diego, CA, United States, pp. 581-599.

Fuji, T. and Nakada, S., 1999. The 15 September 1991 pyroclastic flows at Unzen volcano (Japan): a flow model for associated ash-cloud surges. Journal of Volcanology and Geothermal Research(89): 159-172.

Fujinawa, A., Ban, M., Ohba, T., Kontani, K. and Miura, K., 2008. Characterization of low-temperature pyroclastic surges that occurred in the northeastern Japan arc during the late 19th century. Journal of Volcanology and Geothermal Research, 178(1): 113-130.

Garcia, M.H., 1994. Depositional turbidity currents laden with poorly sorted sediment. Journal of Hydraulic Engineering, 120(11): 1240-1263.

García, M.H. and Parsons, J.D., 1996. Mixing at the front of gravity currents. Dynamics of Atmospheres and Oceans, 24(1–4): 197-205.

GDR-MiDi, 2004. Eur. Phys. J. E 14, 341.

Geldart, D., 1986. Gas Fluidization Technology. Wiley.

Gerber, G., 2011. Particle Image Velocimetry Measurements and Numerical Modeling of a Saline Density Current (vol 137, pg 333, 2011). Journal of Hydraulic Engineering-Asce, 137(9): 1101-1101.

Gidaspow, D., 1994. Multiphase flow and fluidization: Continuum and kinetic theory description.

Girolami, L., Druitt, T.H. and Roche, O., 2007. Dynamics of laboratory ash flows. International Union of Geodesy and Geophysics General Assembly = Union Geodesique et Geophysique Internationale Comptes Rendus de la ...Assemblee Generale, 24.

Girolami, L., Druitt, T.H., Roche, O. and Khrabrykh, Z., 2008. Propagation and hindered settling of laboratory ash flows. Journal of Geophysical Research, 113(B2).

Girolami, L., Roche, O., Druitt, T.H. and Corpetti, T., 2010. Particle velocity fields and depositional processes in laboratory ash flows, with implications for the sedimentation of dense pyroclastic flows. Bulletin of Volcanology, 72(6): 747-759.

Gladstone, Phillips and Sparks, 1998. Experiments on bidisperse, constant-volume gravity currents: propagation and sediment deposition. Sedimentology, 45(5): 833-843.

Gladstone, C., Ritchie, L.J., Sparks, R.S.J. and Woods, A.W., 2004. An experimental investigation of density-stratified inertial gravity currents. Sedimentology, 51(4): 767-789.

Glicken, H. and Nakamura, Y., 1988. Restudy of the 1888 eruption of Bandai Volcano, Japan. Natl. Inst. Res. Advancement, Tokyo.

Gorshkov, G.S., 1959. Gigantic eruption of the volcano Bezymianny. Bulletin of Volcanology, 20: 77-109.

Goto, A., Taniguchi, H., Yoshida, M., Ohba, T. and Oshima, H., 2001. Effects of explosion energy and depth to the formation of blast wave and crater; field explosion experiment for the understanding of volcanic explosion. Geophysical Research Letters, 28(22): 4287-4290.

Graettinger, A.H., Valentine, G.A., Sonder, I., Ross, P.S., White, J.D.L. and Taddeucci, J., 2014. Maar-diatreme geometry and deposits; subsurface blast experiments with

variable explosion depth. Geochemistry, Geophysics, Geosystems - G3, 15(3): 740-764.

Gravina, T., Lirer, L., Marzocchella, A., Petrosino, P. and Salatino, P., 2004. Fluidization and attrition of pyroclastic granular solids. Journal of Volcanology and Geothermal Research, 138(1-2): 27-42.

Gurioli, L., Harris, A.J.L., Colo, L., Bernard, J., Favalli, M., Ripepe, M. and Andronico, D., 2013. Classification, landing distribution, and associated flight parameters for a bomb field emplaced during a single major explosion at Stromboli, Italy. Geology (Boulder), 41(5): 559-562.

Gurioli, L., Pareschi, M.T., Zanella, E., Lanza, R., Deluca, E. and Bisson, M., 2005. Interaction of pyroclastic density currents with human settlements; evidence from ancient Pompeii. Geology (Boulder), 33(6): 441-444.

Hacker, J., Linden, P.F. and Dalziel, S.B., 1996. Mixing in lock-release gravity currents. Dynamics of Atmospheres and Oceans, 24(1-4): 183-195.

Hall, M.L., Steele, A.L., Bernard, B., Mothes, P.A., Vallejo, S.X., Douillet, G.A., Ramón, P.A., Aguaiza, S.X. and Ruiz, M.C., 2015. Sequential plug formation, disintegration by Vulcanian explosions, and the generation of granular Pyroclastic Density Currents at Tungurahua volcano (2013–2014), Ecuador. Journal of Volcanology and Geothermal Research, 306: 90-103.

Hallworth, M.A., Phillips, J.C., Huppert, H.E. and Sparks, R.S.J., 1993. Entrainment in turbulent gravity currents. Nature, 362(6423): 829-831.

Hayashi, J.N. and Self, S., 1992. A comparison of pyroclastic flow and debris avalanche mobility. Journal of Geophysical Research, 97(B6): 9063-9071.

Heinrich, P., Boudon, G., Komorowski, J.C., Sparks, R.S.J., Herd, R. and Voight, B., 2001. Numerical simulation of the December 1997 Debris Avalanche in Montserrat, Lesser Antilles. Geophysical Research Letters, 28(13): 2529-2532.

Hill, H., 1893. The volcanic outburst at Te Māri, Tongariro, in November, 1892. Trans. N. Z. Inst, 24: 388-391.

Hill, H., 1897. On a volcanic dust shower in Napier Trans. N. Z. Inst(19): 571-572.

Hoblitt, R., 1986. Observations of the eruptions of July 22 and August 7, 1980, at Mount St. Helens, Washington. U. S. Geological Survey, Reston, VA, United States, 44 pp.

Hoblitt, R.P., Miller, C.D. and Vallance, J.W., 1981. Origin and stratigraphy of the deposit produced by the May 18 directed blast. U. S. Geological Survey Professional Paper: 401-419.

Hogg, A., Lowe, D.J., Palmer, J., Boswijk, G. and Ramsey, C.B., 2012. Revised calendar date for the Taupo eruption derived by 14C wiggle-matching using a New Zealand kauri 14C calibration data set. Holocene, 22(4): 439-449.

Hogg , A.J. and Pritchard, D., 2004. The effects of hydraulic resistance on dam-break and other shallow inertial flows. Journal of Fluid Mechanics, 501: 179-212.

Houghton, B., White, J.D.L. and Van Eaton, A.R., 2015. Chapter 30 - Phreatomagmatic and Related Eruption Styles. In: H. Sigurdsson (Editor), The Encyclopedia of Volcanoes (Second Edition). Academic Press, Amsterdam, pp. 537-552.

Huppert , H.E., 2006. Gravity currents: a personal perspective. Journal of Fluid Mechanics, 554: 299-322.

Huppert, H.E. and Simpson, J.E., 1980. The slumping of gravity currents. Journal of Fluid Mechanics, 99(04): 785-799.

Iverson, R.H., 1997. The physics of debris flows. Reviews of Geophysics, 35(3): 245-296.

Iverson, R.M. and Vallance, J.W., 2001. New views of granular mass flows. Geology (Boulder), 29(2): 115-118.

Jenkins, J.T. and Savage, S.B., 1983. A theory for the rapid flow of identical, smooth, nearly elastic, spherical particles. Journal of Fluid Mechanics, 130: 187-202.

Jenkins, S., Komorowski, J.C., Baxter, P.J., Spence, R., Picquout, A., Lavigne, F. and Surono, 2013. The Merapi 2010 eruption: An interdisciplinary impact assessment methodology for studying pyroclastic density current dynamics. Journal of Volcanology and Geothermal Research, 261: 316-329.

Jeon, Y.M., Kwon, C.W. and Sohn, Y.K., 2011. Deposition from pyroclastic surges partially blocked by a topographic obstacle; an example from the Ilchulbong tuff cone, Jeju Island, Korea. Geosciences Journal (Seoul), 15(2): 121-130.

Jolly, A.D., Lokmer, I., Kennedy, B., Keys, H.J.R., Proctor, J., Lyons, J.J. and Jolly, G.E., 2014. Active seismic sources as a proxy for seismic surface processes: An example from the 2012 Tongariro volcanic eruptions, New Zealand. Journal of Volcanology and Geothermal Research, 286: 317-330.

Jop, P., Forterre, Y. and Pouliquen, O., 2006. A constitutive law for dense granular flows. Nature(441): 727-730.

Kelfoun, K., 2011. Suitability of simple rheological laws for the numerical simulation of dense pyroclastic flows and long-runout volcanic avalanches. Journal of Geophysical Research, 116(B8).

Kelfoun, K., Druitt, T., van Wyk de Vries, B. and Guilbaud, M.-N., 2008. Topographic reflection of the Socompa debris avalanche, Chile. Bulletin of Volcanology, 70(10): 1169-1187.

Kelfoun, K. and Druitt, T.H., 2005. Numerical modeling of the emplacement of Socompa rock avalanche, Chile. Journal of Geophysical Research: Solid Earth, 110(B12): n/a-n/a.

Kelfoun, K., Samaniego, P., Palacios, P. and Barba, D., 2009. Testing the suitability of frictional behaviour for pyroclastic flow simulation by comparison with a well-constrained eruption at Tungurahua volcano (Ecuador). Bulletin of Volcanology, 71(9): 1057-1075.

Kieffer, S.W., 1981. Fluid dynamics of the May 18 blast at Mount St. Helens. U. S. Geological Survey Professional Paper: 379-400.

Kieffer, S.W., 1984. Factors governing the structure of volcanic jets. Natl. Acad. Press, Washington, DC, Washington, DC, United States (USA).

Kilgour, G., Manville, V., Della Pasqua, F., Graettinger, A., Hodgson, K.A. and Jolly, G.E., 2010. The 25 September 2007 eruption of Mount Ruapehu, New Zealand; directed ballistics, surtseyan jets, and ice-slurry lahars. Journal of Volcanology and Geothermal Research, 191(1-2): 1-14.

Kilgour, G.N., Della-Pasqua, F.N., Christenson, B.W., Jolly, A.D., Jolly, G. and Anonymous, 2008. Directed blast deposits of the 25 September 2007 phreatic eruption at Mount Ruapehu, New Zealand. IAVCEI, Reykjavik, Reykjavik, Iceland (ISL), 1-1 pp.

Kneller, B., Bennett, S.J. and McCaffrey, W.D., 1999. Velocity structure, turbulence and fluid stresses in experimental gravity currents. J. Geophys. Res., Oceans.(104): 5281-5291.

Kneller, B. and Buckee, C., 2000. The structure and fluid mechanics of turbidity currents; a review of some recent studies and their geological implications. Sedimentology, 47, Suppl. 1: 62-94.

Komorowski, J.-C., Jenkins, S., Baxter, P.J., Picquout, A., Lavigne, F., Charbonnier, S., Gertisser, R., Preece, K., Cholik, N., Budi-Santoso, A. and Surono, 2013a. Paroxysmal dome explosion during the Merapi 2010 eruption: Processes and facies relationships of associated high-energy pyroclastic density currents. Journal of Volcanology and Geothermal Research.

Komorowski, J.-C., Jenkins, S., Baxter, P.J., Picquout, A., Lavigne, F., Charbonnier, S., Gertisser, R., Preece, K., Cholik, N., Budi-Santoso, A. and Surono, 2013b. Paroxysmal dome explosion during the Merapi 2010 eruption: Processes and facies relationships of associated high-energy pyroclastic density currents. Journal of Volcanology and Geothermal Research, 261: 260-294.

Kunii, D. and Levespiel, O., 1991. Fluidization Engineering 2nd edition. Butterworth-Heinemann

Lacroix, A., 1904. La Montagne Pele´e et ses eruptions. Masson, Paris, 650 pp.

Lajeunesse, E., Mangeney-Castelnau, A. and Vilotte, J.P., 2004. Spreading of a granular mass on a horizontal plane. Physics of Fluids, 16(7): 2371-2381.

Lajoie, J., Boudon, G. and Bourdier, J.L., 1989. Depositional mechanics of the 1902 pyroclastic nuee-ardente deposits of Mt. Pelee, Martinique. Journal of Volcanology and Geothermal Research, 38(1-2): 131-142.

Latter, J.H., 1982. Tsunamis of volcanic origin; summary of causes, with particular reference to Krakatoa, 1883. Bulletin of Volcanology, 44(3): 467-490.

Li, M.Z. and Komar, P.D., 1992. Selective entrainment and transport of mixed size and density sands; flume experiments simulating the formation of black-sand placers. Journal of Sedimentary Petrology, 62(4): 584-590.

Lindsay, J.M., de Silva, S., Trumbull, R., Emmermann, R. and Wemmer, K., 2001. La Pacana Caldera, N. Chile; a re-evaluation of the stratigraphy and volcanology of one of the

world's largest resurgent calderas. Journal of Volcanology and Geothermal Research, 106(1-2): 145-173.

Lipman, P.W. and Mullineaux, D.R.E., 1981. The 1980 eruptions of Mount St. Helens, Washington. U. S. Geological Survey Professional Paper: 844-844.

Lockwood, J.P. and Hazlett, R.W., 2010. Volcanoes, Global Perspectives. Wiley-Blackwell.

Lombardi, V., Adduce, C., Sciortino, G. and La Rocca, M., 2015. Gravity currents flowing upslope: Laboratory experiments and shallow-water simulations. Physics of Fluids, 27(1).

Louge, M.Y. and Keast, S.C., 2001. On dense granular flows down flat frictional inclines. Physics of Fluids, 13(5): 1213-1233.

Loughlin, S.C., Calder, E.S., Clarke, A.B., Cole, P.D., Luckett, R., Mangan, M.T., Pyle, D.M., Sparks, R.S.J., Voight, B. and Watts, R.B., 2002. Pyroclastic flows and surges generated by the 25 June 1997 dome collapse, Soufriere Hills Volcano, Montserrat. Memoirs of the Geological Society of London, 21: 191-209.

Lowe, D.R., 1976. Grain flow and grain flow deposits. Journal of Sedimentary Petrology(46): 188-199.

Lowe, D.R., 1982. Sediment gravity flows: II. Depositional models with special reference of the deposit of high-density turbidity currents. Journal of Sedimentary Petrology(52): 279-298.

Lube, G., Breard, E.C.P., Cronin, S.J. and Jones, J., 2015. Synthesizing large-scale pyroclastic flows: experimental design, scaling, and first results from PELE. Journal of Geophysical Research: Solid Earth, 120(3): 1487-1502.

Lube, G., Breard, E.C.P., Cronin, S.J., Procter, J.N., Brenna, M., Moebis, A., Pardo, N., Stewart, R.B., Jolly, A. and Fournier, N., 2014. Dynamics of surges generated by

hydrothermal blasts during the 6 August 2012 Te Maari eruption, Mt. Tongariro, New Zealand. Journal of Volcanology and Geothermal Research, 286(0): 348-366.

Lube, G., Breard, E.C.P., Jones, J.R., Fullard, L., Cronin Shane J., Wang, T. and Valentine, G.A., in review. The 'aero-planing' of pyroclastic flows.

Lube, G., Cronin, S.J., Platz, T., Freundt, A., Procter, J.N., Henderson, C. and Sheridan, M.F., 2007a. Flow and deposition of pyroclastic granular flows: A type example from the 1975 Ngauruhoe eruption, New Zealand. Journal of Volcanology and Geothermal Research, 161(3): 165-186.

Lube, G., Cronin, S.J., Thouret, J.-C. and Surono, 2011. Kinematic characteristics of pyroclastic density currents at Merapi and controls on their avulsion from natural and engineered channels. Geological Society of America Bulletin, 123(5-6): 1127-1140.

Lube, G., Freundt, A., Cronin, S.J., Platz, T., Sparks, R.S.J. and Huppert, H.E., 2007b. Flow and deposition of pyroclastic granular flows a combined field and experimental study. International Union of Geodesy and Geophysics General Assembly = Union Geodesique et Geophysique Internationale Comptes Rendus de la ...Assemblee Generale, 24.

Lube, G., Huppert, H.E., Sparks, R.S.J. and Freundt, A., 2004. Axisymetric collapses of granular columns Journal of Fluid Mechanics(508): 175-199.

Lube, G., Huppert, H.E., Sparks, R.S.J. and Freundt, A., 2005. Collapses of two-dimensional granular columns. Physical Review E, 72(4).

Lucas, A. and Mangeney, A., 2007. Mobility and topographic effects for large Valles Marineris landslides on Mars. Geophysical Research Letters, 34(10): n/a-n/a.

Mangeney, A., Roche, O., Hungr, O., Mangold, N., Faccanoni, G. and Lucas, A., 2010. Erosion and mobility in granular collapse over sloping beds. Journal of Geophysical Research: Earth Surface, 115(F3): n/a-n/a.

Marble, F.E., 1970. Dynamics of Dusty Gases. Annual Review of Fluid Mechanics, 2(1): 397-446.

Marino, B.M., Thomas, L.P. and Linden, P.F., 2005. The front condition for gravity currents. Journal of Fluid Mechanics, 536: 49-78.

Mastin, L.G., 2001. A simple calculator of ballistic trajectories for blocks ejected during volcanic eruptions. Open-File Report - U. S. Geological Survey: 16-16.

Mastrolorenzo, G., Petrone, P.P., Pagano, M., Incoronato, A., Baxter, P.J., Canzanella, A. and Fattore, L., 2001. Herculaneum victims of Vesuvius in ad 79. Nature, 410(6830): 769-770.

Maxworthy, T. and Nokes, R.I., 2007. Experiments on gravity currents propagating down slopes. Part 1. The release of a fixed volume of heavy fluid from an enclosed lock into an open channel. Journal of Fluid Mechanics, 584: 433-453.

McEwen, A.S. and Malin, M.C., 1989. Dynamics of Mount St. Helens' 1980 pyroclastic flows, rockslide-avalanche, lahars, and blast. Journal of Volcanology and Geothermal Research, 37(3–4): 205-231.

McTaggart, K.C., 1960. The mobility of nuee ardente. Am. J. Sci., 258: 369-382.

Mellors, R.A. and Sparks, R.S.J., 1991. Spatter-rich pyroclastic flow deposits on Santorini, Greece. Bulletin of Volcanology, 53(5): 327-342.

Middleton, G.V., 1967. Experiments on density and turbidity currents; [Part] 3, Deposition of sediment. Canadian Journal of Earth Sciences = Revue Canadienne des Sciences de la Terre, 4(3): 475-505.

Middleton, G.V. and Neal, W.J., 1989. Experiments on the thickness of beds deposited by turbidity currents. Journal of Sedimentary Petrology, 59(2): 297-307.

Middleton, G.V. and Southward, J.B., 1984. Mechanics of sediment movement. Society of Sedimentary Geology, Tulsa, OK, United States, 400 pp.

Mitani, N.K., Matuttis, H.-G. and Kadono, T., 2004. Density and size segregation in deposits of pyroclastic flow. Geophysical Research Letters, 31(15): n/a-n/a.

Miyabuchi, Y., 1999. Deposits associated with the 1990-1995 eruption of Unzen volcano, Japan. Journal of Volcanology and Geothermal Research, 89(1-4): 139-158.

Moore, J.G., 1967. Base surge in recent volcanic eruptions. Bulletin of Volcanology, 30: 337-363.

Mullineaux, D.R. and Crandell, D.R., 1981. The eruptive history of Mount St. Helens. U. S. Geological Survey Professional Paper: 3-15.

Nairn, I.A. and Self, S., 1978. Explosive eruptions and pyroclastic avalanches from Ngauruhoe in February 1975. Journal of Volcanology and Geothermal Research, 3(1-2): 39-60.

Nakada, S. and Ballard, R.D., 2000. Hazards from pyroclastic flows and surges. Academic Press, San Diego, CA.

Nedderman, R.M. and Laohakul, C., 1980. The thickness of the shear zone of flowing granular materials. Powder Technology, 25(1): 91-100.

Neri, A. and Dobran, F., 1994. Influence of eruption parameters on the thermofluid dynamics of collapsing volcanic columns. Journal of Geophysical Research: Solid Earth, 99(B6): 11833-11857.

Neri, A., Esposti Ongaro, T., Macedonio, G. and Gidaspow, D., 2003a. Multiparticle simulation of collapsing volcanic columns and pyroclastic flow. Journal of Geophysical Research: Solid Earth, 108(B4).

Neri, A., Esposti Ongaro, T., Menconi, G., De'Michieli Vitturi, M., Cavazzoni, C., Erbacci, G. and Baxter, P.J., 2007. 4D simulation of explosive eruption dynamics at Vesuvius. Geophysical Research Letters, 34(4): n/a-n/a.

Neri, A., EspostiOngaro, T., Macedonio, G. and Gidaspow, D., 2003b. Multiparticle simulation of collapsing volcanic columns and pyroclastic flow. Journal of Geophysical Research, 108(B4): 24.

Newhall, C.G., Bronto, S., Alloway, B.V., Banks, N.G., Bahar, I., del Marmol, M.A., Hadisantono, R.D., Holcomb, R.T., McGeehin, J.P., Miksic, J.N., Rubin, M., Sayudi, D.S., Sukhyar, R., Andreastuti, S.D., Tilling, R.I., Torley, R., Trimble, D.A. and Wirakusumah, A.D., 2000. 10,000 years of explosive eruptions of Merapi Volcano, central Java; archaeological and modern implications. Journal of Volcanology and Geothermal Research, 100(1-4): 9-50.

Nogueira, H.I.S., Adduce, C., Alves, E. and Franca, M.J., 2013. Dynamics of the head of gravity currents. Environmental Fluid Mechanics, 14(2): 519-540.

Ogburn, S.E., Calder, E.S., Cole, P.D. and Stinton, A.J., 2014. The effect of topography on ash-cloud surge generation and propagation. Memoirs of the Geological Society of London, 39: 179-194.

Ongaro, T.E., Cavazzoni, C., Erbacci, G., Neri, A. and Salvetti, M.V., 2007. A parallel multiphase flow code for the 3D simulation of explosive volcanic eruptions. Parallel Comput., 33(7-8): 541-560.

Palladino, D.M. and Simei, S., 2002. Three types of pyroclastic currents and their deposits: examples from the Vulsini Volcanoes, Italy. Journal of Volcanology and Geothermal Research, 116(1–2): 97-118.

Palladino, D.M., Simei, S., Sottili, G. and Trigila, R., 2010. Integrated approach for the reconstruction of stratigraphy and geology of Quaternary volcanic terrains: an application to the Vulsini Volcanoes (central Italy). In G. Groppelli e L. Viereck (Eds.), "Stratigraphy and geology in volcanic areas". Geol. Soc. Am., Spec. Pap., 464: 66-84.

Palladino, D.M. and Valentine, G.A., 1995. Coarse-tail vertical and lateral grading in pyroclastic flow deposits of the Latera Volcanic Complex (Vulsini, central Italy): Origin and implications for flow dynamics. Journal of Volcanology and Geothermal Research, 69(3-4): 343-343.

Pardo, N., Cronin, S.J., Németh, K., Brenna, M., Schipper, C.I., Breard, E., White, J.D.L., Procter, J., Stewart, B., Agustín-Flores, J., Moebis, A., Zernack, A., Kereszturi, G., Lube, G., Auer, A., Neall, V. and Wallace, C., 2014a. Perils in distinguishing phreatic from phreatomagmatic ash; insights into the eruption mechanisms of the 6 August 2012 Mt. Tongariro eruption, New Zealand. Journal of Volcanology and Geothermal Research, 286: 397-414.

Pardo, N., Cronin, S.J., Wright, H.M.N., Schipper, C.I., Smith, I. and Stewart, B., 2014b. Pyroclast textural variation as an indicator of eruption column steadiness in andesitic Plinian eruptions at Mt. Ruapehu. Bulletin of Volcanology, 76(5): 1-19.

Parker, G., Garcia, M., Fukushima, Y. and Yu, W., 1987. Experiments on turbidity currents over an erodible bed. Journal of Hydraulic Research = Journal de Recherches Hydrauliques, 25(1): 123-147.

Patra, A.K., Bauer, A.C., Nichita, C.C., Pitman, E.B., Sheridan, M.F., Bursik, M.I., Rupp, B., Webber, A., Stinton, A.J., Namikawa, L.M. and Renschler, C.S., 2005. Parallel adaptive numerical simulation of dry avalanches over natural terrain. Journal of Volcanology and Geothermal Research, 139(1-2): 1-21.

Pfeiffer, T., 2001. Vent development during the Minoan eruption (1640 BC) of Santorini, Greece, as suggested by ballistic blocks. Journal of Volcanology and Geothermal Research, 106(3-4): 229-242.

Phillips, J.C., Hogg, A.J., Kerswell, R.R. and Thomas, N.H., 2006. Enhanced mobility of granular mixtures of fine and coarse particles. Earth and Planetary Science Letters, 246(3–4): 466-480.

Pitman, E.B., Nichita, C.C., Patra, A., Bauer, A., Sheridan, M. and Bursik, M., 2003. Computing granular avalanches and landslides. Physics of Fluids, 15(12): 3638-3646.

Pouliquen, O., 1999. Scaling laws in granular flows down rough inclined planes. Physics of Fluids, 11(3): 542-548.

Pouliquen, O., Delour, J. and Savage, S.B., 1997. Fingering in granular flows. Nature(386): 816-817.

Pouliquen, O. and Vallance, J.W., 1999. Segregation induced instabilities of granular fronts. Chaos, 3(9): 621-630.

Procter, J.N., Cronin, S.J., Zernack, A.V., Lube, G., Stewart, R.B., Nemeth, K. and Keys, H., 2014. Debris flow evolution and the activation of an explosive hydrothermal system; Te Maari, Tongariro, New Zealand. Journal of Volcanology and Geothermal Research(0).

Quane, S.L. and Russell, J.K., 2005. Ranking welding intensity in pyroclastic deposits. Bulletin of Volcanology, 67(2): 129-143.

Ragan, D.M. and Sheridan, M.F., 1972. Compaction of the Bishop Tuff, California. Geological Society of America Bulletin, 83(1): 95-106.

Rastello, M. and Hopfinger, E.J., 2004. Sediment-entraining suspension clouds: a model of powder-snow avalanches. Journal of Fluid Mechanics, 509: 181-206.

Rivard, W.C. and Torrey, M.D., 1977. K-FIX: A computer program for transient, two-dimensional, two-fluid flow. LA-NUREG-6623, Los Alamos Natl. Lab., Los Alamos, N. M.

Rivard, W.C. and Torrey, M.D., 1978. PERM: Corrections to the K-FIX code, LA-NUREG-6623 Suppl., Los Alamos Natl. Lab., Los Alamos, N. M.

Rivard, W.C. and Torrey, M.D., 1979. THREED: An extension of the K-FIX code for three-dimensional calculations, LA-NUREG-6623 Suppl. II, Los Alamos Natl. Lab., Los Alamos, N. M.

Roche, O., 2012. Depositional processes and gas pore pressure in pyroclastic flows: an experimental perspective. Bulletin of Volcanology, 74(8): 1807-1820.

Roche, O., Gilbertson, M., Phillips, J. and Sparks, R.S.J., 2002. Mobility of pyroclastic flows; new insights from experiments on gas-fluidized granular flows, Mount Pelee 1902-2002; explosive volcanism in subduction zones; program and abstracts--Montagne Pelee 1902-2002; volcanisme explosif en zones de subduction; programme et resumes. Institut de Physique du Globe de Paris, Paris, France, pp. 39.

Roche, O., Gilbertson, M.A., Phillips, J.C. and Sparks, R.S.J., 2005. Inviscid behaviour of fines-rich pyroclastic flows inferred from experiments on gas–particle mixtures. Earth and Planetary Science Letters, 240(2): 401-414.

Roche, O., Montserrat, S., Niño, Y. and Tamburrino, A., 2008. Experimental observations of water-like behavior of initially fluidized, dam break granular flows and their relevance for the propagation of ash-rich pyroclastic flows. Journal of Geophysical Research: Solid Earth, 113(B12): n/a-n/a.

Roche, O., Nino, Y., Mangeney, A., Brand, B., Pollock, N. and Valentine, G.A., 2013a. Dynamic pore-pressure variations induce substrate erosion by pyroclastic flows. Geology (Boulder), 41(10): 1107-1110.

Roche, O., Phillips, C. and Kelfoun, K., 2013b. Pyroclastic density currents. In: S.A. Fagents, T.K.P. Gregg and R.M.C. Lopes (Editors), Modeling Volcanic Processes: The Physics and Mathematics of Volcanism. Cambridge, New York.

Rose, W.I. and Chesner, C.A., 1987. Dispersal of ash in the great Toba eruption, 75 ka. Geology, 15(10): 913-917.

Rose, W.I., Jr., Pearson, T. and Bonis, S., 1977. Nuee ardente eruption from the foot of a dacite lava flow, Santiaguito Volcano, Guatemala. Bulletin Volcanologique, 40(1): 23-38.

Rosenbaum, J.G. and Waitt, R.B., Jr., 1981. Summary of eyewitness accounts of the May 18 eruption. U. S. Geological Survey Professional Paper: 53-67.

Ross, P.S., White, J.D.L., Valentine, G.A., Taddeucci, J., Sonder, I. and Andrews, R.G., 2013. Experimental birth of a maar-diatreme volcano. Journal of Volcanology and Geothermal Research, 260: 1-12.

Rouse, H.U.S.S.C.S.A.S.o.C.E.M., 1939. An analysis of sediment transportation in the light of fluid turbulence. U.S. Dept. of Agriculture, Soil Conservation Service, Washington, D.C.

Rowlands, D.P., White, R.S. and Haines, A.J., 2005. Seismic tomography of the Tongariro volcanic centre, New Zealand. Geophysical Journal International, 163(3): 1180-1194.

Rowley, P., Roche, O., Druitt, T. and Cas, R., 2014. Experimental study of dense pyroclastic density currents using sustained, gas-fluidized granular flows. Bulletin of Volcanology, 76(9): 1-13.

Saucedo, R., Macías, J.L., Sheridan, M.F., Bursik, M.I. and Komorowski, J.C., 2005. Modeling of pyroclastic flows of Colima Volcano, Mexico: implications for hazard assessment. Journal of Volcanology and Geothermal Research, 139(1–2): 103-115.

Savage, S.B., 1979. Gravity flow of cohesionless granular material in chutes and channels. Journal of Fluid Mechanics(92): 53-96.

Savage, S.B., 1983. Granular flows down rough inclines - review and extension. In: Jenkins, J.T. and Satake, M. (Eds), Mechanics of granular materials: new models and constitutive relations. Elsevier, pp.261-281, Amsterdam.

Savage, S.B., 1984. The mechanics of rapid granular flows. Adv. Appl. Mech, 24: 289-366.

Savage, S.B. and Hutter, K., 1989a. The motion of a finite granular material down a rough incline. Journal of Fluid Mechanics(199): 177-215.

Savage, S.B. and Hutter, K., 1989b. The motion of a finite mass of granular material down a rough incline. Journal of Fluid Mechanics, 199: 177-215.

Scarth, A., 1999. Savage Earth. HarperCollins Publishers Ltd. Copyright .

Schmincke, H.U., Fisher, R.V. and Waters, A.C., 1973. Antidune and chute and pool structures in the base surge deposits of the Laacher See area, Germany. Sedimentology, 20(4): 553-574.

Scolamacchia, T. and Schouwenaars, R., 2009. High-speed impacts by ash particles in the 1982 eruption of El Chichon, Mexico. Journal of Geophysical Research, 114(B12): 0-Citation B12206.

Scott, A.C., Sparks, R.S.J., Bull, I.D., Knicker, H. and Evershed, R.P., 2008. Temperature proxy data and their significance for the understanding of pyroclastic density currents. Geology (Boulder), 36(2): 143-146.

Scott, W.E. and Tilling, R.I., 1989. Volcanic-hazard zonation and long-term forecasts. Am. Geophys. Union, Washington, DC.

Self, S., Kienle, J. and Huot, J.P., 1980. Ukinrek Maars, Alaska; II, Deposits and formation of the 1977 craters. Journal of Volcanology and Geothermal Research, 7(1-2): 39-65.

Sequeiros, O.E., 2012a. Estimating turbidity current conditions from channel morphology: A Froude number approach. Journal of Geophysical Research. C. Oceans, 117(C4).

Sequeiros, O.E., 2012b. Estimating turbidity current conditions from channel morphology: A Froude number approach. Journal of Geophysical Research: Oceans, 117(C4): n/a-n/a.

Sequeiros, O.E., Cantelli, A., Viparelli, E., White, J.D.L., Garcia, M.H. and Parker, G., 2009a. Modeling turbidity currents with nonuniform sediment and reverse buoyancy. Water Resources Research, 45(6): W06408.

Sequeiros, O.E., Naruse, H., Endo, N., Garcia, M.H. and Parker, G., 2009b. Experimental study on self-accelerating turbidity currents. Journal of Geophysical Research: Oceans, 114(C5): n/a-n/a.

Sequeiros, O.E., Spinewine, B., Beaubouef, R.T., Sun, T., Garcia, M.H. and Parker, G., 2010. Bedload transport and bed resistance associated with density and turbidity currents. Sedimentology, 57(6): 1463-1490.

Sheridan, M.F. and Malin, M.C., 1983. Explosive Volcanism Application of computer-assisted mapping to volcanic hazard evaluation of surge eruptions: Vulcano, lipari, and vesuvius. Journal of Volcanology and Geothermal Research, 17(1): 187-202.

Sheridan, M.F. and Wang, Y., 2005. Cooling and welding history of the Bishop Tuff in Adobe Valley and Chidago Canyon, California. Journal of Volcanology and Geothermal Research, 142(1-2): 119-144.

Shin, J.O., Dalziel, S.B. and Linden, P.F., 2004. Gravity currents produced by lock exchange. J. Fluid Mech., 521: 1-34.

Siebert, L., Glicken, H. and Tadahide, U., 1987. Volcanic hazards from Bezymianny and Bandai-type eruptions. Bulletin of Volcanology, 49(1): 435-459.

Sigurdsson, H., Carey, C., Cornell, W. and Pescatore, T., 1985. The eruption of Vesivius in A.D. 79. National Geographic Research 1: 332-387.

Sigurdsson, H., Carey, S.N. and Fisher, R.V., 1987. The 1982 eruption of El Chichon Volcano, Mexico; 3, Physical properties of pyroclastic surges. Bulletin of Volcanology, 49(2): 467-488.

Sigurdsson, H., Cashdollar, S. and Sparks, R.S.J., 1982. The eruption of Vesuvius in AD 79: reconstruction from historical and volcanological evidence. Am. J. Archaeol. 86: 39-51.

Silva Parejas, C., Druitt, T.H., Robin, C., Moreno, H. and Naranjo, J.A., 2010. The Holocene Pucon eruption of Volcan Villarrica, Chile; deposit architecture and eruption chronology. Bulletin of Volcanology, 72(6): 677-692.

Simpson, J., 1972. Effects of the lower boundary on the head of a gravity current. Journal of Fluid Mechanics, 53(04): 759-768.

Simpson, J., 1997. Gravity currents in the Environment and the Laboratory 2nd edition, Cambridge University Press, Cambridge.

Simpson, J. and Britter, R.E., 1979a. The dynamics of the head of a gravity current advancing over a horizontal surface. J. Fluid. Mech.(94): 477-495.

Simpson, J.E., 1982. Gravity Currents in the Laboratory, Atmosphere, and Ocean. Annual Review of Fluid Mechanics, 14(1): 213-234.

Simpson, J.E. and Britter, R.E., 1979b. The dynamics of the head of a gravity current advancing over a horizontal surface. Journal of Fluid Mechanics, 94(03): 477-495.

Smith, R.L., 1960. Zones and zonal variations in welded ash flows. U. S. Geological Survey Professional Paper: 149-159.

Sohn, Y.K., 1997. On traction-carpet sedimentation. Journal of Sedimentary Research, 67(3): 502-509.

Sohn, Y.K. and Chough, S.K., 1989. Depositional processes of the Suwolbong tuff ring, Cheju Island (Korea). Sedimentology, 36(5): 837-855.

Sohn, Y.K. and Chough, S.K., 1993. The Udo tuff cone, Cheju Island, south Korea - transformation of pyroclastic fall into debris fall and grain flow on a steep volcanic cone slope. Sedimentology, 40: 769-786.

Sparks, R.S.J., 1976. Grain size variations in ignimbrites and implications for the transport of pyroclastic flows. Sedimentology, 23(2): 147-188.

Sparks, R.S.J., Barclay, J., Calder, E.S., Herd, R.A., Komorowski, J.C., Luckett, R., Norton, G.E., Ritchie, L.J., Voight, B. and Woods, A.W., 2002. Generation of a debris avalanche and violent pyroclastic density current on 26 December (Boxing Day) 1997 at Soufriere Hills Volcano, Montserrat. Memoirs of the Geological Society of London, 21: 409-434.

Sparks, R.S.J., Bonnecaze, R.T., Huppert, H.E., Lister, J.R., Hallworth, M.A., Mader, H. and Phillips, J., 1993. Sediment-laden gravity currents with reversing buoyancy. Earth and Planetary Science Letters, 114(2–3): 243-257.

Sparks, R.S.J., Bursik, M.I., Carey, S.N., Gilbert, J.S., Glaze, L.S., Sigurdsson, H. and Woods, A.W., 1997. Volcanic plumes. John Wiley and Sons, Chichester, Chichester, United Kingdom (GBR), 574-574 pp.

Sparks, R.S.J., Francis, P.W., Hamer, R.D., Pankhurst, R.J., O'Callaghan, L.O., Thorpe, R.S. and Page, R., 1985. Ignimbrites of the Cerro Galan Caldera, NW Argentina. Journal of Volcanology and Geothermal Research, 24(3-4): 205-248.

Sparks, R.S.J., Self, S. and Walker, G.P.L., 1973. Products of Ignimbrite Eruptions. Geology (Boulder), 1(3): 115-118.

Sparks, R.S.J. and Walker, G.P.L., 1973. The Ground Surge Deposit: a third type of pyroclastic rock. Nature; Physical Science (London), 241(107): 62-64.

Sparks, R.S.J., Wilson, L. and Hulme, G., 1978a. Theoretical modeling of the generation, movement, and emplacement of pyroclastic flows by column collapse. Journal of Geophysical Research: Solid Earth, 83(B4): 1727-1739.

Sparks, R.S.J., Wilson, L. and Hulme, G., 1978b. Theoritical modeling of generation, movement, and emplacement of pyroclastic flows by column collapse. Journal of Geophysical Research, 83(NB4): 1727-1739.

Stamhuis, E., 2006. Basics and principles of particle image velocimetry (PIV) for mapping biogenic and biologically relevant flows. Aquat Ecol, 40(4): 463-479.

Stothers, R.B., 1984. The great Tambora eruption in 1815 and its aftermath. Science, 224(4654): 1191-1198.

Sugioka, I. and Bursik, M., 1995. Explosive fragmentation of erupting magma. Nature (London), 373(6516): 689-692.

Sulpizio, R. and Dellino, P., 2008. Sedimentology, depositional mechanisms and pulsating behaviour of pyroclastic density currents. In: Martí, J., Gottsman, J. (Eds.), Caldera Volcanism: Analysis, Modelling and Response. Developments in Volcanology, 10, Elsevier: 57-96.

Sulpizio, R., Dellino, P., Doronzo, D.M. and Sarocchi, D., 2014. Pyroclastic density currents; state of the art and perspectives. Journal of Volcanology and Geothermal Research, 283: 36-65.

Sulpizio, R., Mele, D., Dellino, P. and La Volpe, L., 2007. Deposits and physical properties of pyroclastic density currents during complex Subplinian eruptions: the AD 472 (Pollena) eruption of Somma-Vesuvius, Italy. Sedimentology, 54(3): 607-635.

Sulpizio, R., Sarocchi, D., Bartali, R. and Rodriguez-Sedano, L.A., 2013. Laboratory experiments on transport and deposition of granular flows over a variable break in

slope: insights for depositional behaviour of pyroclastic and volcaniclastic density currents. IAVCEAI general assembly, Kagoshima, Japan, Abstract volume.

Swanson, D.A., Zolkos, S.P. and Haravitch, B., 2012. Ballistic blocks around Kilauea Caldera; their vent locations and number of eruptions in the late 18th century. Journal of Volcanology and Geothermal Research, 231-232: 1-11.

Syamlal, M., 1994. MFIX documentation: User's manual, DOE/METC-95/1013, DE9500,031, 87 pp., U.S. Dep. of Energy, Washington, D. C.

Syamlal, M., 1998. MFIX documentation: Numerical technique, 80 pp., DOE/MC/31346-5824, DE98002029, U.S. Dep. of Energy, Washington, D. C.

Syamlal, M.W.R. and O'Brien, T.J., 1993. MFIX documentation: Theory guide, 49 pp., DOE/METC-94/1004, DE9400,097, U.S. Dep. of Energy, Washington, D. C.

Taberlet, N., Richard, P., Jenkins, J.T. and Delannay, R., 2007. Density inversion in rapid granular flows: the supported regime. Eur. Phys. J. E, 22(1): 17-24.

Taddeucci, J., Valentine, G.A., Sonder, I., White, J.D.L., Ross, P.S. and Scarlato, P., 2013 The effect of pre-existing craters on the initial development of explosive volcanic eruptions; an experimental investigation. Geophys. Res. Lett. , 40(3): 507-510.

Tanguy, J.-C., 1994. The 1902-1905 eruptions of Montagne Pelee, Martinique: anatomy and retrospection. Journal of Volcanology and Geothermal Research, 60(2): 87-107.

Taylor, G.A., 1958. The 1951 eruption of Mount Lamington. Papua. Aust. Bur. Miner. Resour. Geol. Bull., 38: 1-117.

Thielicke, W. and Stamhuis, E.J., 2014. PIVlab-Towards user-friendly, affordable and accurate digital particle image velocimetry in MATLAB. J. Open Res. Software, 2(1).

Topping, W.W., 1974. Some aspects of Quaternary history of Tongariro volcanic centre. (Doctoral Thesis)

Toro, E.F., 2001. Shock-Capturing Methods for Free-Surface Shallow Flows. Wiley, New York.

Turner, J.S., 1986. Turbulent entrainment: the development of the entrainment assumption, and its application to geophysical flows. . J Fluid Mech, 173: 431-471.

Ui, T., Matsuwo, N., Sumita, M. and Fujinawa, A., 1999. Generation of block and ash flows during the 1990-1995 eruption of Unzen Volcano, Japan. Journal of Volcanology and Geothermal Research, 89(1-4): 123-137.

Valentine, G.A., 1987. Stratified flow in pyroclastic surges. Bulletin of Volcanology, 49(4): 616-630.

Valentine, G.A., 1998. Damage to structures by pyroclastic flows and surges, inferred from nuclear weapons effects. Journal of Volcanology and Geothermal Research, 87(1-4): 117-140.

Valentine, G.A. and Fisher, R.V., 2000. Pyroclastic surges and blasts. (Los Alamos National Laboratory, Los Alamos, NM, United States); Fisher, Richard V., Editors: Sigurdsson, Haraldur; Houghton, Bruce F.; McNutt, Stephen R.; Rymer, Hazel; Stix, John; Ballard, Robert D. , Encyclopedia of volcanoes: 571-580.

Valentine, G.A., Graettinger, A.H. and Sonder, I., 2014. Explosion depths for phreatomagmatic eruptions. Geophysical Research Letters, 41(9): 3045-3051.

Valentine, G.A. and Wohletz, K.H., 1989. Numerical models of Plinian eruption columns and pyroclastic flows. Journal of Geophysical Research, 94(B2): 1867-1887.

Voight, B., 1981. Time scale for the first moments of the May 18 eruption. U. S. Geological Survey Professional Paper: 69-86.

Voight, B., Komorowski, J.C., Norton, G.E., Belousov, A.B., Belousova, M., Boudon, G., Francis, P.W., Franz, W., Heinrich, P., Sparks, R.S.J. and Young, S.R., 2002. The 26

December (Boxing Day) 1997 sector collapse and debris avalanche at Soufriere Hills Volcano, Montserrat. Memoirs of the Geological Society of London, 21: 363-407.

Voight, B., Young, K.D., Hidayat, D., Subandriyo, Purbawinata, M.A., Ratdomopurbo, A., Suharna, Panut, Sayudi, D.S., LaHusen, R.G., Marso, J., Murray, T.L., Dejean, M., Iguchi, M. and Ishihara, K., 2000. Deformation and seismic precursors to dome-collapse and fountain-collapse nuees ardentes at Merapi Volcano, Java, Indonesia; 1994-1998. Journal of Volcanology and Geothermal Research, 100(1-4): 261-287.

Wadge, G., Jackson, P., Bower, S.M., Woods, A.W. and Calder, E., 1998. Computer simulations of pyroclastic flows from dome collapse. Geophysical Research Letters, 25(19): 3677-3680.

Wadge, G., Voight, B., Sparks, R.S.J., Cole, P.D., Loughlin, S.C. and Robertson, R.E.A., 2014. An overview of the eruption of Soufriere Hills Volcano, Montserrat from 2000 to 2010. Memoirs of the Geological Society of London, 39: 1-40.

Waitt, R.B., Mastin, L.G. and Miller, T.P., 1995. Ballistic showers during Crater Peak eruptions of Mount Spurr Volcano, summer 1992. U. S. Geological Survey Bulletin: 89-106.

Walker, G.P.L., 1971. Grain-size characteristics of pyroclastic deposits. Journal of Geology, 79(6): 696-714.

Walker, G.P.L., 1983. Ignimbrite types and ignimbrite problems. Journal of Volcanology and Geothermal Research, 17(1-4): 65-88.

Walker, G.P.L., Hayashi, J.N. and Self, S., 1995. Travel of pyroclastic flows as transient waves; implications for the energy line concept and particle-concentration assessment. Journal of Volcanology and Geothermal Research, 66(1-4): 265-282.

Walker, G.P.L., Heming, R.F. and Wilson, C.J.N., 1980. Low-aspect ratio ignimbrites. Nature, 283(5744): 286-287.

Walter, T.R., Subandriyo, J., Kirbani, S., Bathke, H., Suryanto, W., Aisyah, N., Darmawan, H., Jousset, P., Luehr, B.G. and Dahm, T., 2015. Volcano-tectonic control of Merapi's lava dome splitting; the November 2013 fracture observed from high-resolution TerraSAR-X data. Tectonophysics, 639: 23-33.

Waythomas, C.F. and Neal, C.A., 1998. Tsunami generation by pyroclastic flow during the 3500-year B.P. caldera-forming eruption of Aniakchak Volcano, Alaska. Bulletin of Volcanology, 60(2): 110-124.

Wells, M., Cenedese, C. and Caulfield, C.P., 2010. The relationship between flux coefficient and entrainment ratio in density currents. . J Phys Oceanogr (40): 2713-2727.

Wilson, C.J.N., 1980. The role of fluidization in the emplacement of pyroclastic flows: an experimental approach. J. Volcanol. Geotherm. Res.(8): 231-249.

Wilson, C.J.N., 1984a. The role of fluidization in the emplacement of pyroclastic flows, 2: Experimental results and their interpretation. Journal of Volcanology and Geothermal Research, 20(1): 55-84.

Wilson, C.J.N., 1984b. The role of fluidization in the emplacement of pyroclastic flows; 2, Experimental results and their interpretation. Journal of Volcanology and Geothermal Research, 20(1-2): 55-84.

Wilson, C.J.N., 1985. The Taupo eruption, New Zealand; II, The Taupo ignimbrite. Philosophical Transactions of the Royal Society of London, Series A: Mathematical and Physical Sciences, 314(1529): 229-310.

Wilson, C.J.N., Dade, W.B. and Huppert, H.E., 1997. Emplacement of Taupo ignimbrite; discussion and reply. Nature (London), 385(6614): 306-308.

Wilson, C.J.N., Houghton, B.F., Kamp, P.J.J. and McWilliams, M.O., 1995. An exceptionally widespread ignimbrite with implications for pyroclastic flow emplacement. Nature (London), 378(6557): 605-607.

Wilson, C.J.N. and Walker, G.P.L., 1982. Ignimbrite depositional facies; the anatomy of a pyroclastic flow. Journal of the Geological Society of London, 139, Part 5: 581-592.

Wohletz, K.H., 1998. Pyroclastic surges and compressible two-phase flow. Developments in Volcanology: 247-312.

Wohletz, K.H., McGetchin, T.R., Sandford, M.T. and Jones, E.M., 1984. Hydrodynamic aspects of caldera-forming eruptions: Numerical models. Journal of Geophysical Research: Solid Earth, 89(B10): 8269-8285.

Wohletz, K.H. and Sheridan, M.F., 1979. A model of pyroclastic surge. Special Paper - Geological Society of America(180): 177-194.

Wohletz, K.H., Sheridan, M.F. and Brown, W.K., 1989. Particle size distributions and the sequential fragmentation/transport theory applied to volcanic ash. Journal of Geophysical Research: Solid Earth, 94(B11): 15703-15721.

Wohletz, K.H. and Valentine, G.A., 1990. Cumputer simulations of explosive volcanic eruptions. In: M.P. Ryan (Editor), Magma Transport and Storage. Wiley, London, pp. 113-135.

Wright, J.V. and Walker, G.P.L., 1981. Eruption, transport and deposition of ignimbrite - a case study from Mexico. . J. Volcanol. Geotherm. Res., 9: 111-131.

Yamamoto, T., Nakamura, Y. and Glicken, H., 1999. Pyroclastic density current from the 1888 phreatic eruption of Bandai Volcano, NE Japan. Journal of Volcanology and Geothermal Research, 90(3-4): 191-207.

Yamamoto, T., Takarada, S. and Suto, S., 1993. Pyroclastic flows from the 1991 eruption of Unzen Volcano, Japan. Bulletin of Volcanology, 55(3): 166-175.

Zanella, E., Gurioli, L., Lanza, R., Sulpizio, R. and Bontempi, M., 2008. Deposition temperature of the AD 472 Pollena pyroclastic density current deposits, Somma-Vesuvius, Italy. Bulletin of Volcanology, 70(10): 1237-1248.

Zehner, P. and Schlunder, E.U., 1970. Warmeleiftahigkeit von Schuttungen bei mabigen Temperaturen. Chem. Ing. Tech.(42): 933-941.

Zhang, D.Z. and VanderHeyden, W.B., 2002. The effect of mesoscale structures on the macroscopic momentum equations for two phase flows. Int. J. Multiph. Flow(28): 805- 822.

Zhu, J.B., Lee, C.B., Chen, G.Q. and Lee, J.H.W., 2006. PIV observation of instantaneous velocity structure of lock release gravity currents in the slumping phase. Communications in Nonlinear Science and Numerical Simulation, 11(2): 262-270.

Zimanowski, B., Büttner, R., Dellino, P., White, J.D.L. and Wohletz, K.H., 2015. Chapter 26 - Magma–Water Interaction and Phreatomagmatic Fragmentation. In: H. Sigurdsson (Editor), The Encyclopedia of Volcanoes (Second Edition). Academic Press, Amsterdam, pp. 473-484.

Zollinger, H., 1855. Besteigung des Vulkanes Tambora auf der Insel Sumbawa und Schilderung der Erupzion desselben im Jahr 1815 Wurster, Winterthur.

Appendices

A DVD accompanies the thesis and is stored in a pocket at the rear. The DVD contains all the following files:

Appendix A: Supplementary data

This appendix comprises the relevant data of Chapters 4–8 which are organized into folders by chapters.

Appendix for Chapter 3.

- Supplementary videos 1 and 2 referred to in Chapter 3. The supplementary video 1 shows the large-scale experiments from various angles while the supplementary video 2 displays the high-speed movie showing the intermediate regime with mesoscale structures.
- Velocity profiles used in Surfer 10.0 are presented in the file “Velocities.xlsx”.

Appendix for Chapter 4.

- The video display the different transport regimes in PDCs as described in Chapter 4 through Lagrangian and Eulerian approaches.
- The spreadsheet used to estimate settling velocities from particle size, fluid density and shape factor is presented as “Settling velocity.xlsx”.
- Velocity and concentration data used for fluid dynamic parameter estimates and dynamic pressure calculations are presented in “Chapter 4- supplementary data”.

- The spreadsheet used to estimate the dynamic viscosity as a function of concentration is given in “Dynamic viscosity calculator.xlsx”
- Grain-size distributions collected in vertical samplers and used in the Stokes and Stability are also presented are presented in “grain-size distribution.xlsx”

Appendix for Chapter 5.

- All kinematic data are presented in the file “Kinematic data.xlsx”.
- Geometrical data of the head shape is given in “Supplementary data_Chapter 5.xlsx”

Appendix for Chapter 6.

- Mapped boundaries of the debris avalanche “debris_avalanche.shp”, Upper Te Maari crater “crater2.shp”and fissure “fissure_w.shp”, ballistic field “extent ballisticsCopy.shp”
- Mapped ballistic craters “ballistic craters_NZTM-SIZE.shp” and size distributions “ballistic craters_NZTM-SIZECopy” are also presented.

Appendix for Chapter 7.

- Tables of the grain-size distributions of all samples are presented in “Chapter 7-grain-size data.xlsx”
- Mapped boundary of the maximum extent of the PDC “Surge extent.sph” and sample point map is presented in “Sample locations.shp”

Appendix B: Statement of contribution

This thesis contains chapters that were published as journal articles. This appendix contains the “Statement of contributions to doctoral thesis containing publications” form DRC 16.